THESE DE DOCTORAT

Présentée à
L'UNIVERSITE DE LILLE 1
Ecole Doctoral Régionale Sciences Pour l'Ingénieur Lille Nord-de-France

Pour obtenir le grade de
DOCTEUR EN SCIENCES
Dans la spécialité :
Micro et Nano Technologies, Acoustique et Télécommunications
Par

Qian WANG

Carbon-based Materials: Application in Electrochemical Sensing

Directeur de thèse :
Dr. Rabah BOUKHERROUB

Co-directrice de thèse :
Prof. Sabine SZUNERITS

Soutenue le 24 Octobre 2016 devant le jury composé de :

Prof. Petra HELLWIG	Rapporteur	Université de Strasbourg
Dr. Souhir BOUJDAY	Rapporteur	Université Paris 6
Dr. Liza RASSAEI	Examinateur	Delft University of Technology
Prof. Tuami LASRI	Président	Université Lille 1

© 2016 Tous droits réservés.

lilliad.univ-lille.fr

ACKNOWLEDGEMENTS

During the three years' stay in France, I have received tremendous support, help and encouragement from which I get the energy to move forward. At this moment, I would like to express my thanks to those amazing individuals around me.

First of all, my deepest thanks go to my PhD supervisors, Dr. Rabah Boukherroub and Prof. Sabine Szunerits, who are always there for me with their continued guidance, scientific ideas and discussions, encouragement and support during the past three years. When hundreds of time I got stuck in research, it is always their sharp view and professional advice that drag me out of the dilemma. Those valuable talks make my PhD journey thoughtful and fruitful. I also thank them for the time and patience of correcting the thesis manuscript even on weekends. Their professional attitude and scientific thinking will always encourage me to move forward in future work. I also thank Rabah for the papers which helped me with the residence permit issues and Sabine for her kindness as my guarantor for apartment application.

I would like to thank Dr. Palaniappan Subramanian for providing the carbon nanotube carpet electrode and Dr. Nianjun Yang for carbon nanofiber powders.

My special thanks go to Prof. Musen Li in Shandong University, who encouraged me to pursue new academic career in France and gives valuable advices and help in future career plans. I greatly appreciate his kindness and generosity. He shows the characters that one can learn to be a better person.

My heartfelt thanks go to the colleagues in NanoBioInterfaces group of IEMN. Thanks Alex for his patience in teaching me the manipulation and basic rules of the instruments in the lab, and help with language issues. It is a pleasant memory working with him in the same office during three years. To Yannick, thanks for all the help in performing SEM images. Many thanks to Palan, who showed me some experiments in electrochemistry at the very beginning of my PhD, which helped me to move faster into the field. I would like to thank Stefka for her always being nice and help with the prefecture problems. I also remember those discussions and relaxing talks with Florina after work. In addition, I would like to thank Nadia, Manu, Amer, Kostian, Fouazia, Roxana, Ioana, Houcem, Hakim, Sawsen, Patrik and all the lab members I met in this wonderful group for sharing ideas with mutual improvement.

© 2016 Tous droits réservés.

lilliad.univ-lille.fr

ACKNOWLEDGEMENTS

I would like to thank my friends (or even mentors) who have offered great help and encouragement to me. To Qi Wang and Bing Hong, thanks for picking me up at the station and the guidance in many ways to help me survive in France when I arrived. To dear Shixiang Lu, who is at my mother's age and treated me as a daughter while she was here as a visiting scholar. Her encouragements helped me go through the hardest time here. To Lijie He, her strength, independence and diligence has inspired me to become more concentrated on work. I would like also to express my thanks to Ning Cao for his taking care and valuable advices on many aspects. Furthermore, I am grateful to the invitations of parties organized by Chengnan Li, Fei Wang, Yuanyuan Cheng, Zijie Wang, Xiaofeng Yi and other friends (mainly from UCCS). Thanks for their companion and delicious food while I am homesick with thousands of miles away from home.

In particular, I thank Chinese government for offering me with the Chinese Scholarship Council (CSC) Award as financial support, which allowed me to conduct this research work in France.

Most importantly, I owe my most sincere gratitude to my beloved parents. They are always there for me with unconditional love, support, encouragement and understanding throughout my life. I also thank my brother and sister in law for taking care of my parents and families while I am away from home for almost ten years.

At last, I offer my regards and blessings to all the people who have supported me in different ways during this memorable period.

Qian Wang

Villeneuve d'Ascq, France

September 5th, 2016

© 2016 Tous droits réservés.

lilliad.univ-lille.fr

RÉSUMÉ

Les nanomatériaux à base de carbone ont suscité un intérêt considérable en raison de leurs applications potentielles dans divers domaines. Ces matériaux sont également considérés comme des matrices idéales pour le développement de capteurs/biocapteurs électrochimiques avec une grande sensibilité. Au cours de ce travail de thèse, on a utilisé des nanotubes de carbone alignés verticalement dopés à l'azote (VA-NCNT), des électrodes d'or modifiées avec des nanofibres de carbone/hydroxyde de cobalt (CNFs/$Co(OH)_2$) par dépôt électrophorétique, ou avec des nanoparticules de cuivre /oxyde de graphène réduit (Cu NPs/rGO), ainsi que des électrodes de carbone vitreux modifiées avec des nanoparticules d'or/rGO (Au NPs/rGO), et évalué leurs caractéristiques électrochimiques pour la construction de capteurs/biocapteurs .

La modification des électrodes de VA-NCNT avec des aptamères lysozyme a permis une détection sensible (du l'ordre du femtomolaire) de lysozyme dans le sérum. Cette méthode a été appliquée avec succès pour la détection de lysozyme chez des personnes atteintes de la maladie inflammatoire de l'intestin (IBD).

Les électrodes d'or modifiées par rGO/Cu NPs et CNFs/$Co(OH)_2$ ont montré un excellent comportement pour l'oxydation électro-catalytique du glucose. Elles ont été utilisées pour la détection non enzymatique du glucose dans des solutions tampons de façon sélective mais aussi pour la détermination du glucose dans le sérum humain. La détection non enzymatique du peroxyde d'hydrogène a également été réalisée sur des électrodes modifiées par rGO/Au NPs, ce dernier a été préparé en utilisant la tyrosine pour la réduction d'oxyde de graphène (GO) et le sel d'Au.

Mots clés : Nanotubes de carbone alignés verticalement; Nanofibres de carbone; Réduction d'oxyde de graphène; Nanoparticules; Tyrosine; Glucose; Peroxyde d'hydrogène; Détection électrochimique.

© 2016 Tous droits réservés.

lilliad.univ-lille.fr

ABSTRACT

Carbon-based nanomaterials have attracted tremendous interest because of their potential applications in various fields. These materials are also considered ideal matrixes for the development of highly sensitive electrochemical based sensing platforms. In this thesis, vertically aligned nitrogen-doped carbon nanotube (VA-NCNT) electrodes, gold electrodes modified with cobalt hydroxide embedded carbon nanofibers (CNFs/$Co(OH)_2$) through electrophoretic deposition, or copper nanoparticles loaded reduced graphene oxide (rGO/Cu NPs), as well as chemically formed gold nanoparticle decorated rGO (rGO/Au NPs) modified glassy carbon electrodes were developed, and their electrochemical and sensing capabilities were investigated.

Modification of VA-NCNT electrodes with lysozyme aptamers resulted in a sensor with femtomolar sensitivity to lysozyme in serum and was successfully applied for the differentiation of healthy patients and inflammatory bowel disease (IBD) affected ones.

rGO/Cu NPs and CNFs/$Co(OH)_2$ coated gold electrodes showed excellent electro-catalytic oxidation behavior towards glucose and were employed as non-enzymatic glucose sensors for glucose determination in human serum. Non-enzymatic hydrogen peroxide detection was also achieved on rGO/Au NPs modified electrodes, where the matrix was formed using tyrosine as dual reductant of graphene oxide (GO) and Au salt.

Key words: Vertically aligned nitrogen doped carbon nanotubes; Carbon nanofibers; Reduced graphene oxide; Nanoparticles; Tyrosine; Glucose; Hydrogen peroxide; Electrochemical sensing.

© 2016 Tous droits réservés.

lilliad.univ-lille.fr

TABLE OF CONTENTS

© 2016 Tous droits réservés.

lilliad.univ-lille.fr

TABLE OF CONTENTS

© 2016 Tous droits réservés.

lilliad.univ-lille.fr

TABLE OF CONTENTS

© 2016 Tous droits réservés.

lilliad.univ-lille.fr

ACRONYMS

AA	Ascorbic acid
Au NPs	Gold nanoparticles
BSA	Bovine serum albumin
CNFs	Carbon nanofibers
CNT	Carbon nanotubes
Cu NPs	Copper nanoparticles
CV	Cyclic voltammetry
CVD	Chemical vapor deposition
DA	Dopamine
DMF	Dimethylformamide
DPV	Differential pulse voltammetry
EDX	Energy dispersive X-ray spectroscopy
EPD	Electrophoretic deposition
FTIR	Fourier transform infrared spectroscopy
GC	Glassy carbon
GO	Graphene oxide
GOx	Glucose oxidase
GRM	Graphene related materials
HRTEM	High-resolution transmission electron microscopy
IBD	Inflammatory bowel disease
LOD	Limit of detection
NCNT	Nitrogen-doped carbon nanotubes
PBS	Phosphate buffered saline

© 2016 Tous droits réservés.

lilliad.univ-lille.fr

ACRONYMS

rGO	Reduced graphene oxide
RSD	Relative standard deviation
SDS	Sodium dodecyl sulfate
SEM	Scanning electron microscopy
TEM	Transmission electron microscopy
Tyr	Tyrosine
UA	Uric acid
UV-vis	Ultraviolet-visible spectrophotometry
VA-CNT	Vertically aligned carbon nanotubes
VA-NCNT	Vertically aligned nitrogen-doped carbon nanotubes
XPS	X-ray photoelectron spectroscopy
XRD	X-ray diffraction

© 2016 Tous droits réservés.

lilliad.univ-lille.fr

CHAPTER 1

INTRODUCTION

Biosensors based on electrochemical detection principles have become routine analytical tools for the sensitive and selective detection of a variety of biological analytes in an inexpensive way [1]. They have thus found numerous potential applications ranging from clinical diagnosis, food analysis, bioprocess monitoring, environmental control to bioassays [2]. Biosensors are defined as analytical devices capable of identifying and quantifying specific analytes in a real-time mode. They generally consist of two main parts: biorecognition components (*e.g.*, enzyme, antibody, cell and nucleic acid) and a transducer, which eventually leads to a read-out signal related to the information (presence or concentration) of the analytes [3-5]. **Figure 1.1** illustrates the operative scheme of a biosensor.

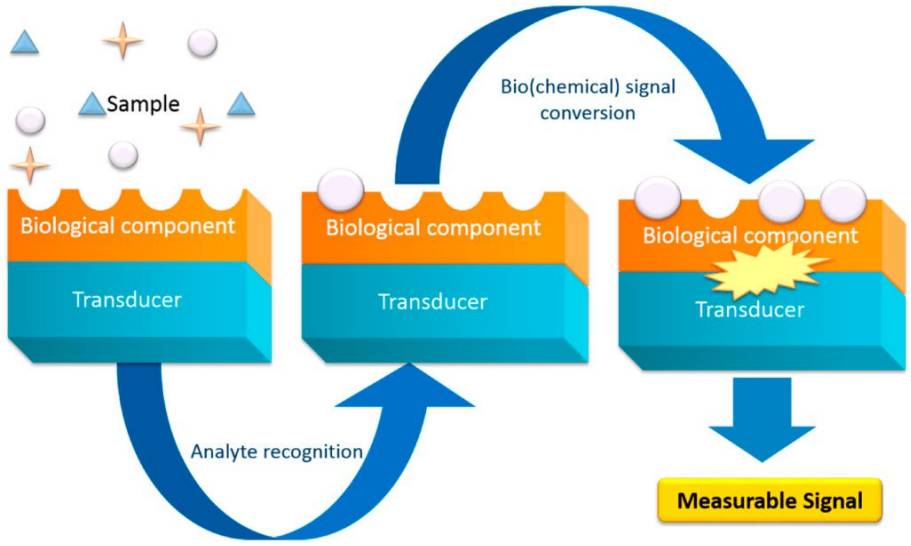

Figure 1.1: Operative scheme of a standard biosensor [3].

Taking into account the biological component that recognizes the target analyte, biosensors can be categorized into:

(I) affinity sensors, when the bioreceptor uses non-covalent interactions like antibody-antigen affinities or DNA strand hybridization;

© 2016 Tous droits réservés.

lilliad.univ-lille.fr

Thèse de Qian Wang, Lille 1, 2016

(II) catalytic or enzyme sensors, when enzymes or active materials are used in the enzymatic or catalytic reaction involving the analyte [6].

A robust biosensor must provide a low-cost, rapid, precise and stable platform for selective and sensitive detection of target molecules [7,8]. Although different transducers can be applied for the development of biosensors, electrochemical based sensors are predominantly used as they offer the possibility of sensor miniaturization, use of low-cost instrumentation, multiplexing, continuous monitoring as well as signal amplification using simple chemical approaches [9,10]. In addition, electroanalytical techniques like differential pulse voltammetry (DPV) and square wave voltammetry (SWV) allow improving the signal/noise ratio of the signal, enabling to reach low detection limits (~ nM) and thus pave the way for the development of sensitive electrochemical biosensors.

For many electrochemical applications, the good electron transfer kinetics and biocompatibility of carbon-based electrodes together with well-established surface functionalization strategies have put them to the forefront of interest as transducer materials in electrochemical biosensors (**Figure 1.2**). In comparison to metal electrodes such as gold or platinum, carbon-based electrode materials display wider potential window and are cost effective. With the development of nanotechnology, diverse allotropes of carbon nanomaterials from zero-dimensional (0D) to three-dimensional (3D) have been discovered. Among them, graphene, carbon nanotubes (CNT) and carbon nanofibers (CNFs) have shown to be of particular interest for electrochemical sensing.

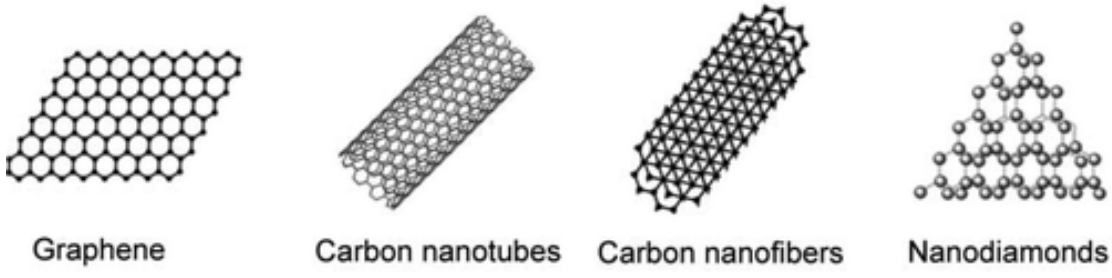

Figure 1.2: Schematic illustration of certain allotropes of carbon nanomaterials used in electrochemical applications [11].

In the case of graphene-based electrodes, for example, next to a large potential window, outstanding electrical conductivity and fast heterogeneous electron transfer (HET) kinetics for various analytes, the involvement of additional "chemical amplification effects" (*e.g.* in the case of aromatic structures such as a dopamine interacting strongly with rGO *via* π-π stacking interactions) have made these electrodes well adapted for electrochemical sensing [12-14].

© 2016 Tous droits réservés.
lilliad.univ-lille.fr

Thèse de Qian Wang, Lille 1, 2016

These properties are not only offered by single-layer graphene, but also by multi-layer graphene, often termed as stacked graphene platelets. Most importantly, electrochemistry of graphene sheets is driven by its edges where HET is fast. A defect-free basal plane is, in fact, electrochemically inert [15,16].

The interest in using CNT electrodes is that they can be simply adsorbed onto electrodes or embedded in polymer networks as binders and linking the matrix to the surface of the chosen transducer [17]. The direct growth of CNT on different substrates is a particular appealing approach as it allows controlling morphological parameters such as the CNT length and density [18-21]. Dense arrays of vertically aligned carbon nanotubes, often called CNT forests or CNT carpets, which can be directly synthesized on bulk metals using chemical vapor deposition (CVD) are promising electrode materials [22-24].

Carbon nanofibers (CNFs) can be synthesized using thermal CVD technique at low temperature. These cylindrical nanostructures have a diameter in the nanometer range and are several micrometers in length; their high conductivity makes them ideal materials for electrochemical sensing applications [25-27].

As these three carbon materials were used in this thesis, a more detailed discussion about their properties and the way they can be synthesized are given in the following part.

1.1 Graphene

One of the several allotropes of carbon is graphene, a densely packed one atom thick two-dimensional (2D) layer of sp^2 bonded carbon material (**Figure 1.3**) [28]. However, in the literature, graphene may also refer to a few layered materials held together by van der Waals forces with a high density of defects such as graphene oxide (GO) and reduced graphene oxide (rGO) (**Figure 1.3**) [29], the most widely used material for electrochemical sensing. Indeed, while the synthesis of defect-free graphene can be achieved with carbon sources through chemical vapor deposition (CVD) [30], arc discharge [31], epitaxial growth on SiC [32], or mechanical exfoliation [28], these methods fail in producing graphene in large quantities (**Figure 1.3**) [33]. In addition, exfoliated graphene has the tendency to restack to form graphite through $\pi-\pi$ stacking and van der Waals interactions if the sheets are not well separated from each other [34]. Therefore, these physical methods are limited only for fundamental studies. Moreover, the electrochemical reactivity of pristine graphene was found to be not as beneficial as believed [35]. High quality graphene, with low density of defects across the basal plane surface of the graphene sheet and low oxygen content, exhibited in fact

© 2016 Tous droits réservés.
lilliad.univ-lille.fr

slow electron transfer kinetics. A large proportion of edge plane-like sites/defects across the basal surface was found to be favorable for direct electron transfer (DET) [36]. This all calls for the necessity to develop, on one hand, alternative production processes and, on the other hand, to reduce and control aggregation of single-layer graphene into multilayered structures. Organic chemistry and surface chemistry offer the needed toolboxes for both demands.

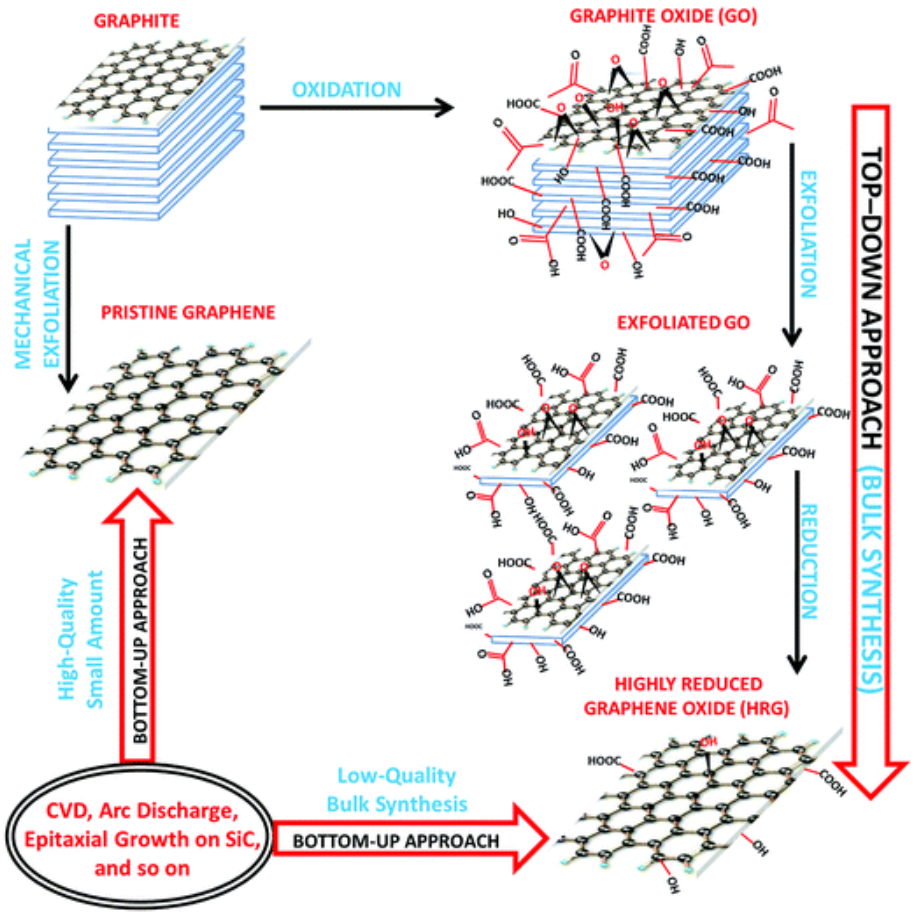

Figure 1.3: Schematic representation of the methods used for the synthesis of graphene: top-down and bottom-up approaches. The bottom-up approach involves direct synthesis of graphene from carbon sources using chemical vapor deposition (CVD), arc discharge, epitaxial growth, *etc.*, appropriate for pristine graphene with high quality; bottom-up approaches start with graphite, using techniques including mechanical exfoliation and chemical paths for graphene synthesis. In a chemical process, bulk quantity of reduced graphene oxide (rGO) is obtained through reduction of exfoliated graphene oxide (GO) originating from oxidized graphite [33].

Chemically derived graphene with defects and residual oxygen containing groups on the surface appears to be the most suitable candidate for electrochemical applications (**Figure 1.3**). The first success in dissolving graphite dates back to the 19th century and gradually developed by Staudenmaier, Hummer and Offeman, who showed that treating graphite with strong acids afforded products referred to as graphite oxide [37,38]. Subsequent

© 2016 Tous droits réservés.

lilliad.univ-lille.fr

Thèse de Qian Wang, Lille 1, 2016

mechanical/chemical or thermal exfoliations of graphite oxide form graphene oxide (GO) sheets [33]. GO was found to swell once in contact with water, an indication of its hydrophilic nature. Indeed, the surface of GO is highly oxygenated, bearing hydroxyl, epoxide, diol, ketone and carbonyl functional groups allowing GO to readily disperse in water (**Figure 1.3**). The negatively charged oxygen species help in addition to disperse GO as a single sheet by providing electrostatic repulsion and solvation. The drawback is that the presence of oxygen groups on the basal plane of graphene disrupts the π-conjugation, as a result, GO is insulating [39].

However, GO can be reduced to restore partially the graphitic π-network by chemical, electrochemical, thermal, hydrothermal and photothermal techniques [40-42]. Hydrazine [43], hydroquinone [44] and sodium borohydride [45] are commonly used reducing agents for rGO formation from GO reduction. The agents show strong reduction activity to remove most of the oxygen-containing groups of GO, offering partial recovery of the graphene-conjugated structure. However, these reducing agents are hazardous chemicals in terms of both human health and environmental consideration. Toxic gas generation, external element attachment are also limitations that hindered their widespread application [46,47]. Therefore, many environmentally friendly reductants have been developed for the reduction of GO, including vitamin C [48], reducing sugars [49,50], amino acids [51,52], gallic acid [53], bovine serum albumin (BSA) [54], peptide [55], heparin [56], urea [57], tea [58], dopamine [59] *etc.,* resulting in rGO materials with good electrical conductivity, of low charge transfer resistance and rapid electron transfer kinetics at the basal planes. These properties make rGO favorable for electrochemical sensing applications with excellent sensing performance [60].

1.2 Carbon nanotube (CNT)

CNT was first discovered by Iijima in 1991 [61]. There are two main structures of CNT: single-walled carbon nanotube (SWCNT) and multi-walled carbon nanotube (MWCNT). SWCNT can be visualized as a rolled-up of graphene sheet with an individual cylinder of 1-2 nm in diameter. MWCNT comprise several to tens of concentric cylinders of rolled graphite sheets with an interlayer spacing of 0.34 nm and diameters in the range of 2-100 nm [62,63].

© 2016 Tous droits réservés.
lilliad.univ-lille.fr

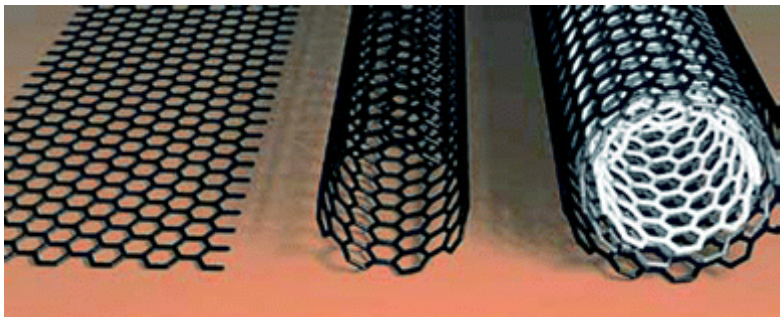

Figure 1.4: Graphical representations of pristine graphene sheet, SWCNT, and MWCNT [63].

Synthesis techniques of CNT like electric arc discharge, laser vaporization and chemical vapor deposition (CVD) are now well-established and allow the synthesis of substrate-free CNT with good crystallinity at high temperature, which is usually inefficient and expensive as they use high purity graphite with controlled atmosphere or laser beams with high power [64]. CVD is regarded as one of the most promising manufacturing techniques for large scale production [65], especially when CNT on substrate is needed for electronic applications. In a CVD process, CNT are grown through decomposition of the precursor gases under typical growth temperature between 700 to 900°C. A major advantage of CVD is that CNT can be used directly without further purifications.

Numerous reports have demonstrated that the unique properties of CNT such as small size, excellent conductivity, large surface area together with good chemical compatibility with biomolecules [66,67], allow CNT to promote electron transfer reactions between biomolecules and electrode substrates [68,69]. CNT substrate can provide direct electron transfer between the electrode and redox enzymes, avoiding the requirement of mediators and is thus attractive for reagentless biosensors [70]. These properties have made CNT an ideal material for a wide variety of electrochemically based sensing processes with high sensitivity, fast response and good reversibility [68,71].

1.3 Carbon nanofibers (CNFs)

The history of CNFs goes back to 19th century when they were first described as carbon filaments [72]. Carbon nanofibers (CNFs) have cylindrical nanostructures similar to CNT (**Figure 1.2**), while with graphene sheets stacked in platelet, ribbon and herringbone [25]. They have lengths in the order of micrometers, while their diameters vary between tens to hundreds of nanometers.

© 2016 Tous droits réservés.

lilliad.univ-lille.fr

Thèse de Qian Wang, Lille 1, 2016

CNFs can be synthesized by various methods, including laser vaporization [73], arc discharge [61], catalytic chemical vapor deposition (CCVD) [74] and plasma-enhanced chemical vapor deposition (PECVD) [75]. The most developed method for the synthesis of CNFs is CCVD technique. The synthesis of CNFs by CCVD method is based on the catalytic decomposition of carbon source (methane, ethylene, acetylene, methanol, ethanol, *etc.*) on a variety of transition metals (Fe, Co, Ni and their alloys) over the temperature range of 400-1000°C [76]. The advantage of the method consists in the possibility to control morphology and structure with improved alignment of CNFs in large amount with high purity and low cost for all kinds of applications.

CNFs have similar mechanical strength and electrical properties to CNT [77] with the advantage of controlled size, shape and orientation [78]. While unlike CNT, CNFs are not hollow in the core and expose the edge plane rather than the basal plane of graphene sheet, making them exhibit a very large active surface area [79], which allows easy immobilization and stabilization of various biomolecules [11]. At the same time, the high conductivity of CNFs makes them ideal materials as electrochemical signal transducers [80]. These features offer CNFs a great potential in the design of electrochemical biosensors.

1.4 Functionalization of carbon nanomaterials

One of the first steps in developing a sensitive and selective biosensor concerns surface modification of the electrode with ligands of interest. There are numerous surface modification strategies available in the literature (**Figure 1.5**) and it is out of the scope of this thesis to discuss all of them. We will thus focus on the ones used during this thesis work to give more detailed information about their interest.

Generally, the functionalization of carbon nanomaterials can be realized through either covalent or non-covalent interactions. Covalent functionalization is often achieved by two general routes: (I) the formation of covalent bonds with unsaturated π bonds of carbon nanostructures and (II) covalent bonds between organic functional groups and the oxygen groups on carbon materials [82]. To enable reaction with the C=C bond of carbon structure, diazonium salts are used to generate highly reactive free radicals, yielding various aryl groups bonded with a carbon atom in the lattice after grafting with release of a molecule of N_2 (**Figure 1.6**) [83-85]. The reaction converts the carbon atoms from sp^2 to sp^3 hybridization and generates insulating or semiconducting regions with a wide variety of functional groups (-OH, -COOH, $-NO_2$, -C≡C, *etc.*), feasible for further linkage or modification [86].

© 2016 Tous droits réservés.
lilliad.univ-lille.fr

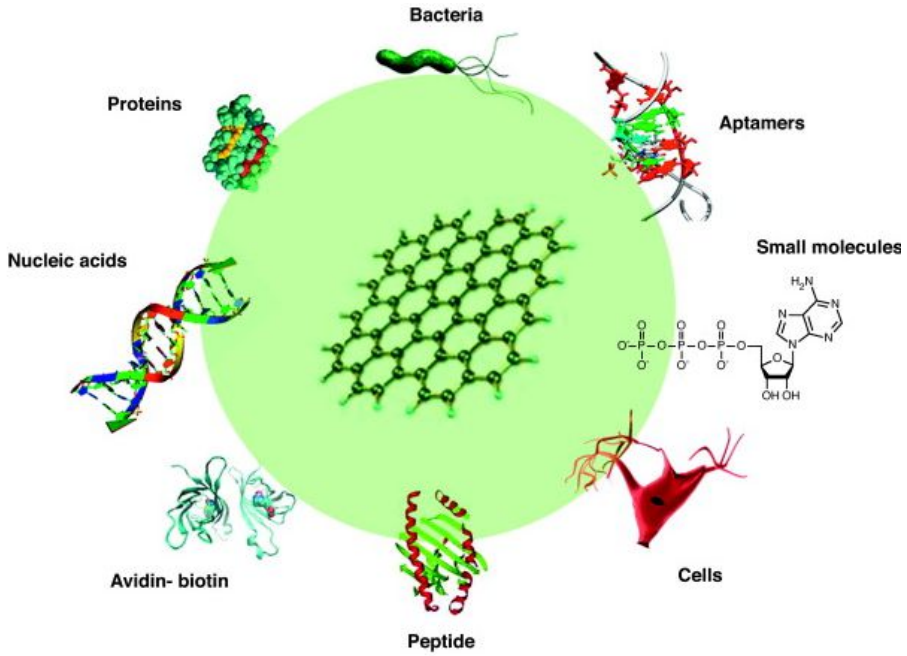

Figure 1.5: Graphene and its derivatives have been reported to be functionalized with avidin-biotin, peptides, DNAs, proteins, aptamers, small molecules, bacteria, and cells through physical adsorption or chemical conjugation for biosensing applications [81].

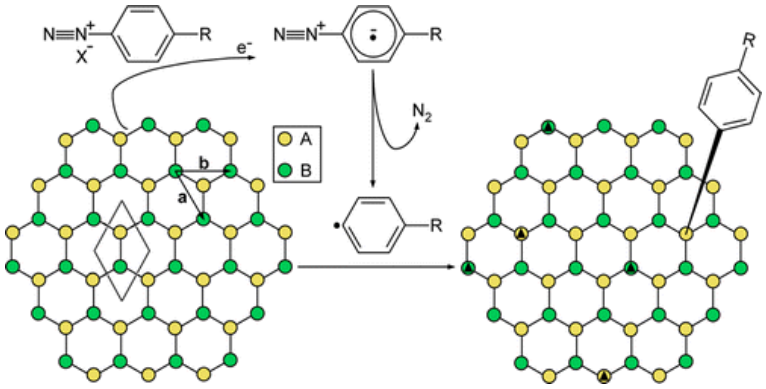

Figure 1.6: Schematic illustration of grafting a diazonium salt with functional group R to a graphene sheet [87].

The oxygen functional groups on carbon materials are, on the other hand, widely employed for covalent grafting with ligands. The carboxyl groups are used to link to the amino groups of proteins or molecules using a carbodiimide procedure. Active esters are generated on graphene oxide surfaces by reaction between carboxyl groups of graphene oxide and 1-ethyl-3-(3-dimethyl-aminopropyl) carbodiimide (EDC) or *N, N'*-dicyclohexylcarbodiimide (DCC) in the presence of *N*-hydroxysuccinimide (NHS) under ambient conditions. Then, the ester reacts with amine groups of a molecule (DNA, enzyme, *etc.*) of interest to form an amide bond, achieving covalently bonded DNA [88], aptamer [89], antibody [90] and protein [91] for further development of electrochemical sensing platforms.

© 2016 Tous droits réservés.

lilliad.univ-lille.fr

Eissa *et al.*, for example, immobilized okadaic acid antibodies on carboxyphenyl-modified graphene electrodes *via* carbodiimide chemistry and achieved competitive voltammetric determination of okadaic acid in shellfish (**Figure 1.7**) [92]. The carboxyphenyl groups were grafted on graphene surface through electrochemical reduction of diazonium compounds.

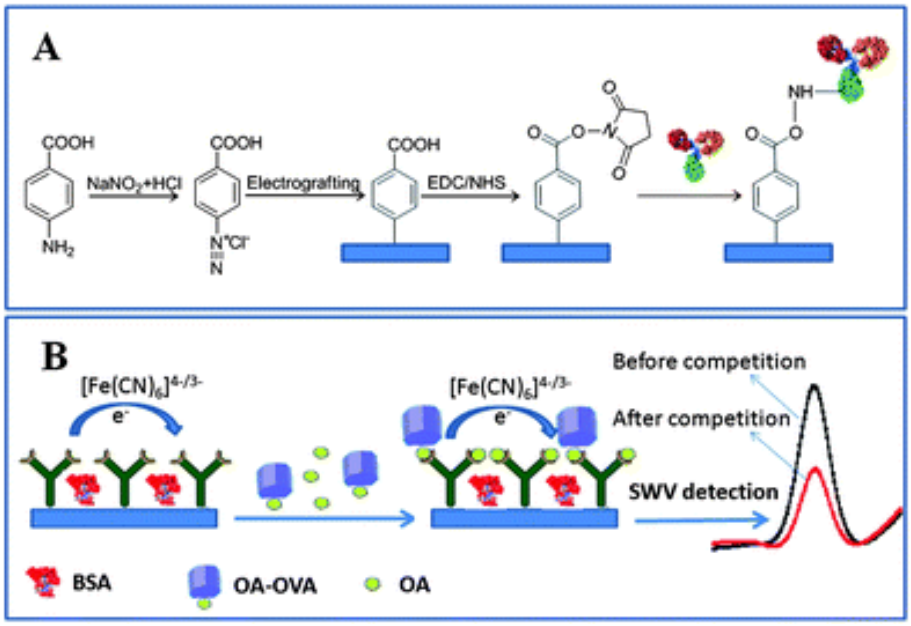

Figure 1.7: (A) Carboxyphenyl modification of graphene electrode surface and the covalent immobilization of antibodies: carboxyphenyl groups are grafted to graphene by diazonium chemistry, followed by activation and covalent bonding of antibodies through EDC/NHS carbodiimide process; (B) the working principal of the immunosensor for okadaic acid (OA) detection with direct competitive immunoassay [92].

Another widely used approach to increase the sensitivity of electrodes is based on the incorporation of electrocatalytic nanostructures. Many studies have demonstrated that carbon nanomaterials modified with metal nanoparticles can enhance the performances of non-enzymatic electrochemical biosensors (will be discussed in detail in **Chapter 3**) [93-95]. A number of strategies have been put forward for the synthesis of metal nanoparticles modified carbon nanocomposites, which can be broadly classified into two categories *viz. in situ* and *ex situ* approach [33].

In the *ex-situ* method, the metal nanoparticles are pre-synthesized separately and integrated onto carbon nanostructures through chemical bond formation with functional groups on carbon-based structures or by utilizing electrostatic, π-π or/and van der Waals interactions for binding. The ex-*situ* method offers good control over size, shape and functionality of the metal nanoparticles, being one of the main advantages of this approach. One of the limitations is that this approach is rather time consuming and involves several

© 2016 Tous droits réservés.

lilliad.univ-lille.fr

steps (**Figure 1.8**).

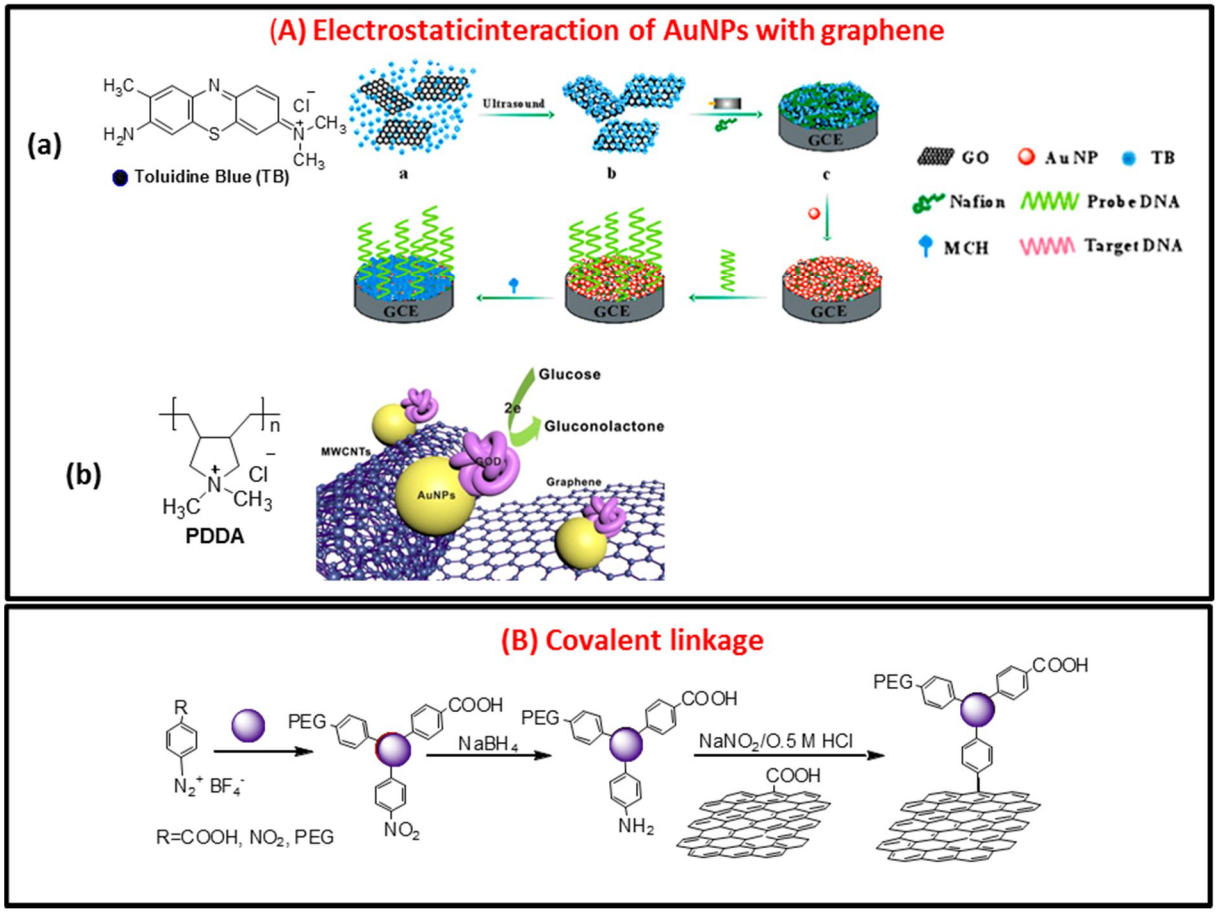

Figure 1.8: *Ex situ* approaches for the integration of Au nanoparticles (Au NPs) onto graphene sheets: (A) electrostatic interactions: (a) fabrication of a DNA sensor based on Toluidine Blue (TB) as molecular linkage between rGO and Au NPs due to electrostatic interaction of the positively charged TB with negatively charged rGO [96]; (b) integration of positively charged PDDA capped Au NPs onto negatively charged rGO. Further integration of GOx resulted in the construction of a glucose sensor [97]; (B) covalent linkage between COOH groups of graphene and NH_2-functionalized Au NPs [98].

While the *ex-situ* approach is well adapted to form controlled nanoparticles on carbon structures, most work focused on *in situ* method. The *in situ* approach involves the formation of metal nanoparticles on the surface of carbon nanomaterials, *i.e.* simultaneous reduction of GO and the respective metal salts with a reducing agent (*e.g.* sodium borohydride, sodium citrate, hydrazine hydrate, ascorbic acid, glucose, *etc.*) (**Figure 1.9**). The process can be carried out by chemical reduction [99], hydrothermal and solvothermal method [100], electrochemical deposition [101], microwave assisted reduction method [102], layer by layer assembly [103], *etc.* The advantages of the *in situ* reduction is that generally there is no need of the use of capping agents or extra linker molecules, which can have a negative influence on

© 2016 Tous droits réservés.

lilliad.univ-lille.fr

Thèse de Qian Wang, Lille 1, 2016

the charge transfer characteristics. It is cost effective and a one-pot process. These advantages seem to override the limitation in controlling size and morphology of the embedded metal nanoparticles in the resulting composite.

Figure 1.9: *In situ* strategy for the formation of metal nanoparticles (Metal NP) loaded rGO matrix using formic acid as a reducing agent in a one-pot reduction and synthesis approach [104].

1.5 Electrophoretic deposition (EPD)

Considering the fabrication of carbon nanomaterials modified electrode, the most widely used method involves the preparation of stable dispersions of the materials, followed by casting the resulting dispersion at the surface of electrode substrate. Though the approach benefits from its simplicity and low cost, coated films often confront problems of non-uniformity, poor thickness controllability and weak stickiness to electrode [105]. The application of attractive electrophoretic deposition (EPD) technique for manipulation and deposition of nanomaterials seems to be an appealing strategy to solve these limitations.

EPD is a widely used technique in the process of ceramics, coatings and composite materials [106]. In EPD processes, charged particles dispersed in a suitable solvent, move towards cathode/anode under an applied electric field to form a coherent deposit layer (**Figure 1.10**). The deposition can be carried out in both organic solvents and aqueous media, making it suitable with a wide variety of materials. Moreover, the process parameters like applied voltage, deposition time, suspension concentration and selected electrode substrate can be properly controlled to adjust the chemical and morphological formation of the deposited films with considerable flexibility [107]. In addition, EPD offers the possibility to produce thin films with adequate homogeneity in short processing time with simple and cost-effective

© 2016 Tous droits réservés.
lilliad.univ-lille.fr

equipment, making it possible of scaling up to large, application relevant dimensions [108-110].

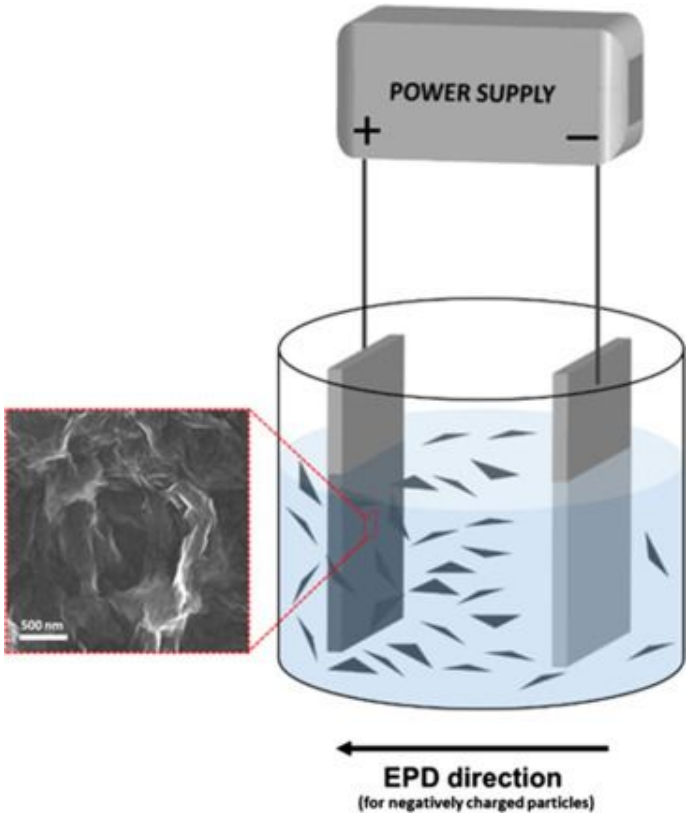

Figure 1.10: Schematic illustration of two electrodes cell setup for electrophoretic deposition (EPD) and an example of graphene coating. Depending on the surface charges of the graphene related materials, anodic (if the particles are negatively charged) or cathodic (if the particles are positively charged) EPD occurs [111].

EPD has shown to be a well-adapted technique for the deposition of rGO and CNT. It is an ideal technique providing a facile means to produce tightly packed films. Du *et al.* initiated the EPD of CNT in 2002 [112]. After that EPD technique undergoes further developments in the deposition of graphene [113], and CNFs [114] thin films on different conducting substrates. This makes EPD an alternative environmentally friendly, and cost effective route for producing rGO coatings. **Figure 1.11** gives an overview of process for EPD of graphene related materials (GRM). The EPD formed graphene structures have been used in a wide variety of applications ranging from solar cells [115,116], supercapacitors [117,118], field emission devices [119] to electrochemical biosensors [120,121].

© 2016 Tous droits réservés.

lilliad.univ-lille.fr

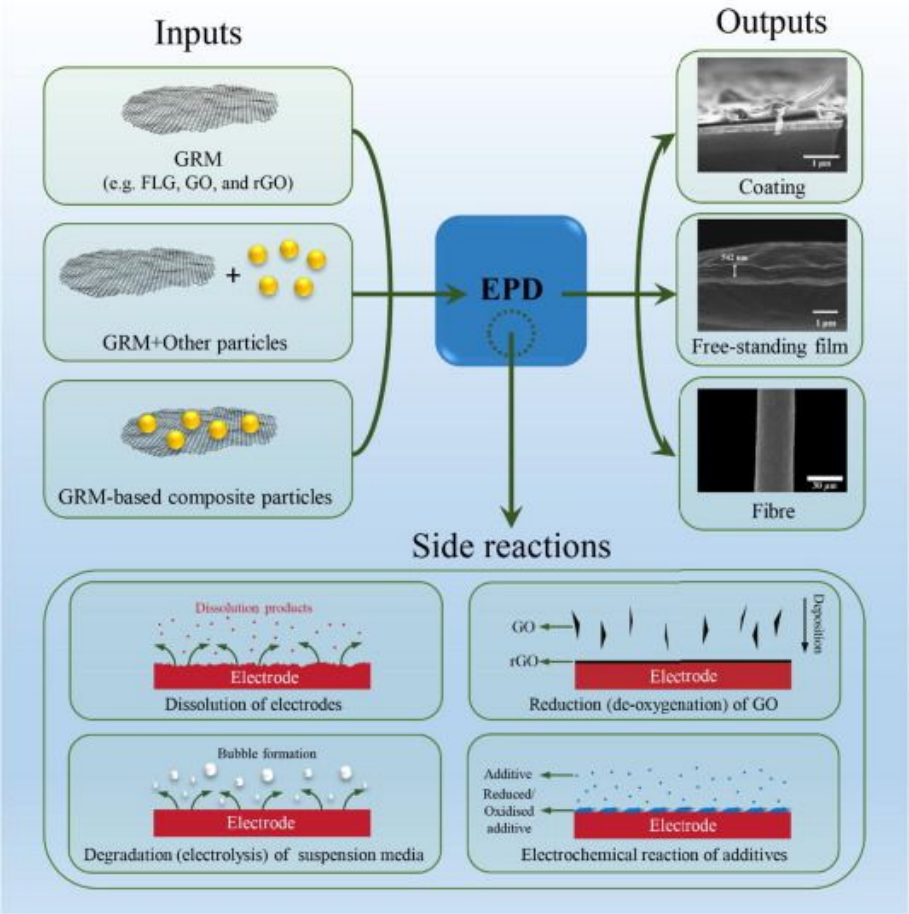

Figure 1.11: An overview of inputs, outputs and possible side reactions for the EPD of graphene related materials (GRM). In an EPD process, graphene based materials, alone or in combination with other particle types, can be used as input materials. Coatings, films or fibers can be obtained based on the EPD setup. Various side-reactions can occur during the EPD process, *e.g.* GO could be reduced into rGO after deposition [111].

In addition to its controllability over deposited films, EPD offers special features when dealing with GO deposition. Several studies have reported that EPD of GO at high voltages caused its simultaneous reduction to rGO during deposition (**Figure 1.12A**) [122,123]. This appears beneficial for the production of rGO films, since it potentially avoids the use of reducing agents and post-EPD reduction processes, and may prevent the passivation of the growing film due to the insulating nature of GO [111]. Another typical characteristic of EPD-processed graphene films is the presence of wrinkles (**Figure 1.12A**) [124,125]. The highly wrinkled structure of GO can provide an enhanced surface area, making graphene surface produced through EPD a good substrate for the nucleation and growth of metal nanoparticles [116]. Metal ions adsorb onto graphene sheets and produce suspensions of positively charged graphene, making cathodic deposition feasible (**Figure 1.12B**). Various metal salts including nickel nitrate, cobalt nitrate, copper sulphate and magnesium chloride were used for the charging effects to obtain metal particles decorated graphene composites.

© 2016 Tous droits réservés.

lilliad.univ-lille.fr

The addition of secondary particles in suspension may also affect the deposition rate thus avoiding the restacking and agglomeration of graphene sheets, possibly resulting in aligned rGO sheets in the deposit and porous structure with larger surface area [126,127]. The controlled structure, enhanced surface area together with the catalytic ability of metal nanoparticles has put electrophoretically deposited graphene/metal-based composites as promising candidates in electrochemical devices like supercapacitors and biosensors (**Figure 1.12B**) [128,129].

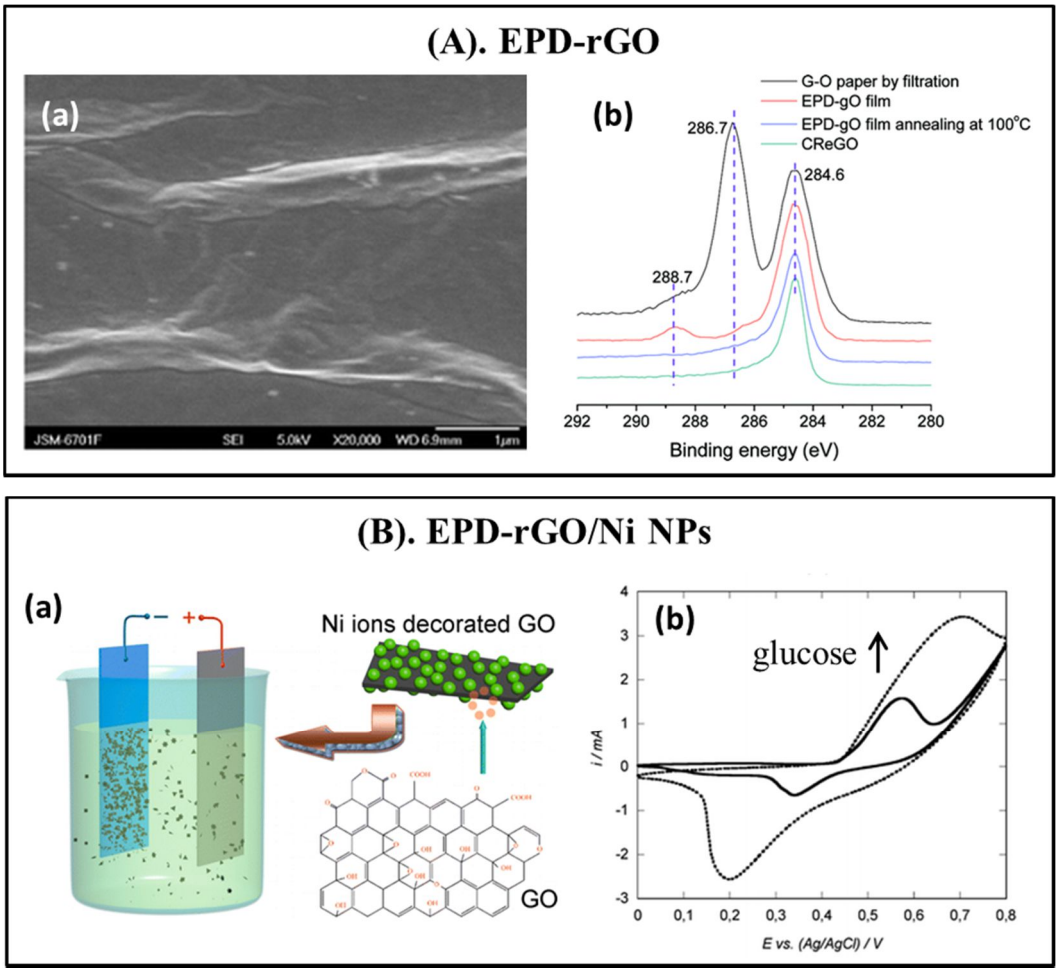

Figure 1.12: EPD of GO-based materials: (A) GO after EPD resulting in rGO with (a) winkled flakes [130] and (b) C_{1s} high resolution XPS spectra of electrophoretically deposited rGO from GO solution with sp^2 carbon being dominant [123]; (B) EPD of GO with metal nanoparticles: (a) rGO/Ni NPs obtained on cathode from Ni ions decorated GO solution and (b) its application for non-enzymatic glucose sensing [128,129].

1.6 Objectives of this thesis

In this thesis, we take advantage of the outstanding properties of selected carbon nanostructures: carbon nanotubes (CNT), carbon nanofibers (CNFs) and reduced graphene

© 2016 Tous droits réservés.

lilliad.univ-lille.fr

Thèse de Qian Wang, Lille 1, 2016

oxide (rGO) to construct sensitive sensing platforms for lysozyme, glucose and H_2O_2 in a simple and straightforward way.

In **Chapter 2**, we show the potential of CNT for aptasensor construction. Vertically aligned carbon nanotubes (VA-NCNT) exhibited excellent electron transfer ability, therefore they were functionalized with biotinylated lysozyme aptamer through covalent attachment. Various characterization techniques have been used to confirm the successful binding of the biotinylated lysozyme aptamer onto neutravidin modified VA-NCNT interface. The aptamer modified interface was applied for lysozyme detection and the ability of the as-constructed sensing platform towards lysozyme detection in human serum from patients affected by inflammatory bowel disease (IBD) was also discussed.

In **Chapter 3**, a facile electrophoretic deposition (EPD) technique was applied for the fabrication of reduced graphene oxide/copper nanoparticles (rGO/Cu NPs) and carbon nanofibers/cobalt hydroxide (CNFs/$Co(OH)_2$) composite on Au/Ti/glass interfaces. The technique was found to be controllable by varying deposition parameters in a reproducible manner, resulting in films with good uniformity. The modified Au/Ti/glass interfaces were successfully used for non-enzymatic glucose sensing. Furthermore, the feasibility of glucose sensors was explored by determining glucose content in human serum.

In **Chapter 4**, an easy and environmentally friendly method was described for the *in situ* synthesis of a reduced graphene oxide/gold nanoparticles (rGO/Au NPs) nanocomposite through the simultaneous reduction of GO and $HAuCl_4$ using tyrosine as a reducing agent. The Au NPs decorated nanocomposites exhibited direct electrocatalytic activity towards H_2O_2 reduction and were explored as non-enzymatic H_2O_2 sensor.

1.7 References

[1] Wang, J. Electrochemical detection for microscale analytical systems: a review. *Talanta* **2002**, *56*, 223-231.

[2] Wang, J. Electrochemical glucose biosensors. *Chemical Reviews* **2008**, *108*, 814-825.

[3] Gonçalves, A M; Pedro, A Q; Santos, F M; Martins, L M; Maia, C J; Queiroz, J A; Passarinha, L A. Trends in protein-based biosensor assemblies for drug screening and pharmaceutical kinetic studies. *Molecules* **2014**, *19*, 12461-12485.

[4] Belluzo, M S; Ribone, M É; Lagier, C M. Assembling amperometric biosensors for clinical diagnostics. *Sensors* **2008**, *8*, 1366-1399.

[5] Saei, A A; Dolatabadi, J E N; Najafi-Marandi, P; Abhari, A; de la Guardia, M. Electrochemical biosensors for glucose based on metal nanoparticles. *TrAC Trends in Analytical Chemistry* **2013**, *42*, 216-227.

[6] Thévenot, D R; Toth, K; Durst, R A; Wilson, G S. Electrochemical biosensors: recommended definitions and classification. *Biosensors and Bioelectronics* **2001**, *16*,

© 2016 Tous droits réservés.
lilliad.univ-lille.fr

121-131.

[7] Coradin, T; Livage, J. Mesoporous alginate/silica biocomposites for enzyme immobilisation. *Comptes Rendus Chimie* **2003**, *6*, 147-152.

[8] Hasanzadeh, M; Shadjou, N; Saghatforoush, L; Dolatabadi, J E N. Preparation of a new electrochemical sensor based on iron (III) complexes modified carbon paste electrode for simultaneous determination of mefenamic acid and indomethacin. *Colloids and Surfaces B: Biointerfaces* **2012**, *92*, 91-97.

[9] Kang, X; Wang, J; Wu, H; Liu, J; Aksay, I A; Lin, Y. A graphene-based electrochemical sensor for sensitive detection of paracetamol. *Talanta* **2010**, *81*, 754-759.

[10] Fan, C; Plaxco, K W; Heeger, A J. Electrochemical interrogation of conformational changes as a reagentless method for the sequence-specific detection of DNA. *Proceedings of the National Academy of Sciences* **2003**, *100*, 9134-9137.

[11] Wang, Z; Dai, Z. Carbon nanomaterial-based electrochemical biosensors: an overview. *Nanoscale* **2015**, *7*, 6420-6431.

[12] Tang, L; Wang, Y; Li, Y; Feng, H; Lu, J; Li, J. Preparation, structure, and electrochemical properties of reduced graphene sheet films. *Advanced Functional Materials* **2009**, *19*, 2782-2789.

[13] Brownson, D A C; Banks, C E. Graphene electrochemistry: an overview of potential applications. *Analyst* **2010**, *135*, 2768-2778.

[14] Sun, C L; Lee, H H; Yang, J M; Wu, C C. The simultaneous electrochemical detection of ascorbic acid, dopamine, and uric acid using graphene/size-selected Pt nanocomposites. *Biosensors and Bioelectronics* **2011**, *26*, 3450-3455.

[15] Ryu, S; Han, M Y; Maultzsch, J; Heinz, T F; Kim, P; Steigerwald, M L; Brus, L E. Reversible basal plane hydrogenation of graphene. *Nano Letters* **2008**, *8*, 4597-4602.

[16] Ambrosi, A; Chua, C K; Bonanni, A; Pumera, M. Electrochemistry of graphene and related materials. *Chemical Reviews* **2014**, *114*, 7150-7188.

[17] Jacobs, C B; Peairs, M J; Venton, B J. Review: Carbon nanotube based electrochemical sensors for biomolecules. *Analytica Chimica Acta* **2010**, *662*, 105-127.

[18] Teblum, E; Noked, M; Grinblat, J; Kremen, A; Muallem, M; Fleger, Y; Tischler, Y R; Aurbach, D; Nessim, G D. Millimeter-tall carpets of vertically aligned crystalline carbon nanotubes synthesized on copper substrates for electrical applications. *The Journal of Physical Chemistry C* **2014**, *118*, 19345-19355.

[19] Subramanian, P; Cohen, A; Teblum, E; Nessim, G D; Bormasheko, E; Schechter, A. Electrocatalytic activity of nitrogen plasma treated vertically aligned carbon nanotube carpets towards oxygen reduction reaction. *Electrochemistry Communications* **2014**, *49*, 42-46.

[20] Talapatra, S; Kar, S; Pal, S K; Vajtai, R; Ci, L; Victor, P; Shaijumon, M M; Kaur, S; Nalamasu, O; Ajayan, P M. Direct growth of aligned carbon nanotubes on bulk metals. *Nature Nanotechnology* **2006**, *1*, 112-116.

[21] Nessim, G D; Hart, A J; Kim, J S; Acquaviva, D; Oh, J; Morgan, C D; Seita, M; Leib, J S; Thompson, C V. Tuning of vertically-aligned carbon nanotube diameter and areal density through catalyst pre-treatment. *Nano Letters* **2008**, *8*, 3587-3593.

[22] Li, D J; Maiti, U N; Lim, J; Choi, D S; Lee, W J; Oh, Y; Lee, G Y; Kim, S O. Molybdenum sulfide/N-doped CNT forest hybrid catalysts for high-performance hydrogen evolution reaction. *Nano Letters* **2014**, *14*, 1228-1233.

[23] Zhu, Z G; Garcia-Gancedo, L; Chen, C; Zhu, X R; Xie, H Q; Flewitt, A J; Milne, W I. Enzyme-free glucose biosensor based on low density CNT forest grown directly on a Si/SiO_2 substrate. *Sensors and Actuators B: Chemical* **2013**, *178*, 586-592.

[24] Malhotra, R; Patel, V; Vaqué, J P; Gutkind, J S; Rusling, J F. Ultrasensitive electrochemical immunosensor for oral cancer biomarker IL-6 using carbon nanotube forest electrodes and multilabel amplification. *Analytical Chemistry* **2010**, *82*,

© 2016 Tous droits réservés.

lilliad.univ-lille.fr

3118-3123.

[25] Huang, J; Liu, Y; You, T. Carbon nanofiber based electrochemical biosensors: A review. *Analytical Methods* **2010**, *2*, 202-211.

[26] Jia, X; Hu, G; Nitze, F; Barzegar, H R; Sharifi, T; Tai, C W; Wågberg, T. Synthesis of palladium/helical carbon nanofiber hybrid nanostructures and their application for hydrogen peroxide and glucose detection. *ACS Applied Materials & Interfaces* **2013**, *5*, 12017-12022.

[27] Liu, Y; Teng, H; Hou, H; You, T. Nonenzymatic glucose sensor based on renewable electrospun Ni nanoparticle-loaded carbon nanofiber paste electrode. *Biosensors and Bioelectronics* **2009**, *24*, 3329-3334.

[28] Novoselov, K S; Geim, A K; Morozov, S V; Jiang, D; Zhang, Y; Dubonos, S V; Grigorieva, I V; Firsov, A A. Electric field effect in atomically thin carbon films. *Science* **2004**, *306*, 666-669.

[29] Yang, W; Ratinac, K R; Ringer, S P; Thordarson, P; Gooding, J J; Braet, F. Carbon nanomaterials in biosensors: should you use nanotubes or graphene? *Angewandte Chemie International Edition* **2010**, *49*, 2114-2138.

[30] Ito, Y; Christodoulou, C; Nardi, M V; Koch, N; Sachdev, H; Müllen, K. Chemical vapor deposition of N-doped graphene and carbon films: the role of precursors and gas phase. *ACS Nano* **2014**, *8*, 3337-3346.

[31] Shen, B; Ding, J; Yan, X; Feng, W; Li, J; Xue, Q. Influence of different buffer gases on synthesis of few-layered graphene by arc discharge method. *Applied Surface Science* **2012**, *258*, 4523-4531.

[32] Huang, Q; Kim, J J; Ali, G; Cho, S O. Width tunable graphene nanoribbons on a SiC substrate with a controlled step height. *Advanced Materials* **2013**, *25*, 1144-1148.

[33] Khan, M; Tahir, M N; Adil, S F; Khan, H U; Siddiqui, M R H; Al-warthan, A A; Tremel, W. Graphene based metal and metal oxide nanocomposites: synthesis, properties and their applications. *Journal of Materials Chemistry A* **2015**, *3*, 18753-18808.

[34] Li, D; Mueller, M B; Gilje, S; Kaner, R B; Wallace, G G. Processable aqueous dispersions of graphene nanosheets. *Nature Nanotechnology* **2008**, *3*, 101-105.

[35] Brownson, D A C; Munro, L J; Kampouris, D K; Banks, C E. Electrochemistry of graphene: not such a beneficial electrode material? *RSC Advances* **2011**, *1*, 978-988.

[36] Brownson, D A C; Kampouris, D K; Banks, C E. Graphene electrochemistry: fundamental concepts through to prominent applications. *Chemical Society Reviews* **2012**, *41*, 6944-6976.

[37] Hummers Jr, W S; Offeman, R E. Preparation of graphitic oxide. *Journal of the American Chemical Society* **1958**, *80*, 1339-1339.

[38] Staudenmaier, L. Verfahren zur darstellung der graphitsäure. *Berichte der Deutschen Chemischen Gesellschaft* **1898**, *31*, 1481-1487.

[39] Stankovich, S; Dikin, D A; Piner, R D; Kohlhaas, K A; Kleinhammes, A; Jia, Y; Wu, Y; Nguyen, S T; Ruoff, R S. Synthesis of graphene-based nanosheets via chemical reduction of exfoliated graphite oxide. *carbon* **2007**, *45*, 1558-1565.

[40] Sheng, Z H; Shao, L; Chen, J J; Bao, W J; Wang, F B; Xia, X H. Catalyst-free synthesis of nitrogen-doped graphene via thermal annealing graphite oxide with melamine and its excellent electrocatalysis. *ACS Nano* **2011**, *5*, 4350-4358.

[41] Park, S; Ruoff, R S. Chemical methods for the production of graphenes. *Nature Nanotechnology* **2009**, *4*, 217-224.

[42] Pei, S; Cheng, H M. The reduction of graphene oxide. *Carbon* **2012**, *50*, 3210-3228.

[43] Mao, S; Pu, H; Chen, J. Graphene oxide and its reduction: modeling and experimental progress. *RSC Advances* **2012**, *2*, 2643-2662.

[44] Wang, G; Yang, J; Park, J; Gou, X; Wang, B; Liu, H; Yao, J. Facile synthesis and characterization of graphene nanosheets. *The Journal of Physical Chemistry C* **2008**, *112*,

© 2016 Tous droits réservés.

lilliad.univ-lille.fr

8192-8195.

[45] Shin, H J; Kim, K K; Benayad, A; Yoon, S M; Park, H K; Jung, I S; Jin, M H; Jeong, H K; Kim, J M; Choi, J Y. Efficient reduction of graphite oxide by sodium borohydride and its effect on electrical conductance. *Advanced Functional Materials* **2009**, *19*, 1987-1992.

[46] Guo, H L; Wang, X F; Qian, Q Y; Wang, F B; Xia, X H. A green approach to the synthesis of graphene nanosheets. *ACS Nano* **2009**, *3*, 2653-2659.

[47] Thakur, S; Karak, N. Alternative methods and nature-based reagents for the reduction of graphene oxide: A review. *Carbon* **2015**, *94*, 224-242.

[48] Zhang, J; Yang, H; Shen, G; Cheng, P; Zhang, J; Guo, S. Reduction of graphene oxide via L-ascorbic acid. *Chemical Communications* **2010**, *46*, 1112-1114.

[49] Zhu, C; Guo, S; Fang, Y; Dong, S. Reducing sugar: new functional molecules for the green synthesis of graphene nanosheets. *ACS Nano* **2010**, *4*, 2429-2437.

[50] Akhavan, O; Ghaderi, E; Aghayee, S; Fereydooni, Y; Talebi, A. The use of a glucose-reduced graphene oxide suspension for photothermal cancer therapy. *Journal of Materials Chemistry* **2012**, *22*, 13773-13781.

[51] Chen, D; Li, L; Guo, L. An environment-friendly preparation of reduced graphene oxide nanosheets via amino acid. *Nanotechnology* **2011**, *22*, 325601.

[52] Ma, J; Wang, X; Liu, Y; Wu, T; Liu, Y; Guo, Y; Li, R; Sun, X; Wu, F; Li, C. Reduction of graphene oxide with l-lysine to prepare reduced graphene oxide stabilized with polysaccharide polyelectrolyte. *Journal of Materials Chemistry A* **2013**, *1*, 2192-2201.

[53] Li, J; Xiao, G; Chen, C; Li, R; Yan, D. Superior dispersions of reduced graphene oxide synthesized by using gallic acid as a reductant and stabilizer. *Journal of Materials Chemistry A* **2013**, *1*, 1481-1487.

[54] Liu, J; Fu, S; Yuan, B; Li, Y; Deng, Z. Toward a universal "adhesive nanosheet" for the assembly of multiple nanoparticles based on a protein-induced reduction/decoration of graphene oxide. *Journal of the American Chemical Society* **2010**, *132*, 7279-7281.

[55] Pham, T A; Kim, J S; Kim, J S; Jeong, Y T. One-step reduction of graphene oxide with L-glutathione. *Colloids and Surfaces A: Physicochemical and Engineering Aspects* **2011**, *384*, 543-548.

[56] Wang, Y; Zhang, P; Liu, C F; Zhan, L; Li, Y F; Huang, C Z. Green and easy synthesis of biocompatible graphene for use as an anticoagulant. *RSC Advances* **2012**, *2*, 2322-2328.

[57] Lei, Z; Lu, L; Zhao, X S. The electrocapacitive properties of graphene oxide reduced by urea. *Energy & Environmental Science* **2012**, *5*, 6391-6399.

[58] Wang, Y; Shi, Z; Yin, J. Facile synthesis of soluble graphene via a green reduction of graphene oxide in tea solution and its biocomposites. *ACS Applied Materials & Interfaces* **2011**, *3*, 1127-1133.

[59] Xu, L Q; Yang, W J; Neoh, K G; Kang, E T; Fu, G D. Dopamine-induced reduction and functionalization of graphene oxide nanosheets. *Macromolecules* **2010**, *43*, 8336-8339.

[60] Pandikumar, A; How, G T S; See, T P; Omar, F S; Jayabal, S; Kamali, K Z; Yusoff, N; Jamil, A; Ramaraj, R; John, S A. Graphene and its nanocomposite material based electrochemical sensor platform for dopamine. *RSC Advances* **2014**, *4*, 63296-63323.

[61] Iijima, S. Helical microtubules of graphitic carbon. *Nature* **1991**, *354*, 56-58.

[62] Merkoçi, A; Pumera, M; Llopis, X; Pérez, B; del Valle, M; Alegret, S. New materials for electrochemical sensing VI: carbon nanotubes. *TrAC Trends in Analytical Chemistry* **2005**, *24*, 826-838.

[63] Nessim, G D. Properties, synthesis, and growth mechanisms of carbon nanotubes with special focus on thermal chemical vapor deposition. *Nanoscale* **2010**, *2*, 1306-1323.

[64] Awasthi, K; Srivastava, A; Srivastava, O N. Synthesis of carbon nanotubes. *Journal of Nanoscience and Nanotechnology* **2005**, *5*, 1616-1636.

[65] Cassell, A M; Raymakers, J A; Kong, J; Dai, H. Large scale CVD synthesis of

© 2016 Tous droits réservés.

lilliad.univ-lille.fr

single-walled carbon nanotubes. *The Journal of Physical Chemistry B* **1999**, *103*, 6484-6492.

[66] Gooding, J J; Wibowo, R; Liu, J; Yang, W; Losic, D; Orbons, S; Mearns, F J; Shapter, J G; Hibbert, D B. Protein electrochemistry using aligned carbon nanotube arrays. *Journal of the American Chemical Society* **2003**, *125*, 9006-9007.

[67] Yu, X; Chattopadhyay, D; Galeska, I; Papadimitrakopoulos, F; Rusling, J F. Peroxidase activity of enzymes bound to the ends of single-wall carbon nanotube forest electrodes. *Electrochemistry Communications* **2003**, *5*, 408-411.

[68] Zhao, Q; Gan, Z; Zhuang, Q. Electrochemical sensors based on carbon nanotubes. *Electroanalysis* **2002**, *14*, 1609-1613.

[69] Musameh, M; Wang, J; Merkoci, A; Lin, Y. Low-potential stable NADH detection at carbon-nanotube-modified glassy carbon electrodes. *Electrochemistry Communications* **2002**, *4*, 743-746.

[70] Zhu, Z; Garcia Gancedo, L; Flewitt, A J; Xie, H; Moussy, F; Milne, W I. A critical review of glucose biosensors based on carbon nanomaterials: carbon nanotubes and graphene. *Sensors* **2012**, *12*, 5996-6022.

[71] Wang, J. Carbon-nanotube based electrochemical biosensors: A review. *Electroanalysis* **2005**, *17*, 7-14.

[72] De Jong, K P; Geus, J W. Carbon nanofibers: catalytic synthesis and applications. *Catalysis Reviews* **2000**, *42*, 481-510.

[73] Baker, R T K; Kim, M S; Chambers, A; Park, C; Rodriguez, N M. The relationship between metal particle morphology and the structural characteristics of carbon deposits. *Studies in Surface Science and Catalysis* **1997**, *111*, 99-109.

[74] Zheng, G B; Kouda, K; Sano, H; Uchiyama, Y; Shi, Y F; Quan, H J. A model for the structure and growth of carbon nanofibers synthesized by the CVD method using nickel as a catalyst. *Carbon* **2004**, *42*, 635-640.

[75] Lupu, D; Biriş, A R; Jianu, A; Bunescu, C; Burkel, E; Indrea, E; Mihăilescu, G; Pruneanu, S; Olenic, L; Mişan, I. Carbon nanostructures produced by CCVD with induction heating. *Carbon* **2004**, *42*, 503-507.

[76] Olenic, L; Biris, A R; Pruneanu, S; Almasan, V. *Electrochemical and adsorption properties of catalytically formed carbon nanofibers*. INTECH Open Access Publisher: 2010; p 227-252.

[77] Endo, M; Kim, Y A; Hayashi, T; Fukai, Y; Oshida, K; Terrones, M; Yanagisawa, T; Higaki, S; Dresselhaus, M S. Structural characterization of cup-stacked-type nanofibers with an entirely hollow core. *Applied Physics Letters* **2002**, *80*, 1267-1269.

[78] Merkulov, V I; Hensley, D K; Melechko, A V; Guillorn, M A; Lowndes, D H; Simpson, M L. Control mechanisms for the growth of isolated vertically aligned carbon nanofibers. *The Journal of Physical Chemistry B* **2002**, *106*, 10570-10577.

[79] Toghill, K E; Compton, R G. Electrochemical non-enzymatic glucose sensors: a perspective and an evaluation. *International Journal of Electrochemical Science* **2010**, *5*, 1246-1301.

[80] Vamvakaki, V; Tsagaraki, K; Chaniotakis, N. Carbon nanofiber-based glucose biosensor. *Analytical Chemistry* **2006**, *78*, 5538-5542.

[81] Wang, Y; Li, Z; Wang, J; Li, J; Lin, Y. Graphene and graphene oxide: biofunctionalization and applications in biotechnology. *Trends in Biotechnology* **2011**, *29*, 205-212.

[82] Georgakilas, V; Otyepka, M; Bourlinos, A B; Chandra, V; Kim, N; Kemp, K C; Hobza, P; Zboril, R; Kim, K S. Functionalization of graphene: covalent and non-covalent approaches, derivatives and applications. *Chemical Reviews* **2012**, *112*, 6156-6214.

[83] Lomeda, J R; Doyle, C D; Kosynkin, D V; Hwang, W-F; Tour, J M. Diazonium functionalization of surfactant-wrapped chemically converted graphene sheets. *Journal*

© 2016 Tous droits réservés.

lilliad.univ-lille.fr

Thèse de Qian Wang, Lille 1, 2016

of the American Chemical Society **2008**, *130*, 16201-16206.
[84] Bahr, J L; Yang, J; Kosynkin, D V; Bronikowski, M J; Smalley, R E; Tour, J M. Functionalization of carbon nanotubes by electrochemical reduction of aryl diazonium salts: a bucky paper electrode. *Journal of the American Chemical Society* **2001**, *123*, 6536-6542.
[85] Baker, S E; Tse, K-Y; Lee, C-S; Hamers, R J. Fabrication and characterization of vertically aligned carbon nanofiber electrodes for biosensing applications. *Diamond and Related Materials* **2006**, *15*, 433-439.
[86] Bekyarova, E; Itkis, M E; Ramesh, P; Berger, C; Sprinkle, M; de Heer, W A; Haddon, R C. Chemical modification of epitaxial graphene: spontaneous grafting of aryl groups. *Journal of the American Chemical Society* **2009**, *131*, 1336-1337.
[87] Paulus, G L C; Wang, Q H; Strano, M S. Covalent electron transfer chemistry of graphene with diazonium salts. *Accounts of Chemical Research* **2012**, *46*, 160-170.
[88] Bonanni, A; Ambrosi, A; Pumera, M. Nucleic acid functionalized graphene for biosensing. *Chemistry–A European Journal* **2012**, *18*, 1668-1673.
[89] Düzgün, A; Maroto, A; Mairal, T; O'Sullivan, C; Rius, F X. Solid-contact potentiometric aptasensor based on aptamer functionalized carbon nanotubes for the direct determination of proteins. *Analyst* **2010**, *135*, 1037-1041.
[90] Eissa, S; L'Hocine, L; Siaj, M; Zourob, M. A graphene-based label-free voltammetric immunosensor for sensitive detection of the egg allergen ovalbumin. *Analyst* **2013**, *138*, 4378-4384.
[91] Srivastava, R K; Srivastava, S; Narayanan, T N; Mahlotra, B D; Vajtai, R; Ajayan, P M; Srivastava, A. Functionalized multilayered graphene platform for urea sensor. *ACS Nano* **2011**, *6*, 168-175.
[92] Eissa, S; Zourob, M. A graphene-based electrochemical competitive immunosensor for the sensitive detection of okadaic acid in shellfish. *Nanoscale* **2012**, *4*, 7593-7599.
[93] Giovanni, M; Poh, H L; Ambrosi, A; Zhao, G; Sofer, Z; Šaněk, F; Khezri, B; Webster, R D; Pumera, M. Noble metal (Pd, Ru, Rh, Pt, Au, Ag) doped graphene hybrids for electrocatalysis. *Nanoscale* **2012**, *4*, 5002-5008.
[94] Wang, G; He, X; Wang, L; Gu, A; Huang, Y; Fang, B; Geng, B; Zhang, X. Non-enzymatic electrochemical sensing of glucose. *Microchimica Acta* **2013**, *180*, 161-186.
[95] Chen, S; Yuan, R; Chai, Y; Hu, F. Electrochemical sensing of hydrogen peroxide using metal nanoparticles: a review. *Microchimica Acta* **2013**, *180*, 15-32.
[96] Peng, H P; Hu, Y; Liu, P; Deng, Y N; Wang, P; Chen, W; Liu, A L; Chen, Y Z; Lin, X H. Label-free electrochemical DNA biosensor for rapid detection of mutidrug resistance gene based on Au nanoparticles/toluidine blue–graphene oxide nanocomposites. *Sensors and Actuators B: Chemical* **2015**, *207*, 269-276.
[97] Yu, Y; Chen, Z; He, S; Zhang, B; Li, X; Yao, M. Direct electron transfer of glucose oxidase and biosensing for glucose based on PDDA-capped gold nanoparticle modified graphene/multi-walled carbon nanotubes electrode. *Biosensors and Bioelectronics* **2014**, *52*, 147-152.
[98] Liu, G; Qi, M; Zhang, Y; Cao, C; Goldys, E M. Nanocomposites of gold nanoparticles and graphene oxide towards an stable label-free electrochemical immunosensor for detection of cardiac marker troponin-I. *Analytica Chimica Acta* **2016**, *909*, 1-8.
[99] Cui, F; Zhang, X. Electrochemical sensor for epinephrine based on a glassy carbon electrode modified with graphene/gold nanocomposites. *Journal of Electroanalytical Chemistry* **2012**, *669*, 35-41.
[100] Zhao, Y; Zhang, H; Huang, C; Chen, S; Liu, Z. Pt/Titania/reduced graphite oxide nanocomposite: An efficient catalyst for nitrobenzene hydrogenation. *Journal of Colloid and Interface Science* **2012**, *374*, 83-88.

© 2016 Tous droits réservés.
lilliad.univ-lille.fr

[101]Zhang, B; Cui, Y; Chen, H; Liu, B; Chen, G; Tang, D. A new electrochemical biosensor for determination of hydrogen peroxide in food based on well-dispersive gold nanoparticles on graphene oxide. *Electroanalysis* **2011**, *23*, 1821-1829.

[102]Xu, W P; Zhang, L C; Li, J P; Lu, Y; Li, H H; Ma, Y N; Wang, W D; Yu, S H. Facile synthesis of silver@graphene oxide nanocomposites and their enhanced antibacterial properties. *Journal of Materials Chemistry* **2011**, *21*, 4593-4597.

[103]Gong, F; Wang, H; Wang, Z S. Self-assembled monolayer of graphene/Pt as counter electrode for efficient dye-sensitized solar cell. *Physical Chemistry Chemical Physics* **2011**, *13*, 17676-17682.

[104]Yoon, Y; Samanta, K; Lee, H; Lee, K; Tiwari, A P; Lee, J; Yang, J; Lee, H. Highly Stretchable and Conductive Silver Nanoparticle Embedded Graphene Flake Electrode Prepared by In situ Dual Reduction Reaction. *Scientific Reports* **2015**, *5*, 14177.

[105]Fang, Y; Wang, E. Electrochemical biosensors on platforms of graphene. *Chemical Communications* **2013**, *49*, 9526-9539.

[106]Besra, L; Liu, M. A review on fundamentals and applications of electrophoretic deposition (EPD). *Progress in Materials Science* **2007**, *52*, 1-61.

[107]Corni, I; Ryan, M P; Boccaccini, A R. Electrophoretic deposition: from traditional ceramics to nanotechnology. *Journal of the European Ceramic Society* **2008**, *28*, 1353-1367.

[108]Oakes, L; Hanken, T; Carter, R; Yates, W; Pint, C L. Roll-to-roll nanomanufacturing of hybrid nanostructures for energy storage device design. *ACS Applied Materials & Interfaces* **2015**, *7*, 14201-14210.

[109]Boccaccini, A R; Zhitomirsky, I. Application of electrophoretic and electrolytic deposition techniques in ceramics processing. *Current Opinion in Solid State and Materials Science* **2002**, *6*, 251-260.

[110]Huang, S Y; Wu, G P; Chen, C M; Yang, Y; Zhang, S C; Lu, C X. Electrophoretic deposition and thermal annealing of a graphene oxide thin film on carbon fiber surfaces. *Carbon* **2013**, *52*, 613-616.

[111]Diba, M; Fam, D W H; Boccaccini, A R; Shaffer, M S P. Electrophoretic deposition of graphene-related materials: A review of the fundamentals. *Progress in Materials Science* **2016**, *82*, 83-117.

[112]Du, C; Heldbrant, D; Pan, N. Preparation and preliminary property study of carbon nanotubes films by electrophoretic deposition. *Materials Letters* **2002**, *57*, 434-438.

[113]Wu, M S; Lin, Y P; Lin, C H; Lee, J T. Formation of nano-scaled crevices and spacers in NiO-attached graphene oxide nanosheets for supercapacitors. *Journal of Materials Chemistry* **2012**, *22*, 2442-2448.

[114]Zheng, J S; Wang, M X; Zhang, X S; Wu, Y X; Li, P; Zhou, X G; Yuan, W K. Platinum/carbon nanofiber nanocomposite synthesized by electrophoretic deposition as electrocatalyst for oxygen reduction. *Journal of Power Sources* **2008**, *175*, 211-216.

[115]Lin, J Y; Chan, C Y; Chou, S W. Electrophoretic deposition of transparent MoS_2–graphene nanosheet composite films as counter electrodes in dye-sensitized solar cells. *Chemical Communications* **2013**, *49*, 1440-1442.

[116]Luan, X; Chen, L; Zhang, J; Qu, G; Flake, J C; Wang, Y. Electrophoretic deposition of reduced graphene oxide nanosheets on TiO_2 nanotube arrays for dye-sensitized solar cells. *Electrochimica Acta* **2013**, *111*, 216-222.

[117]Zhang, H; Zhang, X; Zhang, D; Sun, X; Lin, H; Wang, C; Ma, Y. One-step electrophoretic deposition of reduced graphene oxide and $Ni(OH)_2$ composite films for controlled syntheses supercapacitor electrodes. *The Journal of Physical Chemistry B* **2012**, *117*, 1616-1627.

[118]Fang, H; Zhang, S; Wu, X; Liu, W; Wen, B; Du, Z; Jiang, T. Facile fabrication of multiwalled carbon nanotube/α-MnOOH coaxial nanocable films by electrophoretic

© 2016 Tous droits réservés.

lilliad.univ-lille.fr

deposition for supercapacitors. *Journal of Power Sources* **2013**, *235*, 95-104.

[119]Wu, Z S; Pei, S; Ren, W; Tang, D; Gao, L; Liu, B; Li, F; Liu, C; Cheng, H M. Field emission of single layer graphene films prepared by electrophoretic deposition. *Advanced Materials* **2009**, *21*, 1756-1760.

[120]Abraham, S; Ciobota, V; Srivastava, S; Srivastava, S K; Singh, R K; Dellith, J; Malhotra, B D; Schmitt, M; Popp, J; Srivastava, A. Mesoporous silica particle embedded functional graphene oxide as an efficient platform for urea biosensing. *Analytical Methods* **2014**, *6*, 6711-6720.

[121]Tajabadi, M T; Basirun, W J; Lorestani, F; Zakaria, R; Baradaran, S; Amin, Y M; Mahmoudian, M R; Rezayi, M; Sookhakian, M. Nitrogen-doped graphene-silver nanodendrites for the non-enzymatic detection of hydrogen peroxide. *Electrochimica Acta* **2015**, *151*, 126-133.

[122]Diba, M; García-Gallastegui, A; Taylor, R N K; Pishbin, F; Ryan, M P; Shaffer, M S P; Boccaccini, A R. Quantitative evaluation of electrophoretic deposition kinetics of graphene oxide. *Carbon* **2014**, *67*, 656-661.

[123]An, S J; Zhu, Y; Lee, S H; Stoller, M D; Emilsson, T; Park, S; Velamakanni, A; An, J; Ruoff, R S. Thin film fabrication and simultaneous anodic reduction of deposited graphene oxide platelets by electrophoretic deposition. *The Journal of Physical Chemistry Letters* **2010**, *1*, 1259-1263.

[124]Wang, M; Duong, L D; Oh, J S; Mai, N T; Kim, S; Hong, S; Hwang, T; Lee, Y; Nam, J D. Large-area, conductive and flexible reduced graphene oxide (RGO) membrane fabricated by electrophoretic deposition (EPD). *ACS Applied Materials & Interfaces* **2014**, *6*, 1747-1753.

[125]Tang, L; Feng, H; Cheng, J; Li, J. Uniform and rich-wrinkled electrophoretic deposited graphene film: a robust electrochemical platform for TNT sensing. *Chemical Communications* **2010**, *46*, 5882-5884.

[126]Akhavan, O; Ghaderi, E; Rahighi, R. Toward single-DNA electrochemical biosensing by graphene nanowalls. *ACS Nano* **2012**, *6*, 2904-2916.

[127]Lee, Y R; Kim, I Y; Kim, T W; Lee, J M; Hwang, S J. Mixed colloidal suspensions of reduced graphene oxide and layered metal oxide nanosheets: useful precursors for the porous nanocomposites and hybrid films of graphene/metal oxide. *Chemistry–A European Journal* **2012**, *18*, 2263-2271.

[128]Zhang, H; Zhang, X; Zhang, D; Sun, X; Lin, H; Wang, C; Ma, Y. One-step electrophoretic deposition of reduced graphene oxide and Ni $(OH)_2$ composite films for controlled syntheses supercapacitor electrodes. *The Journal of Physical Chemistry B* **2012**, *117*, 1616-1627.

[129]Subramanian, P; Niedziolka-Jonsson, J; Lesniewski, A; Wang, Q; Li, M; Boukherroub, R; Szunerits, S. Preparation of reduced graphene oxide–Ni $(OH)_2$ composites by electrophoretic deposition: application for non-enzymatic glucose sensing. *Journal of Materials Chemistry A* **2014**, *2*, 5525-5533.

[130]Liu, S; Ou, J; Wang, J; Liu, X; Yang, S. A simple two-step electrochemical synthesis of graphene sheets film on the ITO electrode as supercapacitors. *Journal of Applied Electrochemistry* **2011**, *41*, 881-884.

© 2016 Tous droits réservés.

lilliad.univ-lille.fr

Thèse de Qian Wang, Lille 1, 2016

CHAPTER 2

VERTICALLY ALIGNED NITROGEN-DOPED CARBON NANOTUBE CARPET ELECTRODE FOR LYSOZYME SENSING

2.1 Introduction

Lysozyme, also known as *N*-acetylmuramide glycanhydrolase, is a relatively small protein (molecular weight: 14.3 kDa) consisting of only 129 amino acid residues. Lysozyme exhibits good anti-bacterial ability due to its capability of hydrolyzing the β-linkage between *N*-acetylneuraminic acid and *N*-acetylelucosamine in the bacterial cell wall [1]. This enzymatic activity gives lysozyme often the notation as "body's own antibiotic" (**Figure 2.1**). Due to its antibacterial properties, hen egg derived lysozyme has been widely used as a preservative in food industries. However, it has been confirmed that even a small amount of lysozyme in food products might be a potential allergen to people sensitive to egg proteins and thus the development of approaches to identify fast and accurately lysozyme levels in food has become an important issue.

Lysozyme itself also plays an important role in human health [2] as it is widely distributed in biological fluids and most living organisms (**Figure 2.1**). Under normal physiological conditions, the concentration of lysozyme in body secretions and tissues is low; however, increase in the lysozyme level in serum, cells, urine and saliva has been found to be connected with many diseases such as cancer, HIV, leukemia, renal diseases, *etc.* [3-7]. Therefore, the development of rapid, cheap, sensitive and specific means of detecting lysozyme has also become of great significance in this field.

© 2016 Tous droits réservés.
lilliad.univ-lille.fr

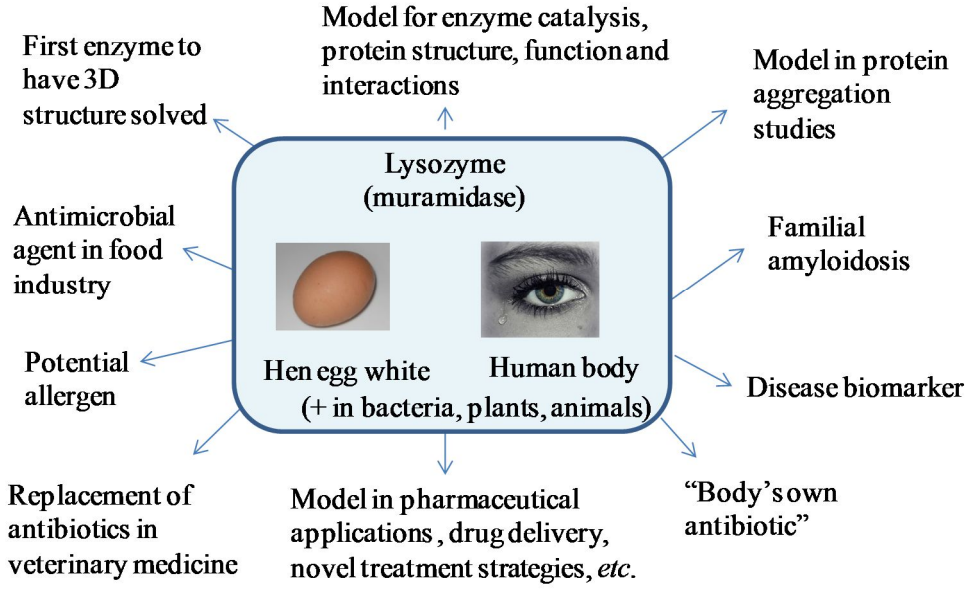

Figure 2.1: The relevance of lysozyme for protein science, medicine and industrial applications.

During the past years, quantitative detection of lysozyme has been achieved in various ways, including classical turbidimetry [8], colorimetry [9], chemiluminescence [10], fluorescence [11], resonance light-scattering [12], surface plasmon resonance [13] and electrochemistry [14]. Among them, electrochemical methods have found widespread applications due to the use of low cost instrumentation and the possibility of achieving high sensitivity and selectivity in the presence of interference analytes [15]. For the electrochemical detection of lysozyme, one sensing scheme widely employed is based on the high affinity of lysozyme with lysozyme specific aptamers. Aptamers are artificial single-stranded oligonucleotides (DNA or RNA) selected *in vitro* from nucleic acid libraries [16]. They can bind to a wide variety of targets ranging from metal ions, small molecules to proteins and even cells with high affinity, selectivity and specificity. The application of an aptamer as the analyte specific ligand has several advantages, including ease of synthesis, chemical stability, possibility of reusability and general adaptability for various proteins, accordingly making it a good alternative to the commonly used antibody [17]. Various electrochemical aptasensors based on direct, sandwiched or competitive assays have, therefore, been developed for lysozyme sensing, as summarized in **Table 2.1**.

© 2016 Tous droits réservés.
lilliad.univ-lille.fr

Table 2.1: Electrochemical aptasensors developed for lysozyme sensing.

Electrode	LOD	Linear Range	Real sample	Ref.
Direct assays				
Au/TiO_2/3D-rGO/PPy/LBA	5.5 pM	0.007–3.5 nM	Egg white	[18]
Au/TiO_2@PPAA/LBA	1.04 pM	3.5 pM–7 nM	Egg white	[19]
SPCE/AuNPs/LBA	21 fM	0.07–3.4 pM	Egg white	[20]
Au/AuNPs/LBA	0.01 pM	0.1–500 pM	Egg white	[21]
SPCE/LBA1 and LBA2	25 nM	0.025–0.8 µM	Wine	[22]
GCE/chitosan-GR/LBA	6 fM	0.01–0.5 pM	Chicken egg + saliva	[17]
Au/Cu_2O@rGO@PpPG	60 pM	0.1–200 nM	Saliva + urine + plasma	[23]
GCE/ THH Au NCs/APT	0.1 pM	0.1 pM–10 nM	Egg white + serum	[24]
PGE/chitosan–GO/LBA	28.53 nM	-	-	[25]
ITO/PABA/SA/LBA	14 nM	-	-	[26]
MWCNT–SPE/LBA	862 nM	-	-	[27]
GR-GCE/LBA	0.08 nM	0.2 –1040 nM	-	[28]
Fe_2O_3-GR-GCE/LBA	11.1 pM	35 pM–350 nM	-	[29]
GCE/O-GNs/LBA	1 pM	5.0 pM–0.7 nM	-	[30]
Au/LBA	-	35 nM–3.5 µM	-	[14]
ITO/(Fc-PEI/CNTs/Fc-PEI/LBA)	11.8 pM	13.9 pM–116 nM	-	[31]
Sandwich assay				
SPCE/LBA/Lysozyme/B-AB/SA-ALP	4.3 fM	5 fM–5 nM	Wine	[32]
Competitive Assays				
Au/CD/DLAP1 + DLAP2	64 pM	100–1000 pM	Serum	[33]
Au/MeB-cDNA/LBA	16.4 pM	0.1–100 nM	Serum	[34]
Au/LBA-(DNA-Fc)	0.45 nM	7–30 nM	Urine	[35]
Au/LBA/TCA/AuNPs/cDNA	0.1 pM	5 pM–1 nM	Egg white	[36]
Au/cDNA/LBA	1 pM	1.0 pM–1.1 nM	Egg white	[37]
Au/DNA1/BiDNA/DNA3-AuNPs	0.7 nM	-	-	[38]
Au/p-ATP-AuNPs/(LBA/Fc-cDNA)	0.1 pM	0.1 pM–1 nM	-	[39]
Au/cDNA/LBA	70 pM	0.2–4.0 nM	-	[40]
GCE/Au/(Fc-cDNA/LBA TWJ)	0.2 nM	0.2–100 nM	-	[41]

Abbreviations-AuNPs: gold nanoparticles; **B-AB**: biotinylated antibody; **BiDNA**: bifunctional aptamer for adenosine and lysozyme, linker DNA; **CD**: cyclodextrin; **CPE**: carbon paste electrode; **Cu_2O@rGO@PpPG**: nanocomposite of reduced graphene oxide, cuprous oxide and plasma-polymerized propargylamine; **DLAP**: dabcyl-labeled aptamer modified metal nanoparticles; **Fc**: ferrocene; **GCE**: glassy carbon electrode; **GO**: graphene oxide; **GR**: graphene; **IDA–Cu/AuNps/GCE**: iminodiacetic acid–copper ion complex immobilized on a glassy carbon electrode; **ITO**: indium tin oxide; **LBA**: lysozyme binding aptamer; **MeB-cDNA**: methylene blue-tagged complementary DNA; **O-GNs**: Orange II functionalized graphene nanosheets; **PABA**: poly-aminobenzoic acid; **PEI**: polyethyleneimine; **PGE**: pencil graphite electrode; **SA-ALP**: streptavidin-conjugate of alkaline phosphatase; **SPCE**: screen-printed carbon electrode;

© 2016 Tous droits réservés.

lilliad.univ-lille.fr

TCA/AuNP/ssDNA: thiocyanuric acid (TCA)/gold nanoparticles (AuNPs) modified with ssDNA; **THH Au NCs**: tetrahexahedral gold nanocrystals; **TiO_2@PPAA**: composite made of hollow TiO_2 spheres and polyacrylic acid; **TiO_2/3D-rGO/PPy**: hollow titanium dioxide nanoball, three-dimensional reduced graphene oxide and polypyrrole; **TWJ**: three-way junction.

Direct Assays

In order to translate the lysozyme-aptamer binding event into a measurable electrochemical signal, various techniques have been employed, including cyclic voltammetry (CV), differential pulse voltammetry (DPV), square wave voltammetry (SWV) or electrochemical impedance spectroscopy (EIS). Cheng *et al.* reported a simple detection scheme of lysozyme by CV response of positively charged $[Ru(NH_3)_6]^{3+}$ bound to the negatively charged DNA phosphate backbone of lysozyme aptamer through electrostatic interaction [14]. The difference in current intensity due to $[Ru(NH_3)_6]^{3+}$ reduction before and after incubation with lysozyme correlates with the concentration of lysozyme, which is the basic principle of the direct assay measurement. Similarly, negatively charged $[Fe(CN)_6]^{4-/3-}$ redox couple was also used to quantify bound lysozyme with changes in electron transfer when the aptamer-lysozyme complex was formed [22]. Direct assays are practical, label-free and easy in manipulating and exhibit wide linear range and limit of detections from fM to nM level, depending on the properties of electrode and aptamer linking strategies (**Table 2.1**).

Sandwich assays

Some of the aptasensors constructed based on direct schemes lack the required sensitivity for more demanding applications, such as the detection of lysozyme in biological samples or of trace amounts of lysozyme in wine. To achieve sensitive lysozyme detection, approaches based on labelled aptamers [35], displacement of complementary DNA [37] and sandwich assays were investigated for signal amplification. Ocaña *et al.* proposed a sandwich assay between the linked aptamer, the captured lysozyme and a biotinylated anti-lysozyme antibody [32]. Labeling the assembly with avidin-modified alkaline phosphatase ("ALP") and the addition of the enzyme specific substrate 1-naphtyl phosphate ("1-NPP") allow the indirect quantification of lysozyme, by recording the current response upon the formation of the electrochemically-active product, 1-naphtol. This assay exhibited a detection limit of 4.3 fM with a wide linear range from 5 fM to 5 nM. The strategy consists of multiple modifications and brings the inconvenience associated with enzyme stability, being complicated and time-consuming.

© 2016 Tous droits réservés.

lilliad.univ-lille.fr

Competitive Assays

Next to the direct and sandwich assays, competitive detection schemes based on displacement of lysozyme binding aptamer in the presence of lysozyme allowed sensitive lysozyme sensing [33-35], which could be adopted to various analytes. Xia *et al.* developed a novel biosensor for simultaneous electrochemical detection of interferon gamma (IFN-γ) and lysozyme (Lys) based on aptamer recognition by coupling "signal-on" and "signal-off" modes [34]. On one Au electrode, two kinds of signaling probes labeled by the thiolated ferrocene (Fc) and methyl blue (MB) were designed to hybridize with IFN-γ and Lys aptamers respectively to form partial complementary DNA duplexes. In the presence of IFN-γ and Lys, the target-aptamer interaction led to the release of aptamer from duplex DNA structure. The single-stranded signaling probes thus suffered from the conformation changes, which resulted in the decreased (or increased) oxidation peak current of Fc (or MB) according to the "signal-off (or signal-on)" mode. **Figure 2.2** illustrates the detection schemes of electrochemical lysozyme aptasensors.

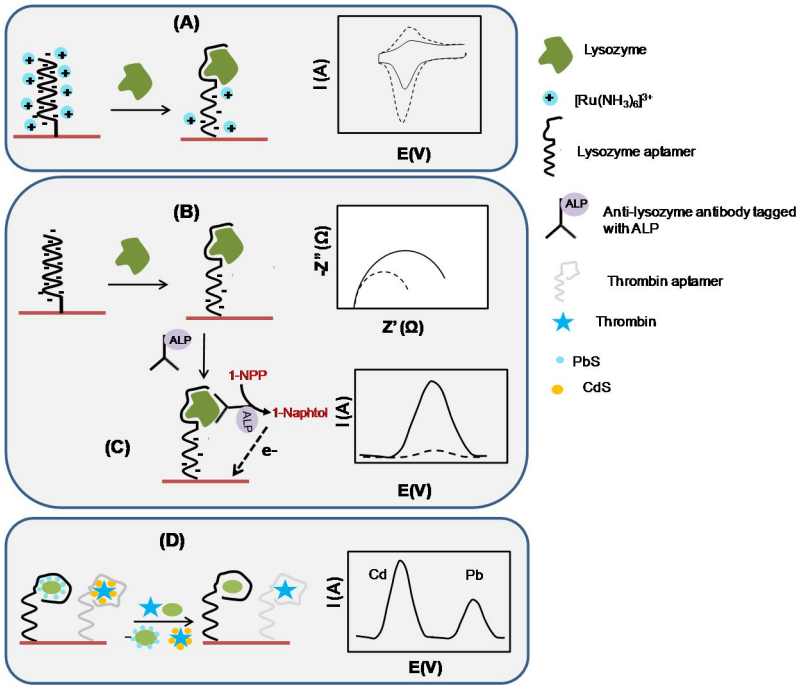

Figure 2.2: Detection schemes of electrochemical lysozyme aptasensors: (A) direct assay by recording the conformational changes of surface-linked aptamers upon lysozyme binding, which results in a decrease in electrostatically-bound $Ru(NH_3)_6]^{3+}$ detectable by CV [14]; (B) formation of the aptamer-lysozyme complex creates a barrier for the electron transfer of $(Fe(CN)_6]^{4-/3-}$ in solution proportional to lysozyme concentration and detectable by EIS [22]; (C) sandwich assay for lysozyme analysis using amplification with a lysozyme antibody labeled with alkaline phosphatase [32]; (D) competitive assay where free lysozyme in solution displaces quantum dot-tagged lysozyme, previously bound to surface-immobilized aptamer [42].

© 2016 Tous droits réservés.

lilliad.univ-lille.fr

From **Table 2.1**, it becomes clear that only half of the presented matrices were applicable for lysozyme detection in real biological samples. This is linked to the fact that only some sensors achieve the required picomolar sensitivity for real time sensing in biological samples [14,22,39].

The aim of the work in this chapter is thus the development of a new sensing strategy which will allow sensitive and selective lysozyme sensing to be achieved in a routine manner in biological fluids. As will be discussed in the following, we opted for the use of carbon nanotubes (CNT) structures.

CNT can be directly grown on different substrates [43,44]. Particularly, the formation of vertically aligned carbon nanotubes (VA-CNT) is desirable, as the growth process can be controlled, thus providing a well-defined large surface area that is of particular importance in devices such as field emitters [45] and sensors [46]. Apart from the controlled growth of CNT, modification of the CNT structure can strongly affect the performance of CNT in analytical applications. Replacement of some of the carbon atoms (C) with either boron (B) or nitrogen (N) through doping can tailor the electronic, chemical and mechanical properties of CNT [47]. Doping CNT with nitrogen is one strategy developed to yield a large number of defective sites and to highly increase the surface area [48]. Nitrogen-doped carbon nanotubes (NCNT) have also been proposed as promising electrocatalytic electrodes for oxygen reduction [49], hydrogen peroxide oxidation [50] and analysis of other molecules [51].

In this chapter, we took advantage of the excellent properties of nitrogen-doped vertically aligned CNT (VA-NCNT) for the development of a lysozyme aptasensor with fM level detection limit without any need of further amplification strategy. The excellent analytical performance of the sensor allowed its use for the analysis of serum samples from healthy patients and people infected with inflammatory bowel disease (IBD).

2.2 Construction of lysozyme sensitive aptasensor

2.2.1 Synthesis and characterization of VA-NCNT

The VA-NCNT carpet electrodes used in this work were provided by Palaniappan Subramanian (Ariel University, Israel). They were synthesized by a chemical vapor deposition

© 2016 Tous droits réservés.

lilliad.univ-lille.fr

(CVD) growth in a three-zone tube furnace (**Figure 2.3**) using a single fused-silica tube with an internal diameter of 22 mm [44,52]. The first two zones of the furnace preheated the precursor gases at 770°C to decompose the hydrocarbon gases. The sample was positioned in the last zone (zone 3) of the furnace for the annealing and growing steps at 755°C. All experiments were performed with "fast-heat" technique (**Figure 2.3**) by which the samples were exposed to heated zone until the annealing and growth process (details in experimental part, **Appendix**).

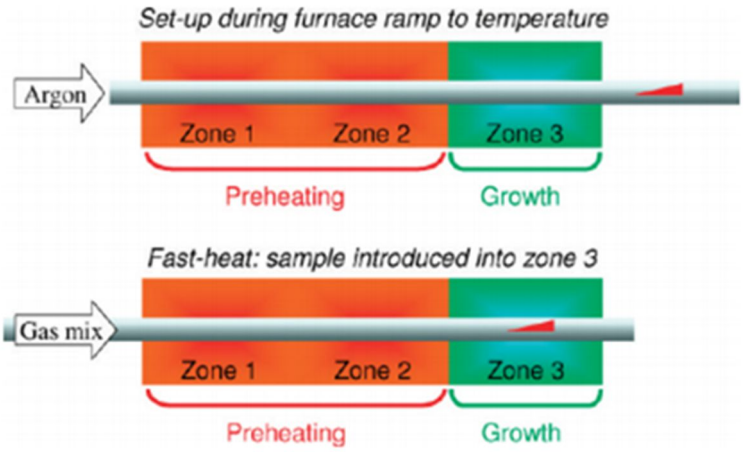

Figure 2.3: Structure of the furnace used in CVD growth of VA-CNT and scheme of "fast-heat" approach: the sample sits in a quartz tube outside the furnace (but still in an argon flow) while the temperature is ramped in the growth zone. It is then introduced into the growth zone when all temperatures are stable and the gas mixture is introduced [53].

The as-synthesized VA-CNT on stainless steel carpets were introduced into nitrogen plasma to obtain nitrogen doped interfaces (VA-NCNT). The morphology and chemical composition of the VA-NCNT were characterized by scanning electron microscopy (SEM), transmission electron microscopy (TEM), Raman spectroscopy and X-ray photoelectron spectroscopy (XPS) (**Figure 2.4**). The SEM image shows that dense VA-NCNT forests with a height of 7 ± 1 µm are formed (**Figure 2.4A**). The HRTEM image of the dispersed CNT indicates that the CNT have an average diameter of 10 ± 1 nm with 4-5 walls and exhibit a high degree of crystallinity (**Figure 2.4B**). A further analysis of the CNT structure was inferred in the Raman spectrum, which displays the characteristic D bands at ~1339 cm^{-1}, ~1340 cm^{-1} associated with carbon defect sites and G bands at ~1574 cm^{-1}, ~1578 cm^{-1} attributed to stretching of sp^2 carbon for VA-CNT and VA-NCNT, respectively (**Figure 2.4C**). The intensity of the D and G bands value (I_D/I_G) increased from 1.07 for VA-CNT to 1.16 after nitrogen doping for VA-NCNT, which reflected the increase in defect level [48].

© 2016 Tous droits réservés.

lilliad.univ-lille.fr

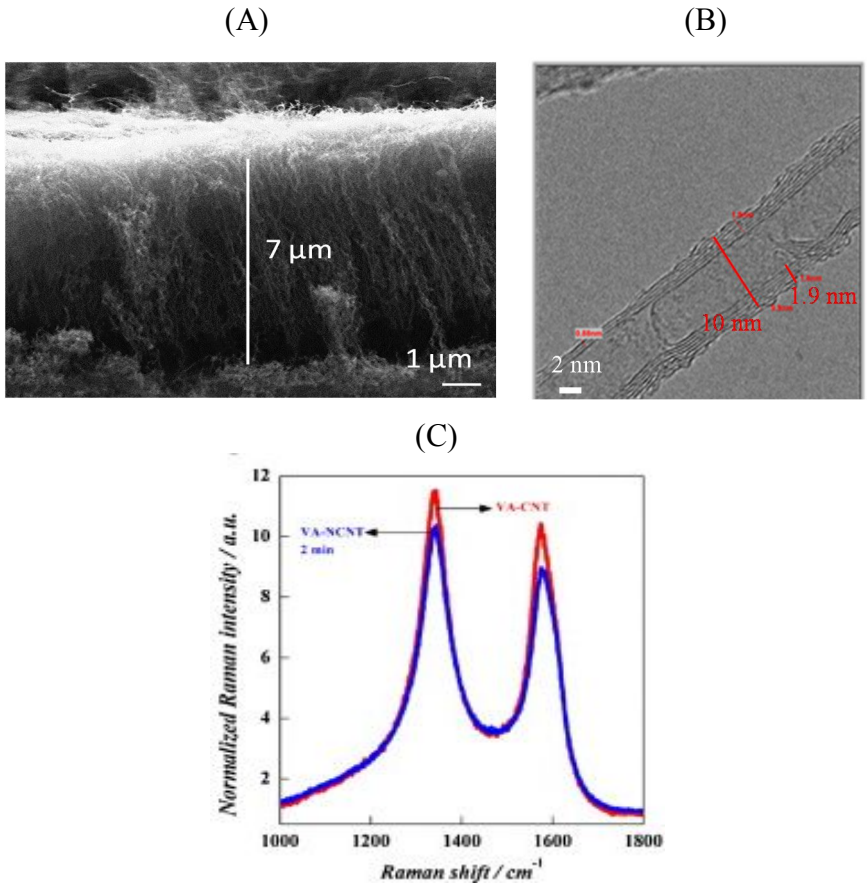

Figure 2.4: Characterizations of VA-NCNT: (A) SEM and (B) TEM images; (C) Raman spectra [48].

The chemical composition of the VA-NCNT was further examined by XPS. The full survey XPS spectra of VA-CNT and VA-NCNT are shown in **Figure 2.5A**. While the XPS survey spectrum of VA-CNT consists of only carbon, the XPS survey spectrum of VA-NCNT shows, in addition, the presence of N_{1s} with an atomic percentage of 2.1 % (**Table 2.2**). It also reveals that the nitrogen doping of VA-CNT introduces oxygen incorporation upon exposure to air, with a significant amount (12.5 at. %) of oxygen functions (**Table 2.2**), mainly in the form of C-O and C=O on the CNT's surface. The high resolution N_{1s} spectrum can be deconvoluted into two bands at 400.1 and 401.9 eV assigned to pyrrolic and quaternary N-functional groups, respectively (**Figure 2.5B**) [54]. In the case of C_{1s} high resolution in **Figure 2.5C**, the main peak at 284.5 eV is associated with sp^2 C-C with a band at 285.0 eV from C-C/C-H. Contributions at 286.5 eV (C-O/C-N) and 288.9 eV (C=O) confirm the introduction of oxygen during nitrogen doping process.

© 2016 Tous droits réservés.

lilliad.univ-lille.fr

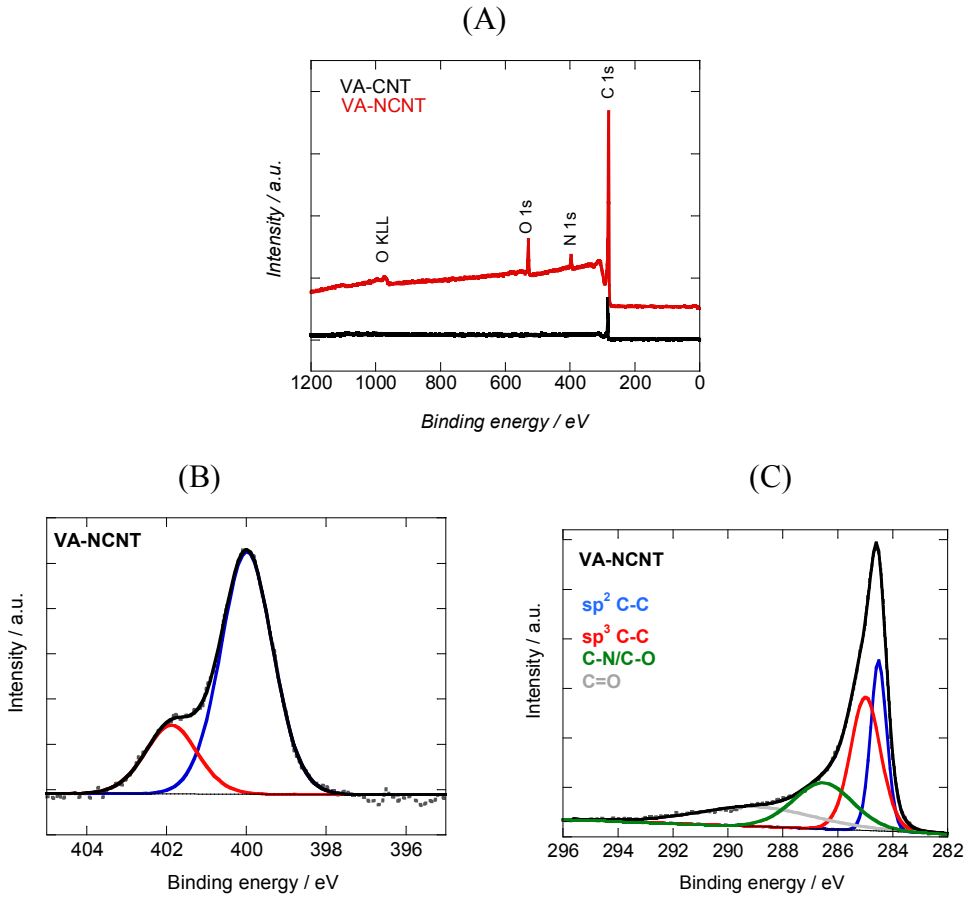

Figure 2.5: Characterizations of VA-NCNT: (A) full survey of XPS spectra: VA-CNT(black) and VA-NCNT(red); (B) N_{1s} and (C) C_{1s} high resolution spectra.

The electrochemical properties of the VA-NCNT carpet electrodes were determined by cyclic voltammetry (CV) using $[Fe(CN)_6]^{4-/3-}$ as redox couple. The VA-NCNT electrode shows a quasi-reversible electron transfer behavior with a peak separation (ΔE) of 116 mV (**Figure 2.6A**). This contrasts with the undoped VA-CNT of the same height, with a strongly decreased peak current and enlarged $\Delta E \approx 871$ mV, indicative of slow electron transfer occurring at undoped VA-CNT interfaces. Thus nitrogen-doped VA-NCNT are preferential for electrochemical sensing applications.

The rate of electron transfer depends not only on doping, but also on the overall height of the VA-NCNT. Increasing the height of the wires from 7 to 37 µm results in an increased peak separation ($\Delta E \approx 265$ mV) for the VA-NCNT with height of 37 µm (**Figure 2.6B**). The slower kinetics of the 37 µm long wire electrode is likely to be explained by the slower diffusion of the redox mediator through the densely packed nanotubes. For the integration into electrochemical sensing devices, VA-NCNT with fast heterogeneous electron transfer are advantageous [55-57]. Thus the VA-NCNT carpet electrodes of 7 µm in height were chosen for further construction of a lysozyme biosensor.

© 2016 Tous droits réservés.

lilliad.univ-lille.fr

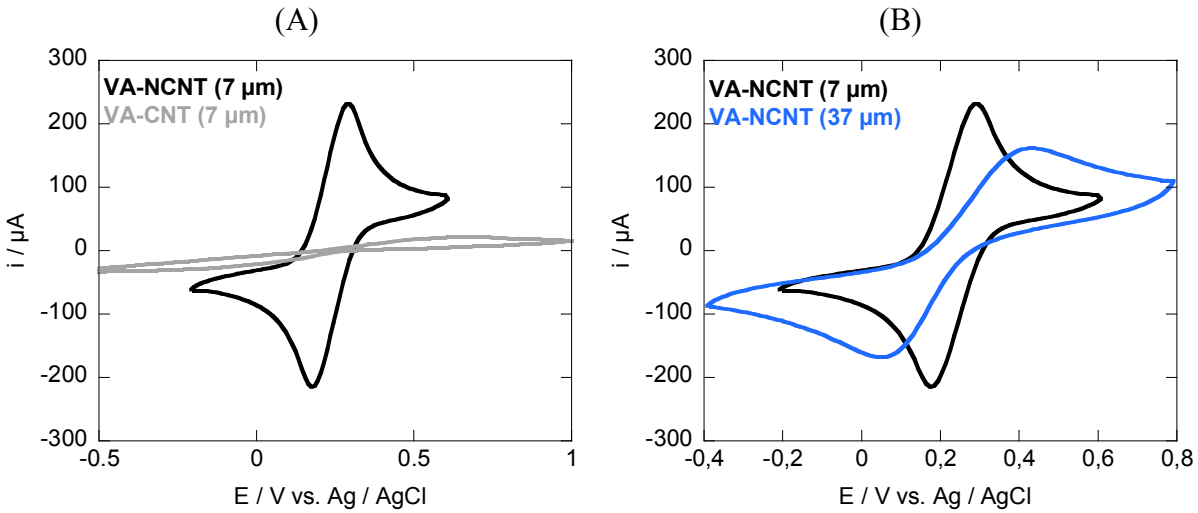

Figure 2.6: Cyclic voltammograms of (A) VA-CNT (height 7 µm) (gray), VA-NCNT (height 7 µm) (black) and (B) VA-NCNT (height 7 µm) (black), VA-NCNT (height 37 µm) (blue) in 5 mM $[Fe(CN)_6]^{4-/3-}$ in 0.01 M PBS, scan rate=50 mV s^{-1}.

2.2.2 Surface functionalization of VA-NCNT with biotinylated-lysozyme aptamers

Surface immobilization of lysozyme specific ligands, aptamers in our case, is of significant importance to achieve satisfactory selectivity in sensing. Various methods for aptamers immobilization onto solid supports have been reported, including physical adsorption, self-assembly, direct attachment to gold surfaces, covalent attachment to functionalized surfaces, coupling by affinity reactions (biotin-avidin affinity), and hybridization through complementary oligonucleotides [58,59]. In most cases, covalent linking to surfaces is preferred over physisorption as it can somehow increase the specificity and decrease interference signal of non-specific adsorption [58,60]. A recent report by Ocaña *et al*. compared 4 protocols for the immobilization of an aptamer on graphite composite electrodes for thrombin sensing [61]. It was found that sensors, prepared by covalent immobilization and particularly those using avidin-biotin affinity linkages of aptamers exhibited relatively higher sensitivity and wider linear range than those obtained through aptamer physisorption.

Moreover, electrochemical grafting of diazonium salts followed by covalent immobilization of aptamers showed to be the best sensor interface. In this work, we have thus opted the following strategy for aptamer linkage (**Figure 2.7**). First, electrochemical reduction of 4-carboxyl phenyl diazonium cations were synthesized *in situ* by mixing $NaNO_2$ and 4-aminobenzoic acid in HCl, and then transferred to an electrochemical cell. The grafting

© 2016 Tous droits réservés.

lilliad.univ-lille.fr

process of the very reactive aryl radicals was obtained upon reduction of diazonium cations (**Figure 2.7A**). Therefore, modification of the VA-NCNT electrode with the formed diazonium salt was performed by electrochemical reduction through scanning cyclic voltammetry from +0.4V to -0.6 V at a scan rate of 100 mV s^{-1}. Under electrochemical effect, the aryl radicals are formed through a one-electron reduction [62]. In **Figure 2.7B**, the irreversible wave disappears upon the performance of successive scans, indicating the blocking of electron transfer by the newly formed radical groups. Five scans were sufficient for subsequent generation of a satisfying organic layer [63]. Similar behaviors were observed in recently published works [64-66].

The introduction of carboxylic acid groups onto VA-NCNT after electrochemical reduction was validated by XPS analysis (**Figure 2.7C**). In addition to bands at 284.5 eV (sp^2 C-C), 285.0 eV (C-C/C-H), 286.5 eV (C-O/C-N), and 288.9 eV (C=O), the presence of a band at 291.3 eV (O-C=O), absent in the C_{1s} core level spectrum of VA-NCNT, indicates the successful incorporation of COOH groups onto VA-NCNT. At the same time, the atomic percentage of oxygen increased from 12.5% to 15.6% (**Table 2.2**).

The introduction of carboxylic groups onto VA-NCNT had an important effect on the electron transfer process (**Figure 2.8**). Inhibition of the electron transfer due to electrostatic repulsion between the negatively charged COOH groups and negatively charged $[Fe(CN)_6]^{4-/3-}$ redox probe was observed as pointed out by Chung *et al.* [67].

As shown in **Figure 2.7D**, after grafting of 4-carboxyphenyl diazonium salt, the terminal acid groups of VA-NCNT-COOH electrode were activated by EDC/NHS carbodiimide, followed by covalent linkage of neutravidin *via* amine bond formation. Finally, immobilization of biotinylated aptamer probe based on high affinity between avidin and biotin was realized by immersing VA-NCNT-neutravidin surface in a buffer solution containing the biotinylated aptamer. The specific aptamer for lysozyme used here has the following sequence: 5'-biotin-TTT TTT TTT TTT TTT TTT TTT TTT ATC AGG GCT AAA GAG TGC AGA GTT ACT TAG-3' [68].

© 2016 Tous droits réservés.

lilliad.univ-lille.fr

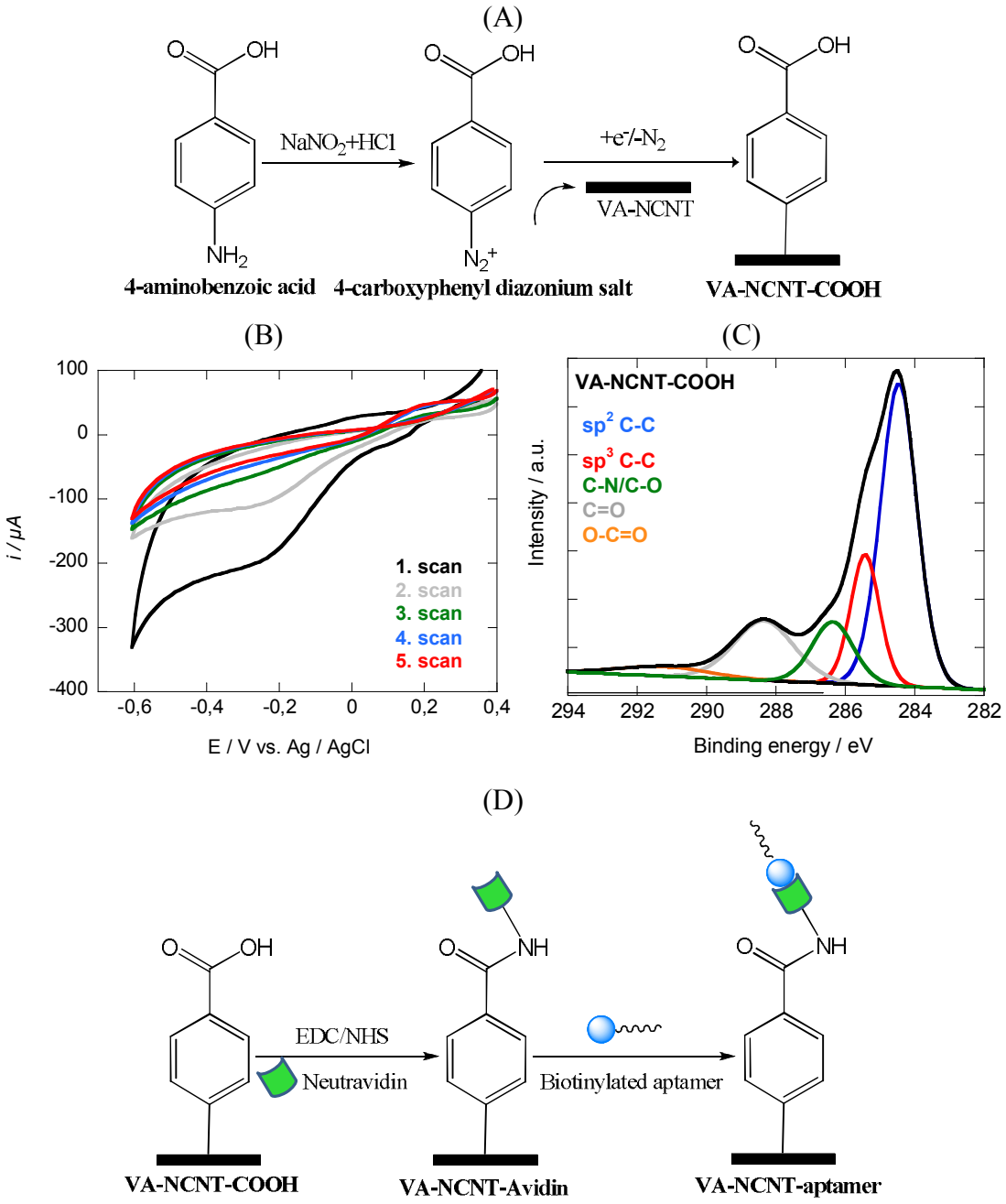

Figure 2.7: (A) Scheme of 4-carboxyphenyl diazonium salt formation; (B) Cyclic voltammograms of VA-NCNT electrode in a solution of 4-aminobenzoic acid (10 mM), $NaNO_2$ (10 mM)/HCl (0.5 M), scan rate: 100 mV s^{-1}; (C) C_{1s} high resolution spectrum of VA-NCNT-COOH; (D) Surface modification of VA-NCNT-COOH electrode through covalent immobilization of neutravidin and interaction with biotinylated lysozyme aptamer.

After neutravidin coupling, XPS analysis of the VA-NCNT-neutravidin electrode shows a significant increase in N_{1s} signal from 2.1 at. % to 6.8 at. % (**Table 2.2**). In addition, partial restoration of the electron transfer was observed (**Figure 2.8**). After binding of biotinylated aptamer to neutravidin-modified VA-NCNT electrode, additional peaks due to P_{2p} and S_{2p} appeared in the XPS survey spectrum (**Figure 2.9A**, **Table 2.2**), indicating the successful immobilization of the biotinylated aptamer onto VA-NCNT. A further decrease of the

© 2016 Tous droits réservés.

lilliad.univ-lille.fr

voltammetric peak current response of the $[Fe(CN)_6]^{4-/3-}$ redox probe is observed, which might be due to the electrostatic repulsion with the negatively charged phosphate backbone of the aptamer. **Figure 2.9B** displays the HRTEM image collected from the aptamer functionalized VA-NCNT. The image clearly shows the presence of a functionalized layer both on the lateral sides and tip (inset image) of the carbon nanotubes, suggesting that VA-NCNT are uniformly modified throughout their length.

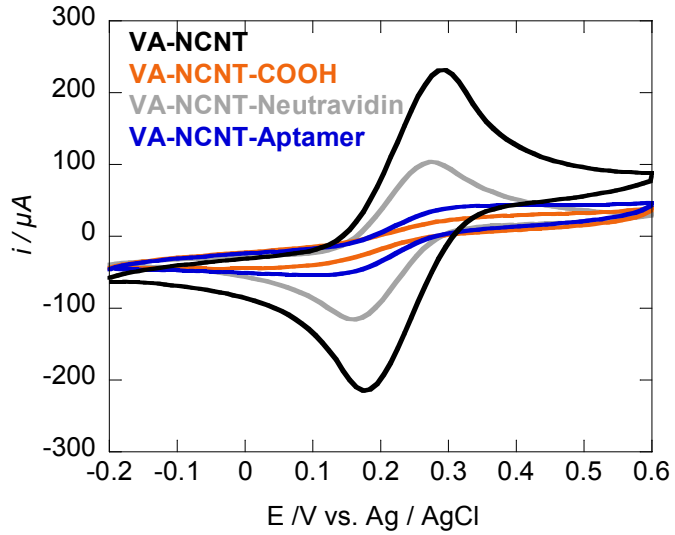

Figure 2.8: Cyclic voltammograms of VA-NCNT (black), VA-NCNT–COOH (orange), VA-NCNT-Neutravidin (grey), and VA-NCNT-Aptamer (blue) in 5 mM $[Fe(CN)_6]^{4-/3-}$ in 0.01 M PBS; scan rate: 50 mVs^{-1}.

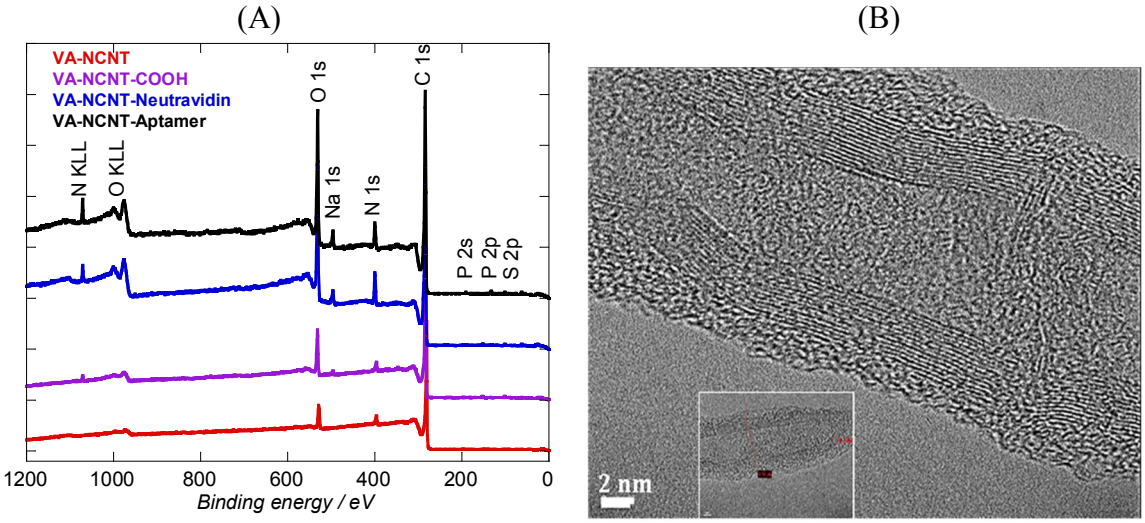

Figure 2.9: (A) Survey XPS spectra of VA-NCNTs: VA-NCNT (red), VA-NCNT-COOH (purple), VA-NCNT-Neutravidin (blue) and VA-NCNT-Aptamer (black); (B) HRTEM of aptamer modified VA-NCNT (lateral sides and inset image of tip part).

© 2016 Tous droits réservés.

lilliad.univ-lille.fr

Table 2.2: Atomic percentage (at. %) of elements as determined by XPS analysis of different VA-NCNT electrodes.

Sample	C_{1s} (at. %)	O_{1s} (at. %)	N_{1s} (at. %)	P_{2p} (at. %)	S_{2p} (at. %)
VA-NCNT	85.4	12.5	2.1	-	-
VA-NCNT-COOH	82.3	15.6	2.1	-	-
VA-NCNT-Neutravidin	75.1	18.1	6.8	-	-
VA-NCNT-Aptamer	69.3	19.4	9.3	1.2	0.8

2.3 Lysozyme sensing

To evaluate the performance of the developed sensor for the quantitative analysis of lysozyme, DPV is chosen to record the change of the oxidative current values of $[Fe(CN)_6]^{4-}$ upon incubating the aptamer modified interface with increasing concentrations of lysozyme. DPV is a very sensitive electroanalytical technique to study the redox properties of extremely small amount of chemicals due to effective discrimination against the charging current. As is illustrated in **Figure 2.10**, upon binding its target, the surface-linked aptamer experiences conformational changes, and the negative charges of the phosphate backbone in DNA are screened in part by the positively charged protein, as reported in previous literatures [17,24]. At the same time, formation of bulky lysozyme-aptamer complex at the surface of VA-NCNT results in partial blocking of the electron transfer from the redox probe to the electrode and this is the dominant effect observed with the $[Fe(CN)_6]^{4-}$ probe, translated in a smaller peak current intensity in DPV upon increasing lysozyme concentrations (**Figure 2.11A**). A similar behavior has been reported by Yang *et al*. for electrochemical sensing of DNA on CNT based aptasensor [69].

As shown in **Figure 2.11B**, a good linear relationship with a correlation coefficient of R=0.999 was observed between the change in the anodic peak current density of $[Fe(CN)_6]^{4-}$ redox probe and lysozyme concentration according to j(mA cm^{-2})=0.56-0.045×[lysozyme] (pM). The response curve saturates at≈7 pM, most likely due to the saturation in the number of binding sites. The detection limit of lysozyme was determined to be≈100 fM from five blank noise signals (95% confidence level), a concentration range that is appropriate for analysis of biological samples.

© 2016 Tous droits réservés.

lilliad.univ-lille.fr

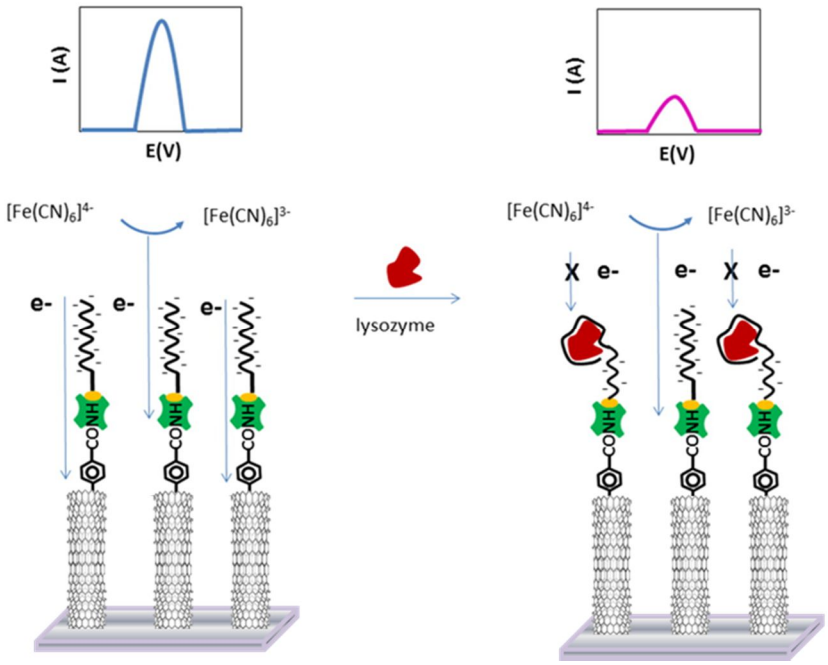

Figure 2.10: Principle of lysozyme sensing with the VA-NCNT-aptasensor.

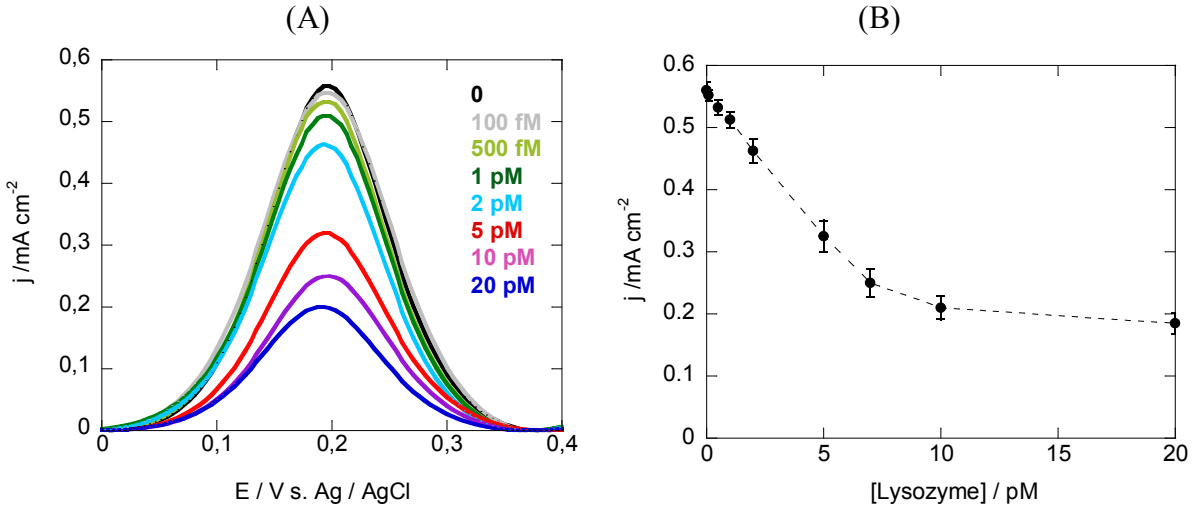

Figure 2.11: (A) DPVs of the VA-NCNT-aptamer electrode in 5 mM $[Fe(CN)_6]^{4-}$ in 0.01 M PBS after incubation with different concentrations of lysozyme; (B) calibration curve for lysozyme based on peak current intensity recorded by DPV.

The performance of the VA-NCNT-aptamer interface for lysozyme sensing is considerably improved when compared to most reported electrochemical interfaces as well as optical detection approaches (**Table 2.3**) without using amplification strategies or additional modification steps. A recently developed aptamer-antibody sandwich assay reported a detection limit of 4.3 fM by using chemical amplification [22]. Xiao *et al*. reported an impedimetric lysozyme aptasensor based on graphene modified glassy carbon electrode,

© 2016 Tous droits réservés.

lilliad.univ-lille.fr

exhibiting fM level limit detection [17]. While in the case of impedimetric aptasensor, it consists of several lengthy modification steps such as manual deposition of chitosan-graphene oxide mixture, chemical reduction of graphene oxide prior to aptamer binding, which is much more time-consuming as compared to VA-NCNT growth on stainless electrode.

However, one drawback of the VA-NCNT-aptamer sensor is the limited linear range, which is comparable to that of the impedimetric lysozyme aptasensor, but much smaller than that reported for screen printed carbon electrodes using chemical amplification [22]. This is most likely due to the saturation of aptamer binding sites.

Table 2.3: Comparison with other lysozyme sensing platforms.

Method	Interface	LOD	Linear range	Ref.
Fluorescence	GO/aptamer + amplification using exonuclease III	5.6 nM	8.7-70 nM	[70]
Electroluminescence	Au electrode, aptamer, $Ru(bpy)_3^{2+}$	120 pM	64 pM–0.64 μM	[71]
Square wave voltammetry	THH Au NCs/GCE-aptamer	0.1 pM	0.1 pM–10 nM	[24]
Cyclic voltammetry	Au with thiocyanuric acid /AuNPs-aptamer	0.1 pM	5 pM–1 nM	[36]
SPR	rGO-Au, aptamer	0.5 nM	0.5-200 nM	[13]
Impedance	GR–GCE-aptamer	6 fM	0.01–0.5 pM	[17]
DPV	SPCE-aptamer-antibody sandwich	4.3 fM	5 fM–5 nM	[22]
DPV	**VA-NCNT-aptamer**	**100 fM**	**0.1-7 pM**	**Our work**

The reproducibility of the electrodes was expressed in terms of the relative standard deviation (RSD) which was determined to be 2.3 % at a lysozyme concentration of 4 pM (n=5). The long-term stability of the VA-NCNT sensor was in addition evaluated showing a loss of 2.5 % in the cathodic peak current when testing 2 pM lysozyme solution after the electrode has been stored at 4 °C in 0.01M PBS for 2 weeks. This indicates that the VA-NCNT-aptamer lysozyme sensor kept its sensing ability during the storage.

The fact that the current drop was due to specific interaction between the biotinylated aptamer on the surface and lysozyme in solution was further investigated. To illustrate the selectivity of the sensor, VA-NCNT-aptamer electrode was incubated with four non-specific proteins. As can be seen in **Figure 2.12A**, the change in current was much lower with the other proteins like bovine serum albumin (BSA), cytochrome C (cyt C) and casein when compared to lysozyme, indicating the good selectivity of the sensor with negligible

© 2016 Tous droits réservés.

lilliad.univ-lille.fr

non-specific interaction with other proteins. In addition, the current response of lysozyme addition (5 pM) to non-functionalized VA-NCNT with aptamer was examined to ensure the lysozyme's specific binding to the aptamer. The observed current change was significantly smaller than in the presence of the aptamer.

A major concern inherent in protein detection assays is the possibility of background interference. It is thus important to assess the impact of serum proteins. Human serum protein solutions (diluted 10 times with PBS) were spiked with lysozyme (5 pM final concentration) and the current density signal was recorded by DPV (**Figure 2.12B**). When compared to the current density observed for the same lysozyme concentration in PBS, no change in signal was observed. Together with the good analytical performances, this demonstrated the feasibility of detecting lysozyme in real serum samples and the potential utility of VA-NCNT-aptamer electrodes to monitor the lysozyme level in patients affected by inflammatory bowel disease (IBD).

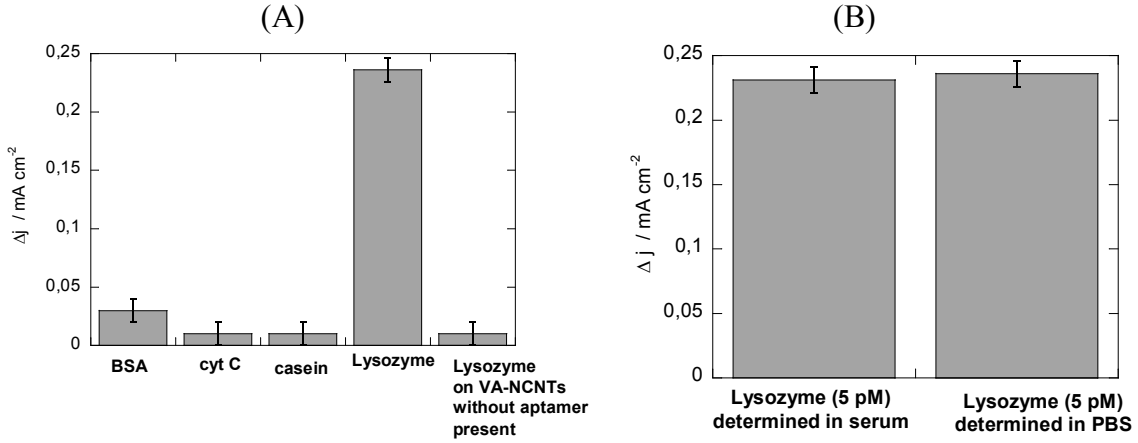

Figure 2.12: (A) Comparison of the analytical signal of the VA-NCNT-aptamer sensor to addition of bovine serum albumin (BSA, 5 pM), cytochrome C (cyt C, 5 pM), casein (5 pM) and lysozyme (5 pM), also shown is the response of unmodified VA-NCNT to 5 pM of lysozyme; (B) comparison of the current response on VA-NCNT-aptamer interfaces towards 5 pM lysozyme when measured in PBS or spiked human serum. Δj represents the change in current density measured by DPV in 5 mM $[Fe(CN)_6]^{4-}$/0.01 M PBS at pH 7.4, after incubation of the VA-NCNT-aptamer sensor with different proteins or spiked serum.

To evaluate the reliability and potential application of the proposed sensor, the lysozyme level in human serum samples from healthy people and patients suffering from IBD is determined using the VA-NCNT-aptamer sensor (**Table 2.4**). **Figure 2.13A** shows the electrochemical signals determined from diluted serum samples of healthy people and IBD patients. In the case of healthy individuals, the human serum sample was found to contain 0.23 ± 0.05 μM lysozyme. On the other hand, IBD infected patients showed lysozyme levels

© 2016 Tous droits réservés.

lilliad.univ-lille.fr

as high as 0.85 ± 0.07 µM. To confirm the results, the lysozyme concentration was in parallel determined by a classic turbidimetric assay [72]. In this assay, a suspension of killed Micrococcus lysodeikticus is made up in PBS, test serums are added and the decrease in optical density is recorded at 450 nm. The activity obtained was compared to those using standard (0-20 µg mL^{-1}) concentrations of egg white lysozyme (**Figure 2.13B**). For healthy individuals, the human serum sample was found to contain 3.36 ± 0.45 µg mL^{-1} (0.24 ± 0.03 µM) lysozyme. IBD infected patients showed 11.20 ± 0.98 µg mL^{-1} (0.80 ± 0.07 µM). These levels are consistent with lysozyme concentrations determined using the newly developed VT-NCNT-aptamer based assay as shown in **Table 2.4**. The results indicate that the newly developed biosensor is highly reliable for the analysis of clinical samples.

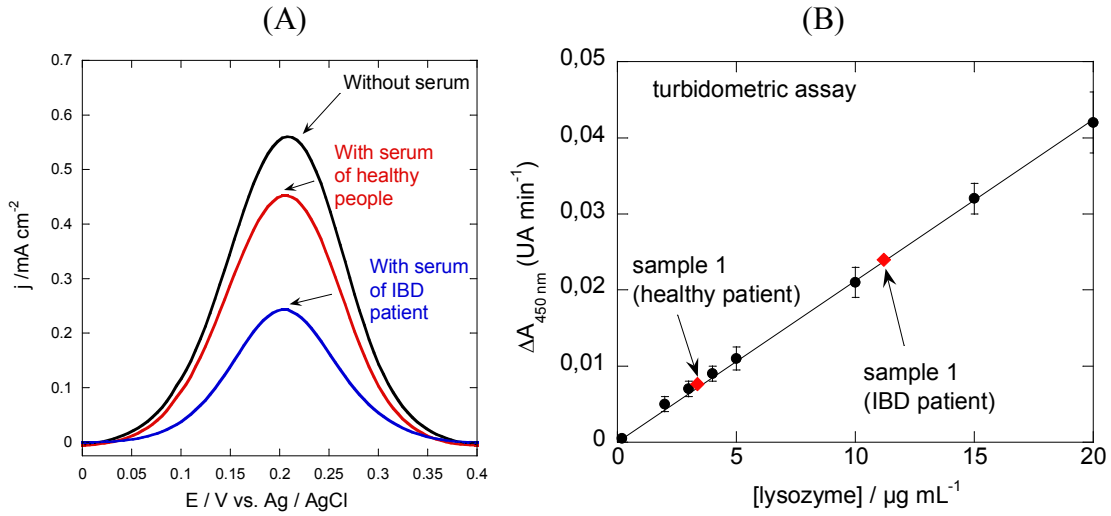

Figure 2.13: (A) DPVs of the VA-NCNT-aptamer electrode in 5 mM $[Fe(CN)_6]^{4-}$/0.01 M PBS after incubation with serum samples (10,000 times diluted) from healthy people (red) and IBD patient (blue); (B) calibration curve of turbidimetric assay for the determination of lysozyme concentrations in serum from healthy and IBD infected patients.

Table 2.4: Results of lysozyme concentrations in serum of healthy people and IBD infected patient.

Serum sample	Method	Determined concentration of lysozyme
1-Healthy people	Turbidimetric assay	3.36 ± 0.45 µg mL^{-1} (0.24 ± 0.03 µM)
2-IBD patient	Turbidimetric assay	11.2 ± 0.98 µg mL^{-1} (0.80 ± 0.07 µM)
1-Healthy people	DPV on VA-NCNT-aptamer electrode	3.22 ± 0.89 µg mL^{-1} (0.23 ± 0.05 µM)
2-IBD patient	DPV on VA-NCNT-aptamer electrode	11.9 ± 0.48 µg mL^{-1} (0.85 ± 0.03 µM)

© 2016 Tous droits réservés.

lilliad.univ-lille.fr

2.4 Conclusion

In this chapter, the great potential of chemically modified VA-NCNT electrodes for electrochemical sensing of lysozyme was demonstrated. Specific sensing was achieved through covalent integration of a biotinylated lysozyme aptamer on the carbon nanotube structures. The decrease in DPV current by using $[Fe(CN)_6]^{4-}$ as redox probe was treated as an indicator of lysozyme binding. A determined detection limit of 100 fM was achieved without any need of amplification, appropriate for detection of lysozyme levels in serum and urine. Furthermore, the feasibility and reliable use of the VA-NCNT-aptamer lysozyme sensing assay in clinical samples through the analysis of serum samples from healthy people and IBD infected patients were evaluated. The assay presented here also has the potential to serve as an interesting alternative for the analysis and diagnosis of patients suffering from leukemia and other diseases associated with higher or lower lysozyme levels.

2.5 References

[1] Huopalahti, R; Anton, M; López-Fandiño, R; Schade, R. *Bioactive egg compounds*. Springer: Berlin, 2007; p 33-66.

[2] Zhang, Z; Wang, Y; Zheng, F; Ren, R; Zhang, S. Ultrasensitive SERS assay of lysozyme using a novel and unique four-way helical junction molecule probe for signal amplification. *Chemical Communications* **2015**, *51*, 907-910.

[3] Levinson, S S; Elin, R J; Yam, L. Light chain proteinuria and lysozymuria in a patient with acute monocytic leukemia. *Clinical Chemistry* **2002**, *48*, 1131-1132.

[4] Guo, T K; Zhao, X H; Xie, X D; Chen, Z H; Zhou, C S; Wei, L L; Zhang, H. The anti-proliferative effects of recombinant human lysozyme on human gastric cancer cells. *Journal of International Medical Research* **2007**, *35*, 353-360.

[5] Lee-Huang, S; Maiorov, V; Huang, P L; Ng, A; Lee, H C; Chang, Y-T; Kallenbach, N; Huang, P L; Chen, H-C. Structural and functional modeling of human lysozyme reveals a unique nonapeptide, HL9, with anti-HIV activity. *Biochemistry* **2005**, *44*, 4648-4655.

[6] Tasca, S; Furlanello, T; Caldin, M. High serum and urine lysozyme levels in a dog with acute myeloid leukemia. *Journal of Veterinary Diagnostic Investigation* **2010**, *22*, 111-115.

[7] Åström, M; Bodin, L; Hörnsten, P; Wahlin, A; Tidefelt, U. Evidence for a bimodal relation between serum lysozyme and prognosis in 232 patients with acute myeloid leukaemia. *European Journal of Haematology* **2003**, *70*, 26-33.

[8] Liao, Y H; Brown, M B; Martin, G P. Turbidimetric and HPLC assays for the determination of formulated lysozyme activity. *Journal of Pharmacy and Pharmacology* **2001**, *53*, 549-554.

[9] Song, Y; Xu, C; Wei, W; Ren, J; Qu, X. Light regulation of peroxidase activity by spiropyran functionalized carbon nanotubes used for label-free colorimetric detection of lysozyme. *Chemical Communications* **2011**, *47*, 9083-9085.

[10] Jing, T; Xia, H; Guan, Q; Lu, W; Dai, Q; Niu, J; Lim, J M; Hao, Q; Lee, Y I; Zhou, Y.

© 2016 Tous droits réservés.

lilliad.univ-lille.fr

Rapid and selective determination of urinary lysozyme based on magnetic molecularly imprinted polymers extraction followed by chemiluminescence detection. *Analytica Chimica Acta* **2011**, *692*, 73-79.

[11] Wang, L; Li, L; Xu, Y; Cheng, G; He, P; Fang, Y. Simultaneously fluorescence detecting thrombin and lysozyme based on magnetic nanoparticle condensation. *Talanta* **2009**, *79*, 557-561.

[12] Toderas, F; Baia, M; Baia, L; Astilean, S. Controlling gold nanoparticle assemblies for efficient surface-enhanced Raman scattering and localized surface plasmon resonance sensors. *Nanotechnology* **2007**, *18*, 255702.

[13] Subramanian, P; Lesniewski, A; Kaminska, I; Vlandas, A; Vasilescu, A; Niedziolka-Jonsson, J; Pichonat, E; Happy, H; Boukherroub, R; Szunerits, S. Lysozyme detection on aptamer functionalized graphene-coated SPR interfaces. *Biosensors and Bioelectronics* **2013**, *50*, 239-243.

[14] Cheng, A K H; Ge, B; Yu, H-Z. Aptamer-based biosensors for label-free voltammetric detection of lysozyme. *Analytical Chemistry* **2007**, *79*, 5158-5164.

[15] Labib, M; Berezovski, M V. Electrochemical sensing of microRNAs: Avenues and paradigms. *Biosensors and Bioelectronics* **2015**, *68*, 83-94.

[16] Hermann, T; Patel, D J. Adaptive recognition by nucleic acid aptamers. *Science* **2000**, *287*, 820-825.

[17] Xiao, Y; Wang, Y; Wu, M; Ma, X; Yang, X. Graphene-based lysozyme binding aptamer nanocomposite for label-free and sensitive lysozyme sensing. *Journal of Electroanalytical Chemistry* **2013**, *702*, 49-55.

[18] Wang, M; Zhai, S; Ye, Z; He, L; Peng, D; Feng, X; Yang, Y; Fang, S; Zhang, H; Zhang, Z. An electrochemical aptasensor based on a TiO_2/three-dimensional reduced graphene oxide/PPy nanocomposite for the sensitive detection of lysozyme. *Dalton Transactions* **2015**, *44*, 6473-6479.

[19] Zhang, Z; Zhang, S; He, L; Peng, D; Yan, F; Wang, M; Zhao, J; Zhang, H; Fang, S. Feasible electrochemical biosensor based on plasma polymerization-assisted composite of polyacrylic acid and hollow TiO_2 spheres for sensitively detecting lysozyme. *Biosensors and Bioelectronics* **2015**, *74*, 384-390.

[20] Xie, D; Li, C; Shangguan, L; Qi, H; Xue, D; Gao, Q; Zhang, C. Click chemistry-assisted self-assembly of DNA aptamer on gold nanoparticles-modified screen-printed carbon electrodes for label-free electrochemical aptasensor. *Sensors and Actuators B: Chemical* **2014**, *192*, 558-564.

[21] Chen, Z; Li, L; Zhao, H; Guo, L; Mu, X. Electrochemical impedance spectroscopy detection of lysozyme based on electrodeposited gold nanoparticles. *Talanta* **2011**, *83*, 1501-1506.

[22] Ocaña, C; Hayat, A; Mishra, R K; Vasilescu, A; Del Valle, M; Marty, J L. Label free aptasensor for lysozyme detection: A comparison of the analytical performance of two aptamers. *Bioelectrochemistry* **2015**, *105*, 72-77.

[23] Fang, S; Dong, X; Ji, H; Liu, S; Yan, F; Peng, D; He, L; Wang, M; Zhang, Z. Electrochemical aptasensor for lysozyme based on a gold electrode modified with a nanocomposite consisting of reduced graphene oxide, cuprous oxide, and plasma-polymerized propargylamine. *Microchimica Acta* **2016**, *183*, 633-642.

[24] Chen, Z; Guo, J; Li, J; Guo, L. Tetrahexahedral Au nanocrystals/aptamer based ultrasensitive electrochemical biosensor. *RSC Advances* **2013**, *3*, 14385-14389.

[25] Erdem, A; Eksin, E; Muti, M. Chitosan–graphene oxide based aptasensor for the impedimetric detection of lysozyme. *Colloids and Surfaces B: Biointerfaces* **2014**, *115*, 205-211.

[26] Rodriguez, M C; Kawde, A N; Wang, J. Aptamer biosensor for label-free impedance spectroscopy detection of proteins based on recognition-induced switching of the surface

© 2016 Tous droits réservés.

lilliad.univ-lille.fr

charge. *Chemical Communications* **2005**, 4267-4269.

[27] Rohrbach, F; Karadeniz, H; Erdem, A; Famulok, M; Mayer, G. Label-free impedimetric aptasensor for lysozyme detection based on carbon nanotube-modified screen-printed electrodes. *Analytical Biochemistry* **2012**, *421*, 454-459.

[28] Du, M; Yang, T; Zhao, C; Jiao, K. Electrochemical logic aptasensor based on graphene. *Sensors and Actuators B: Chemical* **2012**, *169*, 255-260.

[29] Du, M; Yang, T; Guo, X; Zhong, L; Jiao, K. Electrochemical synthesis of Fe_2O_3 on graphene matrix for indicator-free impedimetric aptasensing. *Talanta* **2013**, *105*, 229-234.

[30] Guo, Y; Han, Y; Guo, Y; Dong, C. Graphene-Orange II composite nanosheets with electroactive functions as label-free aptasensing platform for "signal-on" detection of protein. *Biosensors and Bioelectronics* **2013**, *45*, 95-101.

[31] Du, Y; Chen, C; Li, B; Zhou, M; Wang, E; Dong, S. Layer-by-layer electrochemical biosensor with aptamer-appended active polyelectrolyte multilayer for sensitive protein determination. *Biosensors and Bioelectronics* **2010**, *25*, 1902-1907.

[32] Ocaña, C; Hayat, A; Mishra, R; Vasilescu, A; Del Valle, M; Marty, J L. A novel electrochemical aptamer–antibody sandwich assay for lysozyme detection. *Analyst* **2015**, *140*, 4148-4153.

[33] Cheng, L; Zhang, J; Lin, Y; Wang, Q; Zhang, X; Ding, Y; Cui, H; Fan, H. An electrochemical molecular recognition-based aptasensor for multiple protein detection. *Analytical Biochemistry* **2015**, *491*, 31-36.

[34] Xia, J; Song, D; Wang, Z; Zhang, F; Yang, M; Gui, R; Xia, L; Bi, S; Xia, Y; Li, Y. Single electrode biosensor for simultaneous determination of interferon gamma and lysozyme. *Biosensors and Bioelectronics* **2015**, *68*, 55-61.

[35] Chen, Z; Guo, J. A reagentless signal-off architecture for electrochemical aptasensor for the detection of lysozyme. *Electrochimica Acta* **2013**, *111*, 916-920.

[36] Chen, Z; Li, L; Tian, Y; Mu, X; Guo, L. Signal amplification architecture for electrochemical aptasensor based on network-like thiocyanuric acid/gold nanoparticle/ssDNA. *Biosensors and Bioelectronics* **2012**, *38*, 37-42.

[37] Liu, D Y; Zhao, Y; He, X W; Yin, X B. Electrochemical aptasensor using the tripropylamine oxidation to probe intramolecular displacement between target and complementary nucleotide for protein array. *Biosensors and Bioelectronics* **2011**, *26*, 2905-2910.

[38] Deng, C; Chen, J; Nie, L; Nie, Z; Yao, S. Sensitive bifunctional aptamer-based electrochemical biosensor for small molecules and protein. *Analytical Chemistry* **2009**, *81*, 9972-9978.

[39] Li, L D; Chen, Z B; Zhao, H T; Guo, L; Mu, X. An aptamer-based biosensor for the detection of lysozyme with gold nanoparticles amplification. *Sensors and Actuators B: Chemical* **2010**, *149*, 110-115.

[40] Peng, Y; Zhang, D; Li, Y; Qi, H; Gao, Q; Zhang, C. Label-free and sensitive faradic impedance aptasensor for the determination of lysozyme based on target-induced aptamer displacement. *Biosensors and Bioelectronics* **2009**, *25*, 94-99.

[41] Xia, Y; Gan, S; Xu, Q; Qiu, X; Gao, P; Huang, S. A three-way junction aptasensor for lysozyme detection. *Biosensors and Bioelectronics* **2013**, *39*, 250-254.

[42] Hansen, J A; Wang, J; Kawde, A-N; Xiang, Y; Gothelf, K V; Collins, G. Quantum-dot/aptamer-based ultrasensitive multi-analyte electrochemical biosensor. *Journal of the American Chemical Society* **2006**, *128*, 2228-2229.

[43] Talapatra, S; Kar, S; Pal, S K; Vajtai, R; Ci, L; Victor, P; Shaijumon, M M; Kaur, S; Nalamasu, O; Ajayan, P M. Direct growth of aligned carbon nanotubes on bulk metals. *Nature Nanotechnology* **2006**, *1*, 112-116.

[44] Nessim, G D; Hart, A J; Kim, J S; Acquaviva, D; Oh, J; Morgan, C D; Seita, M; Leib, J

© 2016 Tous droits réservés.

lilliad.univ-lille.fr

S; Thompson, C V. Tuning of vertically-aligned carbon nanotube diameter and areal density through catalyst pre-treatment. *Nano Letters* **2008**, *8*, 3587-3593.

[45] De Heer, W A; Chatelain, A; Ugarte, D. A carbon nanotube field-emission electron source. *Science* **1995**, *270*, 1179-1180.

[46] He, P; Dai, L. Aligned carbon nanotube–DNA electrochemical sensors. *Chemical Communications* **2004**, 348-349.

[47] Merkoçi, A; Pumera, M; Llopis, X; Pérez, B; del Valle, M; Alegret, S. New materials for electrochemical sensing VI: carbon nanotubes. *TrAC Trends in Analytical Chemistry* **2005**, *24*, 826-838.

[48] Subramanian, P; Cohen, A; Teblum, E; Nessim, G D; Bormasheko, E; Schechter, A. Electrocatalytic activity of nitrogen plasma treated vertically aligned carbon nanotube carpets towards oxygen reduction reaction. *Electrochemistry Communications* **2014**, *49*, 42-46.

[49] Gong, K; Du, F; Xia, Z; Durstock, M; Dai, L. Nitrogen-doped carbon nanotube arrays with high electrocatalytic activity for oxygen reduction. *Science* **2009**, *323*, 760-764.

[50] Xu, X; Jiang, S; Hu, Z; Liu, S. Nitrogen-doped carbon nanotubes: high electrocatalytic activity toward the oxidation of hydrogen peroxide and its application for biosensing. *ACS Nano* **2010**, *4*, 4292-4298.

[51] Tsierkezos, N; Othman, S H; Ritter, U; Hafermann, L; Knauer, A; Köhler, J M; Downing, C; McCarthy, E K. Electrochemical analysis of ascorbic acid, dopamine, and uric acid on nobel metal modified nitrogen-doped carbon nanotubes. *Sensors and Actuators B: Chemical* **2016**, *231*, 218-229.

[52] Teblum, E; Gofer, Y; Pint, C L; Nessim, G D. Role of catalyst oxidation state in the growth of vertically aligned carbon nanotubes. *The Journal of Physical Chemistry C* **2012**, *116*, 24522-24528.

[53] Nessim, G D; Seita, M; O'brien, K P; Hart, A J; Bonaparte, R K; Mitchell, R R; Thompson, C V. Low temperature synthesis of vertically aligned carbon nanotubes with electrical contact to metallic substrates enabled by thermal decomposition of the carbon feedstock. *Nano Letters* **2009**, *9*, 3398-3405.

[54] Zhao, A; Masa, J; Schuhmann, W; Xia, W. Activation and stabilization of nitrogen-doped carbon nanotubes as electrocatalysts in the oxygen reduction reaction at strongly alkaline conditions. *The Journal of Physical Chemistry C* **2013**, *117*, 24283-24291.

[55] Gao, C; Guo, Z; Liu, J H; Huang, X J. The new age of carbon nanotubes: an updated review of functionalized carbon nanotubes in electrochemical sensors. *Nanoscale* **2012**, *4*, 1948-1963.

[56] Wang, J; Zhang, W D. Sputtering deposition of gold nanoparticles onto vertically aligned carbon nanotubes for electroanalysis of uric acid. *Journal of Electroanalytical Chemistry* **2011**, *654*, 79-84.

[57] Berti, F; Lozzi, L; Palchetti, I; Santucci, S; Marrazza, G. Aligned carbon nanotube thin films for DNA electrochemical sensing. *Electrochimica Acta* **2009**, *54*, 5035-5041.

[58] Zhou, L; Wang, M H; Wang, J P; Ye, Z Z. Application of biosensor surface immobilization methods for aptamer. *Chinese Journal of Analytical Chemistry* **2011**, *39*, 432-438

[59] Acquah, C; Danquah, M K; Yon, J L S; Sidhu, A; Ongkudon, C M. A review on immobilised aptamers for high throughput biomolecular detection and screening. *Analytica Chimica Acta* **2015**, *888*, 10-18.

[60] Zhang, Z; Yang, W; Wang, J; Yang, C; Yang, F; Yang, X. A sensitive impedimetric thrombin aptasensor based on polyamidoamine dendrimer. *Talanta* **2009**, *78*, 1240-1245.

[61] Ocaña, C; del Valle, M. A comparison of four protocols for the immobilization of an aptamer on graphite composite electrodes. *Microchimica Acta* **2014**, *181*, 355-363.

© 2016 Tous droits réservés.

lilliad.univ-lille.fr

[62] Chaussé, A; Chehimi, M M; Karsi, N; Pinson, J; Podvorica, F; Vautrin-Ul, C. The electrochemical reduction of diazonium salts on iron electrodes. The formation of covalently bonded organic layers and their effect on corrosion. *Chemistry of Materials* **2002**, *14*, 392-400.

[63] Kowalczyk, A; Nowicka, A; Jurczakowski, R; Fau, M; Krolikowska, A; Stojek, Z. Construction of DNA biosensor at glassy carbon surface modified with 4-aminoethylbenzenediazonium salt. *Biosensors and Bioelectronics* **2011**, *26*, 2506-2512.

[64] Eissa, S; Zourob, M. A graphene-based electrochemical competitive immunosensor for the sensitive detection of okadaic acid in shellfish. *Nanoscale* **2012**, *4*, 7593-7599.

[65] Chung, D J; Oh, S H; Komathi, S; Gopalan, A I; Lee, K P; Choi, S H. One-step modification of various electrode surfaces using diazonium salt compounds and the application of this technology to electrochemical DNA (E-DNA) sensors. *Electrochimica Acta* **2012**, *76*, 394-403.

[66] Eissa, S; L'Hocine, L; Siaj, M; Zourob, M. A graphene-based label-free voltammetric immunosensor for sensitive detection of the egg allergen ovalbumin. *Analyst* **2013**, *138*, 4378-4384.

[67] Chung, D J; Kim, K C; Choi, S H. Electrochemical DNA biosensor based on avidin–biotin conjugation for influenza virus (type A) detection. *Applied Surface Science* **2011**, *257*, 9390-9396.

[68] Cox, J C; Ellington, A D. Automated selection of anti-protein aptamers. *Bioorganic & Medicinal Chemistry* **2001**, *9*, 2525-2531.

[69] Yang, K; Zhang, C. Simple detection of nucleic acids with a single-walled carbon-nanotube-based electrochemical biosensor. *Biosensors and Bioelectronics* **2011**, *28*, 257-262.

[70] Chen, C; Zhao, J; Jiang, J; Yu, R. A novel exonuclease III-aided amplification assay for lysozyme based on graphene oxide platform. *Talanta* **2012**, *101*, 357-361.

[71] Li, Y; Qi, H; Gao, Q; Zhang, C. Label-free and sensitive electrogenerated chemiluminescence aptasensor for the determination of lysozyme. *Biosensors and Bioelectronics* **2011**, *26*, 2733-2736.

[72] Yuji, I; Hidenori, Y; Taiji, I. Colorimetric assay for lysozyme using Micrococcus luteus labeled with a blue dye, Remazol brilliant blue R, as a substrate. *Chemical and Pharmaceutical Bulletin* **1992**, *40*, 1523-1526.

© 2016 Tous droits réservés.

lilliad.univ-lille.fr

CHAPTER 3

PREPARATION OF CARBON-BASED NANOCOMPOSITES BY ELECTROPHORETIC DEPOSITION: APPLICATION FOR NON-ENZYMATIC GLUCOSE SENSING

3.1 Introduction

Diabetes is a serious, chronic disease that occurs when the body does not produce enough insulin (type 1 diabetes, which requires external insulin injection), or when the body cannot effectively use the insulin it produces (type 2 diabetes). The majority of people with diabetes are affected by type 2 diabetes. Diabetes of all types can lead to complications including heart attack, stroke, kidney failure and vision loss, which can increase the overall risk of dying prematurely [1]. According to World Health Organization's report, the amount of people suffering from diabetes has risen from 108 million in 1980 to 422 million in 2014 [2]. An estimated 1.5 million deaths were directly caused by diabetes and another 2.2 million deaths related to high blood glucose content in 2012. The typical effect of diabetes is the irregular raised sugar concentration in the blood. Therefore, precise monitoring and careful control of glucose level in blood is of great significance in the early diagnosis and follow-up treatment of diabetes.

Over the past few decades, a tremendous amount of work has been dedicated to the field of glucose detection and a substantial progress has been made in this field. Various techniques for detecting glucose by electrochemical methods [3] (amperometry [4], potentiometry [5], *etc*.), optical methods [6] (fluorescence [7], surface plasmon resonance (SPR) [8], luminescence [9], *etc*.), chromatography [10,11], and capillary zone electrophoresis [12] have been proposed. Among these different detection schemes, electrochemical methods are the most established ones with commercial success, because they offer low detection limits, fast response time, enhanced sensitivity, good selectivity, low cost and easy operation [13]. Indeed, the first biosensor developed was a glucose sensor reported by Clark and Lyons in 1962 [14].

© 2016 Tous droits réservés.

lilliad.univ-lille.fr

The detection of glucose is based on the use of enzymes such as glucose oxidase (GOx) or glucose dehydrogenase (GDH) [15] immobilized onto the electrode surface (**Figure 3.1A**). In the presence of GOx, glucose is converted in the presence of oxygen into gluconic acid and hydrogen peroxide (eqn (1)), which can be electrochemically detected. This made up of the principle for the first generation of glucose sensors.

$$glucose + O_2 \xrightarrow{GO_X} gluconic\ acid + H_2O_2 \quad (1)$$

Instead of oxygen, artificial mediators such as ferrocene derivatives and ferricyanide [16] have been employed where the change in their redox current is linearly correlated to glucose. In the process, glucose is oxidized with the reduction of the Flavin adenine dinucleotide (FAD) group of GOx into $FADH_2$, followed by the reoxidation of GOx ($FADH_2$) by the electron mediator (Med_{ox}) to generate FAD again (**Figure 3.1A**), as illustrated in eqn (2) and (3). The glucose sensors can overcome the limitations of the first generation sensors caused by oxygen deficiency in blood samples, however, the performance of sensors was strongly affected by the presence of redox active species like oxygen [17].

$$GO_X(FAD) + glucose \rightarrow GO_X(FADH_2) + gluconic\ acid \quad (2)$$

$$GO_X(FADH_2) + Med_{ox} \rightarrow GO_X(FAD) + Med_{red} \quad (3)$$

The glucose sensors based on the strategy of the direct electron transfer belong to the third generation (**Figure 3.1A**). In this type, electrons are directly transferred from enzyme to the electrode. Direct electrochemistry of enzyme eliminates possible interferences caused by co-substrates such as oxygen or mediators [18]. **Figure 3.1A** summarizes the mechanisms of the different enzymatic glucose sensors.

© 2016 Tous droits réservés.

lilliad.univ-lille.fr

(A)

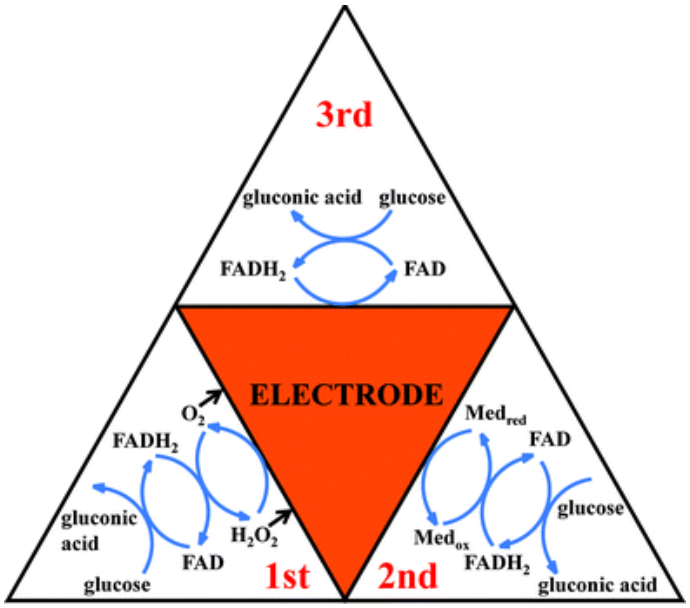

(B)

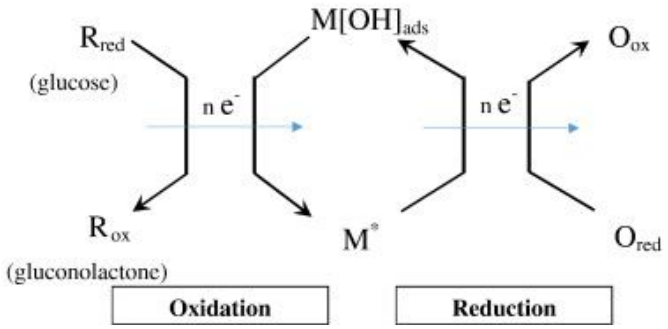

Figure 3.1: Different schemes of glucose sensors: (A) three generations of enzymatic electrodes based on the use of oxygen (1st generation), artificial redox mediators (2nd generation) and direct electron transfer between enzyme and electrode (3rd generation) [3]; (B) possible scheme of non-enzymatic glucose sensors: active metal adsorption site M^* oxidizes to $M[OH]_{ads}$, which catalyzes the oxidation of glucose to gluconolactone during its reduction to M^* [19].

Though enzymatic glucose sensors achieved rapid development and great success with high selectivity and sensitivity, they still suffer from the problem of insufficient stability caused by the dependency of enzyme's activity on temperature, humidity, pH and interferences [20]. Moreover, the introduction of enzymes increases the complexity as well as the cost of sensor construction. Non-enzymatic glucose sensor appears to be an alternative technique to overcome the disadvantages of enzymatic methods.

Unlike the traditional enzymatic sensors, non-enzymatic electrodes themselves act as electrocatalysts instead of enzymes such as GOx (**Figure 3.1B**). Although there is no proved theory explaining the mechanism of glucose oxidation at the electrode yet, two models are

© 2016 Tous droits réservés.

lilliad.univ-lille.fr

generally accepted. The activated chemisorption model proposed by Pletcher [21], which proposes that the adsorption of glucose molecule to the electrode triggers the oxidation by electrocatalysts. Another model known as "Incipient Hydrous Oxide Adatom Mediator" (IHOAM) proposed by Burke [22], which is based on the formation of hydrous oxide layer expressed as $M[OH]_{ads}$ in eqn (5) with aid of active atoms on the electrode surface, mediating the oxidation of glucose, as shown in **Figure 3.1B**.

$$H_2O \rightarrow H^+ + OH^- \quad (4)$$

$$M^* + [OH^-]_{ads} \rightarrow M[OH]_{ads} \quad (5)$$

$$M[OH]_{ads} + glucose \rightarrow M^* + gluconolactone \quad (6)$$

Despite the fact that the electrodes offer less specific electrocatalytic ability than enzymes for glucose oxidation, non-enzymatic glucose sensors usually display many advantages like better stability, and lower cost [23]. A variety of nanomaterials have been proposed for non-enzymatic glucose sensors, including metal nanoparticles or nanostructures based on Au [24], Pt [25], Ni [26], Cu [27], Pd [28], alloys like Au-Ag [29], Pt-Pd [30], Ni-Cu [31], metal oxides like copper oxide [32], cobalt oxide [33], nickel oxide [34] and carbon materials such as graphene [35], carbon nanotubes [36], carbon nanofibers [37]. Materials in the form of nanocomposites consisting of metal-based structures and carbon materials with combined properties are particularly popular [38].

Due to the high cost of noble metals and alloys [39], low-cost transition metal based nanostructures have become good alternatives for the preparation of non-enzymatic glucose sensors. Copper (Cu) and cobalt (Co)-based electrodes represent interesting categories of electrocatalytic materials for glucose oxidation. Indeed, carbohydrate oxidation at Cu electrodes in alkaline media has been investigated already in the early 90s [40,41]. In the case of Co-based electrodes, Co_3O_4 nanofibers were first explored for non-enzymatic electrochemical glucose sensing by Ding *et al.* in 2010 [33]. Since then, researchers reported various non-enzymatic glucose sensors based on Co electrodes with high sensitivity, mainly in the form of cobalt oxides (CoO, $Co(OH)_2$, Co_3O_4, *etc.*). **Table 3.1** summarizes some of the Cu and Co-based materials demonstrated in recent years for their use in non-enzymatic electrochemical glucose detection.

© 2016 Tous droits réservés.

lilliad.univ-lille.fr

Table 3.1: Recently published copper and cobalt-based materials applied for non-enzymatic electrochemical glucose detection.

Material	LOD (μM)	Sensitivity ($\mu A\ mM^{-1}\ cm^{-2}$)	Linear range (mM)	Ref.
Cu nanobelt	10	79.8	0.01-1.3	[23]
CuO nanorod	1.2	0.45	0.01-0.1	[42]
CuS microflower	2	1007	0.02-5.4	[43]
CuO/NiO/PANI	2	340.2 $\mu A\ mM^{-1}$	0.02-2.5	[44]
Cu NPs/PANI/graphene	0.27	150	0.001-3.7	[45]
Cu NPs@Chit–CNT	0.05	148 $\mu A\ mM^{-1}$	0.0005-1	[46]
Cu NPs/PMo_{12}-GR	0.03	153.2 $\mu A\ mM^{-1}$	0.0001-1	[47]
Cu_2O/SMWNTs	0.2	2143	0.0005-2.5	[48]
Cu@TiC/CNF arrays	0.2	415	0.001-1.7	[49]
Cu NPs–N-GR	1.3	48.13	0.004–4.5	[50]
CuO–GR–GCE	0.7	1360	0.002 to 4	[51]
Cu-graphene	0.5	-	up to 4.5	[52]
CuNPs-graphene	0.2	607	0.005-1.4	[53]
CuNPs/PAA/GR	0.08	-	0.0003-0.6	[54]
CuNPs/MWCNTs	0.5	50.47	0.01-0.3	[55]
Cu–CNTs	0.21	17.76	0.0007-3.5	[56]
Cu_2O-MWCNT	0.05	6.53	up to 0.01	[57]
CuO/MWCNTs	0.2	2596	0.0004-1.2	[58]
CuCo-CFs/Nafion/GCE	1.0	507	0.02-11	[59]
CuO nanoneedle/N-rGO	0.01	3.4 $\mu A\ mM^{-1}$	0.0005-0.639	[60]
CuO NPs/SG	0.08	1298.6	0.1-10.5	[39]
Cu/MnO_2/MWCNTs	0.17	1302	0.01-1	[61]
$CuFe_2O_4$–MWCNTs	0.2	32.3 $\mu A\ mM^{-1}$	0.0005-1.4	[62]
Co/GCE	0.5	10 $\mu A\ mM^{-1}$	0.0005-0.5	[63]
Co/GCE	0.3	-	0.0003-3	[64]
Co_3O_4	0.8	27.33	0.5-5	[65]
Co_3O_4 nanofibers	0.97	0.034	up to 2	[33]
CoO nanorods	0.06	0.57	up to 3.5	[66]
3D porous Co_3O_4	0.1	0.47	0.01-0.3	[67]
CoOOH nanosheet	1.37	526.8	0.003-1.109	[68]
CoP nanorods	9	116.8	up to 5.5	[69]
$(Co\text{-}Ni)(OH)_2$	-	122.45	0.025-3.7	[70]
Co-MWCNT	0.3	727.37	up to 3.6	[71]
Co-Ni nanostructures/rGO	3.79	1773.61	0.01-2.65	[72]
Co–CuNPs/TiO_2 nanotube	0.6	4651.0	up to 12	[73]
Graphene -Co_3O_4	10	-	0.05-0.3	[74]
Graphene foam -Co_3O_4	0.025	3.4	up to 0.1	[75]
Co_3O_4/PbO_2 nanorods array	0.31	0.46	0.005-1.2	[76]
CNTs/CoO/$Co(OH)_2$	2	162	up to 4.5	[77]
rGO-chitosan-Cu/Co	10	1920	0.015-6.95	[78]

Abbreviations-Chit: chitosan; **CNT**: carbon nanotube; **CuCo-CFs**: Bimetallic CuCo nanoparticles doped-carbon nanofibers; **Cu NPs**: copper nanoparticles ; **GR**: graphene; **MWCNTs**: multi-walls carbon nanotubes; **N-GR**: nitrogen-doped graphene; **N-rGO**: nitrogen-doped reduced graphene oxide; **PAA/GR**: polyacrylic acid/graphene; **PANI** : polyaniline; **PMo_{12}-GR**: phosphomolybdic acid functionalized graphene; **SG**: S-doped graphene.

© 2016 Tous droits réservés.

lilliad.univ-lille.fr

From **Table 3.1,** it becomes clear that integration of Co and Cu nanostructures into/onto carbon-based materials and electrodes has shown to be advantageous for non-enzymatic glucose sensing, where highly sensitive sensing with low detection limits can be achieved.

Graphene with a high density of edge-plane defect sites is an ideal support for various nanostructures. A Cu nanowire/reduced graphene oxide (Cu NWs/rGO) hybrid with fascinating sensitivity for glucose oxidation was fabricated recently through a one-step wet-chemical synthetic approach, in which hydrazine was used for GO reduction and Cu NWs formation [79]. Dong *et al.* developed a 3D graphene/Co_3O_4 nanowire composite by the *in situ* synthesis of Co_3O_4 nanowires on 3D graphene foam grown by chemical vapor deposition [75]. The composite demonstrated remarkable performance towards non-enzymatic glucose sensing with a sensitivity of 3.9 mA mM^{-1} cm^{-2} and a detection limit of 100 nM. Kong *et al.* took advantage of thionine functionalized graphene oxide (GO) with embedded Au nanoparticles (NPs) for the enzyme-free detection of glucose with a low detection limit of 50 nM [80]. **Table 3.2** summarizes some graphene-based composites for non-enzymatic electrochemical glucose sensing published recently.

Next to rGO, carbon nanofibers (CNFs), cylindric nanostructures comprising graphene layers that are arranged as stacked cones, cups or plates with lengths up to micrometers and diameters in the range of tens to 200 nm [81], have been extensively used as non-enzymatic glucose sensors (**Table 3.2**). Lu *et al.* demonstrated the CuO nanoparticles deposition on nitrogen-doped carbon nanofibers (N-CNFs) through a solvothermal approach [82]. Due to the synergistic effect of the properties of CuO nanoparticles and N-CNFs, the CuO/N-CNFs modified electrodes exhibited excellent activity for direct electrocatalytic oxidation of glucose with much higher sensitivity than electrode modified with pure CuO nanoparticles or N-CNFs. Indeed, the combination of metal nanoparticles with carbon materials can often greatly improve the overall catalytic activity of nanomaterials. A series of bimetallic MCo (M=Cu, Fe, Ni, and Mn) nanoparticles anchored and embedded in CNFs by electrospinning and subsequent thermal treatment processes have been synthesized recently by Li *et al*. [59]. Benefit from the structural advantages of the 3D network and the synergistic effect of the Co(III)/Co(IV) and Cu(II)/Cu(III) redox couples, CuCo-CNFs displayed the best performance for enzyme free detection of glucose with a wide linear range from 0.02 to 11 mM and a detection limit of 1 μM.

© 2016 Tous droits réservés.

lilliad.univ-lille.fr

Table 3.2: Graphene/carbon nanofibers-based nanocomposites and their performance for non-enzymatic electrochemical glucose sensing.

Electrode	Method of electrode fabrication	LOD (μM)	Sensitivity (μA mM^{-1} cm^{-2})	Linear range (mM)	Ref.
Cu nanoflower/RGO paper	Electrochemical deposition / mold-casting	0.5	50.4	0.002-13	[83]
Cu_2O/graphene/GCE	Chemical reduction / drop casting	0.36	1330.03	0.01-3	[84]
Cu_2O/NiO*x*/GO/GCE	Electrodeposition / drop casting	0.4	285	0.002-0.87	[85]
Cu_2O/AlOOH/rGO/GCE	Chemical reduction / drop casting	2.6	155.1	0.005-14.77	[86]
CuO/PrGO-GCE	Hydrothermal reaction / dip coating	0.5	207.3	0.001-6	[87]
AuNPs/NG/ITO	Seed-assisted growth / transfer	12	0.25	0.04-16.1	[88]
Au–CuO/rGO/SPE	Chemical reduction / drop casting	0.1	2356	up to 12	[89]
Pt NPs/graphene/GCE	Hydrothermal method / drop casting	-	137.4	5-20	[90]
Co_3O_4/graphene/GCE	Hydrothermal reaction / dip coating	-	492.8	0.25-10	[91]
Cobalt oxide NPs/rGO/CPE	Electrodeposition / paste	1.44	1.21	0.04-4	[92]
CoO_xNPs/rGO/GCE	Electrodeposition / drop casting	2	79.3	0.01-0.55	[93]
NiO NPs/GO/GCE	Electrodeposition / drop casting	1	1087	0.00313-3.15	[94]
CuO/N–CNFs/GCE	Solvothermal approach / drop casting	-	968 484	0.25-2 2-4	[82]
Pt NPs/CNFs/GCE	Chemical reduction / drop casting	33	2.03	0.3-17	[95]
Ni/CNFs/GCE	Electrospinning / drop casting	0.05	6.3934	0.000125-0.01273	[96]
CNFs-$Ni(OH)_2$/GCE	Hydrothermal method / drop casting	0.76	1038.6	0.001-1.2	[97]
Co-CNFs/GCE CuCo-CNFs/GCE FeCo-CNFs/GCE NiCo-CNFs/GCE MnCo-CNFs/GCE	Electrospinning / heat treatment / drop casting	50 1 10 20 50	97 507 196 141 36	0.5-3.5 0.02-11 0.2-10 0.1-10 0.5-7	[59]
Cu NPs@TiC/CNFs/ Ti6Al4V substrate	Thermal method / electrodeposition	0.2	415.02	0.001-5.2	[49]

© 2016 Tous droits réservés.

lilliad.univ-lille.fr

CuO NPs-CNFs/GCE	*In-situ* growth / drop casting	0.2	2739	0.0005-11.1	[98]
Ni NPs/CNFs paste electrode	Electrospinning / heat treatment / paste	1	420.4	0.002-2.5	[37]
Cu-Co-Ni/CNFs-GCE	Electrodeposition / drop casting	3.05	104.68	0.01-4.3	[99]
CuO/rGO/CNFs/GCE	Electrodeposition / drop casting	0.1	912.7	0.001-5.3	[100]

Abbreviations- CPE: carbon paste electrode; **NG/ITO**: nitrogen doped graphene/indium tin oxide coated glass slide; **PrGO**: porous reduced graphene oxide; **SPE**: screen printed electrode.

In this chapter, we investigated the potential of rGO/Cu NPs and CNFs/$Co(OH)_2$ nanocomposites, formed by electrophoretic deposition (EPD) onto Au/Ti/glass interfaces, as interesting alternative electrodes for non-enzymatic glucose sensing. Indeed, the preparation of electrodes for non-enzymatic glucose sensing, consists mainly in the synthesis of the electrocatalytic materials, followed by the transfer of the synthesized composites to the electrode by drop casting, dip coating, spray coating, *etc*. The process lacks of controllability of the area, thickness and uniformity of deposited films. Furthermore, in the case of rGO, hydrazine reduction of GO is often employed, being harmful for the environment. The use of electrophoretic deposition is thus a viable alternative to overcome both constrains in the preparation of glucose sensitive electrodes.

Recently, our group has demonstrated the EPD of rGO for lysozyme detection by SPR [101], and the preparation of a rGO matrix modified with $Ni(OH)_2$ nanostructures for non-enzymatic determination of glucose with a detection limit of 15 μM [102]. We show, in this chapter, that gold thin films electrophoretically modified with rGO/Cu NPs or CNFs/$Co(OH)_2$ nanocomposites exhibit high activity towards direct electrocatalytic oxidation of glucose with sensitivities of 0.448 and 68 mA mM^{-1} cm^{-2}, respectively.

3.2 Formation of electrocatalytic films towards glucose oxidation

3.2.1 EPD of rGO/Cu NPs

rGO/Cu NPs nanocomposites were deposited on Au/Ti/glass substrate from a colloidal suspension of GO and $CuSO_4$ (**Figure 3.2**). GO produced by the Hummers method displays oxygen-based functional groups such as hydroxyl and epoxide on the basal planes, and carboxyl and carbonyl groups at the edges. The presence of these functional groups makes GO negatively charged with a zeta potential of -23±2 mV. Addition of an equivalent amount

© 2016 Tous droits réservés.

lilliad.univ-lille.fr

of $CuSO_4$ resulted in a colloidal solution with an overall positive zeta potential of +15±2 mV, making cathodic EPD feasible.

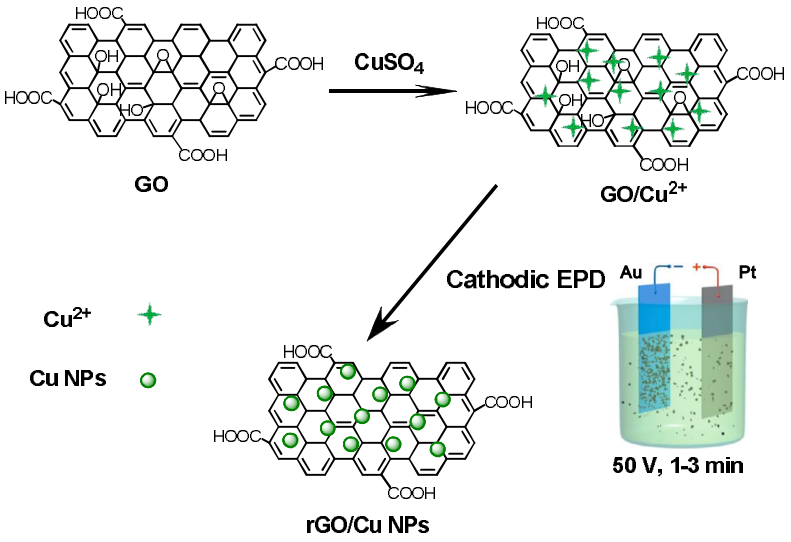

Figure 3.2: Schematic illustration of the preparation of rGO/Cu NPs using EPD.

The morphology and chemical composition of rGO and rGO/Cu NPs nanocomposite were characterized by scanning electron microscopy (SEM) and energy dispersive X-ray (EDX) analysis. **Figure 3.3A** displays the SEM image of rGO deposited on Au/Ti/glass substrate from an ethanol solution of GO (0.5 mg mL^{-1}) at an applied voltage of +50 V for 2 min. It consists of a smooth and homogeneous film. EDX analysis performed on rGO modified Au/Ti/glass substrate shows signals due mainly to C, O, Ti, Au and Si (**Table 3.3**). This is in accordance with the chemical composition of the film and the underlying substrate (glass substrate). Characteristic SEM images of rGO/Cu NPs nanocomposite obtained from an ethanolic solution of GO (0.5 mg mL^{-1}) and $CuSO_4$ (0.5 mg mL^{-1}) by EPD at an applied voltage of +50 V and a deposition time of 1-3 min are depicted in **Figure 3.3B-D**. The presence of a homogeneous film of Cu NPs is clearly visible on all SEM images of interfaces obtained for different deposition times. For the rGO/Cu NPs deposited for 1 min, the Cu NPs have an average diameter of 67±6 nm (estimation from 200 nanoparticles). Compared to the sample prepared by EPD for 1 min, SEM images of rGO/Cu NPs film obtained after 2 min and 3 min deposition times display similar morphology, but denser films of Cu NPs (**Figure 3.3C-D**). The Cu NPs are 50±7 nm (2 min) and 60±7 nm (3 min) in diameter, respectively. EDX analysis of the rGO/Cu NPs films deposited on Au/Ti/glass substrate exhibit signals due to Cu, C, O, Au and Si (**Table 3.3**). The results are in good agreement with simultaneous Cu and rGO deposition on the Au/Ti/glass substrate. The Cu atomic concentration increases from

© 2016 Tous droits réservés.

lilliad.univ-lille.fr

5.72 % (1 min) to 11.96 % (2 min) and 16.35 % (3 min) (**Table 3.3**).

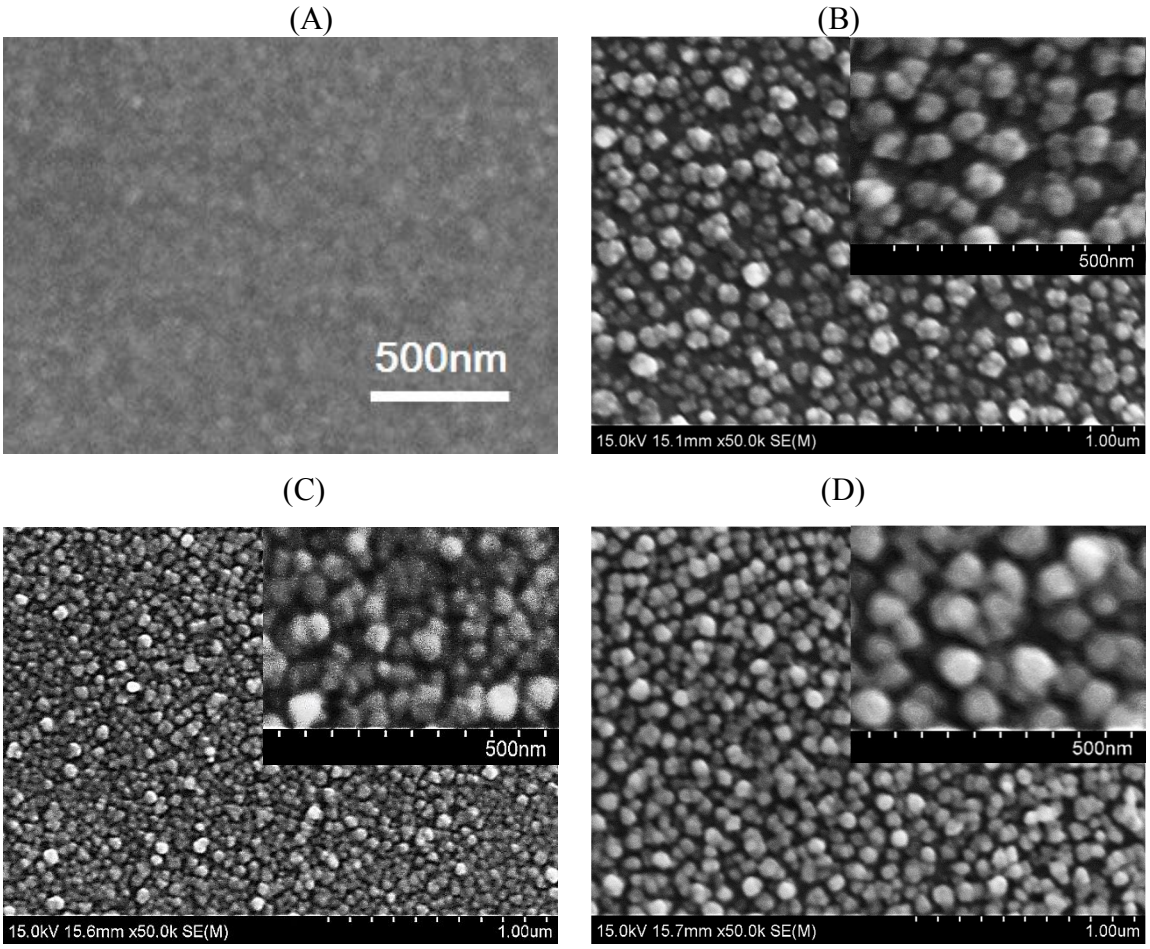

Figure 3.3: SEM images of (A) rGO with deposition time of 2 min; (B) rGO/Cu NPs with deposition time of 1 min; (C) rGO/Cu NPs with deposition time of 2 min and (D) rGO/Cu NPs with deposition time of 3 min deposited by EPD technique using an ethanolic solution of GO (0.5 mg mL^{-1}) and GO (0.5 mg mL^{-1}) + $CuSO_4$ (0.5 mg mL^{-1}), respectively. Applied voltage: +50 V.

Table 3.3: EDX results of rGO and rGO/Cu NPs deposited by EPD technique using GO and GO + $CuSO_4$ in ethanol, respectively. Applied voltage: +50 V; GO (0.5 mg mL^{-1}), $CuSO_4$ (0.5 mg mL^{-1}).

Element	rGO-2 min (at. %)	rGO/Cu NPs-1 min (at. %)	rGO/Cu NPs-2 min (at. %)	rGO/Cu NPs-3 min (at. %)
Cu K	-	5.72	11.96	16.35
C K	19.76	19.84	21.40	18.05
O K	26.20	27.02	24.21	26.80
Ti K	0.80	-	-	-
Au M	10.30	9.42	9.68	8.98
Si K	30.98	28.66	24.85	25.60

© 2016 Tous droits réservés.

lilliad.univ-lille.fr

The crystalline phase of the as-prepared substrates was characterized by X-ray diffraction (XRD) in the range of 10-90°. **Figure 3.4** illustrates the XRD patterns of rGO and rGO/Cu NPs deposited through EPD. The XRD pattern of rGO deposited on Au/Ti/glass sensor displays a broad peak at 24.2° and a small peak at 44.3° (corresponding to the (002) and (100) planes) characteristic of graphene, and peaks of the underlying Au substrate at 38.3° and 81.6° corresponding to the (111) and (222) crystalline planes, respectively (**Figure 3.4a**). The X-ray diffraction (XRD) patterns of rGO/Cu NPs deposited by EPD from an ethanolic solution of GO (0.5 mg mL^{-1}) and $CuSO_4$ (0.5 mg mL^{-1}) at an applied voltage of +50 V for 1-3 min are depicted in **Figure 3.4b-d.** An additional peak at 2θ value of 43.3° corresponding to Cu (111) crystalline plane appears, in accordance with Cu deposition.

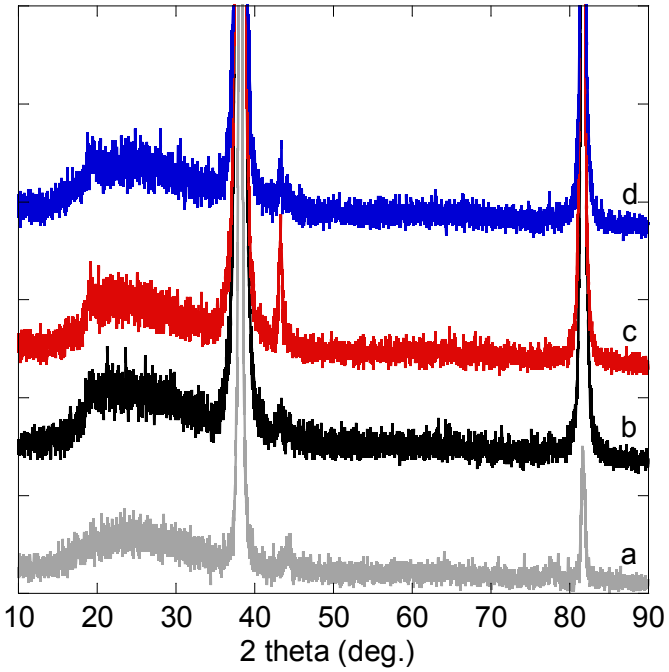

Figure 3.4: XRD patterns of (a) rGO with deposition time of 2 min; (b-d) rGO/Cu NPs for 1-3 min deposition times deposited by EPD technique using an ethanolic solution of GO (0.5 mg mL^{-1}) and GO (0.5 mg mL^{-1}) + $CuSO_4$ (0.5 mg mL^{-1}), respectively. Applied voltage: +50 V.

X-ray photoelectron spectroscopy (XPS) analysis results also confirmed the formation of rGO/Cu NPs nanocomposites. The C_{1s} core level XPS spectrum of GO nanosheets is displayed in **Figure 3.5A**. It can be deconvoluted into four components with binding energies at about 283.8, 284.7, 286.7 and 287.9 eV assigned to sp^2 C, C-H/C-C, C-O and C=O species, respectively. The spectrum is dominated by the peak at 287.6 eV due to C-O, in accordance with a high oxidation degree of GO. **Figure 3.5B** depicts the high resolution XPS C_{1s} core level spectrum of the Au/Ti/glass electrode interface modified with rGO/Cu NPs. It can be

© 2016 Tous droits réservés.

lilliad.univ-lille.fr

deconvoluted into three peaks at 284.08 eV (sp^2 C), 285.1 eV (sp^3 C) and 287.80 eV (C=O) with the sp^2 C component being dominant, suggesting partial reduction of GO during EPD deposition. The high resolution of the core level of Cu_{2p} reveals the presence of several peaks with binding energies at 932.66, 934.2, 941.83, 951.46, 953.94, and 960 eV (**Figure 3.5C**). The peaks at 932.66 and 951.46 eV are attributed to $Cu2p_{3/2}$ and $Cu2p_{1/2}$, respectively from

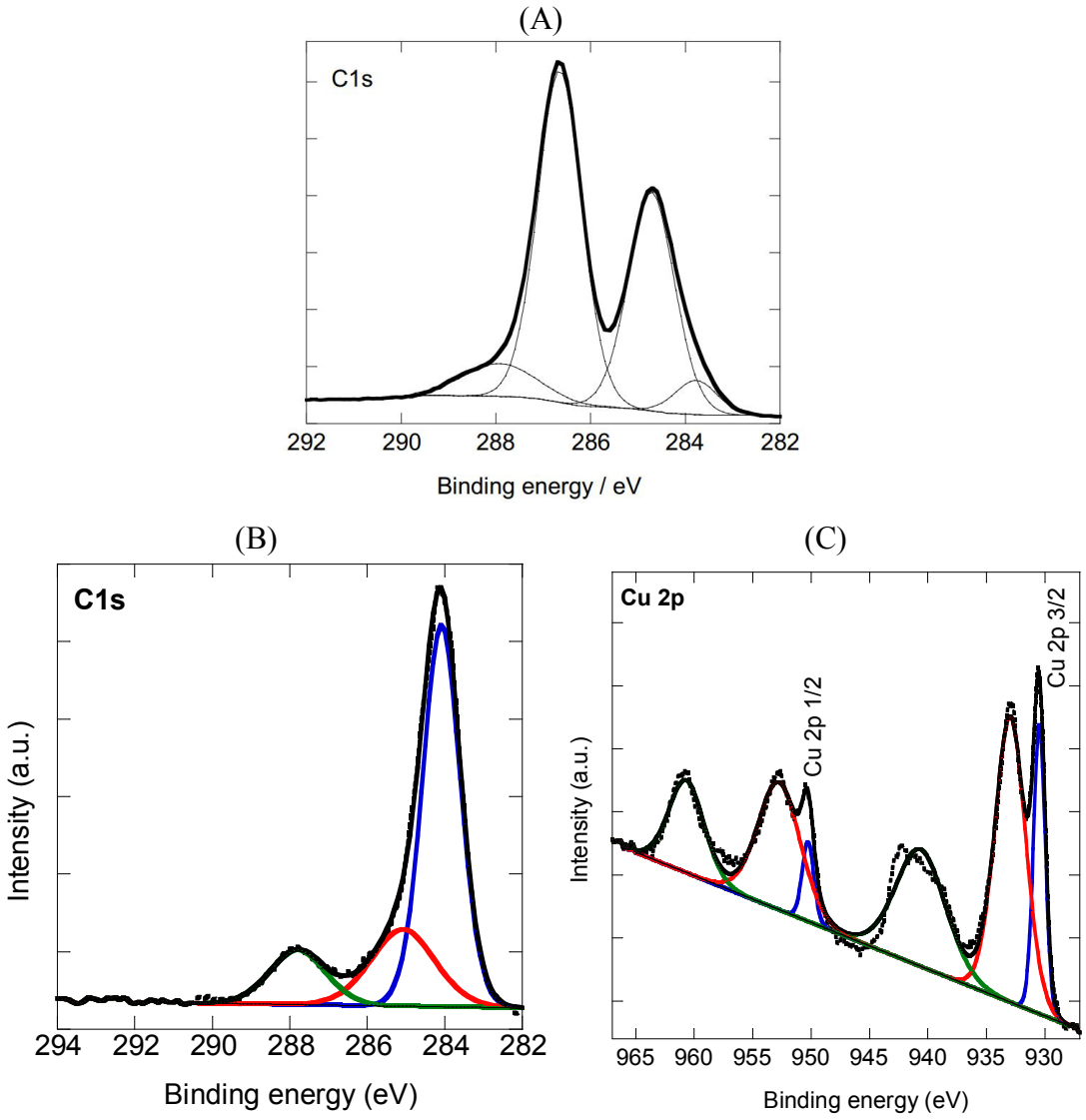

Figure 3.5: High resolution XPS spectra: (A) C_{1s} of GO; (B) C_{1s} and (C) Cu_{2p} of rGO/Cu NPs modified Au/Ti/glass electrode deposited by EPD (+50 V, 2 min).

metallic Cu^0 or Cu^+ (Cu_2O). Based on the literature data, the peak at 932.66 eV is most likely due to Cu^0 (the ISO standard Cu metal line is at 932.63 eV with a deviation set at ±0.025 eV) [103]. The peaks at 934.2 and 953.94 eV are due to $Cu2p_{3/2}$ and $Cu2p_{1/2}$, respectively from Cu^{2+}. These peaks arise from $Cu(OH)_2$ rather than CuO [103]. In addition, the presence of shake-up satellite peaks at higher binding energies *i.e.* 941.83 and 960 eV, characteristic of

© 2016 Tous droits réservés.

lilliad.univ-lille.fr

materials having a d^9 configuration in their ground state, clearly indicates the presence of Cu^{2+}. The overall Cu content is 10.4 at. %, indicating high loading of Cu NPs onto the rGO surface. The result is consistent with EDX analysis (11.96 at. %) of the same sample (**Table 3.3**).

3.2.2 EPD of CNFs/$Co(OH)_2$

Similarly, CNFs/$Co(OH)_2$ nanocomposites were deposited on Au/Ti/glass substrate from an ethanolic suspension of CNFs and $Co(NO_3)_2$ by EPD at +50 V for 1-3 min (**Figure 3.6**). The ratio between CNFs and $Co(NO_3)_2$ was varied as following: 1:1 (0.5:0.5 mg mL^{-1}), 1:2 (0.25:0.5 mg mL^{-1}) and 2:1 (0.5:0.25 mg mL^{-1}) to obtain various CNFs/$Co(OH)_2$ nanocomposites. In the meantime, $Co(NO_3)_2$ solution alone without CNFs was also used for $Co(OH)_2$ deposition by EPD for comparison.

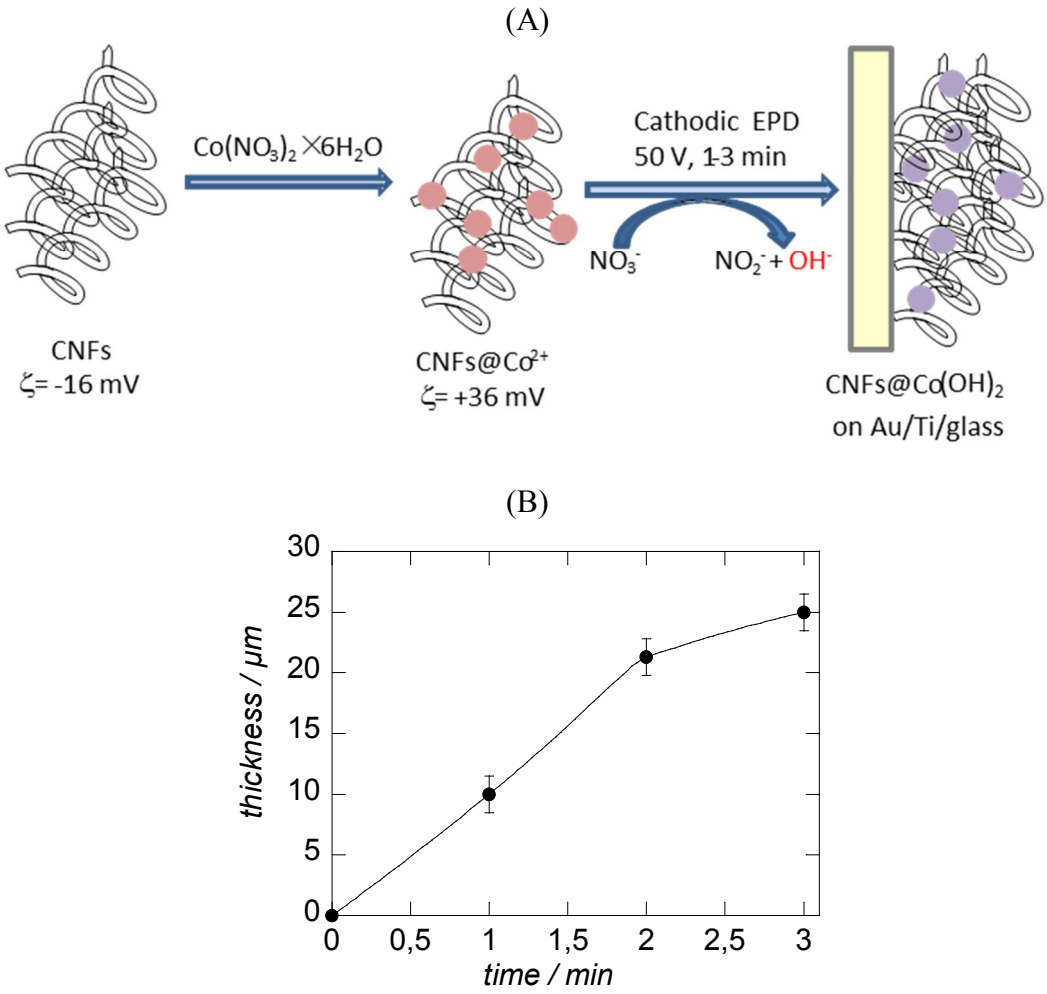

Figure 3.6: (A) Schematic illustration of the fabrication of CNFs/$Co(OH)_2$ films on Au/Ti/glass interfaces using EPD; (B) influence of deposition time on the thickness of CNFs/$Co(OH)_2$ (ratio of CNFs to $Co(NO_3)_2$ is 2:1).

© 2016 Tous droits réservés.

lilliad.univ-lille.fr

The CNFs, formed by thermal chemical vapour deposition method, were kindly provided by Dr. Nianjun Yang (University Siegen, Germany). The morphology of the CNFs consists of a curved structure with a mean diameter of 120-200 nm and a length in the order of 10 µm (**Figure 3.7A**). Prior to EPD, the zeta-potential of CNFs was measured in ethanol and was found to be -16.2±1.0 mV (50 µg mL^{-1}), indicating a negatively charged surface, which is ideal for adsorption of positively charged metal ions. Mixing the CNFs with $Co(NO_3)_2$ in 1:1, 1:2 or 2:1 ratio results in a mixture with an overall positive zeta potential (measured with a dilution by 10 in ethanolic solution) of +36.0±1.4 mV, +37.1±1.3 mV and +35.5±0.7 mV, respectively, confirming the surface adsorption of Co^{2+} ions onto CNFs. The results indicated that the ratio of Co salt has no obvious influence on the zeta potential of the colloidal solution. Application of a DC potential of +50 V results in the formation of CNFs/$Co(OH)_2$. As demonstrated before, one of the great advantages of EPD is the control of film thickness by varying the deposition time (**Figure 3.6B**). The morphology of CNFs/$Co(OH)_2$ and for comparison with $Co(OH)_2$ alone electrophoretically deposited using the same conditions are investigated by SEM (**Figure 3.7B-E**). The CNFs network remains well preserved in CNFs/$Co(OH)_2$. Magnification of the SEM images leads to the appearance of small particles of 20-50 nm in diameter decorating the surface of CNFs (insets of **Figure 3.7C-E**), which is believed to be $Co(OH)_2$.

The influence of the CNFs/$Co(NO_3)_2$ ratio on the distribution of $Co(OH)_2$ was also evaluated by investigation of 1:1, 1:2 and 2:1 ratios. In the case of CNFs/$Co(NO_3)_2$ = 1:1, few particles were formed (**Figure 3.7C)**, which is probably due to the large amount of ions and particles in colloidal solution, leading to a relatively slow kinetics [104]. When the CNFs amount is lowered (CNFs/$Co(NO_3)_2$ = 1:2), cobalt products seem to grow fast and aggregate into tiny clouds alongside the CNFs (**Figure 3.7D**). Using a CNFs/$Co(NO_3)_2$ = 2:1, small amounts of Co^{2+} in the solution results in a mild movement and growth of $Co(OH)_2$ because of a slightly lower zeta potential, making the particles uniformly distributed (**Figure 3.7E**).

© 2016 Tous droits réservés.

lilliad.univ-lille.fr

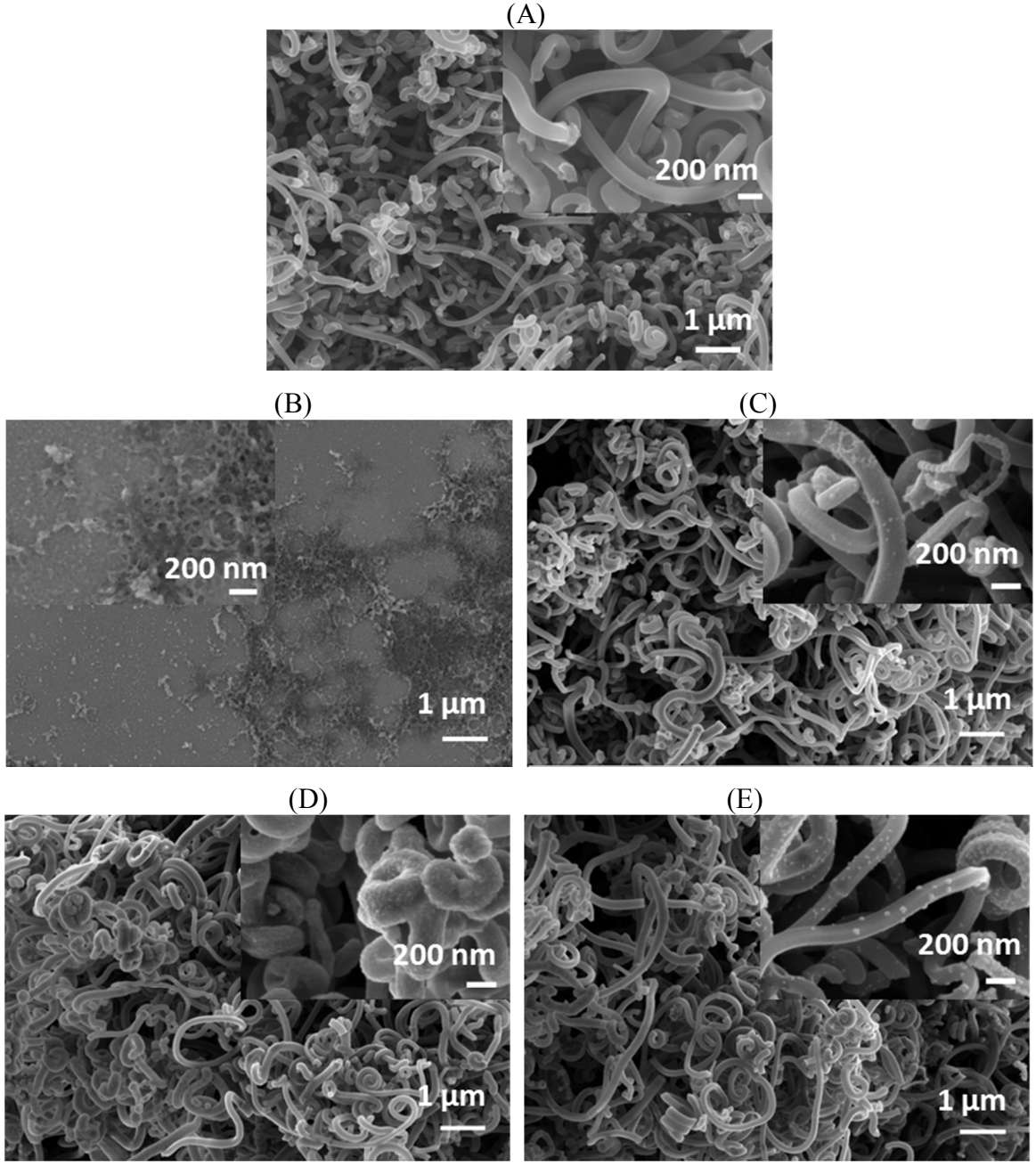

Figure 3.7: SEM images of (A) CNFs on Au/Ti/glass by drop casting; (B) $Co(OH)_2$ on Au/Ti/glass by EPD; (C) CNFs/$Co(OH)_2$ composite on Au/Ti/glass by EPD, CNFs/$Co(NO_3)_2 \cdot 6H_2O$ ratio of 1:1; (D) CNFs/$Co(OH)_2$ composite on Au/Ti/glass by EPD, CNFs/$Co(NO_3)_2 \cdot 6H_2O$ ratio of 1:2, and (E) CNFs/$Co(OH)_2$ composite on Au/Ti/glass by EPD, CNFs/$Co(NO_3)_2 \cdot 6H_2O$ ratio of 2:1. EPD parameters: applied voltage = +50 V, deposition time = 2 min.

The chemical composition of the CNFs/$Co(OH)_2$ composite was further examined by XPS. In **Figure 3.8A**, the Co_{2p} high resolution XPS spectrum shows two characteristic peaks centred at 781.2 and 797.1 eV, corresponding to $Co_{2p3/2}$ and $Co_{2p1/2}$, respectively. The position of the bands as well as the band separation of 15.9 eV confirms that Co mainly exists as $Co(OH)_2$ [105,106]. The bands at 785.7 and 802.9 eV are satellite bands of Co^{2+} [105,106].

© 2016 Tous droits réservés.

lilliad.univ-lille.fr

The atomic percentage of Co was estimated to be 12.5 at.% with an atomic ratio of C/Co=3.1 (CNFs/ $Co(NO_3)_2$ ratio of 2:1, applied voltage=+50V, deposition time=2min). **Figure 3.8B** depicts the C_{1s} spectrum of the CNFs/$Co(OH)_2$ composite. The main peak at 284.8 eV is assigned to the sp^2 carbon of the nanofibers. The other peak components can be assigned to sp^3 carbon at 285.2 eV, C–O bonding at 286.4 eV, and O–C=O at 289.9 eV [107].

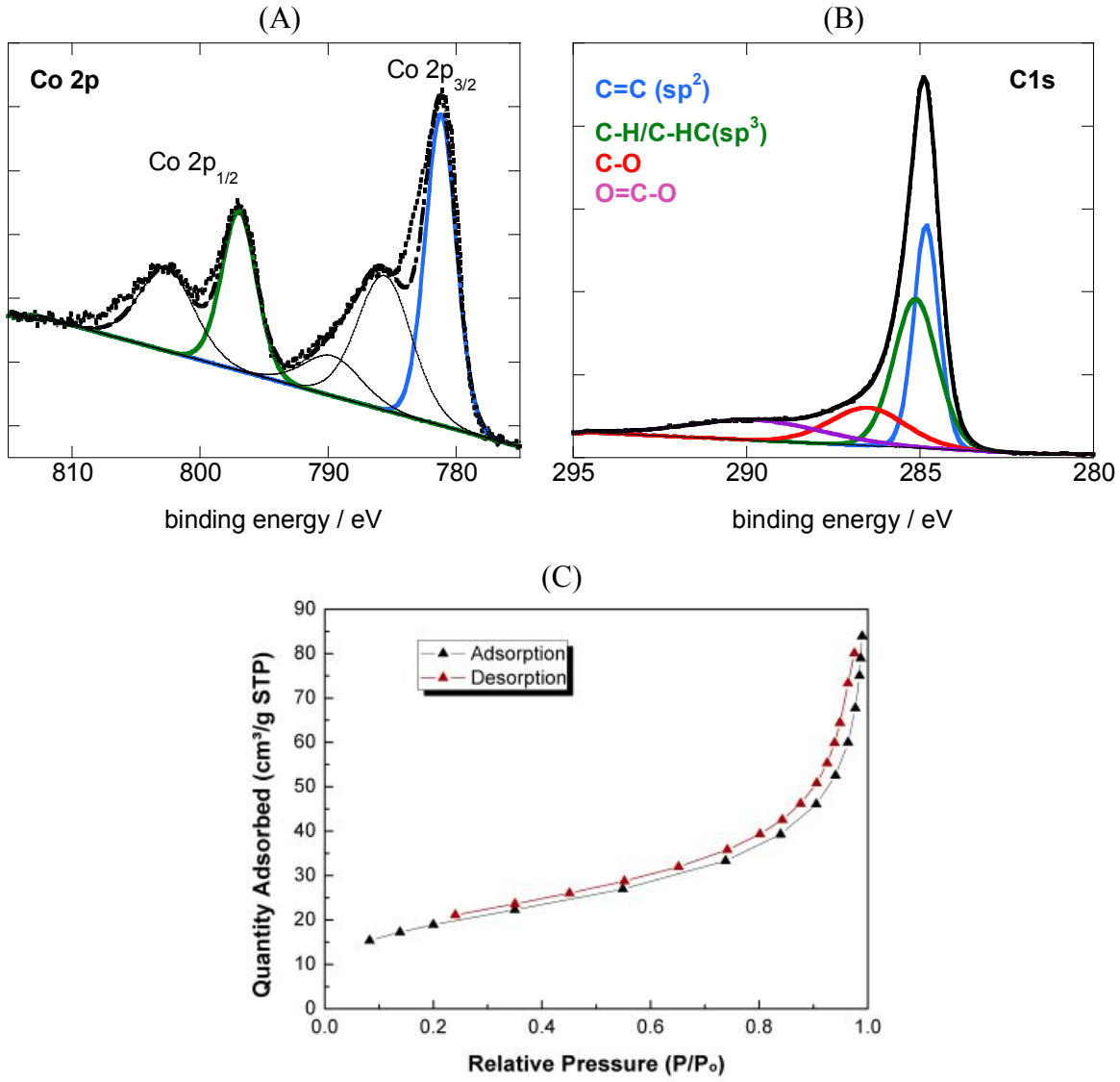

Figure 3.8: High resolution XPS spectra: (A) Co_{2p} and (B) C_{1s} of CNFs/$Co(OH)_2$ modified Au/Ti/glass electrode deposited by EPD, CNFs/$Co(NO_3)_2$ ratio of 2:1, applied voltage=+50V, deposition time=2min; (C) nitrogen adsorption-desorption isotherm analysis of CNFs/$Co(OH)_2$ nanocomposite by EPD.

The specific surface area of CNFs/$Co(OH)_2$ was determined from adsorption-desorption isotherm analysis (**Figure 3.8C**). The specific surface for CNFs/$Co(OH)_2$, calculated using Brunauer-Emmet-Teller (BET) theory and Langmuir equation, is 68.9 $m^2\ g^{-1}$ and 98.8 $m^2\ g^{-1}$,

© 2016 Tous droits réservés.
lilliad.univ-lille.fr

Thèse de Qian Wang, Lille 1, 2016

respectively. These values are comparable with normal carbon nanotubes, which have theoretical specific surface area from 50 to 1315 $m^2 g^{-1}$, depending on their structure [108].

3.3 Non-enzymatic glucose sensing

3.3.1 rGO/Cu NPs modified electrode

Before investigating the electrocatalytic performance of the nanocomposite material toward glucose oxidation, the rGO/CuNPs modified Au/Ti/glass electrode was scanned between -1 V to +0.2 V by cyclic voltammetry (CV) (**Figure 3.9**). The anodic peaks at -0.35 V and -0.12 V correspond to the transitions Cu^0/Cu(I) and Cu(I)/Cu(II), respectively. In the cathodic scan, the peaks at -0.38 V and -0.80 V correspond to the re-formation of Cu(I) and Cu^0, respectively. This behavior is similar to those reported for copper and copper nanowire electrodes in NaOH aqueous solution [40,41,109].

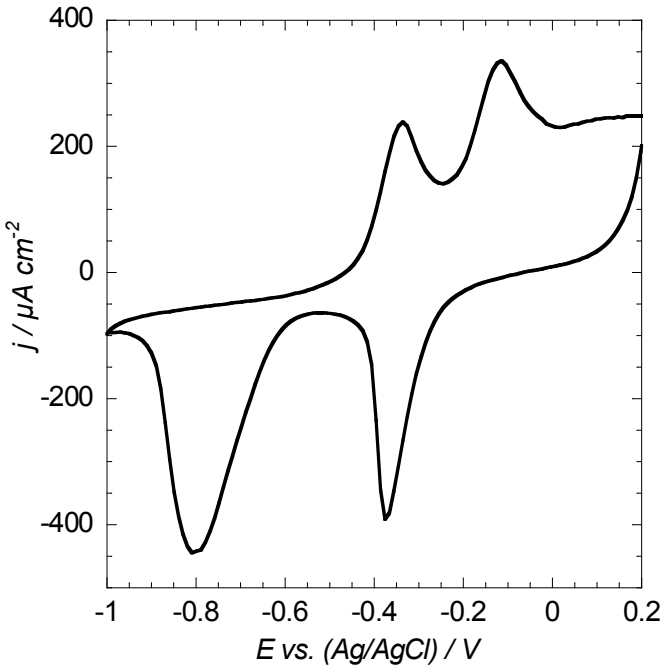

Figure 3.9: Cyclic voltammograms of rGO/Cu NPs deposited by EPD (+50 V, 2 min) on Au/Ti/glass electrode in 0.1 M NaOH, scan rate: 50 mV s^{-1}.

In order to investigate the applicability of the rGO/Cu NPs modified Au/Ti/glass electrode for non-enzymatic glucose sensing, a simplified analysis was carried out in the potential range pertinent for amperometric detection of glucose from +0.2 V to +0.8 V. **Figure 3.10A** depicts the CVs of the rGO/Cu NPs (deposition time = 2 min) modified Au/Ti/glass electrode in 0.1 M NaOH aqueous solution in the absence and presence of 1 mM glucose. A

© 2016 Tous droits réservés.

lilliad.univ-lille.fr

significant increase of the anodic current is obvious upon addition of glucose, suggesting a good electrocatalytic activity of the rGO/Cu NPs film toward glucose oxidation. In contrast, only a slight anodic current increase at the potential above +0.5 V can be detected in the presence of glucose on rGO modified Au/Ti/glass electrode, indicating that rGO alone, deposited by EPD under our experimental conditions (EPD deposition from 0.5 mg mL^{-1} of GO at +50 V for 2 min), is not electroactive toward glucose oxidation (**Figure 3.10B**). Furthermore, the electrocatalytic ability of Cu modified Au/Ti/glass electrode deposited by

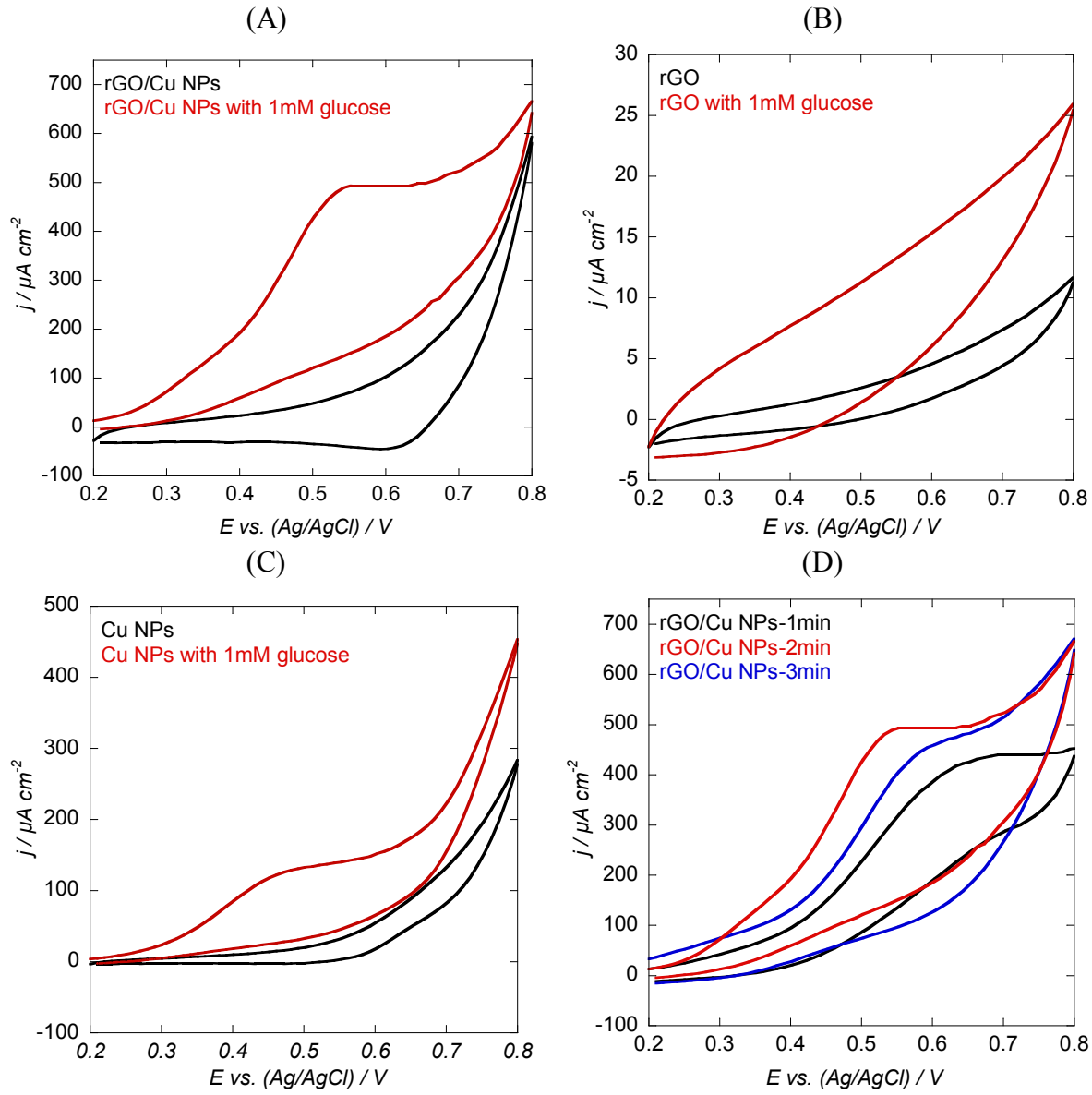

Figure 3.10: Cyclic voltammograms of (A) rGO/Cu NPs deposited by EPD (+50 V, 2 min), (B) rGO deposited by EPD from 0.5 mg mL^{-1} of GO solution and (C) Cu NPs deposited by EPD from 0.5 mg mL^{-1} of $CuSO_4$ in ethanol solution on Au/Ti/glass electrode in 0.1 M NaOH aqueous solution in the absence (black) and presence (red) of 1 mM glucose; (D) rGO/Cu NPs deposited by EPD for 1, 2 and 3 min on Au/Ti/glass electrode in 0.1 M NaOH aqueous solution with 1 mM glucose. Scan rate: 50 mV s^{-1}.

© 2016 Tous droits réservés.

lilliad.univ-lille.fr

EPD from 0.5 mg mL^{-1} of $CuSO_4$ in ethanol at +50 V for 2 min towards glucose oxidation was examined. In **Figure 3.10C**, although the electrode showed an increase of the anodic current upon addition of 1 mM glucose, the current density remains lower than that recorded on rGO/Cu NPs modified Au/Ti/glass electrode. The results indicate a synergistic effect of rGO and Cu NPs in the electrocatalytic system of glucose oxidation. Similarly, the CVs of rGO/Cu NPs modified Au/Ti/glass electrodes for various deposition times (1, 2 and 3 min) were recorded in the presence of 1 mM glucose in the potential range of 0.2-0.8 V under otherwise similar conditions. **Figure 3.10D** shows that both samples for deposition times of 1 min and 3 min exhibited lower current density compared to the electrode prepared through EPD deposition for 2 min. Then the electrode modified with rGO/Cu NPs for 2 min was chosen for further sensing applications.

The electrocatalytic response of Au/Ti/glass electrode modified with rGO/Cu NPs to glucose was further investigated by amperometric current-time response upon successive addition of different concentrations of glucose. **Figure 3.11A** displays the amperometric response of the modified electrode at an applied potential of +0.55 V *vs.* Ag/AgCl. The oxidation current increased gradually upon injection of increasing concentrations of glucose into the NaOH solution and reached the maximum steady state current within 15 s. **Figure 3.11B** shows the corresponding calibration curve of the current response *versus* glucose concentration. A linear current-response relationship was obtained as a function of glucose concentration from 0.01 to 1.2 mM with j ($\mu A\ cm^{-2}$) = 24.892 + 447.65[glucose] (mM), R=0.998) with an estimated sensitivity of 447.65 $\mu A\ mM^{-1}\ cm^{-2}$. A detection limit of 3.4 µM at a signal-to-noise ratio of 3 was achieved using Au/Ti/glass electrode modified with rGO/Cu NPs. The detection limit determined for the sensor is in the same order or slightly higher than 0.03 to 1.3 µM reported in the literature for Cu-based/graphene electrodes prepared using various approaches (**Table 3.4**) [39,45,47,50-54]. However, the proposed strategy for the preparation of metal oxide nanoparticles/rGO is a one-pot, straightforward, and environmentally friendly approach that can be easily used for the integration of other nanoparticles on the same matrix and thus opens up new routes for the design of more sensitive sensors.

© 2016 Tous droits réservés.

lilliad.univ-lille.fr

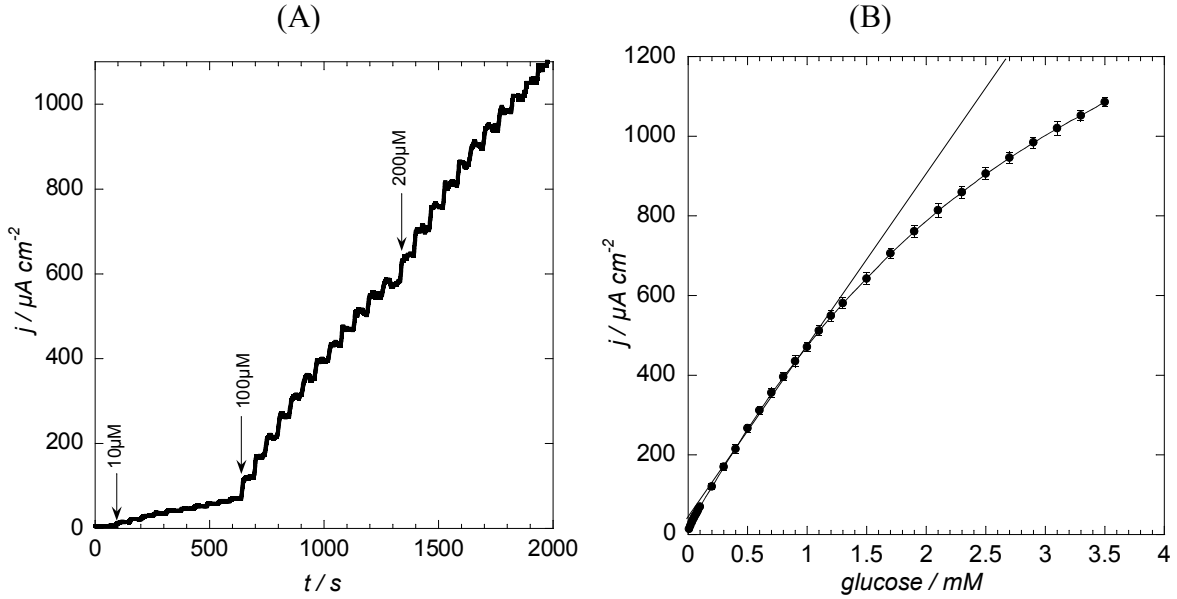

Figure 3.11: (A) Amperometric response of rGO/Cu NPs modified Au/Ti/glass electrode polarized at +0.55 V *vs.* Ag/AgCl in 0.1 M NaOH aqueous solution with subsequent addition of glucose (10 μM, 100 μM or 200 μM); (B) the corresponding calibration curve.

Table 3.4: Comparison of analytical performance with other Cu/rGO-based non-enzymatic glucose sensors.

Material	LOD (μM)	Sensitivity (μA mM^{-1} cm^{-2})	Linear range (mM)	Ref.
CuO NPs/SG	0.08	1298.6	0.1-10.5	[39]
Cu NPs/PANI/graphene	0.27	150	0.001-3.7	[45]
Cu NPs/PMo_{12}-GR	0.03	153.2 μA mM^{-1}	0.0001-1	[47]
Cu NPs–N-GR	1.3	48.13	0.004–4.5	[50]
CuO–GR–GCE	0.7	1360	0.002 to 4	[51]
Cu-graphene	0.5	-	up to 4.5	[52]
CuNPs-graphene	0.2	607	0.005-1.4	[53]
CuNPs/PAA/GR	0.08	-	0.0003-0.6	[54]
Cu NPs/rGO	**3.4**	**447.65**	**0.01-1.2**	**This work**

The detection of glucose is often hampered by the presence of oxidizable molecules, which can compromise the selectivity of detection and hence the overall accuracy of measurement [20]. To evaluate the selectivity of the nanocomposite, a number of oxidizable and interfering molecules such as dopamine (DA), ascorbic acid (AA), uric acid (UA) and other carbohydrate derivatives such as fructose, lactose and galactose were examined at the Au/Ti/glass electrode modified with rGO/Cu NPs. **Figure 3.12** compares the amperometric response of the Au/Ti/glass electrode coated with rGO/Cu NPs upon successive additions of glucose (500 μM), UA (50 μM), AA (50 μM), DA (50 μM), fructose (50 μM), lactose (50 μM) and galactose (50 μM) in 0.1 M NaOH aqueous solution at an applied potential of +0.55 V *vs.*

© 2016 Tous droits réservés.

lilliad.univ-lille.fr

Ag/AgCl. No significant current increase was detected upon addition of AA, UA and DA, as compared to amperometric response obtained upon glucose addition, suggesting that these species do not interfere with glucose detection under our experimental conditions. Similarly, no obvious response of the Au/Ti/glass electrode coated with rGO/Cu NPs was recorded upon addition of different interfering carbohydrate molecules at the physiological concentration level. The results indicate that the Au/Ti/glass electrode modified with rGO/Cu NPs exhibits a good selectivity toward glucose detection.

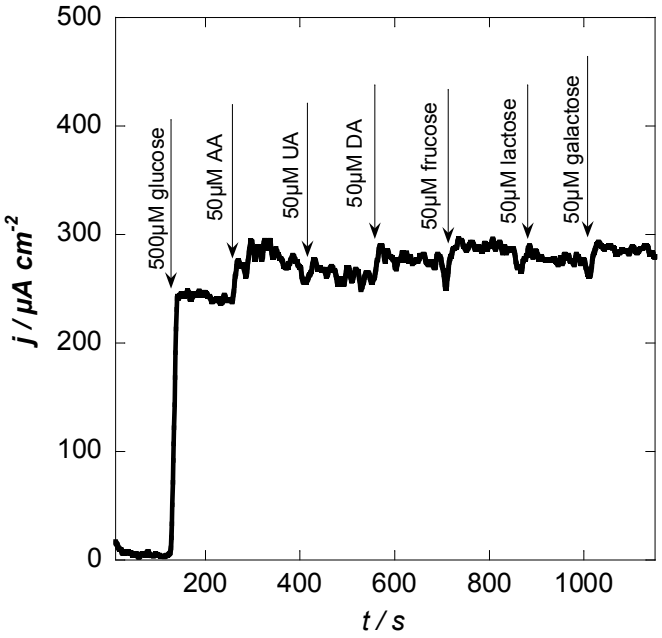

Figure 3.12: The amperometric response of the rGO/Cu NPs modified Au/Ti/glass electrode exposed to glucose (500 μM), ascorbic acid (AA, 50 μM), uric acid (UA, 50 μM), dopamine (DA, 50 μM), fructose (50 μM), lactose (50 μM) and galactose (50 μM). Electrolyte: 0.1 M NaOH aqueous solution, potential: +0.55 V.

The practical applicability of Au/Ti/glass electrode modified rGO/Cu NPs by EPD for the determination of glucose was tested in human serum samples. **Figure 3.13** exhibits the amperometric response of the rGO/Cu NPs coated Au/Ti/glass electrode upon successive additions of different analytes (standard glucose solution, human serum sample, AA and UA) in 0.1 M NaOH aqueous solution at an applied potential of +0.55 V *vs.* Ag/AgCl. The concentration of glucose in the human serum sample was determined to be 4.7 mM by using the calibration curve in **Figure 3.11B**. Considering that the concentration of glucose in human blood serum is in the range of 3.9-6.1 mM [110], the value determined from the calibration curve of the fabricated glucose sensor is quite reasonable. Besides, the addition of 0.1 mM UA and 0.1 mM AA cause insignificant current increase, suggesting that these species do not

© 2016 Tous droits réservés.

lilliad.univ-lille.fr

interfere with glucose detection in real samples.

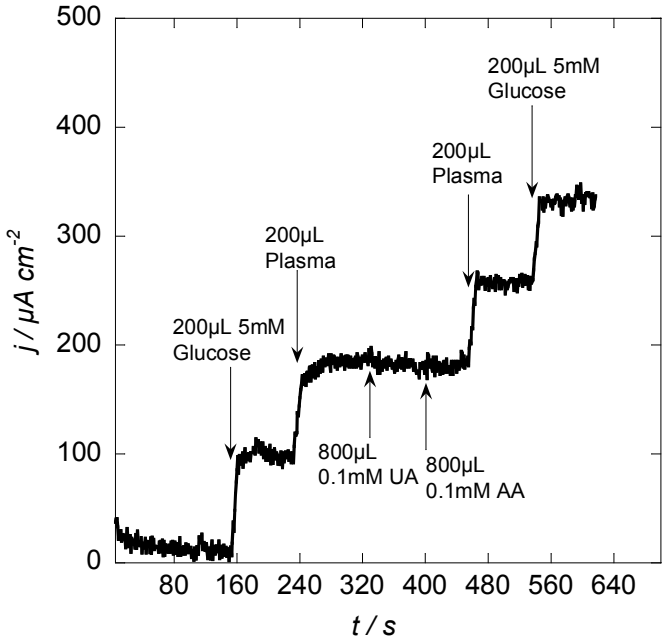

Figure 3.13: The amperometric response of the rGO/Cu NPs modified Au/Ti/glass electrode upon successive additions of different analytes. Electrolyte: 0.1 M NaOH aqueous solution, potential: +0.55 V.

To verify the value obtained by the non-enzymatic glucose sensor of rGO/Cu NPs, a well-established phenol-sulfuric acid colorimetric method was applied for the analysis of carbohydrates [111]. The method is based on the dehydration of carbohydrates by sulfuric acid with further condensation through phenol, resulting in a yellow-orange colored compound [112]. **Figure 3.14A** shows the UV-Vis absorption spectra of a series of standard glucose solution and the tested human plasma sample. The absorbance (λ_{max}≈490 nm) difference was plotted against the glucose concentration to generate a standard calibration curve (**Figure 3.14B**). Then the sugar content in human plasma sample was determined to be 4.51 mM by the colorimetric method. The comparable results obtained using the non-enzymatic glucose sensor constructed by EPD and the well-established colorimetric method proved the feasibility of rGO/Cu NPs electrode for real sample analysis.

© 2016 Tous droits réservés.

lilliad.univ-lille.fr

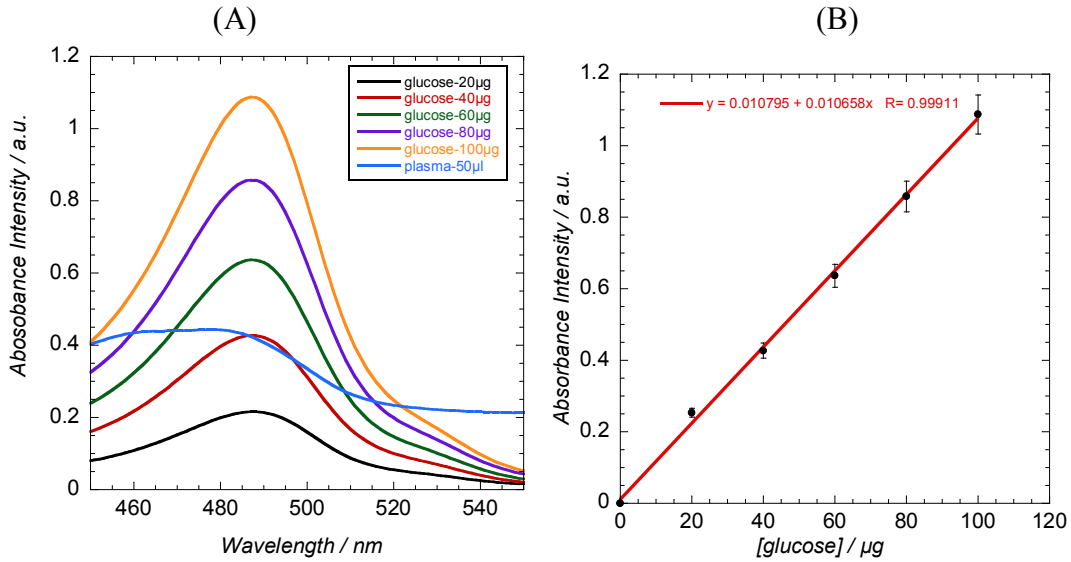

Figure 3.14: Determination of glucose using the well-established phenol-sulfuric acid colorimetric method: (A) UV-Visible absorption spectra of a mixture of phenol (5 wt. %, 1 mL), concentrated H_2SO_4 (5 mL) and a series of 1 mL standard glucose solution (20, 40, 60, 80,100 µg mL $^{-1}$) / human serum sample (50 µL); (B) the corresponding calibration curve.

Finally, the reproducibility of the Au electrode coated with rGO/Cu NPs film was examined by measuring the current signal of 0.1 mM glucose at 6 modified electrodes produced under otherwise similar experimental conditions. A relative standard deviation (RSD) of 6.67% was determined, indicating good reproducibility and reliability of the fabrication method. The long-term stability of the electrode was estimated after storage in a refrigerator at 4°C for 2 weeks. The sensor retained about 89.6% of its initial current response to 0.1 mM glucose in 0.1 M NaOH aqueous solution at +0.55 V, suggesting a good stability of the electrode.

3.3.2 CNFs/ $Co(OH)_2$ modified electrode

Figure 3.15A shows the CVs of CNFs deposited by drop-coasting and electrophoretically deposited CNFs/$Co(OH)_2$ onto Au/Ti/glass electrodes. In 0.1 M NaOH, no features were observed on CNFs coated electrodes. In contrast to CNFs, the CV of the CNFs/$Co(OH)_2$ interface displays a pair of broad redox waves between 0.05 and 0.4 V *vs.* Ag/AgCl, which are assigned respectively to the reversible transition between $Co(OH)_2$ and CoOOH [113,114]. The addition of glucose (0.1 mM) results in a significant increase of the oxidation current of the $Co(OH)_2$/CoOOH redox couple (**Figure 3.15B**). This is probably due to the rapid electrocatalytic oxidation of glucose with the $Co(OH)_2$/CoOOH system,

© 2016 Tous droits réservés.

lilliad.univ-lille.fr

presumably following the reaction described in eqn (7). As expected, CNFs alone did not show any electrocatalytic activity towards glucose under the identified conditions (**Figure 3.15B**).

$$Co(OH)_2 + glucose \rightarrow CoOOH + gluconalactone \quad (7)$$

The synergetic effect of CNFs in the CNFs/$Co(OH)_2$ was demonstrated by investigating the electrocatalytic behaviour of electrophoretically deposited $Co(OH)_2$ film without CNFs. In the case of EPD from $Co(NO_3)_2$, the deposition occurs on the cathode due to the positive zeta potential of the $Co(NO_3)_2$ solution. The electrocatalytic reaction is less marked on $Co(OH)_2$ films than on CNFs/$Co(OH)_2$, resulting mainly in a shift of the peak of $Co(OH)_2$/CoOOH redox in the presence of 0.1 mM glucose (**Figure 3.15C**).

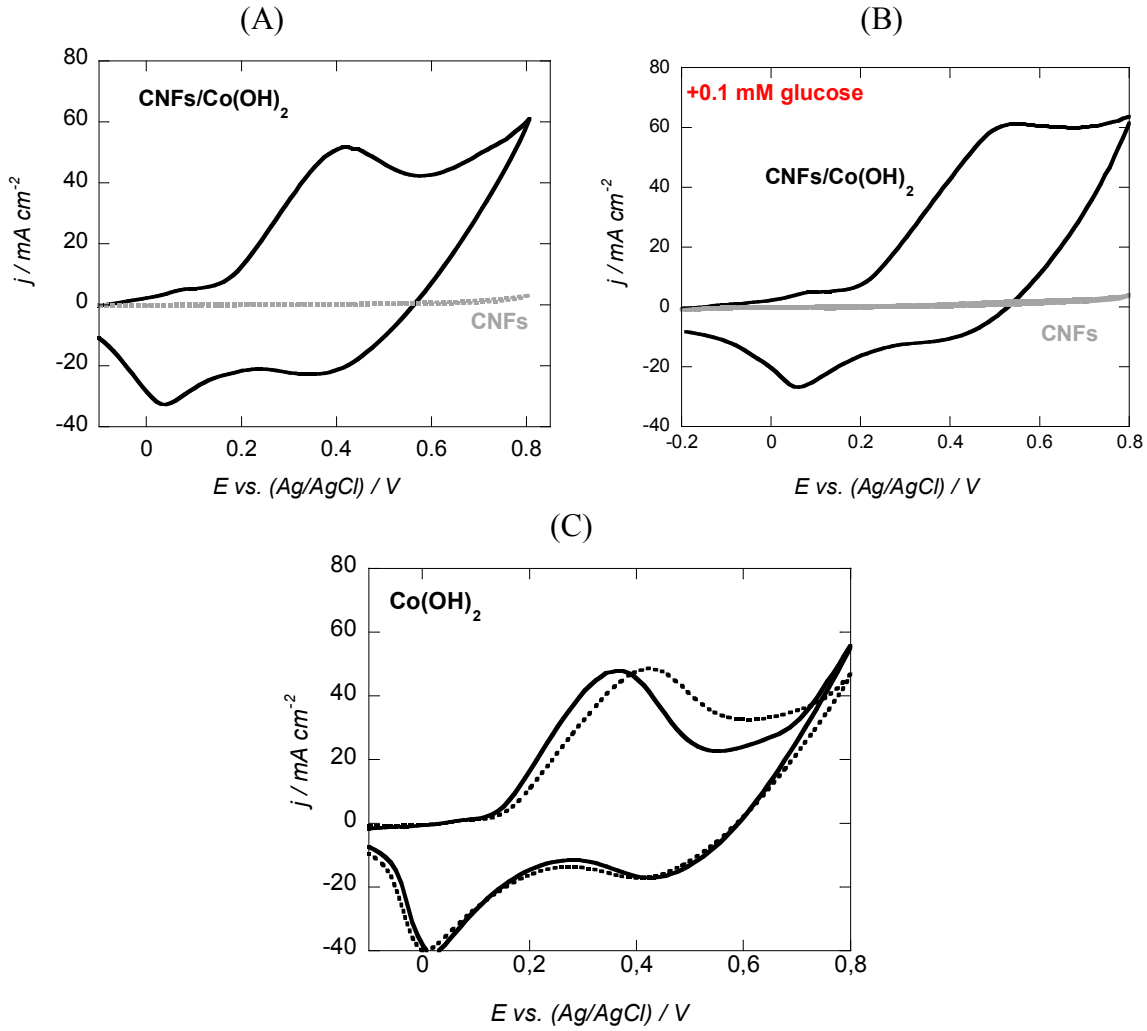

Figure 3.15: (A) Cyclic voltammograms (CV) of CNFs (grey) and CNFs/$Co(OH)_2$ (ratio 2:1, 2 min deposition time) on Au/Ti/glass electrodes in 0.1 M NaOH, scan rate: 50 mV s^{-1}; (B) in the presence of 0.1 mM glucose; (C) CV of Au/Ti/glass electrodes modified with $Co(OH)_2$ through EPD in absence (black) and presence (dotted black) of glucose (0.1 mM) in 0.1 M NaOH, scan rate: 50 mV s^{-1}.

© 2016 Tous droits réservés.

lilliad.univ-lille.fr

Compared with the results on rGO/Cu NPs, it should be noticed that CNFs/$Co(OH)_2$ modified electrode exhibits a much more significant catalytic ability towards glucose oxidation, with an increase of Co(II)/Co(III) redox in current density around 10 mA cm^{-2} with the addition of 0.1 mM glucose (**Figure 3.15A-B**). This makes CNFs/$Co(OH)_2$ modified Au/Ti/glass electrode a competitive matrix for glucose sensing. Under both circumstances, the enhanced synergistic effect of introduced metal nanostructures and carbon materials demonstrates the importance of nanocomposites in sensing applications.

In an attempt to optimise the parameters such as deposition time, and CNFs/$Co(NO_3)_2$ ratio for glucose sensing, different matrices were formed by EPD. **Figure 3.16** summarises in form of a bar diagram the best electrocatalytic response to glucose addition. The strongest electrocatalytic behaviour is observed for Au/Ti/glass electrode coated with CNFs/$Co(OH)_2$ for a deposition time of 2 min from a mixture CNFs/$Co(NO_3)_2$ at a ratio of 2:1. Thus this sample was chosen for further non-enzymatic sensing of glucose.

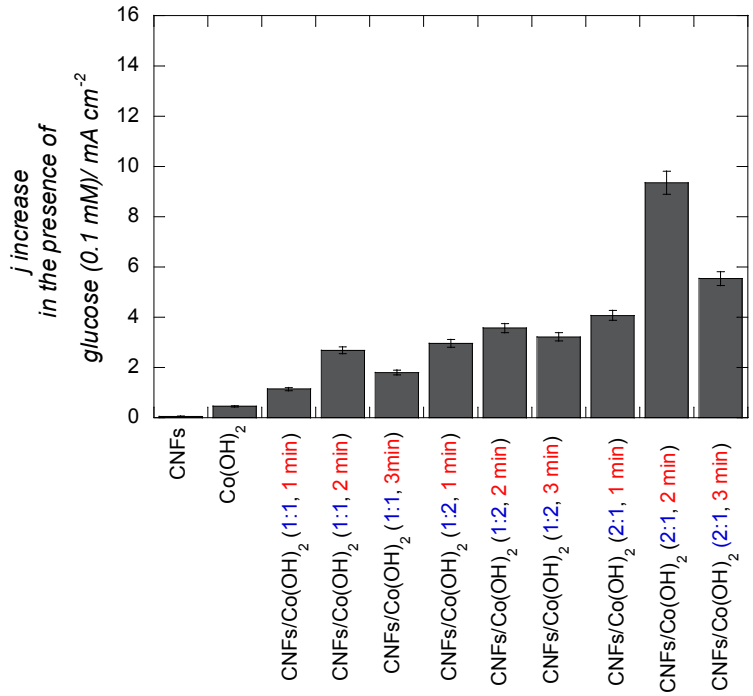

Figure 3.16: Comparison of electrocatalytical response of CNFs, $Co(OH)_2$ films and CNFs/$Co(OH)_2$ films where the ratio CNFs/$Co(NO_3)_2$ was changed as well as the deposition time.

To confirm the ability of CNFs/$Co(OH)_2$ modified Au/Ti/glass electrodes by EPD for glucose sensing in alkaline medium, an amperometric response curve to successive additions of glucose when a potential of +0.55 V was applied to the interface was recorded. As seen in

© 2016 Tous droits réservés.
lilliad.univ-lille.fr

Figure 3.17A, the amperometric response shows a steady-state increase upon the addition of glucose with a very fast response time (10 s). Those steady-state currents were applied to construct the calibration curve. As shown in **Figure 3.17B**, an excellent linearity (R^2=0.999) according to j (mA cm^{-2})=5.3+68[glucose] (mM) over a concentration range from 10 µM to 0.12 mM was recorded. The detection limit of the electrode was calculated to be 5 µM at a signal to noise ratio of 3 (S/N=3). Compared to the analytical performance of other Co-based non-enzymatic glucose sensors, the proposed CNFs/$Co(OH)_2$ sensor here displays comparable or higher detection limit (**Table 3.5**) [68,69,72,74,77,78]. However, the sensitivity is far more remarkable when compared to other cobalt related structures reported (**Table 3.5**).

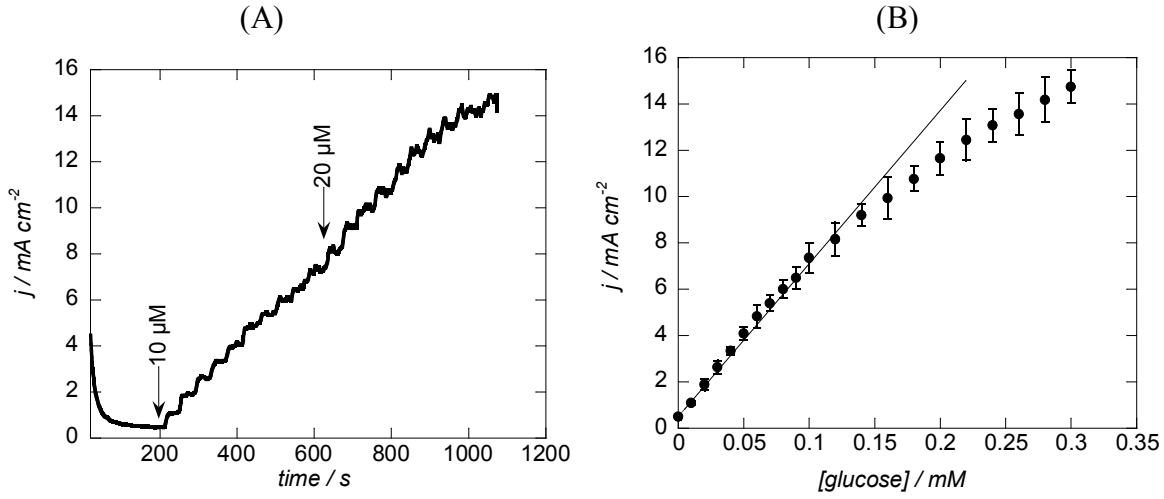

Figure 3.17: (A) Amperometric *j-t* curve of CNFs/$Co(OH)_2$ modified Au/Ti/glass electrode polarized at +0.55 V *vs.* Ag/AgCl upon successive additions of glucose (10 µM or 20 µM) in 0.1 M NaOH, and (B) the corresponding calibration curve.

Table 3.5: Comparison of analytical performance of other non-enzymatic glucose sensors based on cobalt nanostructures.

Material	LOD (µM)	Sensitivity (mA mM^{-1} cm^{-2})	Linear range (mM)	Ref.
CoOOH nanosheet	1.37	0.527	0.003-1.109	[68]
CoP nanorods	9	0.117	up to 5.5	[69]
Co-Ni nanostructures/rGO	3.79	1.774	0.01-2.65	[72]
Graphene -Co_3O_4	10	-	0.05-0.3	[74]
CNTs/CoO/$Co(OH)_2$	2	0.162	up to 4.5	[77]
rGO-chitosan-Cu/Co	10	1.92	0.015-6.95	[78]
CNFs/$Co(OH)_2$	**5**	**68**	**0.01-0.12**	**This work**

The selectivity of CNFs/$Co(OH)_2$ nanocomposite electrode was comparable to that of rGO/Cu NPs (**Figure 3.18**) with no obvious current response observed upon addition of

© 2016 Tous droits réservés.

lilliad.univ-lille.fr

interfering species, thus allowing an accurate and selective non-enzymatic detection of glucose. The same is performed for the reproducibility of CNFs/$Co(OH)_2$ modified Au/Ti/glass electrode for non-enzymatic glucose sensing. A relative standard deviation of 5.3 % of the amperometric response was observed. The long-term stability of the sensor to glucose was in addition evaluated showing a loss of 1.5 % amperometric steady-state current response when testing a 0.1 mM glucose concentration after the electrode has been stored at ambient temperature for a month.

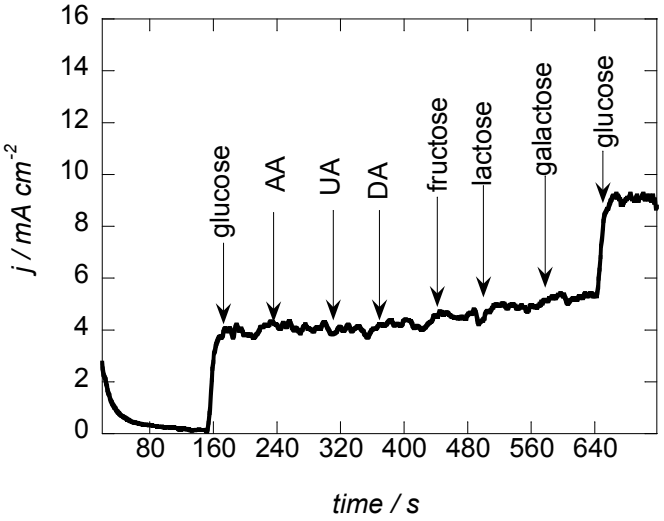

Figure 3.18: Amperometric response of CNFs/$Co(OH)_2$ modified Au/Ti/glass electrode polarized at +0.55 V *vs*. Ag/AgCl to glucose (50 µM), dopamine (DA, 5 µM), ascorbic acid (AA, 5 µM), uric acid (UA, 5 µM), fructose (5 µM), lactose (5 µM), and galactose (5 µM); electrolyte: 0.1 M NaOH.

The CNFs/$Co(OH)_2$ electrode allowed sensing the glucose level in serum samples (**Figure 3.19**). The concentration of glucose in the human serum was determined to be 4.8 mM by using the calibration curve in **Figure 3.17B**. The glucose concentration is comparable to the concentration of 4.5 mM determined using the well-established phenol-sulphuric acid colorimetric method described above. Furthermore, the addition of ascorbic acid, dopamine as well as fructose caused insignificant current increase, suggesting that these species do not interfere with glucose detection in real samples.

© 2016 Tous droits réservés.

lilliad.univ-lille.fr

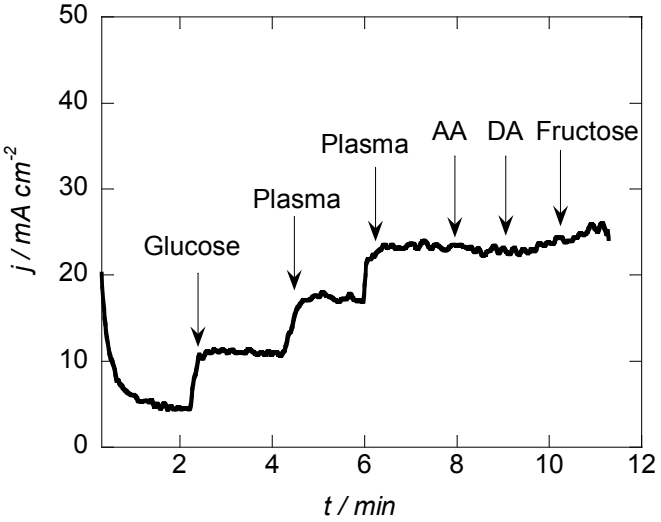

Figure 3.19: Amperometric response of the CNFs/$Co(OH)_2$ modified Au/Ti/glass electrode upon successive additions of different analytes: glucose (0.1 mM), plasma sample (diluted 50 times), ascorbic acid (AA, 0.1 mM), dopamine (DA, 0.1 mM). Electrolyte: 0.1 M NaOH, potential: +0.55 V.

The performances of the developed non-enzymatic glucose sensor constructed by EPD technique are compared in **Table 3.6**. Both electrodes exhibit comparable limit of detection, while CNFs/$Co(OH)_2$ modified Au/Ti/glass interface shows a much higher sensitivity than the electrode modified with rGO/Cu NPs, accompanied with more reliable performance in long term stability. However, the linear range of CNFs/$Co(OH)_2$ based sensor is narrower.

Table 3.6: Performance of rGO/Cu NPs and CNFs/$Co(OH)_2$ modified Au/Ti/glass interface towards non-enzymatic glucose detection.

Electrode	rGO/Cu NPs modified Au/Ti/glass interface	CNFs/$Co(OH)_2$ modified Au/Ti/glass interface
Applied potential (V)	+ 0.55	+ 0.55
Response time	< 15 s	< 10 s
LOD (μM)	3.4	5
Sensitivity	447.65 μA mM^{-1} cm^{-2}	68 mA mM^{-1} cm^{-2}
Linear range (mM)	0.01-1.2	0.01-0.12
Reproducibility (RSD, %)	6.67	5.3
Stability (current loss, %)	10.4	1.5
Glucose analysis in human serum sample (mM)	4.7	4.8

3.4 Conclusion

To summarize, the easy application of electrophoretic technique for deposition of

© 2016 Tous droits réservés.

lilliad.univ-lille.fr

rGO/Cu NPs and CNFs/$Co(OH)_2$ nanocomposites from the corresponding carbon structures and metal salts in ethanolic solution was demonstrated. The morphology, chemical composition, structure or thickness of the resulting composites could be adjusted by varying the deposition time and ratio of the initial components. For sensing application, both rGO/Cu NPs and CNFs/$Co(OH)_2$ modified Au/Ti/glass electrodes were evaluated for their catalytic activity towards non-enzymatic glucose oxidation under alkaline conditions. The electrochemical results showed that the sensors have high sensibility and comparable detection limit with reported literature. Moreover, the rGO/Cu NPs and CNFs/$Co(OH)_2$ nanocomposites modified Au/Ti/glass electrodes exhibited excellent selectivity towards various interfering species, good repeatability and long term stability as non-enzymatic glucose sensors. The sensors were successfully applied for the determination of glucose concentration in human blood serum, with comparable results as those obtained using the well-established phenol-sulfuric acid colorimetric method. Finally, the good catalytic properties of Cu NPs or $Co(OH)_2$ nanostructures combined with the outstanding synergistic properties of carbon structures may find potential applications in various chemical and medical related fields, in the mean time making EPD technique of high interest for prospective development in nanocomposites synthesis.

3.5 References

[1] Coppell, K J; McLean, R M. Risk Factors for Diabetes Type 1 and Type 2. In *Cardiovascular and Metabolic Disease*, 2015; pp 254-273.

[2] Organization, W H. Global report on diabetes. http://apps.who.int/iris/bitstream/10665/204871/1/9789241565257_eng.pdf. 2016.

[3] Chen, C; Xie, Q; Yang, D; Xiao, H; Fu, Y; Tan, Y; Yao, S. Recent advances in electrochemical glucose biosensors: a review. *RSC Advances* **2013**, *3*, 4473-4491.

[4] Matsumoto, F; Harada, M; Koura, N; Uesugi, S. Electrochemical oxidation of glucose at Hg adatom-modified Au electrode in alkaline aqueous solution. *Electrochemistry Communications* **2003**, *5*, 42-46.

[5] Shoji, E; Freund, M S. Potentiometric sensors based on the inductive effect on the pK_a of poly (aniline): a nonenzymatic glucose sensor. *Journal of the American Chemical Society* **2001**, *123*, 3383-3384.

[6] Steiner, M S; Duerkop, A; Wolfbeis, O S. Optical methods for sensing glucose. *Chemical Society Reviews* **2011**, *40*, 4805-4839.

[7] Hussain, F; Birch, D J S; Pickup, J C. Glucose sensing based on the intrinsic fluorescence of sol-gel immobilized yeast hexokinase. *Analytical Biochemistry* **2005**, *339*, 137-143.

[8] Aslan, K; Lakowicz, J R; Geddes, C D. Nanogold plasmon resonance based glucose sensing. *Analytical Biochemistry* **2004**, *330*, 145-155.

[9] Duong, H D; Rhee, J I. Use of CdSe/ZnS core-shell quantum dots as energy transfer

© 2016 Tous droits réservés.

lilliad.univ-lille.fr

donors in sensing glucose. *Talanta* **2007**, *73*, 899-905.
[10] Mason, B S; Slover, H T. Gas-chromatographic method for the determination of sugars in foods. *Journal of Agricultural and Food Chemistry* **1971**, *19*, 551-554.
[11] Ma, J; Hou, X; Zhang, B; Wang, Y; He, L. The analysis of carbohydrates in milk powder by a new "heart-cutting" two-dimensional liquid chromatography method. *Journal of Pharmaceutical and Biomedical Analysis* **2014**, *91*, 24-31.
[12] Klockow, A; Paulus, A; Figueiredo, V; Amado, R; Widmer, H M. Determination of carbohydrates in fruit juices by capillary electrophoresis and high-performance liquid chromatography. *Journal of Chromatography A* **1994**, *680*, 187-200.
[13] Fragkou, V; Turner, A P F. Commercial biosensors for diabetes. *Handbook of Optical Sensing of Glucose in Biological Fluids and Tissues* **2008**, 41-64.
[14] Clark, L C; Lyons, C. Electrode systems for continuous monitoring in cardiovascular surgery. *Annals of the New York Academy of Sciences* **1962**, *102*, 29-45.
[15] D'Costa, E J; Higgins, I J; Turner, A P F. Quinoprotein glucose dehydrogenase and its application in an amperometric glucose sensor. *Biosensors* **1986**, *2*, 71-87.
[16] Zhu, Z; Garcia Gancedo, L; Flewitt, A J; Xie, H; Moussy, F; Milne, W I. A critical review of glucose biosensors based on carbon nanomaterials: carbon nanotubes and graphene. *Sensors* **2012**, *12*, 5996-6022.
[17] Cass, A E G; Davis, G; Francis, G D; Hill, H A O; Aston, W J; Higgins, I J; Plotkin, E V; Scott, L D L; Turner, A P F. Ferrocene-mediated enzyme electrode for amperometric determination of glucose. *Analytical Chemistry* **1984**, *56*, 667-671.
[18] Park, S; Boo, H; Chung, T D. Electrochemical non-enzymatic glucose sensors. *Analytica Chimica Acta* **2006**, *556*, 46-57.
[19] Tian, K; Prestgard, M; Tiwari, A. A review of recent advances in nonenzymatic glucose sensors. *Materials Science and Engineering: C* **2014**, *41*, 100-118.
[20] Toghill, K E; Compton, R G. Electrochemical non-enzymatic glucose sensors: a perspective and an evaluation. *International Journal of Electrochemical Science* **2010**, *5*, 1246-1301.
[21] Pletcher, D. Electrocatalysis: present and future. *Journal of Applied Electrochemistry* **1984**, *14*, 403-415.
[22] Burke, L D. Premonolayer oxidation and its role in electrocatalysis. *Electrochimica Acta* **1994**, *39*, 1841-1848.
[23] Huang, T K; Lin, K W; Tung, S P; Cheng, T M; Chang, I C; Hsieh, Y Z; Lee, C Y; Chiu, H T. Glucose sensing by electrochemically grown copper nanobelt electrode. *Journal of Electroanalytical Chemistry* **2009**, *636*, 123-127.
[24] Kurniawan, F; Tsakova, V; Mirsky, V M. Gold nanoparticles in nonenzymatic electrochemical detection of sugars. *Electroanalysis* **2006**, *18*, 1937-1942.
[25] Park, S; Chung, T D; Kim, H C. Nonenzymatic glucose detection using mesoporous platinum. *Analytical Chemistry* **2003**, *75*, 3046-3049.
[26] Lu, L M; Zhang, L; Qu, F L; Lu, H X; Zhang, X B; Wu, Z S; Huan, S Y; Wang, Q A; Shen, G L; Yu, R Q. A nano-Ni based ultrasensitive nonenzymatic electrochemical sensor for glucose: enhancing sensitivity through a nanowire array strategy. *Biosensors and Bioelectronics* **2009**, *25*, 218-223.
[27] Zhao, J; Wang, F; Yu, J; Hu, S. Electro-oxidation of glucose at self-assembled monolayers incorporated by copper particles. *Talanta* **2006**, *70*, 449-454.
[28] Bai, H; Han, M; Du, Y; Bao, J; Dai, Z. Facile synthesis of porous tubular palladium nanostructures and their application in a nonenzymatic glucose sensor. *Chemical Communications* **2010**, *46*, 1739-1741.
[29] Tominaga, M; Shimazoe, T; Nagashima, M; Taniguchi, I. Composition–activity relationships of carbon electrode-supported bimetallic gold–silver nanoparticles in electrocatalytic oxidation of glucose. *Journal of Electroanalytical Chemistry* **2008**, *615*,

© 2016 Tous droits réservés.
lilliad.univ-lille.fr

51-61.

[30] Niu, X; Lan, M; Chen, C; Zhao, H. Nonenzymatic electrochemical glucose sensor based on novel Pt–Pd nanoflakes. *Talanta* **2012**, *99*, 1062-1067.

[31] Jafarian, M; Forouzandeh, F; Danaee, I; Gobal, F; Mahjani, M G. Electrocatalytic oxidation of glucose on Ni and NiCu alloy modified glassy carbon electrode. *Journal of Solid State Electrochemistry* **2009**, *13*, 1171-1179.

[32] Zhuang, Z; Su, X; Yuan, H; Sun, Q; Xiao, D; Choi, M M F. An improved sensitivity non-enzymatic glucose sensor based on a CuO nanowire modified Cu electrode. *Analyst* **2008**, *133*, 126-132.

[33] Ding, Y; Wang, Y; Su, L; Bellagamba, M; Zhang, H; Lei, Y. Electrospun Co_3O_4 nanofibers for sensitive and selective glucose detection. *Biosensors and Bioelectronics* **2010**, *26*, 542-548.

[34] Mu, Y; Jia, D; He, Y; Miao, Y; Wu, H. Nano nickel oxide modified non-enzymatic glucose sensors with enhanced sensitivity through an electrochemical process strategy at high potential. *Biosensors and Bioelectronics* **2011**, *26*, 2948-2952.

[35] Mallesha, M; Manjunatha, R; Suresh, G S; Melo, J S; D'Souza, S F; Venkatesha, T V. Direct electrochemical non-enzymatic assay of glucose using functionalized graphene. *Journal of Solid State Electrochemistry* **2012**, *16*, 2675-2681.

[36] Ye, J S; Wen, Y; De Zhang, W; Gan, L M; Xu, G Q; Sheu, F S. Nonenzymatic glucose detection using multi-walled carbon nanotube electrodes. *Electrochemistry Communications* **2004**, *6*, 66-70.

[37] Liu, Y; Teng, H; Hou, H; You, T. Nonenzymatic glucose sensor based on renewable electrospun Ni nanoparticle-loaded carbon nanofiber paste electrode. *Biosensors and Bioelectronics* **2009**, *24*, 3329-3334.

[38] Cash, K J; Clark, H A. Nanosensors and nanomaterials for monitoring glucose in diabetes. *Trends in Molecular Medicine* **2010**, *16*, 584-593.

[39] Tian, Y; Liu, Y; Wang, W; Zhang, X; Peng, W. CuO nanoparticles on sulfur-doped graphene for nonenzymatic glucose sensing. *Electrochimica Acta* **2015**, *156*, 244-251.

[40] Marioli, J M; Kuwana, T. Electrochemical characterization of carbohydrate oxidation at copper electrodes. *Electrochimica Acta* **1992**, *37*, 1187-1197.

[41] Luo, M Z; Baldwin, R P. Characterization of carbohydrate oxidation at copper electrodes. *Journal of Electroanalytical Chemistry* **1995**, *387*, 87-94.

[42] Batchelor McAuley, C; Wildgoose, G G; Compton, R G; Shao, L; Green, M L H. Copper oxide nanoparticle impurities are responsible for the electroanalytical detection of glucose seen using multiwalled carbon nanotubes. *Sensors and Actuators B: Chemical* **2008**, *132*, 356-360.

[43] Radhakrishnan, S; Kim, H Y; Kim, B S. A novel CuS microflower superstructure based sensitive and selective nonenzymatic glucose detection. *Sensors and Actuators B: Chemical* **2016**, *233*, 93-99.

[44] Ghanbari, K; Babaei, Z. Fabrication and characterization of non-enzymatic glucose sensor based on ternary NiO/CuO/polyaniline nanocomposite. *Analytical Biochemistry* **2016**, *498*, 37-46.

[45] Zheng, W; Hu, L; Lee, L Y S; Wong, K-Y. Copper Nanoparticles/Polyaniline/Graphene Composite as a Highly Sensitive Electrochemical Glucose Sensor. *Journal of Electroanalytical Chemistry* **2016**. 10.1016/j.jelechem.2016.08.004.

[46] Ensafi, A A; Jafari Asl, M; Dorostkar, N; Ghiaci, M; Martínez Huerta, M V; Fierro, J L G. The fabrication and characterization of Cu-nanoparticle immobilization on a hybrid chitosan derivative-carbon support as a novel electrochemical sensor: application for the sensitive enzymeless oxidation of glucose and reduction of hydrogen peroxide. *Journal of Materials Chemistry B* **2014**, *2*, 706-717.

[47] Xu, J; Cao, X; Xia, J; Gong, S; Wang, Z; Lu, L. Phosphomolybdic acid functionalized

© 2016 Tous droits réservés.

lilliad.univ-lille.fr

graphene loading copper nanoparticles modified electrodes for non-enzymatic electrochemical sensing of glucose. *Analytica Chimica Acta* **2016**. 10.1016/j.aca.2016.06.033.

[48] Zhou, X; Nie, H; Yao, Z; Dong, Y; Yang, Z; Huang, S. Facile synthesis of nanospindle-like Cu_2O/straight multi-walled carbon nanotube hybrid nanostructures and their application in enzyme-free glucose sensing. *Sensors and Actuators B: Chemical* **2012**, *168*, 1-7.

[49] Li, Y; Fu, J; Chen, R; Huang, M; Gao, B; Huo, K; Wang, L; Chu, P K. Core–shell TiC/C nanofiber arrays decorated with copper nanoparticles for high performance non-enzymatic glucose sensing. *Sensors and Actuators B: Chemical* **2014**, *192*, 474-479.

[50] Jiang, D; Liu, Q; Wang, K; Qian, J; Dong, X; Yang, Z; Du, X; Qiu, B. Enhanced non-enzymatic glucose sensing based on copper nanoparticles decorated nitrogen-doped graphene. *Biosensors and Bioelectronics* **2014**, *54*, 273-278.

[51] Luo, L; Zhu, L; Wang, Z. Nonenzymatic amperometric determination of glucose by CuO nanocubes–graphene nanocomposite modified electrode. *Bioelectrochemistry* **2012**, *88*, 156-163.

[52] Luo, J; Jiang, S; Zhang, H; Jiang, J; Liu, X. A novel non-enzymatic glucose sensor based on Cu nanoparticle modified graphene sheets electrode. *Analytica Chimica Acta* **2012**, *709*, 47-53.

[53] Luo, J; Zhang, H; Jiang, S; Jiang, J; Liu, X. Facile one-step electrochemical fabrication of a non-enzymatic glucose-selective glassy carbon electrode modified with copper nanoparticles and graphene. *Microchimica Acta* **2012**, *177*, 485-490.

[54] Wang, Z; Xia, J; Qiang, X; Xia, Y; Shi, G; Zhang, F; Han, G; Xia, L; Tang, J. Polymer-assisted in situ growth of copper nanoparticles on graphene surface for non-enzymatic electrochemical sensing of glucose. *International Journal of Electrochemical Science* **2013**, *8*, 6941-6950.

[55] Wu, H X; Cao, W M; Li, Y; Liu, G; Wen, Y; Yang, H F; Yang, S P. In situ growth of copper nanoparticles on multiwalled carbon nanotubes and their application as non-enzymatic glucose sensor materials. *Electrochimica Acta* **2010**, *55*, 3734-3740.

[56] Kang, X; Mai, Z; Zou, X; Cai, P; Mo, J. A sensitive nonenzymatic glucose sensor in alkaline media with a copper nanocluster/multiwall carbon nanotube-modified glassy carbon electrode. *Analytical Biochemistry* **2007**, *363*, 143-150.

[57] Zhang, X; Wang, G; Zhang, W; Wei, Y; Fang, B. Fixure-reduce method for the synthesis of Cu_2O/MWCNTs nanocomposites and its application as enzyme-free glucose sensor. *Biosensors and Bioelectronics* **2009**, *24*, 3395-3398.

[58] Jiang, L C; Zhang, W D. A highly sensitive nonenzymatic glucose sensor based on CuO nanoparticles-modified carbon nanotube electrode. *Biosensors and Bioelectronics* **2010**, *25*, 1402-1407.

[59] Li, M; Liu, L; Xiong, Y; Liu, X; Nsabimana, A; Bo, X; Guo, L. Bimetallic MCo (M= Cu, Fe, Ni, and Mn) nanoparticles doped-carbon nanofibers synthetized by electrospinning for nonenzymatic glucose detection. *Sensors and Actuators B: Chemical* **2015**, *207*, 614-622.

[60] Yang, S; Li, G; Wang, D; Qiao, Z; Qu, L. Synthesis of nanoneedle-like copper oxide on N-doped reduced graphene oxide: A three-dimensional hybrid for nonenzymatic glucose sensor. *Sensors and Actuators B: Chemical* **2017**, *238*, 588-595.

[61] Wang, Y; Zhang, S; Bai, W; Zheng, J. Layer-by-layer assembly of copper nanoparticles and manganese dioxide-multiwalled carbon nanotubes film: A new nonenzymatic electrochemical sensor for glucose. *Talanta* **2016**, *149*, 211-216.

[62] Zhang, Y; Zhou, E; Li, Y; He, X. A novel nonenzymatic glucose sensor based on magnetic copper ferrite immobilized on multiwalled carbon nanotubes. *Analytical Methods* **2015**, *7*, 2360-2366.

© 2016 Tous droits réservés.

lilliad.univ-lille.fr

[63] Cataldi, T R I; Casella, I G; Desimoni, E; Rotunno, T. Cobalt-based glassy carbon chemically modified electrode for constant-potential amperometric detection of carbohydrates in flow-injection analysis and liquid chromatography. *Analytica Chimica Acta* **1992**, *270*, 161-171.

[64] Casella, I G; Contursi, M. Carbohydrate and alditol analysis by high-performance anion-exchange chromatography coupled with electrochemical detection at a cobalt-modified electrode. *Analytical and Bioanalytical Chemistry* **2003**, *376*, 673-679.

[65] Soomro, R A; Nafady, A; Ibupoto, Z H; Sherazi, S T H; Willander, M; Abro, M I. Development of sensitive non-enzymatic glucose sensor using complex nanostructures of cobalt oxide. *Materials Science in Semiconductor Processing* **2015**, *34*, 373-381.

[66] Kung, C W; Lin, C Y; Lai, Y H; Vittal, R; Ho, K C. Cobalt oxide acicular nanorods with high sensitivity for the non-enzymatic detection of glucose. *Biosensors and Bioelectronics* **2011**, *27*, 125-131.

[67] Han, L; Yang, D P; Liu, A. Leaf-templated synthesis of 3D hierarchical porous cobalt oxide nanostructure as direct electrochemical biosensing interface with enhanced electrocatalysis. *Biosensors and Bioelectronics* **2015**, *63*, 145-152.

[68] Zhang, L; Yang, C; Zhao, G; Mu, J; Wang, Y. Self-supported porous CoOOH nanosheet arrays as a non-enzymatic glucose sensor with good reproducibility. *Sensors and Actuators B: Chemical* **2015**, *210*, 190-196.

[69] Sun, Q Q; Wang, M; Bao, S J; Wang, Y C; Gu, S. Analysis of cobalt phosphide (CoP) nanorods designed for non-enzyme glucose detection. *Analyst* **2016**, *141*, 256-260.

[70] Lien, C H; Chen, J C; Hu, C C; Wong, D S H. Cathodic deposition of binary nickel-cobalt hydroxide for non-enzymatic glucose sensing. *Journal of the Taiwan Institute of Chemical Engineers* **2014**, *45*, 846-851.

[71] Premlatha, S; Sivasakthi, P; Bapu, G N K R. Electrodeposition of a 3D hierarchical porous flower-like cobalt–MWCNT nanocomposite electrode for non-enzymatic glucose sensing. *RSC Advances* **2015**, *5*, 74374-74380.

[72] Wang, L; Lu, X; Ye, Y; Sun, L; Song, Y. Nickel-cobalt nanostructures coated reduced graphene oxide nanocomposite electrode for nonenzymatic glucose biosensing. *Electrochimica Acta* **2013**, *114*, 484-493.

[73] Suneesh, P V; Vargis, V S; Ramachandran, T; Nair, B G; Babu, T G S. Co–Cu alloy nanoparticles decorated TiO_2 nanotube arrays for highly sensitive and selective nonenzymatic sensing of glucose. *Sensors and Actuators B: Chemical* **2015**, *215*, 337-344.

[74] Wang, X; Dong, X; Wen, Y; Li, C; Xiong, Q; Chen, P. A graphene–cobalt oxide based needle electrode for non-enzymatic glucose detection in micro-droplets. *Chemical Communications* **2012**, *48*, 6490-6492.

[75] Dong, X C; Xu, H; Wang, X W; Huang, Y X; Chan Park, M B; Zhang, H; Wang, L H; Huang, W; Chen, P. 3D graphene–cobalt oxide electrode for high-performance supercapacitor and enzymeless glucose detection. *ACS Nano* **2012**, *6*, 3206-3213.

[76] Chen, T; Li, X; Qiu, C; Zhu, W; Ma, H; Chen, S; Meng, O. Electrochemical sensing of glucose by carbon cloth-supported Co_3O_4/PbO_2 core-shell nanorod arrays. *Biosensors and Bioelectronics* **2014**, *53*, 200-206.

[77] Yang, J; Gunasekaran, S. A low-potential, H_2O_2-assisted electrodeposition of cobalt oxide/hydroxide nanostructures onto vertically-aligned multi-walled carbon nanotube arrays for glucose sensing. *Electrochimica Acta* **2011**, *56*, 5538-5544.

[78] Wang, L; Zheng, Y; Lu, X; Li, Z; Sun, L; Song, Y. Dendritic copper-cobalt nanostructures/reduced graphene oxide-chitosan modified glassy carbon electrode for glucose sensing. *Sensors and Actuators B: Chemical* **2014**, *195*, 1-7.

[79] Ju, L; Wu, G; Lu, B; Li, X; Wu, H; Liu, A. Non-enzymatic amperometric glucose sensor based on copper nanowires decorated reduced graphene oxide. *Electroanalysis* **2016**.

© 2016 Tous droits réservés.

lilliad.univ-lille.fr

10.1002/elan.201600100.

[80] Kong, F Y; Li, X R; Zhao, W W; Xu, J J; Chen, H Y. Graphene oxide–thionine–Au nanostructure composites: preparation and applications in non-enzymatic glucose sensing. *Electrochemistry Communications* **2012**, *14*, 59-62.

[81] Lim, S A; Ahmed, M U. A carbon nanofiber-based label free immunosensor for high sensitive detection of recombinant bovine somatotropin. *Biosensors and Bioelectronics* **2015**, *70*, 48-53.

[82] Lu, N; Shao, C; Li, X; Miao, F; Wang, K; Liu, Y. CuO nanoparticles/nitrogen-doped carbon nanofibers modified glassy carbon electrodes for non-enzymatic glucose sensors with improved sensitivity. *Ceramics International* **2016**, *42*, 11285-11293.

[83] Wang, B; Wu, Y; Chen, Y; Weng, B; Li, C. Flexible paper sensor fabricated via in situ growth of Cu nanoflower on RGO sheets towards amperometrically non-enzymatic detection of glucose. *Sensors and Actuators B: Chemical* **2017**, *238*, 802-808.

[84] Yazid, S N A M; Isa, I M; Hashim, N. Novel alkaline-reduced cuprous oxide/graphene nanocomposites for non-enzymatic amperometric glucose sensor application. *Materials Science and Engineering: C* **2016**. 10.1016/j.msec.2016.06.006.

[85] Yuan, B; Xu, C; Liu, L; Zhang, Q; Ji, S; Pi, L; Zhang, D; Huo, Q. Cu_2O/NiOx/graphene oxide modified glassy carbon electrode for the enhanced electrochemical oxidation of reduced glutathione and nonenzyme glucose sensor. *Electrochimica Acta* **2013**, *104*, 78-83.

[86] Yang, Z; Yan, X; Li, Z; Zheng, X; Zheng, J. Synthesis of Cu_2O on AlOOH/reduced graphene oxide for non-enzymatic amperometric glucose sensing. *Analytical Methods* **2016**, *8*, 1527-1531.

[87] Zhao, Y; Bo, X; Guo, L. Highly exposed copper oxide supported on three-dimensional porous reduced graphene oxide for non-enzymatic detection of glucose. *Electrochimica Acta* **2015**, *176*, 1272-1279

[88] Thanh, T D; Balamurugan, J; Lee, S H; Kim, N H; Lee, J H. Effective seed-assisted synthesis of gold nanoparticles anchored nitrogen-doped graphene for electrochemical detection of glucose and dopamine. *Biosensors and Bioelectronics* **2016**, *81*, 259-267.

[89] Dhara, K; Ramachandran, T; Nair, B G; Babu, T G S. Single step synthesis of Au–CuO nanoparticles decorated reduced graphene oxide for high performance disposable nonenzymatic glucose sensor. *Journal of Electroanalytical Chemistry* **2015**, *743*, 1-9

[90] Sun, K G; Hur, S H. Highly sensitive non-enzymatic glucose sensor based on Pt nanoparticle decorated graphene oxide hydrogel. *Sensors and Actuators B: Chemical* **2015**, *210*, 618-623.

[91] Chung, J S; Hur, S H. A highly sensitive enzyme-free glucose sensor based on Co_3O_4 nanoflowers and 3D graphene oxide hydrogel fabricated via hydrothermal synthesis. *Sensors and Actuators B: Chemical* **2016**, *223*, 76-82.

[92] Heidari, H; Habibi, E. Amperometric enzyme-free glucose sensor based on the use of a reduced graphene oxide paste electrode modified with electrodeposited cobalt oxide nanoparticles. *Microchimica Acta* **2016**, *183*, 2259-2266.

[93] Li, S J; Du, J M; Chen, J; Mao, N N; Zhang, M J; Pang, H. Electrodeposition of cobalt oxide nanoparticles on reduced graphene oxide: a two-dimensional hybrid for enzyme-free glucose sensing. *Journal of Solid State Electrochemistry* **2014**, *18*, 1049-1056.

[94] Yuan, B; Xu, C; Deng, D; Xing, Y; Liu, L; Pang, H; Zhang, D. Graphene oxide/nickel oxide modified glassy carbon electrode for supercapacitor and nonenzymatic glucose sensor. *Electrochimica Acta* **2013**, *88*, 708-712.

[95] Ye, J S; Liu, Z T; Lai, C C; Lo, C T; Lee, C L. Diameter effect of electrospun carbon fiber support for the catalysis of Pt nanoparticles in glucose oxidation. *Chemical Engineering Journal* **2016**, *283*, 304-312.

© 2016 Tous droits réservés.

lilliad.univ-lille.fr

[96] Li, L; Zhou, T; Sun, G; Li, Z; Yang, W; Jia, J; Yang, G. Ultrasensitive electrospun nickel-doped carbon nanofibers electrode for sensing paracetamol and glucose. *Electrochimica Acta* **2015**, *152*, 31-37.

[97] Zhang, L; Yuan, S; Lu, X. Amperometric nonenzymatic glucose sensor based on a glassy carbon electrode modified with a nanocomposite made from nickel (II) hydroxide nanoplates and carbon nanofibers. *Microchimica Acta* **2014**, *181*, 365-372.

[98] Zhang, J; Zhu, X; Dong, H; Zhang, X; Wang, W; Chen, Z. In situ growth cupric oxide nanoparticles on carbon nanofibers for sensitive nonenzymatic sensing of glucose. *Electrochimica Acta* **2013**, *105*, 433-438.

[99] Liu, H; Lu, X; Xiao, D; Zhou, M; Xu, D; Sun, L; Song, Y. Hierarchical Cu–Co–Ni nanostructures electrodeposited on carbon nanofiber modified glassy carbon electrode: application to glucose detection. *Analytical Methods* **2013**, *5*, 6360-6367.

[100] Ye, D; Liang, G; Li, H; Luo, J; Zhang, S; Chen, H; Kong, J. A novel nonenzymatic sensor based on CuO nanoneedle/graphene/carbon nanofiber modified electrode for probing glucose in saliva. *Talanta* **2013**, *116*, 223-230.

[101] Subramanian, P; Lesniewski, A; Kaminska, I; Vlandas, A; Vasilescu, A; Niedziolka-Jonsson, J; Pichonat, E; Happy, H; Boukherroub, R; Szunerits, S. Lysozyme detection on aptamer functionalized graphene-coated SPR interfaces. *Biosensors and Bioelectronics* **2013**, *50*, 239-243.

[102] Subramanian, P; Niedziolka-Jonsson, J; Lesniewski, A; Wang, Q; Li, M; Boukherroub, R; Szunerits, S. Preparation of reduced graphene oxide–$Ni(OH)_2$ composites by electrophoretic deposition: application for non-enzymatic glucose sensing. *Journal of Materials Chemistry A* **2014**, *2*, 5525-5533.

[103] Biesinger, M C; Lau, L W M; Gerson, A R; Smart, R S C. Resolving surface chemical states in XPS analysis of first row transition metals, oxides and hydroxides: Sc, Ti, V, Cu and Zn. *Applied Surface Science* **2010**, *257*, 887-898.

[104] Corni, I; Ryan, M P; Boccaccini, A R. Electrophoretic deposition: from traditional ceramics to nanotechnology. *Journal of the European Ceramic Society* **2008**, *28*, 1353-1367.

[105] Li, L; Qian, H; Ren, J. CdTe@$Co(OH)_2$ (core – shell) nanoparticles: aqueous synthesis and characterization. *Chemical Communications* **2005**, 4083-4085.

[106] Brundle, C R; Chuang, T J; Rice, D W. X-ray photoemission study of the interaction of oxygen and air with clean cobalt surfaces. *Surface Science* **1976**, *60*, 286-300.

[107] Singh, B; Murad, L; Laffir, F; Dickinson, C; Dempsey, E. Pt based nanocomposites (mono/bi/tri-metallic) decorated using different carbon supports for methanol electro-oxidation in acidic and basic media. *Nanoscale* **2011**, *3*, 3334-3349.

[108] Peigney, A; Laurent, C; Flahaut, E; Bacsa, R R; Rousset, A. Specific surface area of carbon nanotubes and bundles of carbon nanotubes. *Carbon* **2001**, *39*, 507-514.

[109] Zhang, Y; Su, L; Manuzzi, D; de los Monteros, H V E; Jia, W; Huo, D; Hou, C; Lei, Y. Ultrasensitive and selective non-enzymatic glucose detection using copper nanowires. *Biosensors and Bioelectronics* **2012**, *31*, 426-432.

[110] Pandya, A; Sutariya, P G; Menon, S K. A non enzymatic glucose biosensor based on an ultrasensitive calix [4] arene functionalized boronic acid gold nanoprobe for sensing in human blood serum. *Analyst* **2013**, *138*, 2483-2490.

[111] Wang, Q; Kaminska, I; Niedziolka-Jonsson, J; Opallo, M; Li, M; Boukherroub, R; Szunerits, S. Sensitive sugar detection using 4-aminophenylboronic acid modified graphene. *Biosensors and Bioelectronics* **2013**, *50*, 331-337.

[112] Dubois, M; Gilles, K A; Hamilton, J K; Rebers, P A T; Smith, F. Colorimetric method for determination of sugars and related substances. *Analytical Chemistry* **1956**, *28*, 350-356.

[113] Li, M; Han, C; Zhang, Y; Bo, X; Guo, L. Facile synthesis of ultrafine Co_3O_4

© 2016 Tous droits réservés.

lilliad.univ-lille.fr

nanocrystals embedded carbon matrices with specific skeletal structures as efficient non-enzymatic glucose sensors. *Analytica Chimica Acta* **2015**, *861*, 25-35.

[114]Chen, C H; Tsai, D S; Chung, W H; Lee, K Y; Chen, Y M; Huang, Y S. Electrochemical capacitors of miniature size with patterned carbon nanotubes and cobalt hydroxide. *Journal of Power Sources* **2012**, *205*, 510-515.

© 2016 Tous droits réservés.

lilliad.univ-lille.fr

Thèse de Qian Wang, Lille 1, 2016

CHAPTER 4

ONE-STEP SYNTHESIS OF Au NANOPARTICLES-REDUCED GRAPHENE OXIDE COMPOSITE USING TYROSINE FOR NON-ENZYMATIC H_2O_2 SENSING

4.1 Introduction

Gold nanoparticle (Au NPs) modified graphene sheets are probably the most widely used sensing matrices, due to the unique electronic and optical properties, stability, low cytotoxicity and ease of synthesis of Au NPs with a size ranging between 3 and 200 nm [1], compared to graphene composites loaded with other noble metal nanoparticles. It has been argued that Au NPs/graphene composites could be used in fact in almost any domain related to sensing, ranging from electrochemical [2] to optical [3], and fluorescence [4] approaches. **Table 4.1** lists some of the developed Au NPs/graphene electrodes proposed together with the analytes detected. From this table, it becomes clear that Au NPs/graphene electrodes are capable of detecting molecules such as dopamine, glucose as well as DNA and proteins with low detection limits and wide linear ranges.

Table 4.1: Au NPs/graphene nanocomposites in electrochemical sensing

Material	Analyte	LOD	Linear range	Ref.
Au NPs/NG	dopamine	0.01 µM	0.03-48 µM	[5]
Au NPs/rGO	dopamine	0.02 µM	1-60µM	[6]
Au NPs–β-CD–GR	dopamine ascorbic acid uric acid	0.15 µM 10 µM 0.21 µM	0.5-150 µM 30-2000 µM 0.5-60µM	[7]
rGO-PMS@Au NPs	glucose	2.5 µM	0.01-8 mM	[8]
Au NPs/PPy/rGO	glucose	-	0.2-1.2 mM	[9]
Au NPs/GO nanoribbon	glucose	5 µM	0.005-10 mM	[10]
PDDA-rGO/ Au NPs-aptamer	ractopamine	0.5 fM	1 fM-10 µM	[11]
graphene nanofibers/ Au NPs	bisphenol A	35 nM	80 nM-0.25 mM	[12]
rGO/Au NPs-enzyme	cholesterol	0.05 µM	0.05-0.35 mM	[13]

© 2016 Tous droits réservés.

lilliad.univ-lille.fr

PDDA-rGO/Au NPs-enzyme	paraoxon	0.1 pM	0.1 pM-5nM	[14]
rGO/AuNPs-antibody	17-β-estradiol	0.1 fM	1 fM-1 mM	[15]
Graphene/Au NPs	diethylstilboestrol	9.8 nM	12 nM-12 μM	[16]
carbon ionic liquid-rGO/Au NPs	folic acid	2.7 nM	01-50 μM	[17]
rGO/Au NPs	toxicant Sudan I	1 nM	0.01-70 μM	[18]
Au NPs–rGO–PAH	NADH	3.5 μM	0.01-5 mM	[19]
rGO/Au NPs	NADH	1.13 nM	50 nM-500 μM	[20]
Au NPs/ERGO	nitric oxide	0.133 μM	up to 3.38 μM	[21]
rGO/Au NPs-aptamer	TNT	3.6 pg mL^{-1}	0.01-100 ng mL^{-1}	[22]
ionic liquid-rGO/Au NPs	Hg^{2+}	0.03 nM	LR: 0.1-100 nM	[23]
Au NPs/GR	Cu^{2+}	0.028 nM	5-100 nM	[24]
Orange II–rGO/Au NPs	insulin	6.0 aM	10 aM-50 nM	[25]
GO/Au NPs	P53 protein	0.03 pM	0.2-200 pM	[26]
NG/Au NPs	DNA	3.12 fM	10 fM-100 nM	[27]
toluidine blue–rGO/Au NPs	DNA	2.95 pM	0.1 pM-1 nM	[28]
SH-β-CD-Gr/Au NPs	thrombin	5.2 aM	0.016-8 fM	[29]

Abbreviations- β-CD: β-cyclodextrin; **CS**: chitosan; **ERGO**: electrochemically reduced graphene oxide; **GR**: graphene; **GS**: graphene sheet; **NG**: nitrogen-doped graphene; **PAH**: poly(allyamine hydrochloride); **PDDA**: poly(diallyldimethyl ammonium chloride); **PMS**: periodic mesoporous silica; **PPy**: polypyrrole; **PTBO**: poly(toluidine blue O); **SH**: thiol; **TNT**: 2, 4, 6-trinitrotoluene.

To date, a great amount of electrochemical biosensors to detect H_2O_2 have been developed. These sensors rely mostly on enzymes (catalase) immobilized on the electrode surface. Due to the limitations of enzymatic sensors discussed in **Chapter 3**, the development of enzyme-free strategy for H_2O_2 sensing with high sensitivity and selectivity is thus of great importance. **Table 4.2** summarizes some of the work undertaken so far. Fang *et al.* used cationic poly(diallyldimethyl ammonium chloride) (PDDA) functionalized graphene nanosheets (GNs) for the preparation of GNs/Au NPs heterostructures with enhanced electrochemical catalytic ability [32]. Indeed, the sensor exhibited a detection limit of 0.44 μM over a linear range from 0.5 μM to 0.5 mM for H_2O_2 detection. The good performance of the sensor was ascribed to the high loading and uniform dispersion of the Au NPs on the graphene nanosheets. A similar approach has been adopted for electrostatic assembly of anionic sulfonated graphene sheets (SGS) and positively charged Au NPs to synthesize a 2D hybrid heterostructure SGS/Au NPs [33]. The performance of the SGS/Au NPs material, deposited on GC electrode, for the detection of H_2O_2 was evaluated in PBS at -0.2 V. A good detection limit of 0.25 μM and a linear range from 20 μM to 1.3 mM have been achieved using this material. The layer-by-layer technique was investigated for the fabrication of a 3D Au NPs-embedded porous graphene (AuEPG) thin film [34]. In this approach, the electrode material has been fabricated by electrostatic layer-by-layer assembly of Au NPs and graphene nanosheets functionalized with bovine serum albumin and subsequent thermal annealing in air

© 2016 Tous droits réservés.

lilliad.univ-lille.fr

at 340°C for 2 h. The sensitivity of the sensor is significantly improved (7 times larger) upon annealing as compared to the non-annealed assembled film-modified electrode. The detection limit of the AuEPG film-modified electrode was estimated to be 0.1 μM with a linear range from 0.5 μM to 4.9 mM. Hu *et al.* used hexamethylenetetramine (HMTA) as a reductant for the *in situ* synthesis of rGO/Au NPs from GO and Au precursor [35]. The rGO/Au NPs showed good electrocatalytic activity for H_2O_2 reduction in PBS solution with a detection limit of 6 μM. A one-pot green synthetic method has been described for the synthesis of rGO/Au NPs membrane at a liquid-air interface through the simultaneous reduction of GO and $HAuCl_4$ with glucose at 95°C. The membrane was successfully applied for H_2O_2 sensing with a detection limit of 6.2 μM [36].

Table 4.2: Au NPs/graphene nanocomposites proposed for non-enzymatic electrochemical H_2O_2 sensing.

Material	LOD (μM)	Sensitivity ($\mu A\ mM^{-1}\ cm^{-2}$)	Linear range (mM)	Ref.
Au NPs/PDDA/rGO	0.44	-	0.0005-0.5	[32]
Au NPs/SGS	0.25	3.21	2.3-16	[33]
Au NPs/rGO paper	2	236.8	0.005-8.6	[37]
Au NPs/rGO	6	3	0.020-0.280	[35]
Au NPs/POM/rGO	1.54	58.87	0.005-18	[38]
Au NPs/EPG	0.1	75.9	0.0005-4.9	[34]
rGO/Nafion/AzI/Au NPs	10	-	0.03-5	[39]
Au NPs/MnO_2/rGO	0.05	980	0.022-12.6	[40]
PtAu NPs/rGO/CNTs	0.6	313.4	0.002-8.561	[41]
Au NPs/rGO/GC membrane	6.2	5.3	0.25-22.5	[36]
Ag-Au-rGO	1	-	0.1-5	[42]
Au-MWCNTs-sG@GCE	13	-	1-62	[43]
Au NPs/rGO	1.5	-	0.1-9	[44]
Au NPs-Gr	0.03	-	0.0001-0.07	[45]
Au NPs-N-GQDs	0.12	186.22	0.00025-13.327	[46]
AuNPs/rGO	0.1	1238	0.02-10	[47]
H-GNs/AuNPs	0.11	2774.8	0.0003-1.8	[48]
AuNPS/Gr-CS	1.6	-	0.005-35	[49]
Hb/AuNPs/ZnO/Gr	0.8	-	0.006-1.13	[50]
rGO-Hemin-AuNPs	0.03	-	0.0001-0.04	[51]
Pt-Au NPs/rGO	0.31	-	0.001-16.8	[52]
rGO/AuNPs/PTBO	0.2	63.39±1.56 24.52±2.30	0.005-1.077 1.4745-25.362	[53]
GS@CeO_2/AuNPs	0.26	-	0.001-10	[54]

Abbreviations-Au-MWCNTs-sG: Au nanoparticles-decorated multiwalled carbon nanotube-solar exfoliated graphene; **AzI**: Azur I; **CNTs**: carbon nanotubes; **CS**: chitosan; **EPG**: embedded porous graphene; **GCE**: glassy carbon electrode; **Gr**: graphene; **GS**: graphene sheet; **Hb** : hemoglobin; **H-GNs**: Hemin-graphene nanosheets; **LOD**: limit of detection; **N-GQDs**: nitrogen-doped graphene quantum dots; **POM**: polyoxometalate; **PTBO**: poly(toluidine blue O); **SGS**: sulfonated graphene sheets.

© 2016 Tous droits réservés.

lilliad.univ-lille.fr

Recently, our group has developed an easy and environmentally friendly chemical method for the simultaneous reduction and non-covalent functionalization of GO using tyrosine [55]. In this chapter, we take advantage of the reducing properties of tyrosine for the *in situ* synthesis of aqueous stable rGO/Au NPs hybrids from GO and Au ions (**Figure 4.1**). After reduction from GO to rGO by using tyrosine, $HAuCl_4$ was added to the rGO/Tyr suspension and stirred for additional time. The resulting rGO/Au NPs/Tyr nanocomposite was applied for non-enzymatic detection of H_2O_2.

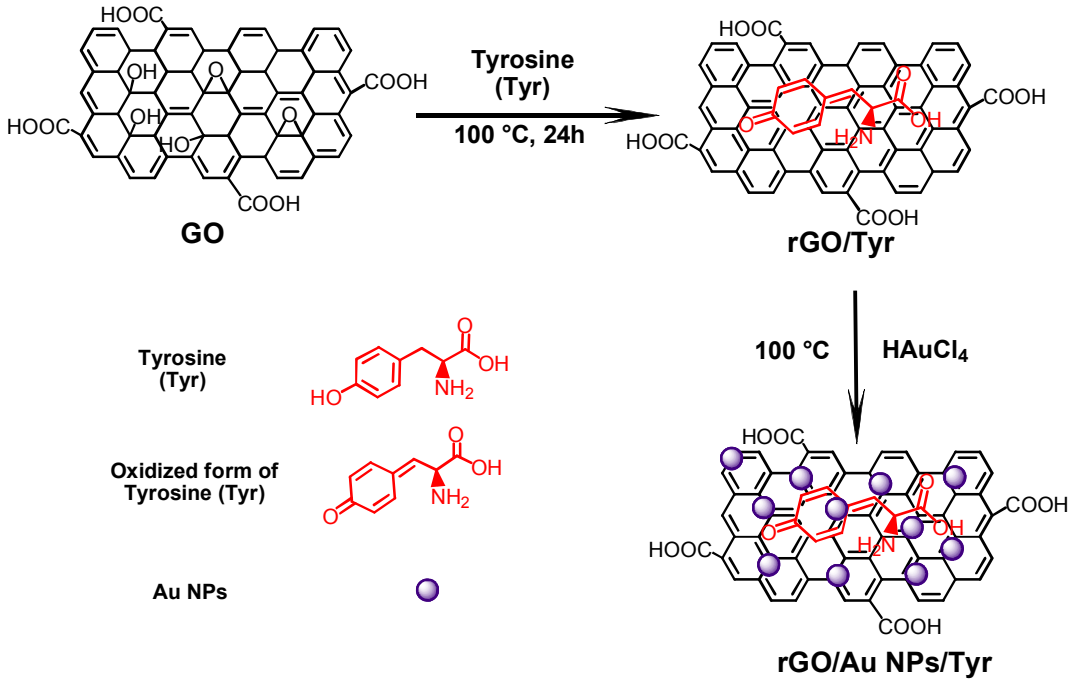

Figure 4.1: Schematic illustration of the formation of rGO/Au NPs/Tyr composite films used for H_2O_2 detection

4.2 *In situ* formation of rGO/Au NPs using tyrosine as reducing agent

There are currently various synthetic routes for the preparation of Au NPs decorated graphene nanocomposites [56,57]. Based upon the structural morphology of the final hybrid, these synthetic methods can be divided into two classes: Au NPs dispersed on graphene sheets and Au NPs wrapped by graphene and its derivatives (**Figure 4.2**). The main difference is the relative surface ratio between the Au NPs and the lateral dimensions of graphene. When the size of the Au NPs is in range of a few nanometers, the particles are small and can be easily

© 2016 Tous droits réservés.

lilliad.univ-lille.fr

deposited onto the graphene nanosheets. When the Au NPs size becomes comparable with that of the 2D graphene sheets, wrapping around the particles occurs preferentially.

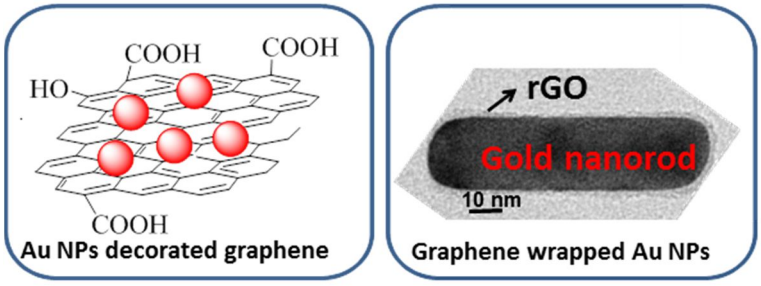

Figure 4.2: Two approaches for the integration of Au NPs with graphene: Au NPs formed *in situ* or *ex situ* on graphene nanosheets and graphene wrapped gold nanostructures (TEM image of a gold nanorod coated with some layers of rGO) [58].

While the *ex-situ* approach is well adapted to form controlled Au NPs loaded GO and rGO, most work focused on *in situ* approaches. In general, a GO suspension is mixed with $HAuCl_4$ and the mixture is treated with a reducing agent resulting in the simultaneous reduction of Au^{3+} solution to Au^0 and GO to rGO (**Figure 4.3**).

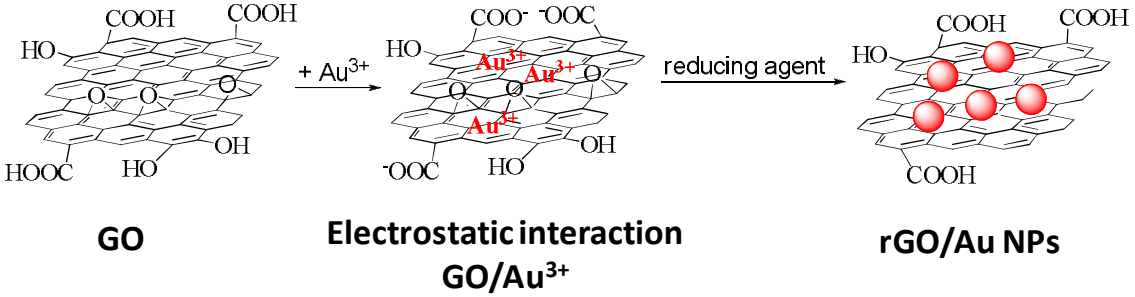

Figure 4.3: *In situ* strategy for the formation of Au NPs loaded rGO matrices through electrostatic integration and reduction of GO/Au^{3+} mixtures.

Although the mechanism of reduction is not clearly understood, involvement of three steps is hypothesized: the oxygen functionalities of GO provide the reactive nucleation sites. After reduction of Au^{3+} cations by the reducing agent such as sodium citrate [59-61], sodium borohydride [62-64], ascorbic acid [65-67], tyrosine [68], poly(diallyldimethylammonium chloride) (PDDA) [69], sodium dodecyl sulfate (SDS) [70], ionic liquid [71] as well as sonolysis [72,73], the growth of Au particles is initiated with the nanoparticles remaining attached to the GO sheet. The reducing agents simultaneously reduce GO to rGO, resulting in the formation of rGO/Au NPs nanocomposites.

We propose here the use of tyrosine for the simultaneous reduction of GO to rGO and the

© 2016 Tous droits réservés.

lilliad.univ-lille.fr

formation of Au NPs on the matrix. The interaction between tyrosine and rGO is most likely dominated by π-stacking between the hexagonal cells of graphene and the aromatic ring structure of tyrosine. The mechanism for the reduction of GO to rGO by tyrosine is believed to be analogous to that reported for dopamine and its derivatives [74,75]. GO oxidizes the phenol structure of tyrosine to radical or quinone intermediates, while being reduced to rGO [76]. The tyrosine quinone intermediates most likely react with each other to form dityrosine or partially integrate with the rGO matrix. Tyrosine is also responsible for the reduction of Au(III) ions into metallic Au and formation of Au NPs, as demonstrated previously [76,77].

The synthesized rGO/Au NPs/Tyr composites were characterized by scanning electron microscopy (SEM), transmission electron microscopy (TEM), energy dispersive X-ray spectroscopy (EDX), X-ray diffraction (XRD), ultraviolet-visible spectroscopy (UV-Vis), Fourier transform infrared (FTIR) spectroscopy, Raman spectroscopy, X-ray photoelectron spectrometry (XPS) prior to the application for non-enzymatic H_2O_2 detection.

Figure 4.4 depicts the SEM images of the as-prepared rGO/Au NPs/Tyr nanohybrids under different synthesis conditions. All images display similar characteristics with uniformly distributed Au NPs decorated on graphene sheets. However, the size of Au NPs varies with different $HAuCl_4$ concentration and stirring time. **Table 4.3** summarizes the size of Au NPs determined from a statistical study of 40 nanoparticles. It can be seen that rGO/Au NPs/Tyr composite prepared by mixing rGO/Tyr with 2 mM $HAuCl_4$ and stirring for 3 h exhibits the smallest particle size with an average diameter of 28±4 nm (**Figure 4.4B**), while longer reaction time (6 h) results in a large increase of particle size up to 69±5 nm (**Figure 4.4C**). Increasing the concentration of $HAuCl_4$ to 4 mM also causes a slight increase of average diameter of Au NPs (**Figure 4.4D**). EDX analysis performed on rGO/AuNPs/Tyr composites shows signals of C, O and Au (**Table 4.4**). The results indicate 3.44 to 5.48 at. % of Au after addition of $HAuCl_4$, where the highest 5.48 at. % resulted from rGO/Tyr mixed with 2 mM $HAuCl_4$ with stirring time of 3 h.

© 2016 Tous droits réservés.

lilliad.univ-lille.fr

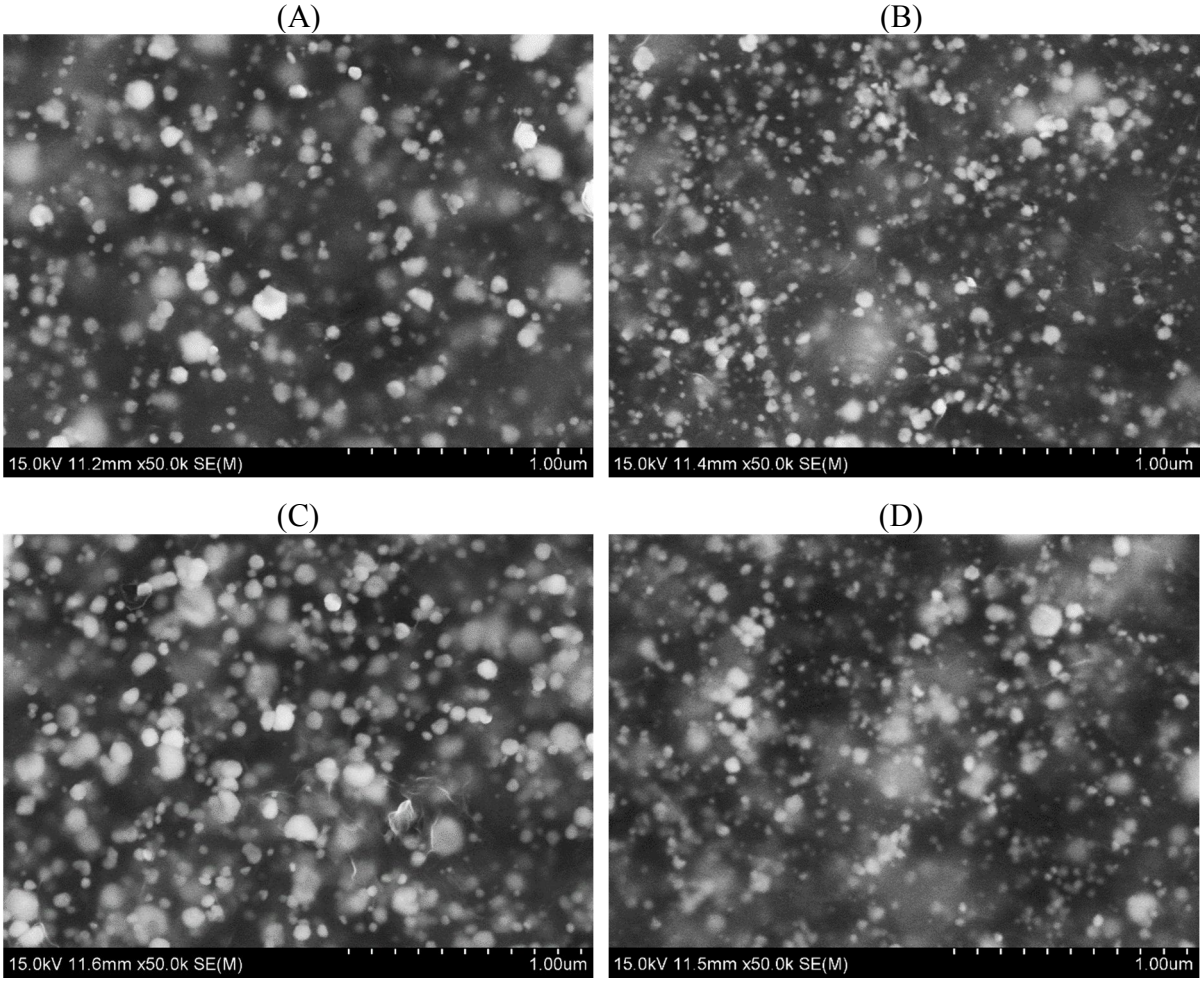

Figure 4.4: SEM images of rGO/Au NPs/Tyr composites prepared by mixing rGO/Tyr with (A) 2 mM $HAuCl_4$ for 1 h, (B) 2 mM $HAuCl_4$ for 3 h, (C) 2 mM $HAuCl_4$ for 6 h and (D) 4 mM $HAuCl_4$ for 3 h, respectively under stirring at 100°C.

Table 4.3: Size of Au NPs of different rGO/Au NPs/Tyr composites.

Samples	$HAuCl_4$ (mM)	Reaction time (h)	Average diameter of Au NPs (nm)
a	2	1	57±6
b	2	3	28±4
c	2	6	69±5
d	4	3	42±5

Table 4.4: EDX results of rGO/Au NPs/Tyr composites prepared by mixing rGO/Tyr with 2 mM $HAuCl_4$ for 1 h, 2 mM $HAuCl_4$ for 3 h, 2 mM $HAuCl_4$ for 6 h and 4 mM $HAuCl_4$ for 3 h, respectively under stirring at 100°C.

Samples	$HAuCl_4$ (mM)	Reaction time (h)	C (at. %)	O (at. %)	N (at. %)	Au (at. %)
a	2	1	75.43	17.51	3.62	3.44
b	2	3	73.56	17.43	3.53	5.48
c	2	6	75.68	17.21	3.25	3.86
d	4	3	74.76	17.97	2.94	4.33

© 2016 Tous droits réservés.

lilliad.univ-lille.fr

The structure and substructure details of the rGO/Au NPs/Tyr nanocomposite were further characterized by TEM and high-resolution TEM. **Figure 4.5A** displays TEM image of the rGO/Au NPs/Tyr nanohybrid with wrinkled and flake-like shape structure of graphene and preferentially dispersed Au NPs on crumpled graphene nanosheets. There are also relatively large Au particles with obvious aggregation on rGO surface. The high resolution TEM image reveals lattice fringes of the nanoparticles with 0.23 nm spacing, corresponding to the (111) crystal plane of cubic Au (**Figure 4.5B**) [78]. Selected-area electron diffraction (SAED) exhibits a mixed diffraction pattern, including (111), (200), (220) and (311) faces (**Figure 4.5C**), suggesting the presence of defects and multiple crystal domains in the Au nanocrystals [79,80].

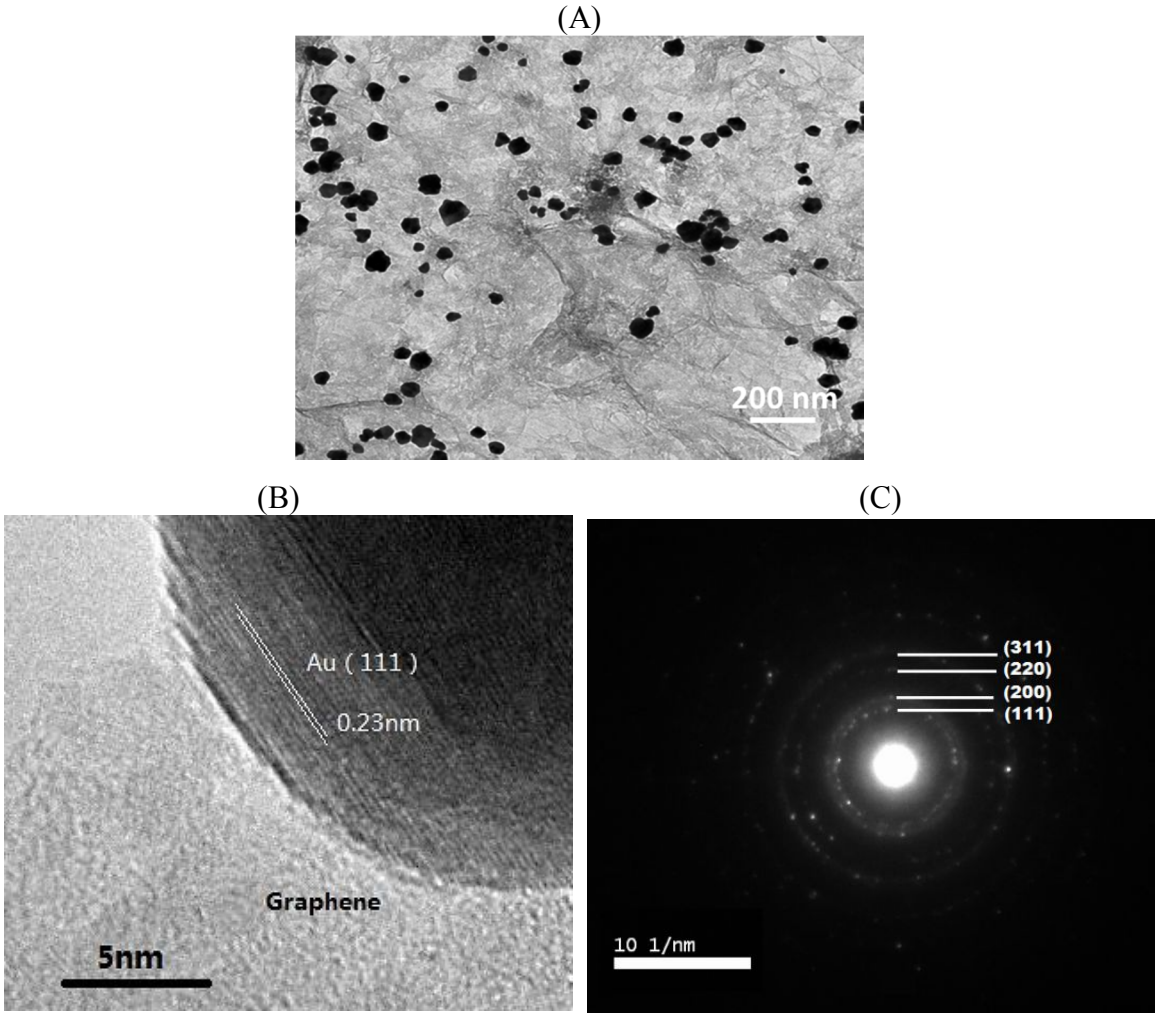

Figure 4.5: (A) TEM image of rGO/Au NPs/Tyr nanohybrids prepared by mixing rGO/Tyr with 2 mM $HAuCl_4$ for 3 h; (B) high resolution TEM of a single Au nanoparticle and (C) selected-area electron diffraction (SAED) of Au NPs.

© 2016 Tous droits réservés.

lilliad.univ-lille.fr

Figure 4.6 displays the XRD patterns of the rGO/AuNPs/Tyr nanocomposites under different synthesis conditions. It can be seen that peaks at 2θ values of ~ 38.0°, 44.2°, 64.6°, 77.6°, and 81.8° assigned to the (111), (200), (220), (311) and (222) crystallographic planes of cubic Au NPs, respectively (JCPDS card N° 004-0784) exist in all the XRD patterns. The diffractogram also indicates the presence of a broad peak at a 2θ value of ~ 22.9° due to (002) plane of rGO. The results confirm Au NPs formation and GO reduction to rGO [81].

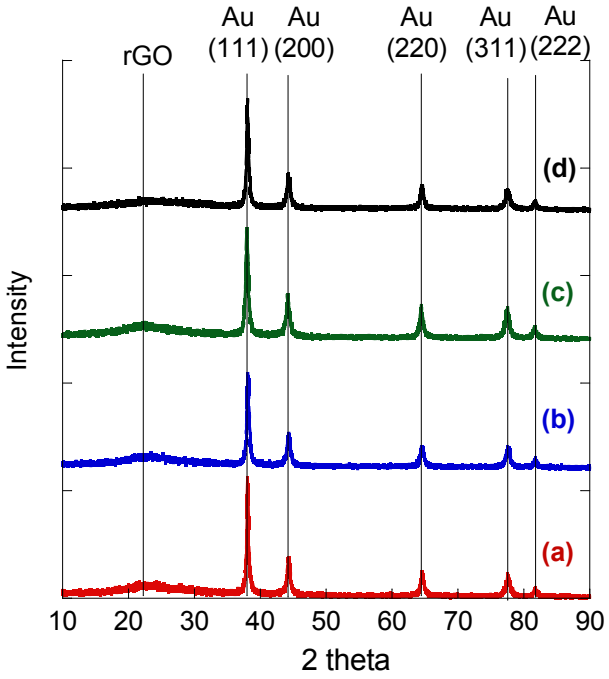

Figure 4.6: XRD patterns of rGO/Au NPs/Tyr composites prepared by mixing rGO/Tyr with (a) 2 mM $HAuCl_4$ for 1 h, (b) 2 mM $HAuCl_4$ for 3 h, (c) 2 mM $HAuCl_4$ for 6 h and (d) 4 mM $HAuCl_4$ for 3 h, respectively under stirring at 100°C.

The optical properties and chemical composition of the as-prepared hybrid nanomaterial were further characterized using UV-vis, FTIR, Raman and XPS spectroscopies. **Figure 4.7A(a)** displays the UV-vis spectrum of the starting GO. It clearly shows two absorption bands at 228 nm and ~300 nm attributed to π-π* transitions of aromatic C=C bond and n-π* transitions of C=O bonds, respectively. Reduction of GO with tyrosine, in absence of Au ions, at 100 °C for 24 h induced a red-shift of the π-π* transition band from 228 to 270 nm, together with the disappearance of the n-π* transition band at ~300 nm (**Figure 4.7A(b)**). The presence of a small shoulder in the absorption spectrum at ~220 nm is most likely due to the incorporation of the tyrosine moieties in the reduced GO (**Figure 4.7B**) [55]. Furthermore, the intensity of the absorption tail in the region (>400 nm) has significantly increased, as compared to that of GO. The results suggest the restoration of the electronic conjugation in

© 2016 Tous droits réservés.

lilliad.univ-lille.fr

the rGO skeleton upon reaction of GO with tyrosine at 100 °C for 24 h.

The first evidence of Au NPs formation was provided by the evident color change of the solution from black to black purple. The successful loading of Au NPs on the rGO surface was confirmed by the peak at around 563 nm, attributed to the localized surface plasmon resonance (LSPR) band of Au nanostructures of 30-70 nm in size (**Figure 4.7A(c)**) [82,83].

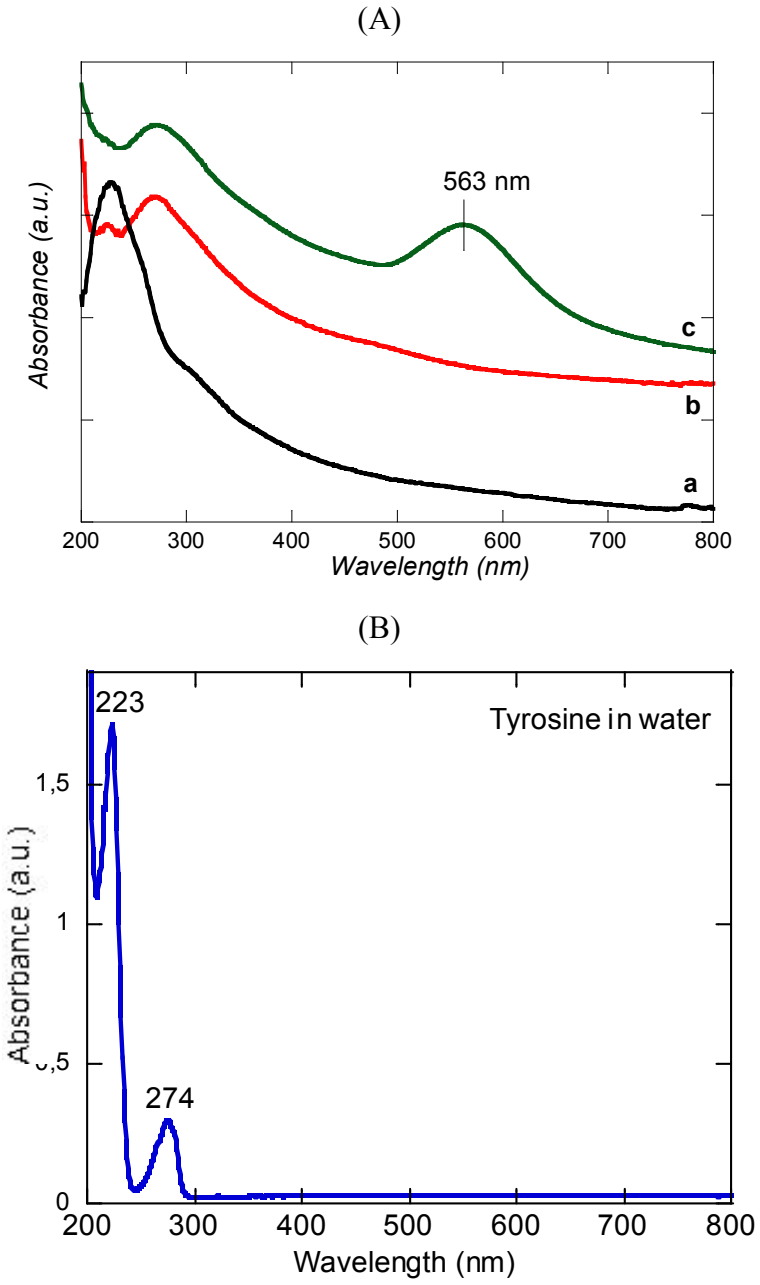

Figure 4.7: UV-Vis absorption spectra of (A) GO (a), rGO/Tyr (b), rGO/Au NPs/Tyr (c) and (B) tyrosine.

FTIR spectroscopy was further employed to evidence the GO reduction in rGO/Au NPs/Tyr hybrid sample. **Figure 4.8a** corresponds to the transmission FTIR spectrum of GO. It

© 2016 Tous droits réservés.

lilliad.univ-lille.fr

comprises a broad and strong band at ~3400 cm^{-1} assigned to the vibration of hydroxyl groups and/or adsorbed water molecules and features due to C=O (-COOH) vibration, OH deformation, and C-O (alkoxy) and C-O (epoxy) stretching modes at 1735, 1420, 1223 and 1081 cm^{-1}, respectively. A band at ~1625 cm^{-1} assigned to C=C stretching modes is also present in the FTIR spectrum of the initial GO. After chemical reduction of GO with tyrosine in absence of Au ions, the intensity of the bands associated with oxygen functionalities decreased significantly. The FTIR spectrum is dominated by a band at ~1570 cm^{-1} due to C=C stretching modes, suggesting that the aromatic network has been restored upon reaction with tyrosine (**Figure 4.8b**). However, the persistence of OH stretching vibration band (~3430 cm^{-1}) as well as other oxygen characteristic groups implies the incomplete removal of oxygen groups after GO reduction. The FTIR spectrum of rGO/Au NPs/Tyr displays similar features as rGO/Tyr, indicating the Au NPs deposition does not induce additional changes to the rGO network (**Figure 4.8c**).

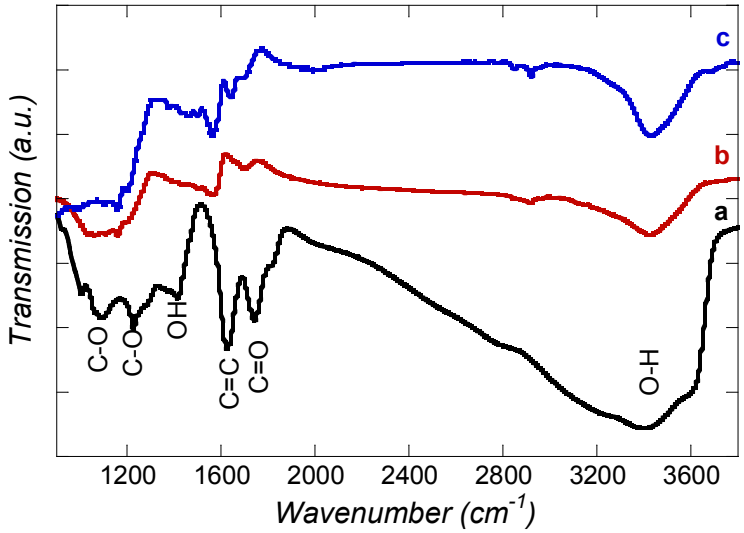

Figure 4.8: Transmission FTIR spectra of (a) GO, (b) rGO/Tyr and (c) rGO/Au NPs/Tyr.

The Raman spectra of GO and rGO/Au NPs/Tyr composites are displayed in **Figure 4.9**. The Raman spectrum recorded on GO displays main features of D band at ~1360 cm^{-1}, G band at ~1592 cm^{-1} and 2D band centered at ~2700 cm^{-1}, with a D/G band intensity of $I_D/I_G \approx$ 0.71. After reaction with tyrosine and $HAuCl_4$, the Raman spectra show typical D, G, 2D bands at ~1331, 1594 and 2645 cm^{-1}, respectively. The D band originates from disorder such as wrinkles, edges, and defects in the graphitic material [84], while the G band is associated with the first-order scattering of E_{2g} phonon mode of the aromatic carbon rings [81,85]. The I_D/I_G ratio exhibited an increase compared to GO (**Table 4.5**), suggesting the partial reduction

© 2016 Tous droits réservés.

lilliad.univ-lille.fr

of GO to rGO during the chemical process [86]. **Table 4.5** compares the I_D/I_G ratio of GO and rGO/Au NPs/Tyr composites under different reaction conditions.

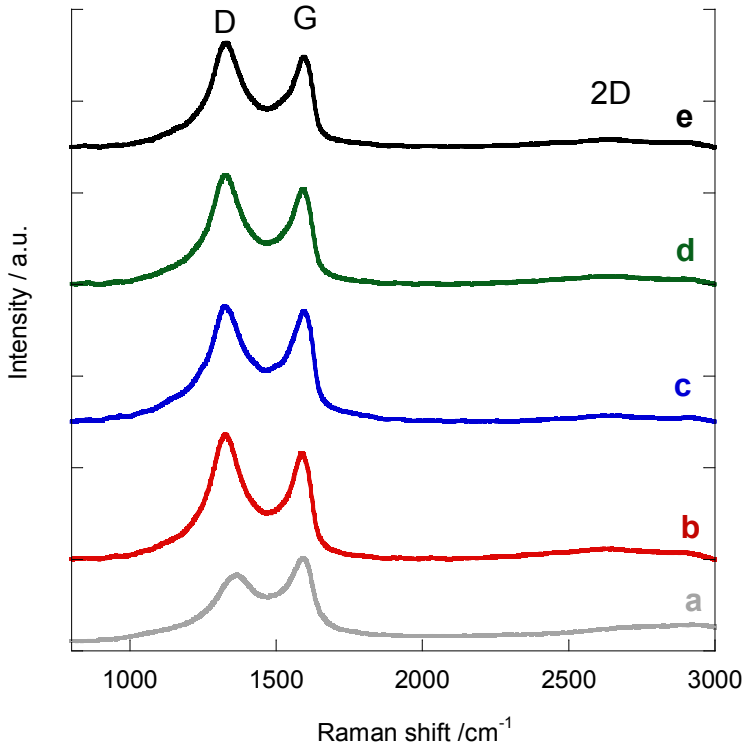

Figure 4.9: Raman spectra of (a) GO and rGO/Au NPs/Tyr composites prepared by mixing rGO/Tyr with (b) 2 mM $HAuCl_4$ for 1 h, (c) 2 mM $HAuCl_4$ for 3 h, (d) 2 mM $HAuCl_4$ for 6 h and (e) 4 mM $HAuCl_4$ for 3 h, respectively under stirring at 100°C.

Table 4.5: I_D/I_G ratio of GO, rGO/Au NPs/Tyr composites prepared by mixing rGO/Tyr with 2 mM $HAuCl_4$ for 1 h, 2 mM $HAuCl_4$ for 3 h, 2 mM $HAuCl_4$ for 6 h and 4 mM $HAuCl_4$ for 3 h, respectively under stirring at 100°C.

Samples	$HAuCl_4$ (mM)	Reaction time (h)	I_D/I_G ratio
GO	-	-	0.71
rGO/Au NPs/Tyr	2	1	1.17
rGO/Au NPs/Tyr	2	3	1.03
rGO/Au NPs/Tyr	2	6	1.15
rGO/Au NPs/Tyr	4	3	1.12

X-ray photoelectron spectroscopy (XPS) analysis results also confirmed the formation of rGO/Au NPs/Tyr nanocomposite. **Figure 4.10A(a)** depicts the high resolution C_{1s} of the starting GO. It can be deconvoluted into four components with binding energies at about 283.8, 284.7, 286.7 and 287.9 eV assigned to C=C, C-H/C-C, C-O and C=O species, respectively, with a C/O ratio of 2.03. After reaction of GO with tyrosine at 100 °C for 24 h in absence of $HAuCl_4$, there is a significant increase of the intensity of the band at 283.8 eV

© 2016 Tous droits réservés.

lilliad.univ-lille.fr

compared to that of the initial GO (**Figure 4.10A(b)**), suggesting that the sp^2 network has been restored during the reduction process with tyrosine. The C_{1s} core level XPS spectrum of rGO/Tyr can be deconvoluted into four components with binding energies at about 283.9 eV (sp^2-hybridized carbon), 285.2 eV (C-H/C-C), 287.5 eV (C-O/C-N) and 290.2 eV (COOH). The ratio of C/O was 6.07 (**Figure 4.10A(b)**). The C_{1s} core level spectrum of rGO/Au NPs/Tyr nanohybrid presents similar features as rGO/Tyr with a C/O ratio of 4.56 (**Figure 4.10A(c)**). Incorporation of tyrosine or its derivatives onto the rGO matrix was further confirmed by the presence of nitrogen in the XPS spectrum at ~400 eV (**Figure 4.10B**) with a content of 2.04 at. %. Au NPs formation is evidenced by the presence of the Au_{4f} doublet. The binding energies of $Au_{4f7/2}$ and $Au_{4f5/2}$ electrons are at 81.9 and 85.6 eV, respectively (**Figure 4.10B**). This is consistent with the reports on gold metal, suggesting that Au NPs deposited on the rGO nanosheets exist in the metallic state [87-89]. The overall Au content was 8.17 at. %, which is higher than the result determined from EDX, indicating an important loading of Au NPs onto the rGO/Tyr structures.

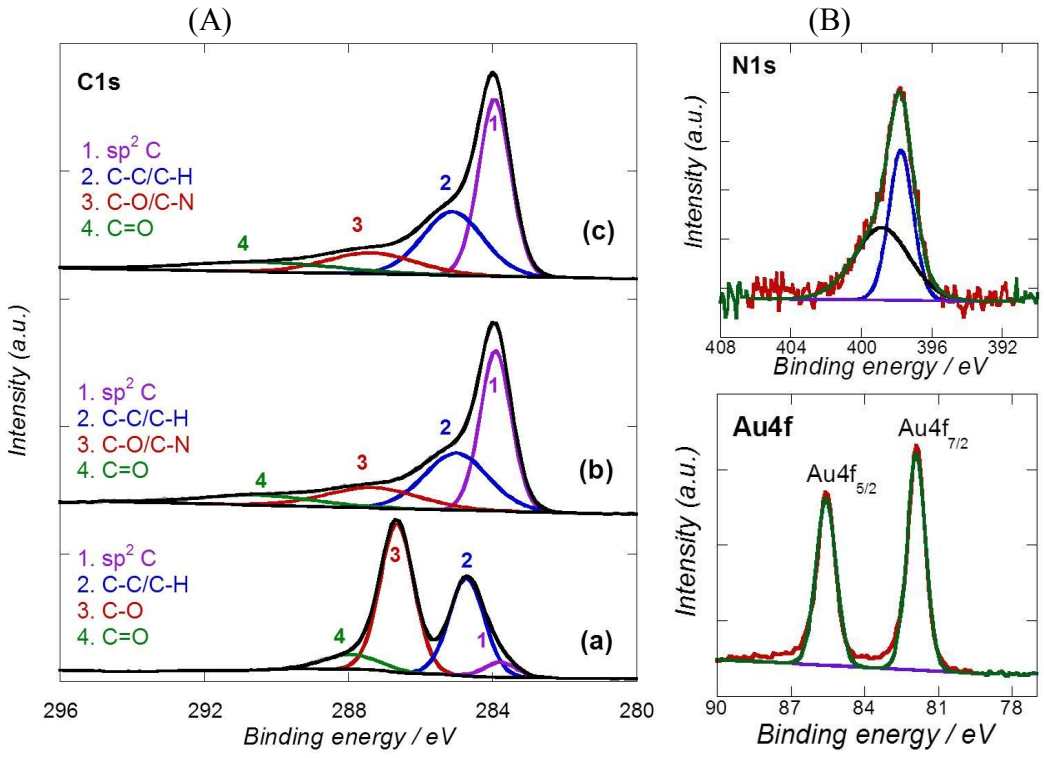

Figure 4.10: High resolution XPS spectra: (A) C_{1s} core level spectra of (a) GO, (b) rGO/Tyr and (c) rGO/Au NPs/Tyr; (B) N_{1s} and Au_{4f} core level spectra of rGO/Au NPs/Tyr composites.

The electrochemical properties of the rGO/Au NPs/Tyr composites were evaluated by cyclic voltammetry using $Fe(CN)_6^{3-/4-}$ (**Figure 4.11A**) and $Ru(NH_3)_6^{3+}$ (**Figure 4.11B**) as redox couples. **Figure 4.11A** displays the CVs of glassy carbon (GC) electrode before and

© 2016 Tous droits réservés.

lilliad.univ-lille.fr

after drop casting a film of rGO/Au NPs/Tyr using $Fe(CN)_6^{3-/4-}$ as redox couple. The GC electrode shows a peak separation (ΔE) of 121 mV, which increased upon coating with rGO/Au NPs/Tyr to 226 mV. Similarly, rGO/Au NPs/Tyr displayed a comparable electrochemical behavior using $Ru(NH_3)_6^{3+}$ as redox couple with a ΔE of 95 mV for bare GCE and 160 mV after coating GCE with rGO/Au NPs/Tyr (**Figure 4.11B**). For both redox couples, the detected currents on rGO/Tyr/Au NPs exceeded that of a bare GCE with a relatively strong capacitive component.

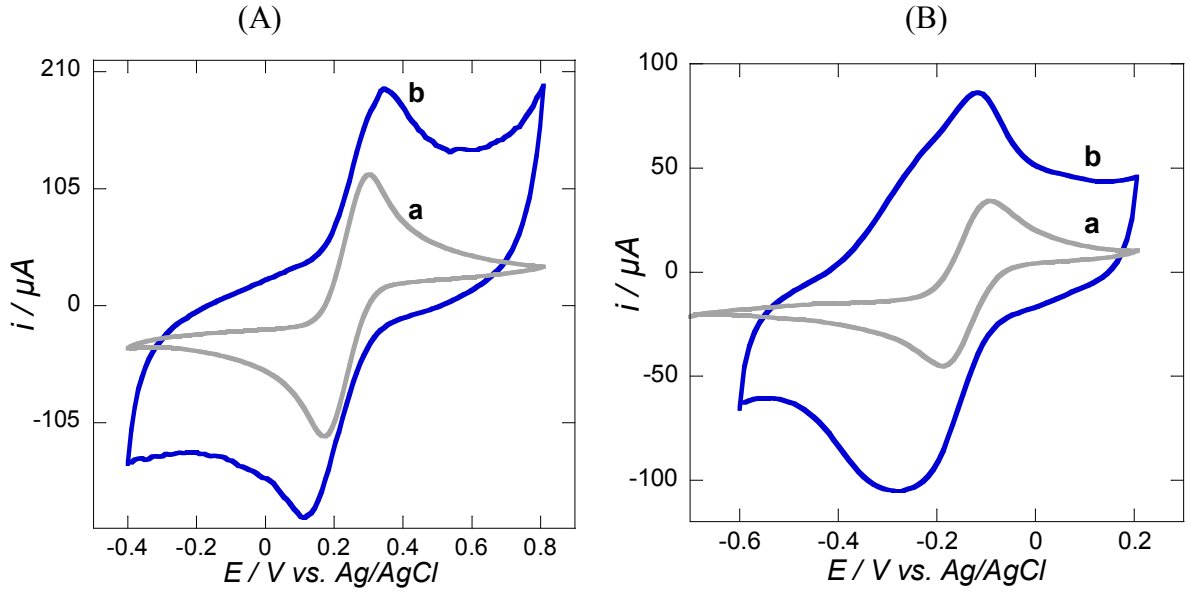

Figure 4.11: Cyclic voltammograms of (A) GC (a) and rGO/Au NPs/Tyr/GC (b) electrodes in 5 mM $Fe(CN)_6^{3-/4-}$/0.1 M KCl, scan rate: 50 mV s^{-1}; (B) GC (a) and rGO/Au NPs/Tyr/GC (b) electrodes in 5 mM $Ru(NH_3)_6^{3+}$/0.1 M KCl, scan rate: 50 mV s^{-1}.

4.3 Amperometric H_2O_2 sensing

The electrocatalytic activity of the rGO/Au NPs/Tyr nanocomposite modified GC electrode towards H_2O_2 reduction was investigated by cyclic voltammetry (CV). **Figure 4.12A(a)** shows a typical CV of the rGO/Au NPs/Tyr electrode in 0.1 M PBS in the absence of H_2O_2 at a scan rate of 50 mV s^{-1}. The modified electrode exhibited no obvious electrochemical response. Upon addition of 10 mM H_2O_2, all the GC electrodes modified with rGO/Au NPs/Tyr nanocomposites under different synthesis conditions showed remarkable increase of the current at around -0.6 V, indicating the good electrocatalytic activity of rGO/Au NPs/Tyr nanocomposites toward H_2O_2 reduction (**Figure 4.12A(b), (c), (d), (e)**). Amongst, the electrode modified with rGO/Au NPs/Tyr composite prepared by mixing

© 2016 Tous droits réservés.

lilliad.univ-lille.fr

rGO/Tyr with 2 mM $HAuCl_4$ stirred for 3 h exhibited the highest change in current, reflecting the best electrocatalytic ability towards H_2O_2 reduction under the same conditions. In a control experiment, the electrocatalytic activity of the GC electrode without modification towards H_2O_2 reduction was performed. In **Figure 4.12B**, it can be seen that naked GC electrode does not show any obvious response to H_2O_2.

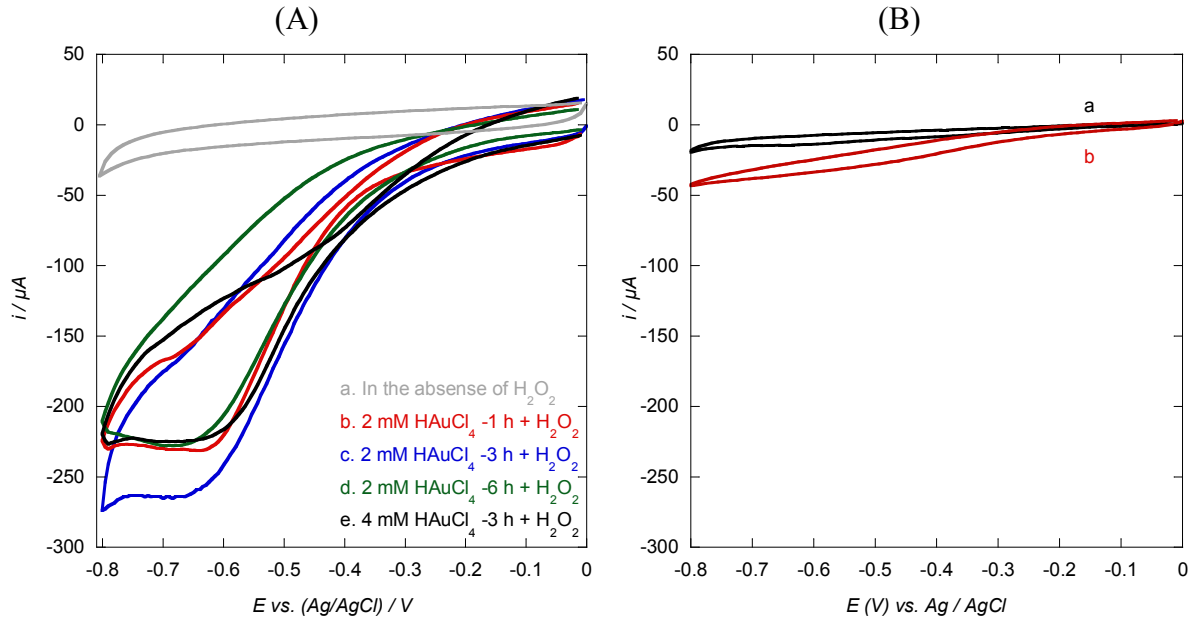

Figure 4.12: (A) Cyclic voltammograms of (a) rGO/Au NPs/Tyr/GC in the absence of H_2O_2 and electrodes modified with rGO/Au NPs/Tyr composites prepared by mixing rGO/Tyr with (b) 2 mM $HAuCl_4$ for 1 h, (c) 2 mM $HAuCl_4$ for 3 h, (d) 2 mM $HAuCl_4$ for 6 h, (e) 4 mM $HAuCl_4$ for 3 h in the presence of 10 mM H_2O_2 in N_2-saturated 0.1 M PBS solution (pH 7.4), scan rate: 50 mV s^{-1}; (B) Cyclic voltammograms of GC electrode in the absence (a) and presence (b) of 10 mM H_2O_2 in N_2-saturated 0.1 M PBS solution (pH 7.4), scan rate: 50 mV s^{-1}.

The electrocatalytic response of rGO/Au NPs/Tyr/GC electrode to H_2O_2 was further investigated by amperometric current-time response upon successive additions of different concentrations of H_2O_2. rGO/Au NPs/Tyr composites prepared by mixing rGO/Tyr with 2 mM $HAuCl_4$ and stirred for 3 h were chosen for the amperometric curve measurement by chronometry. **Figure 4.13A** displays the amperometric response of the modified electrode at an applied potential of -0.6 V *vs.* Ag/AgCl. The reduction current increased gradually upon injection of increasing concentrations of H_2O_2 into the PBS solution and reached the maximum steady state current within 15 s. **Figure 4.13B** shows the corresponding calibration curve of the current response versus H_2O_2 concentration. A linear current-response relationship was identified as a function of H_2O_2 from 0.02 to 25 mM with I (μA) = -2.24-13.01×[H_2O_2] (R=0.988) with an estimated sensitivity of 46.46 μM mM^{-1} cm^{-2}. A

© 2016 Tous droits réservés.

lilliad.univ-lille.fr

detection limit of ≈20 µM at a signal-to-noise ratio of 3 was achieved using rGO/Au NPs/Tyr/GC sensor. The detection limit determined for the sensor is in the same order or slightly higher than 0.03 to 13 µM reported in the literature for Au NPs/rGO electrodes prepared using various approaches (**Table 4.2**) [35,37,39,43-45,49]. However, the proposed strategy for the preparation of metal nanoparticles/rGO is a one-pot, straightforward, and environmentally friendly approach that can be easily used for the integration of other nanoparticles on the same matrix and thus opens up new routes in the design of more sensitive sensors.

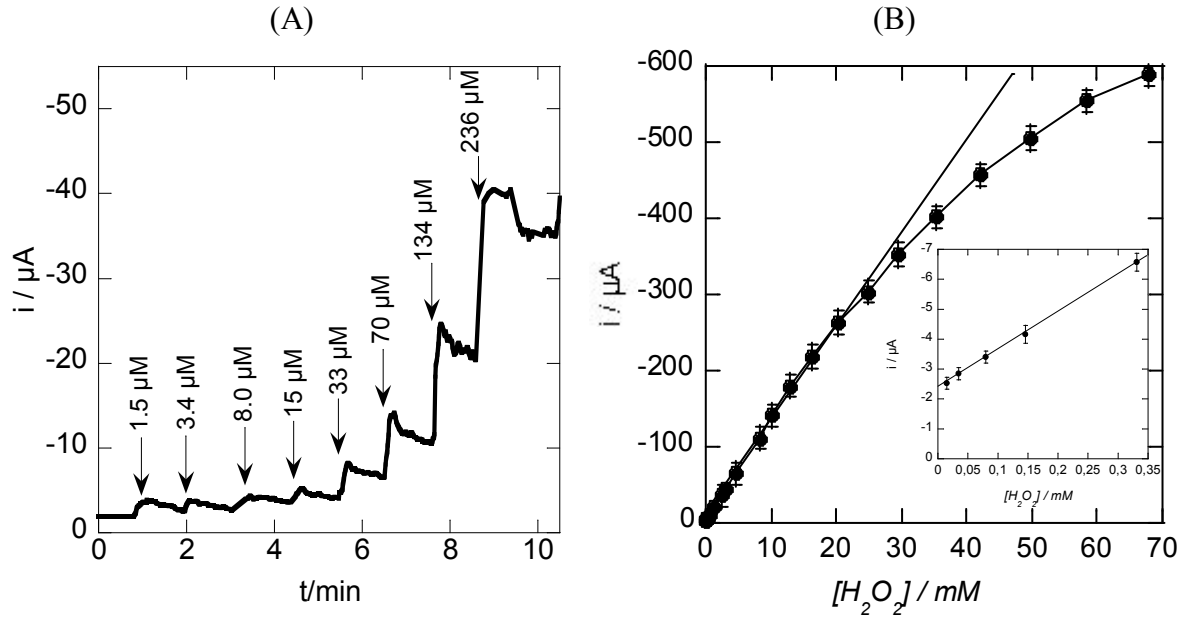

Figure 4.13: (A) Amperometric response curve of rGO/Au NPs/Tyr/GC polarized at -0.6 V *vs.* Ag/AgCl with subsequent addition of H_2O_2; (B) the corresponding calibration curve, supporting electrolyte: N_2-saturated 0.1 M PBS solution (pH 7.4).

Table 4.6: Comparison of analytical performance of other rGO/Au NPs-based non-enzymatic sensors for H_2O_2 detection.

Material	LOD (µM)	Linear range (mM)	Ref.
Au NPs/rGO paper	2	0.005-8.6	[37]
Au NPs/rGO	6	0.020-0.280	[35]
rGO/Nafion/AzI/Au NPs	10	0.03-5	[39]
Au-MWCNTs-sG@GCE	13	1-62	[43]
Au NPs/rGO	1.5	0.1-9	[44]
Au NPs-Gr	0.03	0.0001-0.07	[45]
AuNPS/Gr-CS	1.6	0.005-35	[49]
AuNPs/rGO	**20**	**0.2-25**	**Our work**

© 2016 Tous droits réservés.

lilliad.univ-lille.fr

To assess the selectivity of the GC electrode modified with rGO/Au NPs/Tyr nanocomposite, we have investigated its amperometric response in the presence of some possible interferents. **Figure 4.14** compares the amperometric response of the rGO/Au NPs/Tyr/GC electrode upon successive additions of H_2O_2 (2 mM), uric acid (UA, 0.1 mM), ascorbic acid (AA, 0.1 mM), dopamine (DA, 0.1 mM), glucose (5 mM), and H_2O_2 (2 mM) in N_2-saturated PBS at an applied potential of -0.6 V. No obvious current increase was detected upon addition of UA, AA, DA and glucose, while a significant increase of the current was observed for H_2O_2, suggesting that these species do not cause any interference for the detection of H_2O_2 under our experimental conditions. The results indicate the rGO/Au NPs/Tyr modified GC electrode has a good selectivity toward H_2O_2 detection.

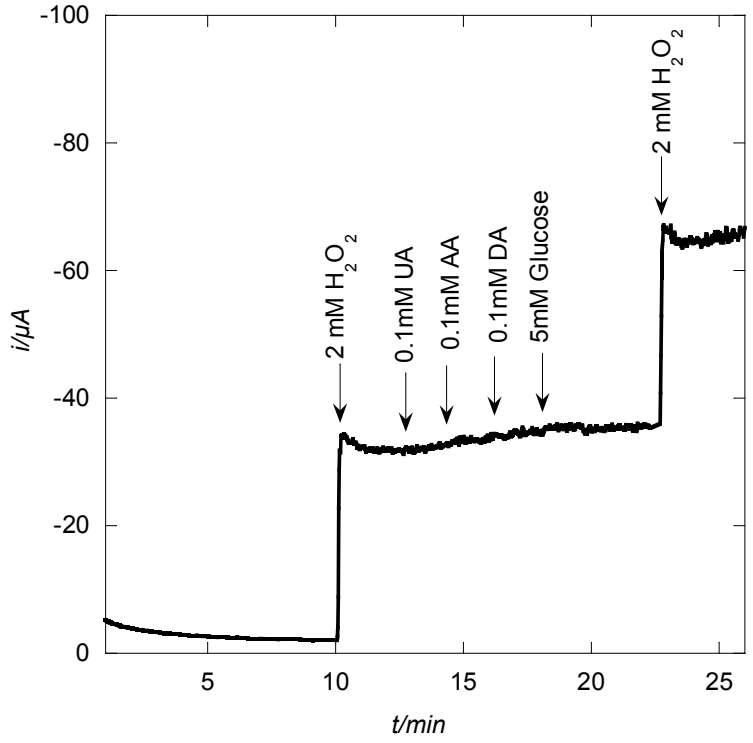

Figure 4.14: The amperometric response of the rGO/Au NPs/Tyr/GC electrode exposed to H_2O_2 (2 mM), ascorbic acid (AA), dopamine (DA), uric acid (UA) (0.1 mM), glucose (5 mM), and H_2O_2 (2 mM), supporting electrolyte: N_2-saturated 0.1 M PBS solution (pH 7.4), potential: -0.6V.

The reproducibility of the rGO/Au NPs/Tyr modified GC electrode was investigated by measuring the current signal for 2 mM H_2O_2 in PBS at 4 modified electrodes prepared under the same experimental conditions. A relative standard deviation (RSD) of 4.46% was determined, indicating a good reproducibility of the fabrication method. The long-term stability of the electrode was examined after storage in a refrigerator at 4°C for 1 week. The

© 2016 Tous droits réservés.

lilliad.univ-lille.fr

sensor retained about 95.6% of its initial current response to 2 mM H_2O_2 in PBS at -0.6 V. The results demonstrate that the sensor exhibits a good stability.

4.4 Conclusion

In conclusion, a green method for the synthesis of rGO/Au NPs/Tyr hybrids in aqueous solution that exploits the ability of tyrosine to operate as an effective dual reducing agent for both GO and gold salts is reported. The morphological and structural characterization of the prepared nanocomposite revealed the formation of Au NPs uniformly distributed on the rGO sheets. Electrochemical measurements showed that rGO/Au NPs/Tyr modified GC electrode shows enhanced current with increased capacitive component. The electrocatalytic activity of the sensor was investigated for non-enzymatic H_2O_2 reduction in PBS (pH 7.4). The electrochemical results showed that the sensor had a good sensitivity of 46.46 $\mu A\ mM^{-1}\ cm^{-2}$ with a detection limit of ≈20 μM over a wide linear range. The sensor exhibited good selectivity for H_2O_2 detection in the presence of potential interfering species such as uric acid, ascorbic acid, dopamine and glucose. In addition, the good stability and reproducibility of the rGO/Au NPs/Tyr modified GC electrode together with the ease of its fabrication make this technique very attractive for the preparation of a sensing platform of different electrochemical species.

4.5 References

[1] Doria, G; Conde, J; Veigas, B; Giestas, L; Almeida, C; Assunção, M; Rosa, J; Baptista, P V. Noble metal nanoparticles for biosensing applications. *Sensors* **2012**, *12*, 1657-1687.

[2] Ruiyi, L; Juanjuan, Z; Zhouping, W; Zaijun, L; Junkang, L; Zhiguo, G; Guangli, W. Novel graphene-gold nanohybrid with excellent electrocatalytic performance for the electrochemical detection of glucose. *Sensors and Actuators B: Chemical* **2015**, *208*, 421-428.

[3] Cittadini, M; Bersani, M; Perrozzi, F; Ottaviano, L; Wlodarski, W; Martucci, A. Graphene oxide coupled with gold nanoparticles for localized surface plasmon resonance based gas sensor. *Carbon* **2014**, *69*, 452-459.

[4] Shi, Y; Dai, H; Sun, Y; Hu, J; Ni, P; Li, Z. Fluorescent sensing of cocaine based on a structure switching aptamer, gold nanoparticles and graphene oxide. *Analyst* **2013**, *138*, 7152-7156.

[5] Thanh, T D; Balamurugan, J; Lee, S H; Kim, N H; Lee, J H. Effective seed-assisted synthesis of gold nanoparticles anchored nitrogen-doped graphene for electrochemical detection of glucose and dopamine. *Biosensors and Bioelectronics* **2016**, *81*, 259-267.

[6] Liu, S; Yan, J; He, G; Zhong, D; Chen, J; Shi, L; Zhou, X; Jiang, H. Layer-by-layer

© 2016 Tous droits réservés.

lilliad.univ-lille.fr

assembled multilayer films of reduced graphene oxide/gold nanoparticles for the electrochemical detection of dopamine. *Journal of Electroanalytical Chemistry* **2012**, *672*, 40-44.

[7] Tian, X; Cheng, C; Yuan, H; Du, J; Xiao, D; Xie, S; Choi, M M F. Simultaneous determination of l-ascorbic acid, dopamine and uric acid with gold nanoparticles–β-cyclodextrin–graphene-modified electrode by square wave voltammetry. *Talanta* **2012**, *93*, 79-85.

[8] Maji, S K; Sreejith, S; Mandal, A K; Ma, X; Zhao, Y. Immobilizing gold nanoparticles in mesoporous silica covered reduced graphene oxide: a hybrid material for cancer cell detection through hydrogen peroxide sensing. *ACS Applied Materials & Interfaces* **2014**, *6*, 13648-13656.

[9] Xue, K; Zhou, S; Shi, H; Feng, X; Xin, H; Song, W. A novel amperometric glucose biosensor based on ternary gold nanoparticles/polypyrrole/reduced graphene oxide nanocomposite. *Sensors and Actuators B: Chemical* **2014**, *203*, 412-416.

[10] Ismail, N S; Le, Q H; Yoshikawa, H; Saito, M; Tamiya, E. Development of non-enzymatic electrochemical glucose sensor based on graphene oxide nanoribbon–gold nanoparticle hybrid. *Electrochimica Acta* **2014**, *146*, 98-105.

[11] Yang, F; Wang, P; Wang, R; Zhou, Y; Su, X; He, Y; Shi, L; Yao, D. Label free electrochemical aptasensor for ultrasensitive detection of ractopamine. *Biosensors and Bioelectronics* **2016**, *77*, 347-352.

[12] Niu, X; Yang, W; Wang, G; Ren, J; Guo, H; Gao, J. A novel electrochemical sensor of bisphenol A based on stacked graphene nanofibers/gold nanoparticles composite modified glassy carbon electrode. *Electrochimica Acta* **2013**, *98*, 167-175.

[13] Parlak, O; Tiwari, A; Turner, A P F; Tiwari, A. Template-directed hierarchical self-assembly of graphene based hybrid structure for electrochemical biosensing. *Biosensors and Bioelectronics* **2013**, *49*, 53-62.

[14] Wang, Y; Zhang, S; Du, D; Shao, Y; Li, Z; Wang, J; Engelhard, M H; Li, J; Lin, Y. Self assembly of acetylcholinesterase on a gold nanoparticles–graphene nanosheet hybrid for organophosphate pesticide detection using polyelectrolyte as a linker. *Journal of Materials Chemistry* **2011**, *21*, 5319-5325.

[15] Dharuman, V; Hahn, J H; Jayakumar, K; Teng, W. Electrochemically reduced graphene–gold nano particle composite on indium tin oxide for label free immuno sensing of estradiol. *Electrochimica Acta* **2013**, *114*, 590-597.

[16] Ma, X; Chen, M. Electrochemical sensor based on graphene doped gold nanoparticles modified electrode for detection of diethylstilboestrol. *Sensors and Actuators B: Chemical* **2015**, *215*, 445-450.

[17] Wang, X; You, Z; Cheng, Y; Sha, H; Li, G; Zhu, H; Sun, W. Application of nanosized gold and graphene modified carbon ionic liquid electrode for the sensitive electrochemical determination of folic acid. *Journal of Molecular Liquids* **2015**, *204*, 112-117.

[18] Li, J; Feng, H; Li, J; Feng, Y; Zhang, Y; Jiang, J; Qian, D. Fabrication of gold nanoparticles-decorated reduced graphene oxide as a high performance electrochemical sensing platform for the detection of toxicant Sudan I. *Electrochimica Acta* **2015**, *167*, 226-236.

[19] Istrate, O M; Rotariu, L; Marinescu, V E; Bala, C. NADH sensing platform based on electrochemically generated reduced graphene oxide–gold nanoparticles composite stabilized with poly (allylamine hydrochloride). *Sensors and Actuators B: Chemical* **2016**, *223*, 697-704.

[20] Govindhan, M; Amiri, M; Chen, A. Au nanoparticle/graphene nanocomposite as a platform for the sensitive detection of NADH in human urine. *Biosensors and Bioelectronics* **2015**, *66*, 474-480.

© 2016 Tous droits réservés.

lilliad.univ-lille.fr

[21] Ting, S L; Guo, C X; Leong, K C; Kim, D H; Li, C M; Chen, P. Gold nanoparticles decorated reduced graphene oxide for detecting the presence and cellular release of nitric oxide. *Electrochimica Acta* **2013**, *111*, 441-446.

[22] Yu, Y; Cao, Q; Zhou, M; Cui, H. A novel homogeneous label-free aptasensor for 2, 4, 6-trinitrotoluene detection based on an assembly strategy of electrochemiluminescent graphene oxide with gold nanoparticles and aptamer. *Biosensors and Bioelectronics* **2013**, *43*, 137-142.

[23] Zhou, N; Li, J; Chen, H; Liao, C; Chen, L. A functional graphene oxide-ionic liquid composites–gold nanoparticle sensing platform for ultrasensitive electrochemical detection of Hg^{2+}. *Analyst* **2013**, *138*, 1091-1097.

[24] Wang, S; Wang, Y; Zhou, L; Li, J; Wang, S; Liu, H. Fabrication of an effective electrochemical platform based on graphene and AuNPs for high sensitive detection of trace Cu^{2+}. *Electrochimica Acta* **2014**, *132*, 7-14.

[25] Li, T; Liu, Z; Wang, L; Guo, Y. Gold nanoparticles/Orange II functionalized graphene nanohybrid based electrochemical aptasensor for label-free determination of insulin. *RSC Advances* **2016**, *6*, 30732-30738.

[26] Afsharan, H; Khalilzadeh, B; Tajalli, H; Mollabashi, M; Navaeipour, F; Rashidi, M-R. A sandwich type immunosensor for ultrasensitive electrochemical quantification of p53 protein based on gold nanoparticles/graphene oxide. *Electrochimica Acta* **2016**, *188*, 153-164.

[27] Chen, M; Hou, C; Huo, D; Bao, J; Fa, H; Shen, C. An electrochemical DNA biosensor based on nitrogen-doped graphene/Au nanoparticles for human multidrug resistance gene detection. *Biosensors and Bioelectronics* **2016**, *85*, 684-691.

[28] Peng, H P; Hu, Y; Liu, P; Deng, Y N; Wang, P; Chen, W; Liu, A L; Chen, Y Z; Lin, X H. Label-free electrochemical DNA biosensor for rapid detection of mutidrug resistance gene based on Au nanoparticles/toluidine blue–graphene oxide nanocomposites. *Sensors and Actuators B: Chemical* **2015**, *207*, 269-276.

[29] Xue, Q; Liu, Z; Guo, Y; Guo, S. Cyclodextrin functionalized graphene–gold nanoparticle hybrids with strong supramolecular capability for electrochemical thrombin aptasensor. *Biosensors and Bioelectronics* **2015**, *68*, 429-436.

[30] Stone, J R. An assessment of proposed mechanisms for sensing hydrogen peroxide in mammalian systems. *Archives of Biochemistry and Biophysics* **2004**, *422*, 119-124.

[31] Wang, J. Electrochemical glucose biosensors. *Chemical Reviews* **2008**, *108*, 814-825.

[32] Fang, Y; Guo, S; Zhu, C; Zhai, Y; Wang, E. Self-assembly of cationic polyelectrolyte-functionalized graphene nanosheets and gold nanoparticles: a two-dimensional heterostructure for hydrogen peroxide sensing. *Langmuir* **2010**, *26*, 11277-11282.

[33] Li, S J; Shi, Y F; Liu, L; Song, L X; Pang, H; Du, J M. Electrostatic self-assembly for preparation of sulfonated graphene/gold nanoparticle hybrids and their application for hydrogen peroxide sensing. *Electrochimica Acta* **2012**, *85*, 628-635.

[34] Xi, Q; Chen, X; Evans, D G; Yang, W. Gold nanoparticle-embedded porous graphene thin films fabricated via layer-by-layer self-assembly and subsequent thermal annealing for electrochemical sensing. *Langmuir* **2012**, *28*, 9885-9892.

[35] Hu, J; Li, F; Wang, K; Han, D; Zhang, Q; Yuan, J; Niu, L. One-step synthesis of graphene–AuNPs by HMTA and the electrocatalytical application for O_2 and H_2O_2. *Talanta* **2012**, *93*, 345-349.

[36] Zhang, P; Zhang, X; Zhang, S; Lu, X; Li, Q; Su, Z; Wei, G. One-pot green synthesis, characterizations, and biosensor application of self-assembled reduced graphene oxide–gold nanoparticle hybrid membranes. *Journal of Materials Chemistry B* **2013**, *1*, 6525-6531.

[37] Xiao, F; Song, J; Gao, H; Zan, X; Xu, R; Duan, H. Coating graphene paper with

© 2016 Tous droits réservés. lilliad.univ-lille.fr

2D-assembly of electrocatalytic nanoparticles: a modular approach toward high-performance flexible electrodes. *ACS Nano* **2011**, *6*, 100-110.

[38] Liu, R; Li, S; Yu, X; Zhang, G; Zhang, S; Yao, J; Keita, B; Nadjo, L; Zhi, L. Facile synthesis of Au nanoparticle/polyoxometalate/graphene tricomponent nanohybrids: an enzyme-free electrochemical biosensor for hydrogen peroxide. *Small* **2012**, *8*, 1398-1406.

[39] Zhang, Y; Liu, Y; He, J; Pang, P; Gao, Y; Hu, Q. Electrochemical behavior of graphene/Nafion/Azure I/Au nanoparticles composites modified glass carbon electrode and its application as nonenzymatic hydrogen peroxide sensor. *Electrochimica Acta* **2013**, *90*, 550-555.

[40] Wang, L; Deng, M; Ding, G; Chen, S; Xu, F. Manganese dioxide based ternary nanocomposite for catalytic reduction and nonenzymatic sensing of hydrogen peroxide. *Electrochimica Acta* **2013**, *114*, 416-423.

[41] Lu, D; Zhang, Y; Lin, S; Wang, L; Wang, C. Synthesis of PtAu bimetallic nanoparticles on graphene–carbon nanotube hybrid nanomaterials for nonenzymatic hydrogen peroxide sensor. *Talanta* **2013**, *112*, 111-116.

[42] Babu, K J; Nahm, K S; Hwang, Y J. A facile one-pot green synthesis of reduced graphene oxide and its composites for non-enzymatic hydrogen peroxide sensor applications. *RSC Advances* **2014**, *4*, 7944-7951.

[43] Nayak, P; Santhosh, P N; Ramaprabhu, S. Synthesis of Au-MWCNT–Graphene hybrid composite for the rapid detection of H_2O_2 and glucose. *RSC Advances* **2014**, *4*, 41670-41677.

[44] Qin, X; Li, Q; Asiri, A M; Al-Youbi, A O; Sun, X. One-pot synthesis of Au nanoparticles/reduced graphene oxide nanocomposites and their application for electrochemical H_2O_2, glucose, and hydrazine sensing. *Gold Bulletin* **2014**, *47*, 3-8.

[45] Liu, H; Su, X; Duan, C; Dong, X; Zhou, S; Zhu, Z. Microwave-assisted hydrothermal synthesis of Au NPs–graphene composites for H_2O_2 detection. *Journal of Electroanalytical Chemistry* **2014**, *731*, 36-42.

[46] Ju, J; Chen, W. In situ growth of surfactant-free gold nanoparticles on nitrogen-doped graphene quantum dots for electrochemical detection of hydrogen peroxide in biological environments. *Analytical Chemistry* **2015**, *87*, 1903-1910.

[47] Dhara, K; Ramachandran, T; Nair, B G; Babu, T G S. Au nanoparticles decorated reduced graphene oxide for the fabrication of disposable nonenzymatic hydrogen peroxide sensor. *Journal of Electroanalytical Chemistry* **2016**, *764*, 64-70.

[48] Song, H; Ni, Y; Kokot, S. A novel electrochemical biosensor based on the hemin-graphene nano-sheets and gold nano-particles hybrid film for the analysis of hydrogen peroxide. *Analytica Chimica Acta* **2013**, *788*, 24-31.

[49] Jia, N; Huang, B; Chen, L; Tan, L; Yao, S. A simple non-enzymatic hydrogen peroxide sensor using gold nanoparticles-graphene-chitosan modified electrode. *Sensors and Actuators B: Chemical* **2014**, *195*, 165-170.

[50] Xie, L; Xu, Y; Cao, X. Hydrogen peroxide biosensor based on hemoglobin immobilized at graphene, flower-like zinc oxide, and gold nanoparticles nanocomposite modified glassy carbon electrode. *Colloids and Surfaces B: Biointerfaces* **2013**, *107*, 245-250.

[51] Gu, C J; Kong, F Y; Chen, Z D; Fan, D H; Fang, H L; Wang, W. Reduced graphene oxide-Hemin-Au nanohybrids: Facile one-pot synthesis and enhanced electrocatalytic activity towards the reduction of hydrogen peroxide. *Biosensors and Bioelectronics* **2016**, *78*, 300-307.

[52] Yu, G; Wu, W; Pan, X; Zhao, Q; Wei, X; Lu, Q. High sensitive and selective sensing of hydrogen peroxide released from pheochromocytoma cells based on Pt-Au bimetallic nanoparticles electrodeposited on reduced graphene sheets. *Sensors* **2015**, *15*, 2709-2722.

© 2016 Tous droits réservés.

lilliad.univ-lille.fr

[53] Chang, H; Wang, X; Shiu, K-K; Zhu, Y; Wang, J; Li, Q; Chen, B; Jiang, H. Layer-by-layer assembly of graphene, Au and poly (toluidine blue O) films sensor for evaluation of oxidative stress of tumor cells elicited by hydrogen peroxide. *Biosensors and Bioelectronics* **2013**, *41*, 789-794.

[54] Yang, X; Ouyang, Y; Wu, F; Hu, Y; Ji, Y; Wu, Z. Size controllable preparation of gold nanoparticles loading on graphene sheets@cerium oxide nanocomposites modified gold electrode for nonenzymatic hydrogen peroxide detection. *Sensors and Actuators B: Chemical* **2017**, *238*, 40-47.

[55] Wang, Q; Li, M; Szunerits, S; Boukherroub, R. Environmentally friendly feduction of graphene oxide using tyrosine for nonenzymatic amperometric H_2O_2 detection. *Electroanalysis* **2014**, *26*, 156-163.

[56] Khalil, I; Julkapli, N M; Yehye, W A; Basirun, W J; Bhargava, S K. Graphene–gold nanoparticles hybrid-synthesis, functionalization, and application in a electrochemical and surface-enhanced Raman scattering biosensor. *Materials* **2016**, *9*, 406.

[57] Turcheniuk, K; Boukherroub, R; Szunerits, S. Gold–graphene nanocomposites for sensing and biomedical applications. *Journal of Materials Chemistry B* **2015**, *3*, 4301-4324.

[58] Turcheniuk, K; Hage, C H; Spadavecchia, J; Serrano, A Y; Larroulet, I; Pesquera, A; Zurutuza, A; Pisfil, M G; Héliot, L; Boukaert, J. Plasmonic photothermal destruction of uropathogenic E. coli with reduced graphene oxide and core/shell nanocomposites of gold nanorods/reduced graphene oxide. *Journal of Materials Chemistry B* **2015**, *3*, 375-386.

[59] Sahu, S R; Devi, M M; Mukherjee, P; Sen, P; Biswas, K. Optical property characterization of novel graphene-X (X= Ag, Au and Cu) nanoparticle hybrids. *Journal of Nanomaterials* **2013**, *2013*, 6.

[60] Zhang, P; Huang, Y; Lu, X; Zhang, S; Li, J; Wei, G; Su, Z. One-step synthesis of large-scale graphene film doped with gold nanoparticles at liquid–air interface for electrochemistry and Raman detection applications. *Langmuir* **2014**, *30*, 8980-8989.

[61] Zhang, Z; Chen, H; Xing, C; Guo, M; Xu, F; Wang, X; Gruber, H J; Zhang, B; Tang, J. Sodium citrate: a universal reducing agent for reduction/decoration of graphene oxide with Au nanoparticles. *Nano Research* **2011**, *4*, 599-611.

[62] Movahed, S K; Fakharian, M; Dabiri, M; Bazgir, A. Gold nanoparticle decorated reduced graphene oxide sheets with high catalytic activity for Ullmann homocoupling. *RSC Advances* **2014**, *4*, 5243-5247.

[63] Muszynski, R; Seger, B; Kamat, P V. Decorating graphene sheets with gold nanoparticles. *The Journal of Physical Chemistry C* **2008**, *112*, 5263-5266.

[64] Huang, X; Li, H; Li, S; Wu, S; Boey, F; Ma, J; Zhang, H. Synthesis of gold square-like plates from ultrathin gold square sheets: the evolution of structure phase and shape. *Angewandte Chemie International Edition* **2011**, *50*, 12245-12248.

[65] Iliut, M; Leordean, C; Canpean, V; Teodorescu, C-M; Astilean, S. A new green, ascorbic acid-assisted method for versatile synthesis of Au–graphene hybrids as efficient surface-enhanced Raman scattering platforms. *Journal of Materials Chemistry C* **2013**, *1*, 4094-4104.

[66] Zhou, L; Gu, H; Wang, C; Zhang, J; Lv, M; He, R. Study on the synthesis and surface enhanced Raman spectroscopy of graphene-based nanocomposites decorated with noble metal nanoparticles. *Colloids and Surfaces A: Physicochemical and Engineering Aspects* **2013**, *430*, 103-109.

[67] Sharma, P; Darabdhara, G; Reddy, T M; Borah, A; Bezboruah, P; Gogoi, P; Hussain, N; Sengupta, P; Das, M R. Synthesis, characterization and catalytic application of Au NPs-reduced graphene oxide composites material: an eco-friendly approach. *Catalysis Communications* **2013**, *40*, 139-144.

© 2016 Tous droits réservés.

lilliad.univ-lille.fr

[68] Fu, W L; Zhen, S J; Huang, C Z. One-pot green synthesis of graphene oxide/gold nanocomposites as SERS substrates for malachite green detection. *Analyst* **2013**, *138*, 3075-3081.

[69] Le, Z; Liu, Z; Qian, Y; Wang, C. A facile and efficient approach to decoration of graphene nanosheets with gold nanoparticles. *Applied Surface Science* **2012**, *258*, 5348-5353.

[70] Yang, K; Zhang, S; Zhang, G; Sun, X; Lee, S T; Liu, Z. Graphene in mice: ultrahigh in vivo tumor uptake and efficient photothermal therapy. *Nano Letters* **2010**, *10*, 3318-3323.

[71] Fu, C; Kuang, Y; Huang, Z; Wang, X; Du, N; Chen, J; Zhou, H. Electrochemical co-reduction synthesis of graphene/Au nanocomposites in ionic liquid and their electrochemical activity. *Chemical Physics Letters* **2010**, *499*, 250-253.

[72] Vinodgopal, K; Neppolian, B; Lightcap, I V; Grieser, F; Ashokkumar, M; Kamat, P V. Sonolytic design of graphene− Au nanocomposites. Simultaneous and sequential reduction of graphene oxide and Au (III). *The Journal of Physical Chemistry Letters* **2010**, *1*, 1987-1993.

[73] Li, X R; Li, X L; Xu, M C; Xu, J J; Chen, H Y. Gold nanodendrities on graphene oxide nanosheets for oxygen reduction reaction. *Journal of Materials Chemistry A* **2014**, *2*, 1697-1703.

[74] Kaminska, I; Das, M R; Coffinier, Y; Niedziolka-Jonsson, J; Sobczak, J; Woisel, P; Lyskawa, J; Opallo, M; Boukherroub, R; Szunerits, S. Reduction and functionalization of graphene oxide sheets using biomimetic dopamine derivatives in one step. *ACS Applied Materials & Interfaces* **2012**, *4*, 1016-1020.

[75] Kaminska, I; Qi, W; Barras, A; Sobczak, J; Niedziolka‐Jonsson, J; Woisel, P; Lyskawa, J; Laure, W; Opallo, M; Li, M. Thiol–yne click reactions on alkynyl-dopamine-modified reduced graphene oxide. *Chemistry–A European Journal* **2013**, *19*, 8673-8678.

[76] Si, S; Bhattacharjee, R R; Banerjee, A; Mandal, T K. A mechanistic and kinetic study of the formation of metal nanoparticles by using synthetic tyrosine-based oligopeptides. *Chemistry–A European Journal* **2006**, *12*, 1256-1265.

[77] Zhou, Y; Chen, W; Itoh, H; Naka, K; Ni, Q; Yamane, H; Chujo, Y. Preparation of a novel core–shell nanostructured gold colloid–silk fibroin bioconjugate by the protein in situ redox technique at room temperature. *Chemical Communications* **2001**, 2518-2519.

[78] Yang, M Q; Pan, X; Zhang, N; Xu, Y J. A facile one-step way to anchor noble metal (Au, Ag, Pd) nanoparticles on a reduced graphene oxide mat with catalytic activity for selective reduction of nitroaromatic compounds. *CrystEngComm* **2013**, *15*, 6819-6828.

[79] Xu, S; Yong, L; Wu, P. One-pot, green, rapid synthesis of flowerlike gold nanoparticles/reduced graphene oxide composite with regenerated silk fibroin as efficient oxygen reduction electrocatalysts. *ACS Applied Materials & Interfaces* **2013**, *5*, 654-662.

[80] Jasuja, K; Berry, V. Implantation and growth of dendritic gold nanostructures on graphene derivatives: electrical property tailoring and Raman enhancement. *ACS Nano* **2009**, *3*, 2358-2366.

[81] Hussain, N; Gogoi, A; Sarma, R K; Sharma, P; Barras, A; Boukherroub, R; Saikia, R; Sengupta, P; Das, M R. Reduced graphene oxide nanosheets decorated with Au nanoparticles as an effective bactericide: investigation of biocompatibility and leakage of sugars and proteins. *ChemPlusChem* **2014**, *79*, 1774-1784.

[82] Toderas, F; Baia, M; Baia, L; Astilean, S. Controlling gold nanoparticle assemblies for efficient surface-enhanced Raman scattering and localized surface plasmon resonance sensors. *Nanotechnology* **2007**, *18*, 255702.

[83] Zhang, B; Cui, Y; Chen, H; Liu, B; Chen, G; Tang, D. A new electrochemical biosensor for determination of hydrogen peroxide in food based on well-dispersive gold

© 2016 Tous droits réservés.

lilliad.univ-lille.fr

nanoparticles on graphene oxide. *Electroanalysis* **2011**, *23*, 1821-1829.

[84] Guo, H L; Wang, X F; Qian, Q Y; Wang, F B; Xia, X H. A green approach to the synthesis of graphene nanosheets. *ACS Nano* **2009**, *3*, 2653-2659.

[85] Stankovich, S; Dikin, D A; Piner, R D; Kohlhaas, K A; Kleinhammes, A; Jia, Y; Wu, Y; Nguyen, S T; Ruoff, R S. Synthesis of graphene-based nanosheets via chemical reduction of exfoliated graphite oxide. *Carbon* **2007**, *45*, 1558-1565.

[86] Tung, V C; Allen, M J; Yang, Y; Kaner, R B. High-throughput solution processing of large-scale graphene. *Nature Nanotechnology* **2009**, *4*, 25-29.

[87] Hashmi, A S K; Hutchings, G J. Gold catalysis. *Angewandte Chemie International Edition* **2006**, *45*, 7896-7936.

[88] Maldotti, A; Molinari, A; Juárez, R; Garcia, H. Photoinduced reactivity of Au–H intermediates in alcohol oxidation by gold nanoparticles supported on ceria. *Chemical Science* **2011**, *2*, 1831-1834.

[89] Kominami, H; Tanaka, A; Hashimoto, K. Gold nanoparticles supported on cerium (IV) oxide powder for mineralization of organic acids in aqueous suspensions under irradiation of visible light of λ= 530nm. *Applied Catalysis A: General* **2011**, *397*, 121-126.

© 2016 Tous droits réservés.

lilliad.univ-lille.fr

Thèse de Qian Wang, Lille 1, 2016

CHAPTER 5

CONCLUSIONS AND PERSPECTIVES

The interest of carbon-based electrodes for electrochemical sensing has been demonstrated in this thesis. After a general introduction on the synthesis of graphene, carbon naotube (CNT) and carbon nanofibers (CNFs), functionalization strategies of carbon-based electrodes used in this thesis were discussed (**Chapter 1**). In **Chapter 2**, the great potential of chemically modified vertically aligned nitrogen-doped carbon nanotubes (VA-NCNT) electrodes for the electrochemical sensing of lysozyme was presented. We took advantage of the fast electron transfer of VA-NCNT and achieved specific lysozyme sensing through covalent integration of a biotinylated lysozyme aptamer on the carbon nanotube structures. The decrease in the differential pulse voltammetry current using $[Fe(CN)_6]^{3-}$ as redox probe was used as indicator for the presence of lysozyme. The described sensor exhibited a detection limit of ≈100 fM without any need of amplification, appropriate for detection of lysozyme levels in serum and urine. The aptasensor also exhibited the ability for reliable analysis of lysozyme quantity in serum samples of inflammatory bowel disease (IBD) infected patients, where the concentration of human lysozyme is up-regulated. The diagnosis of IBD relies currently on clinical findings after radiological, endoscopic and histological examinations. The development of a noninvasive alternative test that is rapid, sensitive, specific and simple is thus a great step further towards preventing patient discomfort, delay in diagnosis, and follow-up of the status of the disease. The required picomolar sensitivity for real time sensing IBD infected patients is easily achieved with our developed sensor interface, making the sensor highly reliable for the analysis of clinical samples.

Non-enzyamic sensing of glucose (**Chapter 3**) and H_2O_2 (**Chapter 4**) were in addition achieved in this work. One of the electrode matrix employed was based on carbon nanofibers (CNFs/$Co(OH)_2$) nanocomposite. The sensing matrix was fabricated by electrophoretic deposition (EPD) of a mixture of $Co(NO_3)_2$ and CNFs in ethanol at +50 V for 2 min onto a gold electrode. Its electrocatalytic properties towards the oxidation of glucose in 0.1 M NaOH

© 2016 Tous droits réservés.

lilliad.univ-lille.fr

were tested and a sensitivity of 68 mA mM^{-1} cm^{-2} was determined. A detection limit of 5 µM with linearity of 10 µM to 0.15 mM was obtained.

Considerable improvements were obtained by coating a gold electrode with rGO/Cu NPs by electrophoretic means from an ethanol solution of GO and $CuSO_4$. This sensor showed a good sensitivity of 447.65 µM mM^{-1} cm^{-2} towards glucose oxidation with a somewhat lower detection limit of 3.4 µM when compared to (CNFs)/$Co(OH)_2$ modified electrode with a linear range from 0.01 to 1.2 mM. Both sensors showed good selectivity towards glucose and were stable over time. The good analytical performance of the nanocomposites allowed for sensing glucose in real human serum samples.

In the case of H_2O_2, the sensor is based on a newly developed electrode matrix, rGO/Au NPs/Tyr hybrid, formed by a one-step procedure from a mixture of GO and Au^{3+} ions in the presence of tyrosine; tyrosine acts as an effective dual reducing agent for both GO and gold salt. The electrocatalytic activity of the sensor for non-enzymatic H_2O_2 reduction was demonstrated. The sensor displayed a good sensitivity of 46.46 µM mM^{-1} cm^{-2} for H_2O_2 reduction with a detection limit of ≈20 µM over a wide linear range. The sensor exhibited in addition a good selectivity for H_2O_2 detection in the presence of potential interfering species such as uric acid, ascorbic acid, dopamine and glucose.

This work opens a plethora of perspectives in the electroanalysis field. The integration of other catalytic particles into carbon-based materials, especially GO, and the use of electrophoretic deposition can widen the scope of such electrodes for other potential electrochemical sensing applications (*e.g.* biomarkers, pesticides, bacteria, *etc.*). The use of the same materials for photocatalytic applications (CO_2 reduction into added value chemicals, photodegradation of organic pollutants…) can be thought after as well. Moreover, the approach used for the diagnostic of people having IBD, which is simply based on the detection of lysozyme levels in serum, can be widened to other diseases. Bacterial infections and in particular wound infections are known to be correlated not only with increase in temperature at the inflammation site, but with an increased secretion of lysozyme. The integration of such sensors in wound healing strips might be a direct means of helping efficient detection of wound infections. In addition, the ease of modification and good electron transfer ability of VA-NCNT electrodes make it a possible support for various biorecognition elements immobilization, thus for further construction of enzyme sensors,

© 2016 Tous droits réservés.

lilliad.univ-lille.fr

immunosensors and other aptasensors.

© 2016 Tous droits réservés.

lilliad.univ-lille.fr

Thèse de Qian Wang, Lille 1, 2016

APPENDIX

EXPERIMENTAL PART

6.1 Chemicals

All chemicals were reagent grade or higher and were used as received unless otherwise specified. 4-Aminobenzoic acid, sodium nitrite ($NaNO_2$), hydrochloric acid (HCl), 1-ethyl-3-(3-dimethylaminopropyl)-carbodiimide (EDC), *N*-hydroxysuccinimide (NHS), 2-(*N*-morpholino)ethanesulfonic acid (MES), phosphate-buffered saline (PBS), tris buffered saline, MES monohydrate, potassium hexacyanoferrate (II) trihydrate ($[K_4Fe(CN)_6]\cdot 3H_2O$), potassium hexacyanoferrate(III) ($[K_3Fe(CN)_6]$), hexaammineruthenium(III) chloride ($[Ru(NH_3)_6Cl_3]$) lysozyme, *Micrococcus lysodeykticus*, bovine serum albumin (BSA), cytochrome c from equine heart (cyt C), casein from bovine milk, sodium dodecyl sulfate (SDS), graphite powder (< 20 micron), potassium permanganate ($KMnO_4$), sulfuric acid (H_2SO_4), phosphoric acid (H_3PO_4), hydrogen peroxide (H_2O_2), copper (II) tartrate hydrate, copper (II) sulphate pentahydrate ($CuSO_4\cdot 5H_2O$), cobalt (II) nitrate hexahydrate ($Co(NO3)_2\cdot 6H_2O$), ethanol, sodium hydroxide (NaOH), D-(+)-glucose, uric acid, L-ascorbic acid, dopamine hydrochloride, D-(-)-fructose, β-lactose, D-(+)-galactose, L-tyrosine, potassium bromide (KBr), gold(III) chloride trihydrate ($HAuCl_4.3H_2O$), dimethylformamide (DMF) and platinum wire were purchased from Sigma-Aldrich.

Neutravidin was purchased from Pierce. The biotinylated aptamer was purchased from Integrated DNA Technologies (Belgium) and had the following sequence: 5'-biotin-TTT TTT TTT TTT TTT TTT TTT ATC AGG GCT AAA GAG TGC AGA GTT ACT TAG-3'. Human serum samples from healthy patients and patients suffering of IBD were kindly provided by Dr. Ionescu Andra (Fundeni Clinical Institute, Department of Gastroenterology and Hepatology, Bucharest, Romania) in accordance with the local ethical committee. Human serum sample for glucose monitoring was provided by Prof. Amar Abderrahmani from Faculty of Medicine, Université du Droit et de la Santé Lille 2.

Au/Ti/glass electrodes were prepared by vacuum deposition of 5 nm of titanium and 48 nm of gold onto cleaned glass slides (76 × 26 × 1 mm^3, n=1.58 at λ=633 nm, CML, France).

© 2016 Tous droits réservés.
lilliad.univ-lille.fr

Thèse de Qian Wang, Lille 1, 2016

Glassy carbon (3 mm in diameter) and Ag/AgCl reference electrodes were obtained from Cambria Scientific. Silicon wafers were purchased from Siltronics.

The water used throughout the experiments was purified with a Milli-Q system from Millipore Co. (resistivity = 18 MΩ.cm).

6.2 Synthesis of carbon materials

6.2.1 Preparation of nitrogen-doped vertically aligned carbon nanotube carpet (VA-NCNT)

The VA-NCNT carpet electrodes were provided by Palaniappan Subramanian (Ariel University, Israel). Typically, CNT synthesis was achieved in a three-zone atmospheric-pressure tube furnace (Carbolite model HZS-E), using a single fused-silica tube with an internal diameter of 22 mm. The two-first zones of the furnace preheated the precursor gases at 770 °C, decomposing the hydrocarbon gases and forming water vapor from O_2 and H_2. The sample was positioned in the last zone of the three-zone furnace (G_3) for the annealing and growth steps at 755 °C. Flows of He (99.9999%), Ar_{O2} (a mixture of 99.9999% argon with 1% oxygen), C_2H_4 (99.999%), and H_2 (99.9999%) were maintained using electronic mass flow controllers (MKS P4B) with digital mass flows control unit (MKS model 247D). All experiments were performed by using the “fast-heat” technique, in which the samples are initially positioned outside the heated zone of the furnace with a fan blowing on the exposed quartz tube to keep the sample at room temperature. Purging of the system was performed by 100 standard cubic centimeters per minute (sccm) and 400 sccm H_2 for 15 minutes while the furnace was ramped to the desired temperature. Once the set temperatures of three-zone furnace were reached, the quartz tube was shifted, positioning the sample in the growth zone (G_3) to start the VA-CNT synthesis which includes three steps. First the stainless steel coin surface was oxidized at 755 °C for 45 min by flowing 1000 sccm Ar_{O2} and 100 sccm Ar. Then the surface was reduced by flowing 400 sccm H_2 and 100 sccm Ar at 755 °C for another 40 min. The third step comprises CNT growth. The flows of Ar, H_2, Ar_{O2} and C_2H_4 were respectively set at 100, 400, 250 and 200 sccm for 15 min. After the growth was completed, the quartz tube was shifted out of the furnace to slowly cool down to room temperature under a flow of helium before the sample was removed from the furnace.

Nitrogen plasma treatment of VA-CNT was performed in a Zepto Low pressure plasma system (Diner electronic Gmbh, Ebenhausen, Germany) equipped with a 40 kHz

© 2016 Tous droits réservés.

lilliad.univ-lille.fr

HF-generator operating between 0 and 100 W. The VA-CNT coated steel coins were introduced into the plasma chamber for 2 min. The chamber pressure and the plasma power were maintained at 1.2 mbar and 130 W, respectively.

6.2.2 Preparation of graphene oxide (GO)

GO nanosheets were produced from natural graphite powder by an improved Hummers and Offeman method. Typically, a mixture of concentrated H_2SO_4 (98%)/H_3PO_4 (90:10 mL) was added to a mixture of graphite flakes (0.75 g) and $KMnO_4$ (4.85 g) in a round flask. The reaction was kept stirring at 50 °C for 12 h. After cooling to room temperature, the mixture was gently poured into ice (100 mL) with slow addition of 30% H_2O_2 (0.75 mL) under stirring. The solid product was separated by centrifugation at 7500 rpm for 30 min. After centrifugation, the product was washed with 5 % HCl solution 5 times to remove the sulphate ions, followed by washing with distilled water repeatedly until removal of chloride ions in neutral pH condition and finally washed with ethanol for 3-5 times. The resultant graphite oxide obtained was dried in vacuum at room temperature.

A homogeneous yellow brown suspension (0.5 mg mL^{-1}) of GO sheets in water/ethanol was achieved by ultrasonication (Fisher Transonic TI-H-10) for 3 h.

6.2.3 Preparation of carbon nanofibers (CNFs)

CNFs were kindly provided by Dr. Nianjun Yang (University of Siegen, Germany). The preparation was carried out *via* thermal chemical vapor deposition (CVD) in a tube furnace, which was equipped with a quartz tube. Copper (II) tartrate hydrate was pre-set in the quartz tube (reaction chamber) as catalyst precursor. After heating the precursor to 250°C in vacuum below 0.1 mbar, the chamber was filled with pure acetylene (C_2H_2) up to 500 mbar. Sequentially, the system was kept at this temperature allowing for the growth. After a growth time of 1 h, the process chamber was quickly evacuated and then heat up to 800°C to eliminate the hydrogen in as-grown nanofibers (so-called carbonization process) for 1 h. Finally, the whole system was cooled down slowly to room temperature.

© 2016 Tous droits réservés.

lilliad.univ-lille.fr

6.3 Modification and functionalization of electrodes

6.3.1 Immobilization of lysozyme aptamer on VA-NCNT

The fabrication of the lysozyme sensor includes three steps. Diazonium cations were prepared *in situ* by mixing $NaNO_2$ (10 mM) with 4-aminobenzoic acid (10 mM) in HCl (0.5 M). The mixture was left stirring for 5 min at 0 °C before being transferred to the electrochemical cell. Electrochemical modification was then performed by the reduction of the *in situ* generated 4-carboxyphenyl diazonium salt using five cyclic voltammetry scans from +0.4V to -0.6 V at a scan rate of 100 mV s^{-1}. The VA-NCNT-COOH electrode was then thoroughly washed with distilled water.

The terminal carboxylic acid groups of VA-NCNT-COOH electrode were activated by immersion in MES buffer (pH=5.0, 100 mM) containing EDC (100 mM) and NHS (20 mM) for 2 h at room temperature. The electrode was washed with MES buffer to remove excess reagents. The electrode was subsequently functionalized with neutravidin (100µg mL^{-1}) in PBS buffer (pH=7.4, 10 mM) for 1 h at room temperature, and rinsed copiously with PBS.
Immobilization of the biotinylated aptamer probe is based on the high affinity between avidin and biotin. The neutravidin modified VA-NCNT electrode was immersed in PBS buffer (pH=7.4, 10 mM) containing the biotinylated aptamer probe (1 µM) for 2 h at room temperature. After washing with PBS (pH=7.4, 10 mM), the electrode was rinsed with 0.1 % SDS to remove unbound aptamer.

6.3.2 Preparation of rGO, Cu NPs and rGO/Cu NPs-modified Au/Ti/glass interfaces by electrophoretic deposition

The electrophoretic deposition (EPD) of rGO/Cu NPs was carried out in a two-electrode cell, where the two electrodes were placed parallel to each other and separated by a distance of 1 cm. A platinum foil (1 × 2 cm^2) acted as the anode and the Au/Ti/glass substrate as the cathode. GO/$CuSO_4$ suspensions were ultrasonicated for 30 min before use. The electrophoretic cell was then filled with an ethanolic solution of GO/$CuSO_4$ (0.5:0.5 mg mL^{-1}) and a DC voltage of +50 V was applied for 1, 2 or 3 min. After deposition, the interfaces were rinsed with deionized water (three times) followed by blow drying with nitrogen.

© 2016 Tous droits réservés.

lilliad.univ-lille.fr

Thèse de Qian Wang, Lille 1, 2016

rGO modified Au/Ti/glass electrode and Cu NPs modified electrode were obtained by EPD in a similar procedure from single solution of GO (0.5 mg mL^{-1}) or $CuSO_4$ (0.5 mg mL^{-1}) in ethanol under otherwise similar conditions.

6.3.3 Preparation of CNFs, $Co(OH)_2$ and CNFs/$Co(OH)_2$-modified Au/Ti/glass interfaces

The EPD of CNFs/$Co(OH)_2$ was carried out by using a two-electrode cell, where the two electrodes are placed parallel to each other and separated by a distance of 1 cm. A platinum foil (1×2 cm^2) acts as the anode and the gold substrate as the cathode. For the EPD experiments, a suspension of CNFs and $Co(NO_3)_2 \cdot 6H_2O$ mixture in ethanol was transferred into the cell and a DC voltage of +50 V was applied for 1-3 min. The investigated ratio of CNFs to $Co(NO_3)_2 \cdot 6H_2O$ was varied as following: 1:1 (0.5:0.5 mg mL^{-1}), 1:2 (0.25:0.5 mg mL^{-1}) and 2:1 (0.5:0.25 mg mL^{-1}). After deposition, the interfaces were rinsed with deionized water (three times), followed by blow drying with nitrogen.

In the case of the formation $Co(OH)_2$ coated Au/Ti/glass interface, $Co(NO_3)_2 \cdot 6H_2O$ (0.5 mg ml^{-1}) dissolved in ethanol was used and electrophoretically deposited $Co(OH)_2$ films were obtained on cathode by applying a DC voltage of +50 V for 2 min.

CNFs modified Au/Ti/glass electrode was prepared by drop casting 30 µL of a DMF solution of CNFs (0.5 mg mL^{-1}) onto Au/Ti/glass substrate, followed by subsequent full evaporation of DMF in the oven at 80 °C.

6.3.4 Preparation of rGO/Au NPs/Tyr modified glassy carbon electrode (GCE)

In a Teflon vial were introduced 20 mL of an aqueous solution of GO (0.5 mg/mL) and tyrosine (10 mM) and heated at 100°C for 24 h, then an aqueous solution of $HAuCl_4$ (2 mM or 4 mM) was added into the mixture while keeping the temperature at 100°C and stirring for 1 h, 3 h or 6 h. The resulting dark purple precipitate, which could be easily separated from the supernatant *via* centrifugation, was washed three times with Milli-Q water. The obtained rGO/AuNPs/Tyr nanocomposites can be facilely re-dispersed in water with the aid of ultrasonication for 20 min.

Prior to modification, the GCE (diameter=3 mm) was polished with alumina and diamond paste and sonicated in a mixture of ethanol/acetone (1/1 v/v) for 15 min. After washing with Milli-Q water and drying with nitrogen, 30 µL of rGO/Au NPs/Tyr suspension

© 2016 Tous droits réservés.
lilliad.univ-lille.fr

Thèse de Qian Wang, Lille 1, 2016

(0.5 mg mL^{-1}) was casted onto the GCE, followed by heating at 80°C until full water evaporation.

6.4 Determination of lysozyme concentration in human serum (turbidimetric assay)

The determination of lysozyme in human serum sample is based on its enzymatic activity using a classic turbidimetric assay [1, 2]. *Micrococcus lysodeykticus* is a suitable substrate for the assay of lysozyme. In the presence of lysozyme, intact *Micrococcus lysodeykticus* Cells will be lysed. During incubation of lysozyme and the substrate, the turbidity of bacterial cell suspensions reduces gradually. A sensitive light scattering signal at 450 nm could be collected over time to explore the lysozyme assay.

In a typical process, *Micrococcus lysodeykticus* (0.1 mg mL^{-1}, 480 µL) in PBS (50 mM, pH 7.4) was incubated with either 20 µL of undiluted serum or lysozyme standard solution (2, 3, 4, 5, 10, 15, 20 µg mL^{-1}) and the decrease in absorbance at 450 nm was monitored over time (10 min). The rate of absorbance decrease at 450 nm was plotted against the concentration of lysozyme to build a calibration curve. The concentration of lysozyme in the human serum samples was deduced from the calibration curve and expressed based on hen egg lysozyme.

6.5 Determination of glucose content in human serum (colorimetric method)

The determination of glucose content in human serum sample is based on a well-established phenol-sulphuric acid method [3, 4]. The scheme depends on the dehydration of hydrolyzed saccharides to furfural derivatives in the presence of sulphuric acid. Further reaction with phenol form yellow complexes that adsorb light strongly around 490 nm (**Figure 6.1**).

© 2016 Tous droits réservés.

lilliad.univ-lille.fr

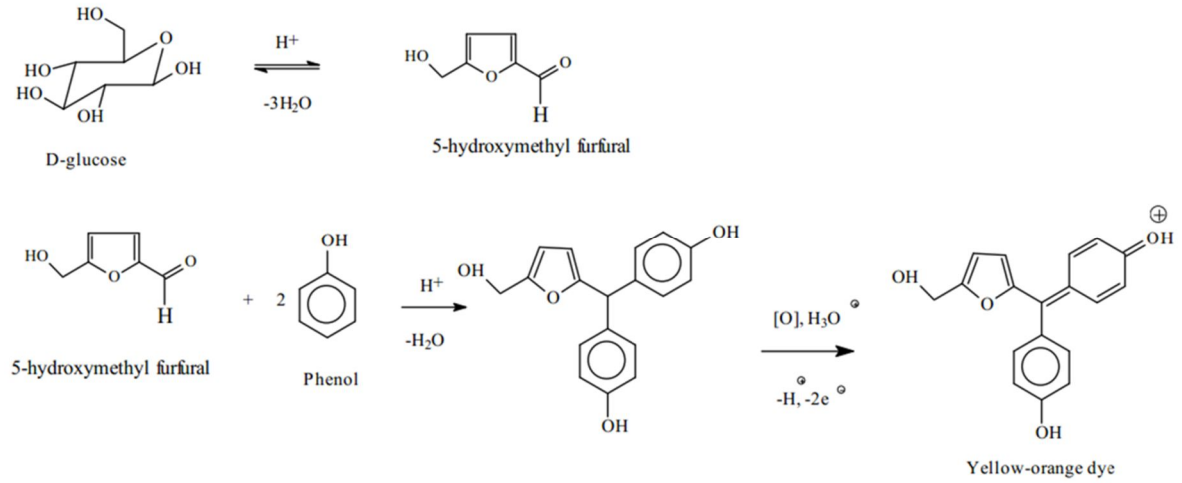

Figure 6.1 Schematic illustration of phenol-sulphuric acid method.

A standard calibration curve for glucose was then generated by mixing aliquots of aqueous phenolic solution (5 wt.%, 1 mL) and concentrated H_2SO_4 (5 mL) to a series of 1 mL aqueous glucose solution (20, 40, 60, 80, 100 μg mL^{-1}). After shaking continuously for 10 min, the absorption spectrum (450–550 nm) was recorded using a phenol-H_2SO_4-water mixture as a blank. The absorbance (λ_{max}=490 nm) difference was plotted against the glucose concentration. 50 μL of the human serum were diluted to 250 μL in water and mixed with 250 μL phenol/1.25 mL H_2SO_4 for glucose determination.

6.6 Instrumentation

For all the characterizations described below, the VA-NCNT carpets and interfaces modified through EPD were applied for analysis directly after corresponding modification unless otherwise specified. For GO, rGO/Tyr and rGO/Cu NPs/Tyr, the samples were prepared by casting 30 μL suspensions (0.5 mg mL^{-1}) dissolved in water 3 times on clean silicon wafer followed by subsequent drying in the oven at 80°C until full water evaporation.

6.6.1 X-ray photoelectron spectroscopy (XPS)

XPS experiments were performed in a PHI 5000 VersaProbe - Scanning ESCA Microprobe (ULVAC-PHI, Japan/USA) instrument at a base pressure below 5×10^{-9} mbar. Core-level spectra were acquired at pass energy of 23.5 eV with a 0.1 eV energy step. All spectra were acquired with 90° between X-ray source and analyzer and with the use of low

© 2016 Tous droits réservés.

lilliad.univ-lille.fr

Thèse de Qian Wang, Lille 1, 2016

energy electrons and low energy argon ions for charge neutralization. After subtraction of the Shirley-type background, the core-level spectra were decomposed into their components with mixed Gaussian-Lorentzian (30:70) shape lines using the Casa XPS software. Quantification calculations were conducted using sensitivity factors supplied by PHI.

6.6.2 Raman spectroscopy

Micro-Raman spectroscopy measurements were performed on a LabRam HR Micro-Raman system (Horiba Jobin Yvon, France) combined with a 473-nm laser diode as excitation source. Visible light is focused by a 100× objective. The scattered light is collected by the same objective in backscattering configuration, dispersed by a 1800 mm focal length monochromator and detected by a CCD camera.

6.6.3 Scanning electron microscopy (SEM) and energy dispersive X-ray (EDX) spectra

SEM images and EDX spectra of the films were obtained using a FEI Nova NanoSEM 450 scanning electron microscope with FEG (field emission gun, Schottky type) system equipped with an energy dispersive X-ray analyzer at an accelerating voltage of 20 kV.

6.6.4 Transmission electron microscopy (TEM)

The morphology and microstructure of the synthesized samples were analyzed using high-resolution transmission electron microscopy (HR-TEM) of JEM-2100 at an acceleration voltage of 200 kV.

For VA-NCNT, HR-TEM samples were prepared by dispersing a section of the CNT carpet in 2-propanol with gentle sonication for 30 min and then placing 1 drop of the solution on a 300 mesh Cu holey carbon grid (from SPI). For rGO/Au NPs/Tyr, the sample was drop-casted from an aqueous dispersion of rGO/Au NPs/Tyr onto a carbon coated TEM grid and the solvent was evaporated under gentle heating by a UV lamp.

6.6.5 X-ray diffraction (XRD)

XRD patterns were recorded in the range of 10-90° on a Rigaku D/Max-kA X-ray

© 2016 Tous droits réservés.

lilliad.univ-lille.fr

Thèse de Qian Wang, Lille 1, 2016

diffractometer using Cu Kα radiation (λ = 1.54 Å) at 40 kV and 30 mA.

6.6.6 UV-vis measurements

Absorption spectra were recorded using a Perkin Elmer Lambda UV/Vis 950 spectrophotometer in plastic cuvettes with an optical path of 10 mm. The wavelength range is 200-800 nm.

GO or rGO composites (20 μg mL^{-1}) were nicely dispersed in water with the aid of 3 h ultrasonication and then filled into the quartz cuvettes for measurements.

6.6.7 Specific surface area measurements

Nitrogen adsorption-desorption isotherm analysis was carried out using an ASAP 2020 Physisorption Analyzer. 0.1547 g sample was loaded into the sample tube for the measurement. The cold and warm free spaces were 50.2400 and 17.1169 cm^3, respectively. The equilibration interval is 5 s. Brunauer-Emmet-Teller (BET) theory and Langmuir Equation were applied to calculate their specific surface areas.

6.6.8 Zeta-potential measurements

Zeta-potential measurements were performed at 25°C using a Zetasizer Nano ZS (Malvern Instruments S.A., Worcestershire, U.K.) in 173° scattering geometry. The zeta potential was measured using the electrophoretic mode. All the measurements were completed by diluting the prepared suspension for EPD by 10.

6.6.9 Fourier transform infrared (FTIR) spectroscopy

FTIR spectra were recorded using a ThermoScientific FTIR instrument (Nicolet 8700) at a resolution of 4 cm^{-1}. Dried GO, rGO/Tyr, rGO/Au NPs/Tyr samples (1 mg) were mixed with KBr powder (100 mg) in an agate mortar, respectively. The mixture was pressed into a pellet under 10 tons load for 2–4 min, and the spectrum was recorded immediately. Sixteen accumulative scans were collected. The signal from a pure KBr pellet was subtracted as the background.

© 2016 Tous droits réservés.
lilliad.univ-lille.fr

Thèse de Qian Wang, Lille 1, 2016

6.6.10 Electrochemical measurements

All electrochemical measurements were performed using an Autolab PGSTAT 101 potentiostat (Eco Chimie, Utrecht, the Netherlands). The electrochemical cell consisted of a three electrodes system, with modified electrodes described above as working electrodes, an Ag/AgCl as the reference electrode and a platinum wire as the counter electrode. All measurements were performed at room temperature.

Cyclic voltammetry (CV) measurements were performed in aqueous solutions of $Fe(CN)_6^{3-/4-}$ (5 mM) containing 0.1 M KCl, 5 mM $Ru(NH_3)_6^{3+}$/0.1 M KCl at a scan rate of 50 mV s^{-1}. To evaluate the catalytic abilities of the electrodes, CV scans were performed in 0.1 M NaOH (in the case of glucose oxidation) as well as in 0.1 M PBS (pH=7.4, in the case of H_2O_2 reduction) at a scan rate of 50 mV s^{-1}.

Electrochemical detection of lysozyme was achieved by incubating the VA-NCNT-aptamer electrode with lysozyme solution in PBS at various concentrations for 30 min at room temperature, followed by rinsing with PBS buffer and transfer to a 5 mM $[Fe(CN)_6]^{4-}$ solution in 0.01 M PBS (pH=7.4) by differential pulse voltammetry (DPV) measurements. DPV measurements were carried out in the following optimized conditions: modulation time 0.05 s; interval time 0.5 s; initial potential -0.1 V; end potential 0.5 V; step potential 5 mV; modulation amplitude 25 mV.

Chronoamperometric detection of glucose was performed in stirring alkaline solution (0.1 M NaOH) by applying a constant potential of +0.55 V to the working electrode. Chronoamperometric detection of H_2O_2 on rGO/Au NPs/Tyr modified GC electrode was performed under N_2-saturated steady-state condition in stirring PBS (0.1 M, pH=7.4) by applying a constant potential of -0.6 V to the working electrode. Under both circumstances, a subsequent addition of glucose/H_2O_2 was realized and the current was measured when the background current became stable.

6.7 References

[1] Shugar, D. The measurement of lysozyme activity and the ultra-violet inactivation of lysozyme. *Biochimica et Biophysica Acta* **1952**, *8*, 302-309.

[2] Avanti, C; Saluja, V; van Streun, E L P; Frijlink, H W; Hinrichs, W L J. Stability of lysozyme in aqueous extremolyte solutions during heat shock and accelerated thermal

© 2016 Tous droits réservés.

lilliad.univ-lille.fr

conditions. *PLoS ONE* **2014**, *9*, 86244.

[3] Kochert, G. Carbohydrate determination by the phenol-sulfuric acid method. *Handbook of Phycological Methods* **1978**, *2*, 95-97.

[4] Boahen, Y; Isaac A. Colorimetric determination of carbohydrates in some brands of beer in Ghana as an indication of their glycemic index in the management of diabetes type II. *African Journal of Food Science and Technology* **2015**, *6*, 204-208.

© 2016 Tous droits réservés.

lilliad.univ-lille.fr

Thèse de Qian Wang, Lille 1, 2016

LIST OF PUBLICATIONS

[1] Qian Wang; Palaniappan Subramanian; Alex Schechter; Eti Teblum; Reut Yemini; Gilbert Daniel Nessim; Alina Vasilescu; Musen Li; Rabah Boukherroub; Sabine Szunerits. Vertically aligned nitrogen-doped carbon nanotube carpet electrodes: highly sensitive interfaces for the analysis of serum from patients with inflammatory bowel disease. *ACS Applied Materials & Interfaces* **2016**, *8*, 9600-9609.

[2] Qian Wang; Yannick Coffinier; Musen Li; Rabah Boukherroub; Sabine Szunerits. Light-triggered release of biomolecules from diamond nanowire electrodes. *Langmuir* **2016**, *32*, 6515-6523.

[3] Qian Wang; Yao Ma; Xin Jiang; Nianjun Yang; Yannick Coffinier; Hakim Belkhalfa; Nahed Dokhane; Musen Li; Rabah Boukherroub; Sabine Szunerits. Electrophoretic deposition of carbon nanofibers/$Co(OH)_2$ nanocomposites: application for non-enzymatic glucose sensing. *Electroanalysis* **2016**, *28*, 119-125.

[4] Qian Wang; Qi Wang; Musen Li; Sabine Szunerits; Rabah Boukherroub. Preparation of reduced graphene oxide/Cu nanoparticle composites through electrophoretic deposition: application for nonenzymatic glucose sensing. *RSC Advances* **2015**, *5*, 15861-15869.

[5] Qi Wang; Qian Wang; Musen Li; Sabine Szunerits; Rabah Boukherroub. One-step synthesis of Au nanoparticle–graphene composites using tyrosine: electrocatalytic and catalytic properties. *New Journal of Chemistry* **2016**, *40*, 5473-5482.

[6] Lijie He; Qian Wang; Daniel Mandler; Musen Li; Rabah Boukherroub; Sabine Szunerits. Detection of folic acid protein in human serum using reduced graphene oxide electrodes modified by folic-acid. *Biosensors and Bioelectronics* **2016**, *75*, 389-395.

[7] Ioana S. Hosu; Qian Wang; Alina Vasilescu; Serban F. Peteu; Valentin Raditoiu; Svetlana Railian; Vladimir Zaitsev; Kostiantyn Turcheniuk; Qi Wang; Musen Li; Rabah Boukherroub; Sabine Szunerits. Cobalt phthalocyanine tetracarboxylic acid modified reduced graphene oxide: a sensitive matrix for the electrocatalytic detection of peroxynitrite and hydrogen peroxide. *RSC Advances* **2015**, *5*, 1474-1484.

[8] Alina Vasilescu; Qian Wang; Musen Li; Rabah Boukherroub; Sabine Szunerits. Aptamer-based electrochemical sensing of lysozyme. *Chemosensors* **2016**, *4*, 10.

[9] Shixiang Lu; Haiyan Gao; Qian Wang; Wenguo Xu; Sabine Szunerits; Rabah Boukherroub. Fabrication of stable homogeneous superhydrophobic HDPE/graphene

© 2016 Tous droits réservés.

lilliad.univ-lille.fr

oxide surfaces on zinc substrates. *RSC Advances* **2016**, *6*, 29823-29829.

[10] Palaniappan Subramanian; Joanna Niedziolka Jonsson; Adam Lesniewski; Qian Wang; Musen Li; Rabah Boukherroub; Sabine Szunerits. Preparation of reduced graphene oxide–$Ni(OH)_2$ composites by electrophoretic deposition: application for non-enzymatic glucose sensing. *Journal of Materials Chemistry A* **2014**, *2*, 5525-5533.

[11] Alina Vasilescu; Szilveszter Gáspár; Mihaela Gheorghiu; Sorin David; Valentina Dinca; Serban Peteu; Qian Wang; Musen Li; Rabah Boukherroub; Sabine Szunerits. Surface Plasmon Resonance based sensing of lysozyme in serum on Micrococcus lysodeikticus-modified graphene oxide surfaces. *Biosensors and Bioelectronics* **2016**. 10.1016/j.bios.2016.03.040.

© 2016 Tous droits réservés.

lilliad.univ-lille.fr